

به نام خدا



مرکز دانلود رایگان مهندسی متالورژی و مواد

www.Iran-mavad.com





ADVANCES IN FATIGUE AND FRACTURE

Proceedings of the 13-th conference *New Trends in Fatigue and Fracture*, Mechanical Engineering Research Institute, Moscow, Russia, May 13-16, 2013

Editors:

Yury G. Matvienko

Moussa Nait Abdelaziz

Dmitry O. Reznikov

ADVANCES IN FATIGUE AND FRACTURE

Proceedings of the 13-th conference *New Trends in Fatigue and Fracture*, Mechanical Engineering Research Institute, Moscow, Russia, May 13-16, 2013

Editors:

Yury G. Matvienko,

Moussa Nait Abdelaziz

Dmitry O. Reznikov

All rights reserved. No part of this publication or the information contained herein may be reproduced, stored in a retrieval system, or transmitted in any form or by any means, electronic, mechanical, by photocopy, recording or otherwise, without written permission from the publisher

Although all care is taken to ensure integrity and quality of the publication and the information herein, no responsibility by the publishers not the author for any damages to the property or persons as a result of operation or use of this publication and/or the information contained herein.

ebook

Published by Mechanical Engineering Research Institute. Russian Academy of Sciences
101990, Maly Kharitonievsky lane, Moscow, Russia, 2013

Table of contents

Foreword	4
Anes V., Reis L., Li B., de Freitas M.. The shear stress space influence in multiaxial fatigue life evaluation	6
Barile C., Casavola C., Pappalettera G., C.Pappalettere Discussion on the Thermal Field Produced by Laser Annealing for the Residual Stress Relaxation	23
Besleaga Cr., Negriu R.M., Popescu I.C., Badea S.G.. Applications to Scrapers of Railway Machines	32
Bolshakov A.M., Zakharova M.I.The Statistical Analysis of Emergence Reasons and Development of Accidents on the Dangerous Objects Working at Low Temperatures by Method of FT and ET.	50
Casavola C., Moramarco V., Pappalettere C. Evaluation of the Impact Response of Polyethylene Sandwich Panel	58
Chausov M.G., Berezin V.B., Pylypenko A.P. Evolution of the Deformation field on the Surface of Sheet Plastic Materials at Dynamic Nonequilibrium Processes	72
Kapustin V.I., Zakharchenko K.V., Maksimovskiy E.A.. Physical Phenomena, Occurring under Periodic Straining of Metal Alloys	79
Kornev V.A Model for Fatigue Crack Growth with a Variable Stress description in terms of Crack Mechanics	86
Likeb A., Gubeljak N., Predan J., Matvienko Y. Determination of η_{pl} Factors for Pipe – Ring Specimens using Finite Element Analysis	94
Makhutov N.A., Reznikov D.O. Analysis of Large Scale Catastrophes in Complex Engineering Safety	104
Meliani M., Azari Z., Pluvinage G., Matvienko Y. Application of the Equivalent Notch Stress Intensity Factor on the Brazilian disk with U and V-notches	117
Močilnik V., Gubeljak N., Predan J. Retardation of Micro-Crack Initiation at Mechanical Components Subjected to Torsion Loading, Using a Discrete Dislocation Technique	130

Mokryakov V. Regimes of Fracture Initiation in a Plane with Square Lattice of Circular Holes under Uniaxial Compression	142
Morozov E.M.. Fracture Toughness for Crack Tip Stress Fields with Non Square Root Singularity	152
Panasyuk V., Nykyforchyn H. A Role of Hydrogen in the Degradation of Pipeline Steels	156
Petrova I.M., Gadolina I.V. Fatigue Damage Summation in Very High Loading Cycle Domain and Under Natural Ageing	167
Shifrin E.I., Shushpannikov P.S. Application of the Reciprocity Gap Functional Method for Identification of Small Well-Separated Defects in an Isotropic Elastic Body Using the Results of One Static Test	171
Skvorcov O. Estimation of Vibrating Durability of Elements of Hydro Power Turbines under Operating Conditions by Results of Vibration Control by Stationary Systems of Vibrating Monitoring.	205
Toribio J, Kharin V. Continuum Modelling of Trap-Affected Hydrogen Diffusion in Metals	223
Žužek B., Vodopivec F., Celin R., Godec M.. Effect of Ageing on Hardness, CV Toughness and Fracture of a Fe-CrNiMo Alloys	239
Author index	247

Foreword

The 13th International Conference “New Trends in Fatigue and Fracture” (NT2F13), Moscow, May 13-16, 2013 is the thirteenth in the series of Conferences on Fatigue and Fracture to be held in Russia. The NT2F conference was established by Prof. Pluvinage (Metz University, France) in 2000 as an annual meeting of the "Without Walls European Institute on Fatigue and Fracture" (WWIFF).

The NT2F13 was intended to be a forum to discuss the present trends in fracture mechanics which consider the actual geometry of defects in light of notch fracture mechanics and new approaches based on mesomechanics and incremental plasticity to offer new interpretations of loading mode and geometrical effects on fracture toughness. Fatigue and fracture of innovative metallic materials such as titanium alloys, as well as studies on nano, composite and biomaterials are certainly a challenge to the scientific community because of the variety of possible new research topics that could be developed. In this sense, NT2F13 Conference was also an excellent place to critically review design codes in view of the increasing complexity of the engineering scenarios.

The conference topics covered all investigations on fracture and fatigue of engineering materials and structures. The first topic was devoted to Multi-scale Models and Criteria, namely, nano, micro, meso and macro levels; experimental methods and numerical modelling; multiaxial/mixed mode fracture and fatigue; transferability of models and criteria. The Characterization of Crack/Notch Tip Stress Fields has been discussed. It includes experimental technique, numerical modeling, constraint and effect of non-singular terms, mixed mode fracture and fatigue. Structural Integrity and Engineering Safety focused on structural integrity assessment, reliability and risk analysis, non-destructive evaluation of structural

components, structural materials ageing, environmental and hydrogen embrittlement effect, residual stress. Approaches of Fracture Mechanics and Fatigue in Design and Technology were also presented, and attention was paid to codes and standards as well as lifetime extension.

We would like to express our thanks to all authors and reviewers who made this Conference fruitful and contributed in making the proceeding volume a valuable record of the recent advances in fracture and fatigue.

Yury G. Matvienko
Moussa Nait Abdelaziz
Dmitry O.Reznikov

THE SHEAR STRESS SPACE INFLUENCE IN MULTIAXIAL FATIGUE LIFE EVALUATION

V. Anes, L. Reis, B. Li, M. de Freitas

Instituto de Ciência e Engenharia de Materiais e Superfícies, Instituto Superior Técnico, T.U. Lisbon, Av. Rovisco Pais, Lisbon, Portugal
luis.g.reis@ist.utl.pt

Abstract: In multiaxial fatigue loading conditions the loading path type will subject the material lattice in different ways resulting in different material responses. However, many multiaxial fatigue criteria proposed in literature consider a constant damage scale for all kinds of loading situations, for instance the von Mises equivalent stress criterion consider that the relation between axial and shear fatigue damage is given by a constant value equal to 0,577. Moreover, the relationship of the equivalent shear stress related to the axial stress component may vary significantly depending on materials' type. In this work systematic fatigue experiments are presented for three structural steels, Ck45, AISI303 and the 42CrMo4, under proportional and non-proportional loading paths. The goal of this study is to quantify the relative damage between proportional and non-proportional loading paths through a proposed Y parameter, based on experimental tests. From this research, it is concluded that the appropriate axial/shear damage relation should be used to estimate multiaxial fatigue life.

Key words: Multiaxial Fatigue; Experimental tests; Shear stress space; Fatigue life

1. INTRODUCTION

Mechanical design against fatigue failure under multiaxial loadings continue to be a great challenge. The scientific research community in the multiaxial fatigue field remains in pursuit for the optimal

criterion to estimate the fatigue life under multiaxial loading conditions. Several criteria have been developed and proposed in the literature, [1], however, some them are difficult to implement and have many constraints. The verification and validation of those criteria discouraged the use of those methods. Moreover, many of the models proposed in the literature are validated by the own author data and usually do not corroborate with other author's lab work.

In this context, a simple multiaxial fatigue method is of prime importance to create a more general methodology to be validated and used by other researchers and engineers in an easy way. There are about three main categories on the multiaxial fatigue characterization, i.e. critical plane, stress invariants and integral approaches [2]. The critical plane approach has been gained great popularity in the last few years due to the simple physical concept involved around the methodology; it is common to find in the literature multiaxial energy models based on the critical plane formulations [3], [4] or even integral ones [2]. The main methodology in this type of approach is to find the critical plane where the shear stress or strain amplitude is greater, once the critical plane is identified the shear contribution can be adjusted with the normal stresses or strains damage contribution in that plane, which is the cases of Findley [5], Socie [6] models among others. Despite the popularity achieved by this type of approach, critical plane criteria have some shortcomings, such as, in some cases, the same stress amplitude is obtained for different planes, indicating several critical planes however the fractographic examination generally indicates only one initiation spot. The integral approaches are based on the stresses average within an elementary volume [2], where the damage is accounted in all possible material planes [7]. The invariant methods are based on the premise that a generic stress tensor can be divided into two other stress tensors, the deviatoric and the hydrostatic one. Another premise is that at HCF regime, the crack nucleation process occurs, mainly from shear stress/strain damage mechanisms. Moreover, the hydrostatic stress had a secondary role during the fatigue degradation process.

Under this paradigm, the shear stress amplitude determination is of prime importance and can be determined from the deviatoric stress tensor. The invariant approaches are based on the shear stress amplitude determination on the π plane which can be adjusted with the hydrostatic stress according to some author's methodology such as Sines [8], Crossland [9], Dang Van [10] or even von Mises, which doesn't consider the effect

of hydrostatic stress. Conventionally, the shear stress amplitude is usually evaluated by the Longest Projection (LP) or the Minimum Circumscribed Circle (MCC) approach in the shear stress space based on the von Mises equivalence ($\tau = \sigma / \sqrt{3}$) or the Tresca equivalence ($\tau = \sigma / 2$) for the multiaxial loading conditions. However, the relationship of the equivalent shear stress component related to the axial stress component may vary significantly depending on the type of the material. For example, the ratio of the torsion fatigue limit over the bending fatigue limit τ_1 / σ_1 varies from 0.5 for mild metals to 1 for brittle metals, [1]. This experimental evidence leads to conclude that the axial and shear stresses have fatigue damage regimes dependent on the material properties and loading conditions.

The loading path type will subject the material lattice in different ways resulting in a different material response for each request type; however many of multiaxial fatigue criteria consider a constant damage scale for all kinds of loading conditions, for instance the von Mises equivalent stress consider that the relation between axial and shear fatigue damages is given by 0,577 where the uniaxial shear stress can be obtained by dividing the axial stress by 0,577, being a constant value and independent on stress level, stress amplitude ratio and loading type. In some cases the von Mises equivalent stress is conservative estimating fatigue lives on the safe side i.e. the equivalent stress is bigger than the one which hits the fatigue life. Sometimes the opposite happens. One example is the uniaxial loading cases where the τ / σ usually is different than 0,577 for steels as mentioned before. Estimating shear SN curves by the axial one dividing by 0,577 is an inaccurate procedure, however plenty of multiaxial criteria have their formulations on shear stress space and the Coffin-Manson cyclic parameters are usually determined under uniaxial axial fatigue loadings, thus it is commonly used the von Mises scale factor to switch from stress spaces.

Determining the damage scale in axial and shear is of prime importance to understand the specific material fatigue behavior under multiaxial loading conditions. This damage scale is a material property and varies with the material type. In this work systematic fatigue experiments are presented for three materials, i.e Ck45, AISI 303 and the structural steel 42CrMo4 under typical axial-torsional multiaxial loading paths.

Five different loading paths are performed to study the non-proportional effect in the scale damage between axial and shear stresses. A series of experimental fatigue tests were carried out in HCF regime, where different non-proportional fatigue parameters such as: the phase angle between axial and shear stress components, a constant stress amplitude ratio and axial steady stresses are used. The experimental fatigue life results obtained under non-proportional loading conditions were analyzed and compared with the reference fatigue data obtained from a proportional loading case with same stress amplitude ratio. Conclusions about the material non-proportionality sensitivity and the non-proportional effect on the axial and shear scale damages are presented.

2. MATERIALS AND METHODOLOGY

Three materials were chosen to perform this work: the high strength steel 42CrMo4, an austenitic AISI 303 steel and the Ck45 a medium carbon steel. The 42CrMo4 is a quenched and tempered high strength steel being a special structural steel. It is commonly used in high and moderately stressed components for automobile industry such as: shafts, connecting rods, crankshafts, screws. The AISI 303 is an austenitic stainless steel with an excellent machinability compared with others austenitic stainless steels. It is primarily used when production involves extensive machining. The AISI 303 typical applications are nuts, bolts, bushings, shafts, electrical switchgear components. The Ck45 is a medium carbon steel used when greater strength and hardness is desired with good machinability. This material has an extreme size accuracy, straightness and concentricity combine to minimize wear in high speed applications. It is normally used on component parts for vehicles, shafts, bushings, crankshafts, connecting rods and parts for the machine building industry and steel for axes, knives, hammers. Specimens used in the test series were produced from rods of 25 mm of diameter, its geometry and dimensions are presented in Figure 1. The specimens were inspected and manually polishing through sandpapers of decreasing grain since the 200 until a 1200. The monotonic and cyclical properties of the selected materials [11, 12] are presented in Table 1.

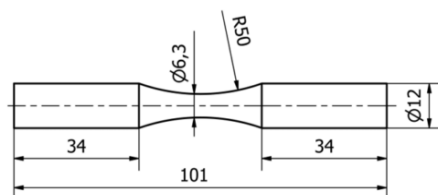


Figure 1. Specimen test dimensions.

Table 1: Monotonic and cyclic properties of the studied materials [11, 12].

	Ck45	AISI 303	42CrMo4
Tensile Strength (MPa)	660	625	1100
Yield Strength (MPa)	410	330	980
Young's Modulus (GPa)	206	178	206
Fatigue Strength Coefficient (MPa)	948	534	1154
Fatigue Strength exponent	-0.102	-0.07	-0.061
Microstructure	bcc	fcc	bcc

Fatigue tests were carried out through a biaxial servo-hydraulic machine. Testing conditions were as follows: frequency 3-5 Hz performed at room temperature and the failure condition was the specimen total separation or after a million cycles (runout). In order to study the materials sensitivity to non-proportionality five different loading paths under the combined loads, axial and torsion were selected. In Figure 2 is shown the loading paths used in this study represented in the von Mises stress space.

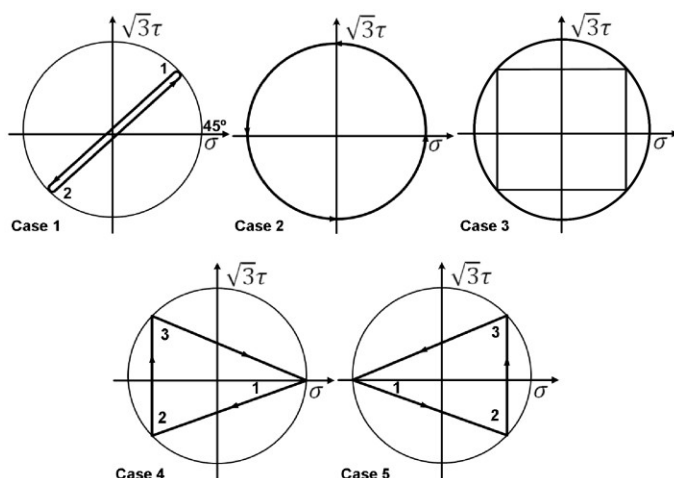


Figure 2. Multiaxial loading paths in the von Mises stress space.

Figures 3 and 4 show the non-proportional stress components variation along loading time. In the loading cases 3, 4 and 5 the maximum axial and shear stress amplitudes occur at the same time as verified in the proportional loading case, case 1. In loading case 2 the maximum stress amplitude in shear and axial never occurs at the same time, moreover in cases 3, 4 and 5 the loading path have steady regions where the applied stress remains constant during a specific loading period of time.

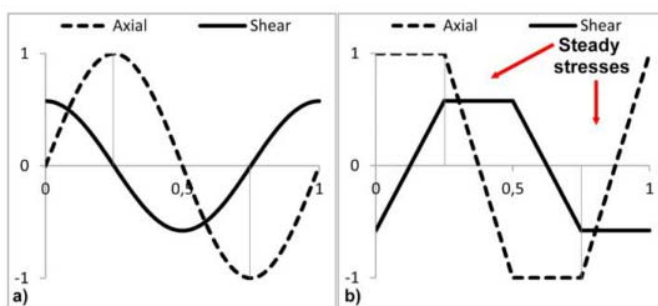


Figure 3. Axial and shear stress time variation for the a) case 2 and b) case 3.

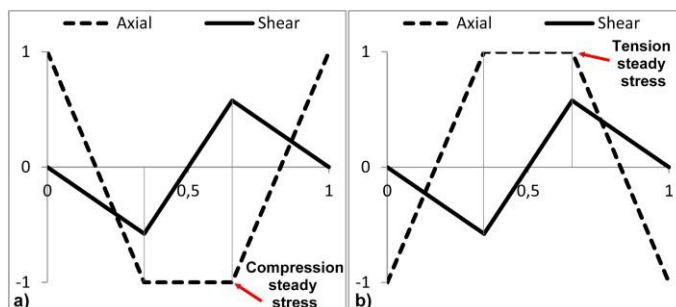


Figure. 4 Axial and shear stress time variation for the a) case 4 and b) case 5.

Non-proportional loading cases are generally identified by the principal directions variation during the loading period, however it is important to consider that principal directions variation is insufficient to fully characterize the non-proportional loading paths damage. The non-proportionality in a loading path creates a variety of damage mechanisms dependent on the loading trajectory type, the steady stresses in tension/compression and shear lead to a different fatigue degradation process on the material, also the simultaneous maximum stress amplitudes (shear and normal) occurrence during a non-proportional loading creates a greater damage. In this way the non-proportionality is much more than a phase angle between axial and shear stresses. As an example, the loading case 3 considered in this study is a non-proportional loading case with steady stresses in tension and compression during some loading periods per cycle. From previous works it was found that the steady stresses can increase or decrease the material fatigue strength, depends on the material type and behavior. Considering that the principal directions variation can be associated with other fatigue phenomena this possibility cannot be ignored when the non-proportionality damage is studied. In order to study the non proportional effect on the material's fatigue life it was considered 4 non-proportional loading cases with the same stress amplitude ratio i.e. $1/\sqrt{3}$, also the reference case, case 1, has this stress amplitude ratio. In previous works authors find out that the stress level effect on the stress amplitude ratio ($1/\sqrt{3}$) can be considered almost constant, thus it is expected that the biaxial loading components axial and shear SN curves between proportional and non-proportional loading paths be almost parallel to each other, which means that the relative position between the proportional stress

components and the non-proportional ones results strictly from the non-proportional effect on the damage process. In this study was considered the loading case 1, a proportional loading case, the reference case in order to quantify for each material the non-proportional effect on the materials fatigue damage. To do that it was compared in the non-proportional loading paths the axial and shear amplitude components with the proportional ones (loading path 1) at the same fatigue life. The reasoning to relate non-proportional and proportional fatigue damage is as follows: for the same fatigue life, and if the non-proportional load components are greater than the proportional ones, then under non- proportional loading conditions it is necessary to apply more energy to achieve the same fatigue life. Under this thinking, for the same amplitude load components in proportional and non-proportional conditions, the non- proportional loading case will have a greater fatigue life compared to the one achieved under proportional loading conditions being less damaging than the proportional one. On the other hand, if the non-proportional load components are lower than the proportional ones, then for the same fatigue life the energy to be spent on the fatigue damage process is less than the one needed under proportional loading conditions. In this situation the non- proportional loading path is more damaging than the proportional one.

To quantify the materials' non-proportional sensitivity it was considered a scale factor, Y , between proportional and non-proportional load amplitude components in order to match the axial and shear stress components (SN curves) from both loading paths, respectively. Figure 5 shows how the Y parameter is defined in order to quantify the material sensitivity to non- proportionality.

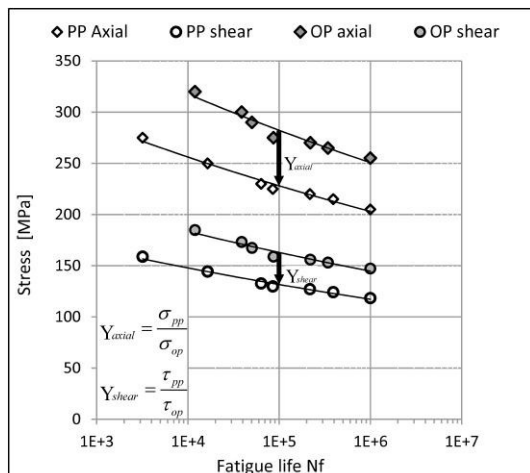


Figure 5. Y parameter definition.

If this scale factor Y , is less than 1 then the material is less sensitive to the non-proportionality, if the scale factor is equal to 1 then the non-proportional loading effect doesn't influence the fatigue life value and if the scale factor is greater than 1, it can be considered that the material is very sensitive to the non-proportional loading conditions, which means that is necessary less stress level for a non-proportional loading comparing with a proportional one, for the same fatigue life.

RESULTS AND DISCUSSION

Figure 6 shows the Ck45 experimental data for the selected multiaxial loading paths, for each non-proportional loading case was made a comparison with the proportional reference case, loading case 1, by representing in the same graph the proportional and non-proportional stress components versus fatigue life.

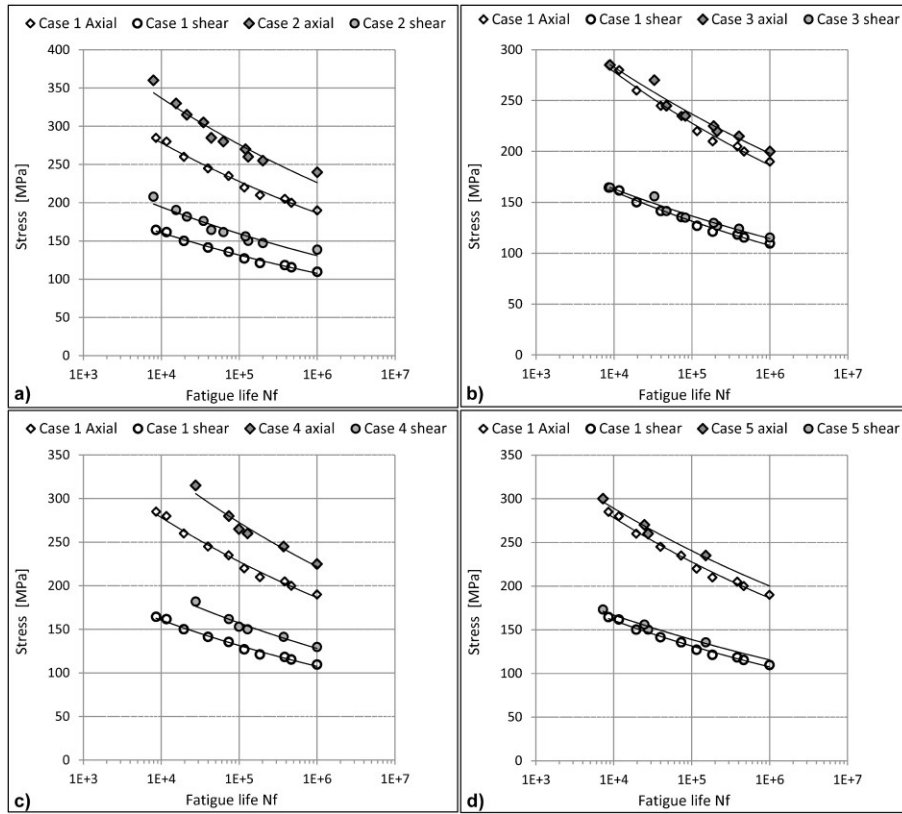


Figure 6. Fatigue life results and comparison with the reference case, Case 1, for the Ck45 material, a) Case 2, b) Case 3, c) Case 4 and d) Case 5.

Table 2 shows the obtained Y values for each non-proportional loading in order to match the stress components of the non-proportional cases against the proportional one, respectively. From the calculated results it was found that the Y parameter for shear and axial stress components is the same for CK45 and for the other selected materials and loading paths, presented ahead, thus the Y mentioned in this discussion concerns to both axial and shear stress components. Regarding loading case 2, Figure 6 a), SN results for the Ck45 are above the proportional ones indicating that the non-proportional stress level needed to cause the same damage is greater than the proportional one, this pattern is observed more or less on the Ck45 fatigue behavior in other cases.

Table 2: Ck45 Y values.

Y	Case 2	Case 3	Case 4	Case 5
Ck45	0.83	0.96	0.84	0.96

From here can be concluded that the loading path non-proportionality don't aggravate the damage process comparatively with the proportional loading case for this material. However comparing the Y value of the cases 3 and 5 can be concluded that the steady stress increases the Y value which means that the non-proportionality in this cases is more damaging than the one verified the case 2. On the case 4 the steady stress at compression don't affect significantly the Y value comparatively with Y from case 2, also the Y values for the cases 3 and 5 are equal which indicates that the steady stress in compression don't contribute significantly to the damage process supporting the previous statement. This increase almost equals the non- proportional damage to the proportional one i.e. in this cases the Y is near 1.

Figure 7 and Table 3 shows the results for the AISI 303, for this material and in all non-proportional loading cases the Y value is less than one indicating that the loading non-proportionality is less damaging than the proportional one. From Table 3 can be concluded that the cases 2,3 and 5 have a Y very similar, however some conclusions can be draw. The Y from the case 4 is the lowest of all, the compression steady stress some how decreases the non- proportional damage.

The highest Y was observed in the case 5, being the non-proportional loading most damaging; this is explained by the tension steady stress. Moreover on case 3 which will have the same value as case 5 if the compression steady stress don't affect the damage process, has a lower Y value indicating that the compression steady stress in this material compensates in some way the tension steady stress damage increase, having a decreasing action on the loading path non-proportionality damage, however this damage reduction don't totally compensate the damage increment resulted from the tension steady stress, to be so the Y value for the case 3 would be equal to the case 2. To corroborate this conclusion we have the Y result for the case 4 which is less than the case 2 Y indicates that the compression steady stress reduces the non-proportional damage in this material.

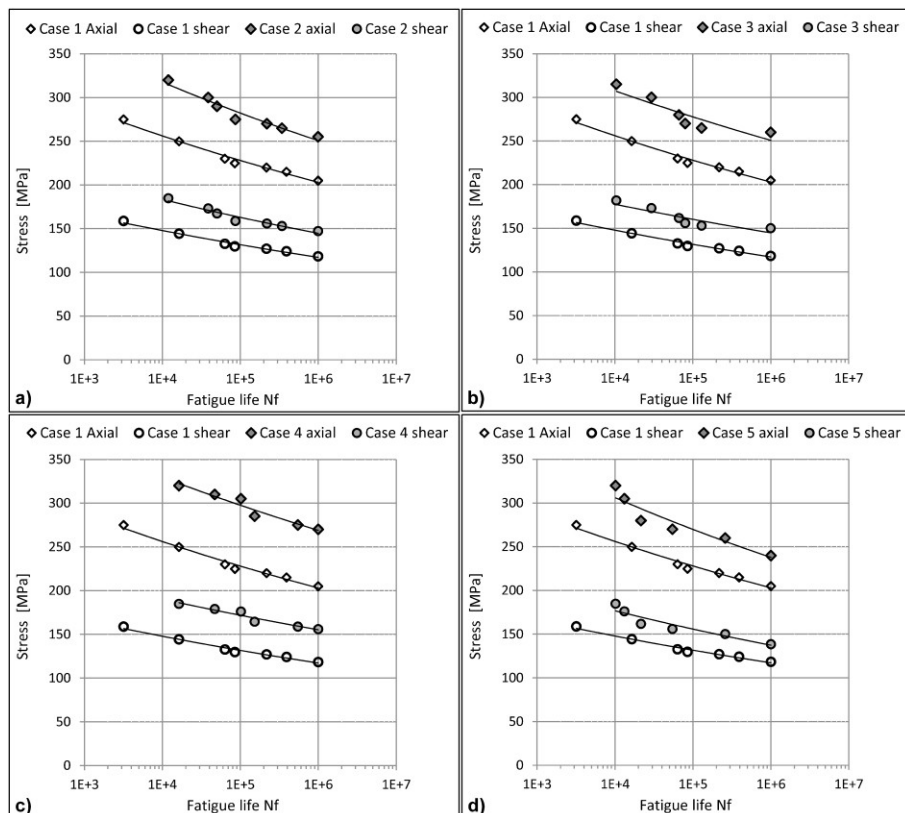


Figure 7. Fatigue life results and comparison with the reference case, Case 1, for the AISI 303 material, a) Case 2, b) Case 3, c) Case 4 and d) Case 5.

Table 3: AISI 303 Y values.

Y	Case 2	Case 3	Case 4	Case 5
AISI 303	0.81	0.83	0.77	0.85

The 42CrMo4 results are shown in Figure 8 and Table 4. For this material the Y values for cases 2, 4 and 5 are very close to the value 1, indicating that the proportional and non-proportional damage for the same fatigue life is very alike. The most damaging loading path is the case 3, where the damage increase due to tension and compression steady stress lead to that highest value. This sentence is corroborated with the fact that Y values for cases 4 and 5 are greater than the one obtained for the case 2. From these results can be concluded that this material is

not too sensitive to the loading path non-proportionality. However can be identified a different damage due to tension compression steady stresses, on this material the compression steady stress causes more damage than the tension one, this can be identified in Table 4 where the Y value of the case 4 is greater than the case 5.

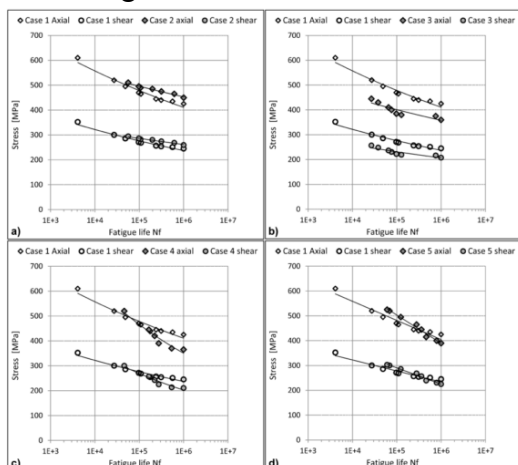


Figure 8. Fatigue life results and comparison with the reference case, Case 1, for the 42CrMo4 material, a) Case 2, b) Case 3, c) Case 4 and d) Case 5.

Table 4: 42CrMo4 Y values.

Y	Case 2	Case 3	Case 4	Case 5
42CrMo4	0.95	1.19	1.08	1

Table 5 summarizes the three materials results for the selected non-proportional loading cases. It can be concluded that for the same material the less damaging non-proportional loading path is the case 2, i.e. the fully out of phase loading case, excepting on the AISI 303 material where the lowest Y value was obtained in the loading case 4.

The 42CrMo4 is the material most sensitive to non-proportionality, regarding these experimental loading cases, this statement is supported by the 42CrMo4 Y values which are the biggest ones among the selected materials. Comparing the Ck45 and AISI 303 results, all Y values are less than 1, however the Ck45 Y values are greater which indicates that Ck45 is more sensitive to non-proportionality than AISI 303, but less than 42CrMo4. Comparing loading case 4 in all materials, it was

observed that the Y value of the loading case 4 on AISI 303 is less than the one obtained in the case 2, this behavior doesn't occur on Ck45 and 42CrMo4 materials, despite the AISI 303 microstructure (fcc) being different from the Ck45 and 42Crmo4 (bcc) in all other cases the AISI 303 follows the same pattern, i.e. the Y parameter in loading cases 3 and 5 are greater than loading case 2.

From here can be concluded that fatigue behavior varies with material type and depend on the material response to the cyclic solicitation type. Moreover, equivalent stresses or damage parameters determined based on a fixed stress space, i.e. based on a constant value for the relation between axial and shear stress components can lead to erroneous conclusions.

Table 5: Y values comparison for the selected materials and loading paths.

Y	Case 2	Case 3	Case 4	Case 5
Ck45	0.83	0.96	0.84	0.96
AISI 303	0.81	0.83	0.77	0.85
42CrMo4	0.95	1.19	1.08	1

4. CONCLUSIONS

The relative damage between non-proportional and proportional loading paths is studied in this work for three different materials. In order to evaluate and quantify that damage it is proposed a Y parameter which relates the non- proportional axial and shear stress amplitude components (SN curves) with the proportional ones, for each loading path, respectively. For Ck45 material the non-proportionality parameters such as phase angle variation, shear and axial steady stress components don't lead to a greater damage than the proportional one. However, between non-proportional loads can be concluded that the shear and compression steady stress components don't increase the non-proportional damage, being the most damaging non- proportional parameter for this material the tension steady stress component. The AISI 303 material has a non-proportional damage behavior similar to the Ck45 material, however one difference was observed in compression steady stress component (loading case

4), where the non-proportional damage is less than the loading case 2, this result was only observed in this material. Finally, the 42CrMo4 is the material most non-proportional damage sensitive.

Some remarks can be drawn from this study: three different materials were tested in multiaxial fatigue loading conditions; it was observed different non- proportional damage behaviors in the selected materials and loading paths; a constant damage scale factor between the axial and shear stress components is inadequate to quantify different damage mechanics in proportional and no- proportional loading paths.

ACKNOWLEDGEMENTS

The authors gratefully acknowledge financial support from FCT - Fundação para Ciência e Tecnologia (Portuguese Foundation for Science and Technology), through the project PTDC/EME-PME/104404/2008.

REFERENCES

1. D. Socie and G. Marquis. *Multiaxial Fatigue*, Society of Automotive Engineers, Warrendale, 2000; PA 15096-0001.
- 2 H. Zenner, A. Simbürger, and J. Liu, “On the fatigue limit of ductile metals under complex multiaxial loading,” *Int. journal of fatigue*, vol. 22, no. 2, pp. 137–145, 2000.
- 3 T. agoda, . Macha, and . d ows i, “A critical plane approach based on energy concepts: application to biaxial random tension-compression high-cycle fatigue regime,” *International journal of fatigue*, vol. 21, no. 5, pp. 431–443, 1999.
- 4 K. alat, M. Kure , P. Ogonows i, and T. agoda, “The multiaxial random fatigue criteria based on strain and energy damage parameters on the critical plane for the low-cycle range,” *International Journal of Fatigue*, 2011.
- 5 W. N. Findley, *A theory for the effect of mean stress on fatigue of metals under combined torsion and axial load or bending*. Engineering Materials Research Laboratory, Division of Engineering, Brown University, 1958.
- 6 D. Socie, “Critical plane approaches for multiaxial fatigue damage

assessment.,” ASTM special technical publication, vol. 1191, pp. 7–7, 1993.

7 I. V. Papadopoulos, “A High-cycle fatigue criterion applied in biaxial and triaxial out-of-phase stress conditions.,” *Fatigue & Fracture of Engineering Materials & Structures*, vol. 18, no. 1, pp. 79–91, 1995.

G. Sines, “Behavior of metals under complex static and alternating stresses,” *Metal fatigue*, vol. 1, pp. 145–169, 1959.

9 . Crossland, “Effect of large hydrostatic pressures on the torsional fatigue strength of an alloy steel,” in *Proceedings of the international conference on fatigue of metals*, 1956, pp. 138–149.

10 K. Dang-Van, “Macro-micro approach in high-cycle multiaxial fatigue,” *ASTM SPECIAL TECHNICAL PUBLICATION*, vol. 1191, pp. 120–120, 1993.

11 B. Li, L. Reis and M. De Freitas, “Simulation of cyclic stress/strain evolutions for multiaxial fatigue life prediction,” *Int. journal of fatigue*, vol. 28, pp. 451–458, 2006.

12 L. Reis, . Li, and M. De Freitas, “Analytical and experimental studies on fatigue crack path under complex multi-axial loading,” *Fatigue & Fracture of Engineering Materials & Structures*, vol. 29, pp. 281–289, 2006.

DISCUSSION ON THE THERMAL FIELD PRODUCED BY LASER ANNEALING FOR THE RESIDUAL STRESS RELAXATION

C. Barile, C. Casavola, G. Pappalettera and C. Pappalettere

Politecnico di Bari, Dipartimento di Meccanica, Matematica e Management, viale Japigia 182 - 70126 Bari (Italy)

c.barile@poliba.it, casavola@poliba.it, g.pappalettera@poliba.it, c.pappalettere@poliba.it

Abstract: In this paper the temperature field generated on the surface of a metal by a focused laser source is analyzed. If the induced temperature distribution is properly designed the process can be used for obtaining local stress relaxation of the material. In order to determine the expected temperature distribution many parameters must be taken into account such as the power and the intensity distribution of the laser source, the duration of the irradiation and the reflectivity of the surface at the specific wavelength. The influence of these parameters is numerically analyzed in this work. Temperature fields have been calculated for a point source and for a gaussian and a bi-gaussian beam in correspondence of different process parameters. Finally results in terms of stress relaxation for a given experimental configuration are presented based upon XRD residual stress measurements performed on an Al sample before and after the annealing process.

Key words: Aluminum, Laser annealing, Residual stress relaxation, Temperature distribution

1. INTRODUCTION

A sufficient high amount of thermal [1, 2, 3] and/or mechanical energy can relax residual stresses present on a sample. Several studies, based on this principle, were carried out in the last years. These studies were about the prolonging fatigue life of a damaged steel by using the annealing treatment in a protective environment atmosphere [4]. The effects of annealing prior to

material dealloying [5] and in cold-rolled stainless steel [6] were also studied; annealing treatments by a laser or a furnace were compared in [2].

Purpose of this study was to analyze the temperature field generated on the surface of a metal by focusing a laser source. In this way a local heating treatment can be performed and, as a consequence, a local stress relaxation can be achieved. This could be used to replace the traditional hole drilling (semi-destructive) method for measuring residual stress. This novel approach for relieving residual stresses would have the advantage of being nondestructive and quite easily applicable to in situ tests. A model of the expected temperature field for the given material is necessary in order to define the process parameters (power, irradiation time, beam diameter) necessities to get the desired annealing cycle. Simulations and measurements presented in this paper were performed on a Al5068 sample. X-ray diffraction was used to evaluate residual stresses before and after the annealing treatment [7,8].

2. MATERIALS AND METHODS

Numerical evaluation of the temperature distribution is carried out for a point source and for a gaussian and a bi-gaussian beam, by means of MatLab[®] Laser Toolbox [9-12]. Temperature field was modeled over a squared area 1.25 mm x 1.25 mm with the heating source centered in this area. An aluminum sample (Al5068) with squared cross section of 10 mm and length of 100 mm was used for the experimental part. A high power laser diode source ($\lambda=810$ nm) was used in order to perform the heating. Simulation and experimental were based on a 20 s interaction time. This is an amount of time sufficient to the laser to reach power stability.

In order to derive the temperature distribution field $T(x,y,z,t)$ at a given instant t the equation (1) can be used:

$$T(x,y,z) = \int_{-\infty}^{\infty} \int_{-\infty}^{\infty} I(x',y',t') \cdot W(x-x',y-y',z,v) dx' dy' \quad (1)$$

Where $I(x',y',z')$ indicated the absorbed intensity distribution.

Equation (1) holds under the assumption of constant material parameters, and a surface heat source (absorbed laser energy) defined by the power density $I(x,y)$ [W/m^2] eventually moving over the surface of the substrate with a velocity v . Eq. (1) can be rewritten in the following way [9-12]:

$$T = F_2^{-1} \{ F_2 \{ T \} \} \quad (2)$$

Where F_2 indicates the Fast Fourier Transform (FFT) so that Eq.(2) allows numerical evaluation of the temperature field. Based upon the results obtained by (2), laser parameter results can be adjusted in order to allow reaching of the desired annealing temperature. Based upon literature review [13], the target value for the material under study in this paper (Al5068) and for the given initial stress state was selected to be above 260 °C. Physical thermal properties of the material are shown in Table 1.

Table 1. Thermal and physical properties of Al5068

Density [kg/m ³]	2650
Specific Heat [J/(kg K)]	920
Thermal conductivity [W/(m K)]	85
Diffusivity [m ² /s]	3.49 10 ⁻⁵

With regard with experimental carried on in this paper it consisted in measuring residual stress on the surface of the sample by means of X-ray diffractometer. A Cr tube was used as radiogen source and residual stresses, along the longitudinal direction of the sample, were evaluated by the $\sin^2\psi$ technique. Measurements of residual stress were executed in several locations of the specimen and each measurement was replicated three times. Successively, the same specimen was locally heated and then the residual stress relieving was evaluated. If the induced temperature distribution is properly designed the process can be used for obtaining specific local stress relaxation of the material.

The heating source used, was a high power laser diode with a wavelength $\lambda=810$ nm and a maximum nominal power equal to 100 W. It was powered at a load-current of 5 A, corresponding to an output power of about 15 W. The diode laser beam was focused by using a biconvex lens with a focal length $f=110$ mm, in this way the spot was focused in a sufficiently small area. The focused spot had an elliptical area with a horizontal diameter of $d_x=386$ μm and a vertical diameter equal to $d_y=705$ μm . For this reason a bi-gaussian beam distribution was used to model the temperature field induced by the laser.

3. RESULTS

Results obtained from simulation for a gaussian and a bigaussian intensity distribution are reported in this section. These modes are typical for laser used in material processing application. For each distribution the temperature field at three different laser power (10 W, 15 W, 20 W) was calculated. As a

comparison also results obtained for a point source (10 W) distribution are reported (Figure 1). It shows, if compared with the other distributions at the same power, the highest temperature because it represents the most focused laser source. Fig.1 also shows that the temperature field is confined within about 100 μm below the surface of the specimen and this finding justifies the use of X-ray diffractometer as a convenient tool to evaluate residual stress relieving before and after the local annealing treatment; this technique, in fact, is characterized by the possibility to measure only up to a few tens of microns of depth into the specimen.

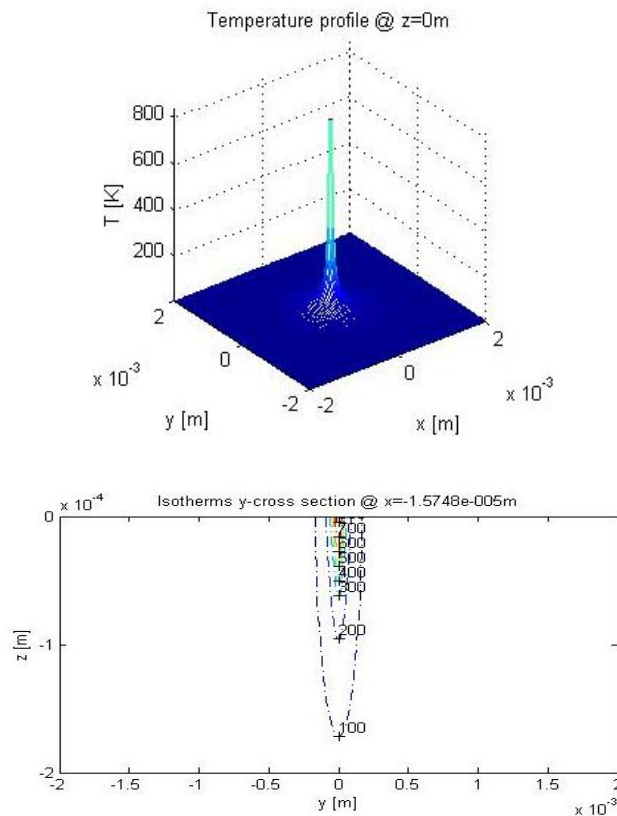


Figure 1. Plot for the point source powered at 10 W: (a) Temperature Field (b) Isotherms y cross section

The numerical results for a gaussian beam are reported in Figure 2-4. The diameter used for the gaussian beam distribution was $d_{\text{gau}} = 500 \mu\text{m}$. It should be noticed that the extension area of interaction is now wider than in the previous case study and having the source a gaussian distribution, the temperature field results symmetric in both directions.

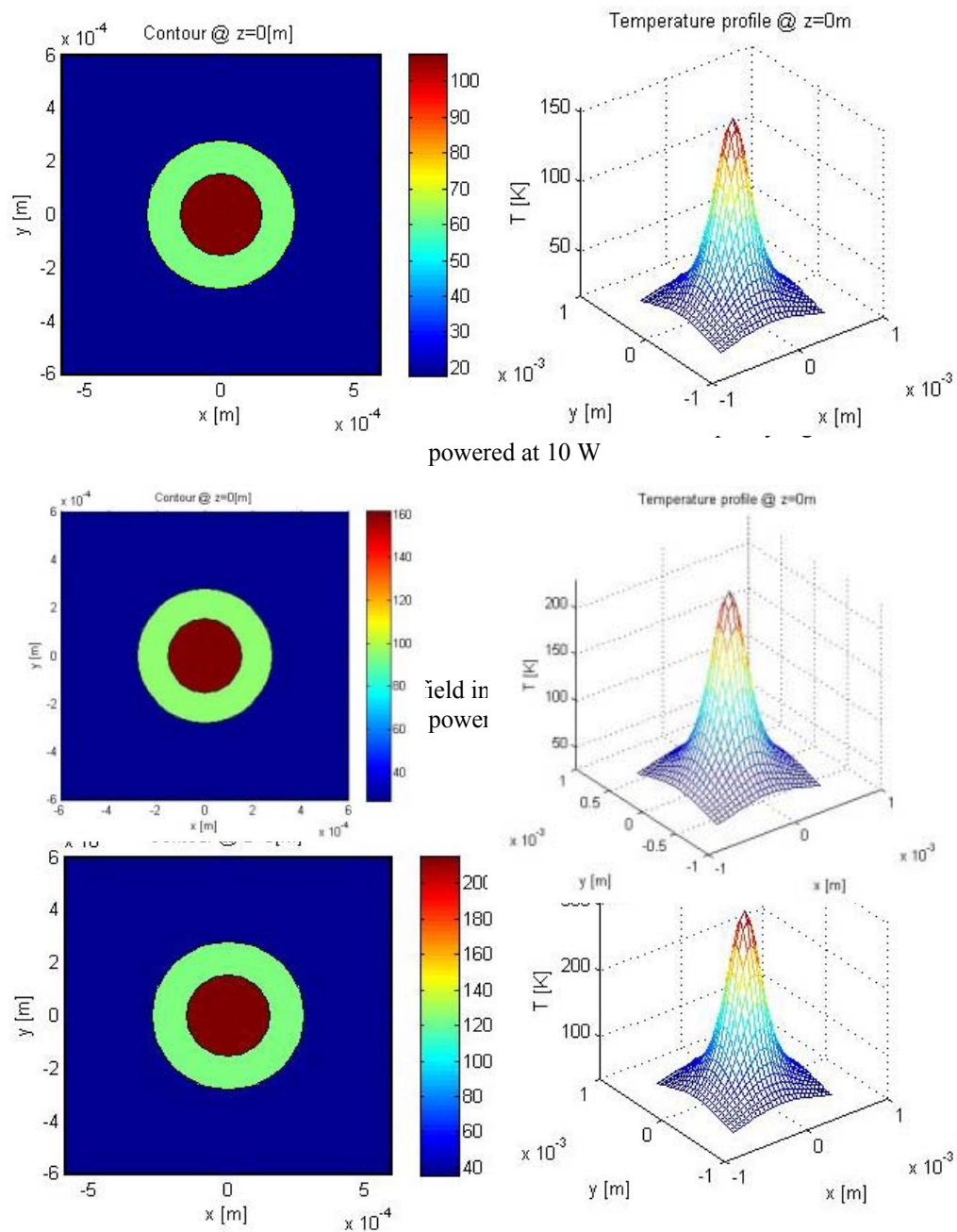


Figure 4. Plot of the temperature field induced in an Al 5068 sample by a Gaussian beam powered at 20 W

The numerical results for a gaussian beam are reported in Figure 5-7 The diameters of the bi-gaussian beam were set to be $d_x= 386 \mu\text{m}$ and $d_y= 705 \mu\text{m}$ that is to say coincident with the parameters of the laser source used for the experiments. It should be noticed that, due to the shape of the beam, also the temperature field appear to be elliptical.

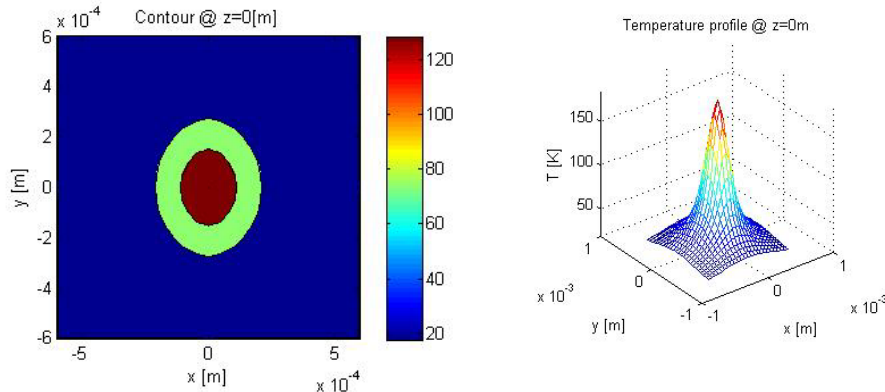


Figure 5. Plot of the temperature field induced an Al 5068 sample by a gaussian beam powered at 10 W

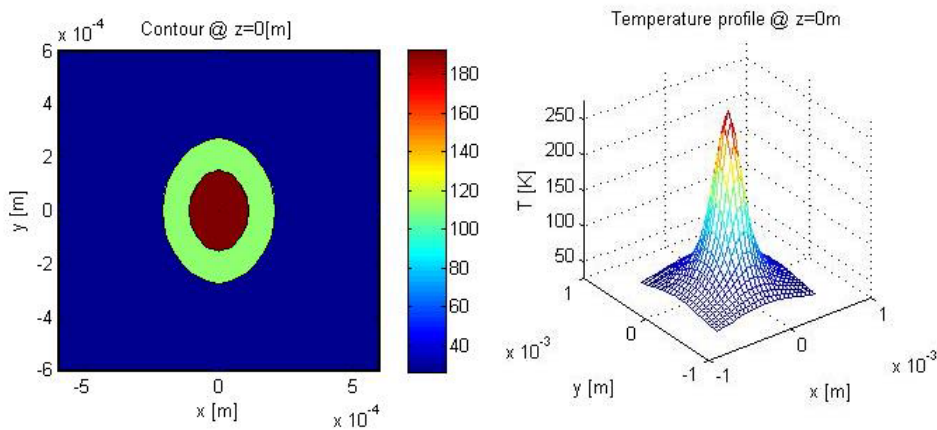


Figure 6. Plot of the temperature field induced an Al 5068 sample by a gaussian beam powered at 15 W

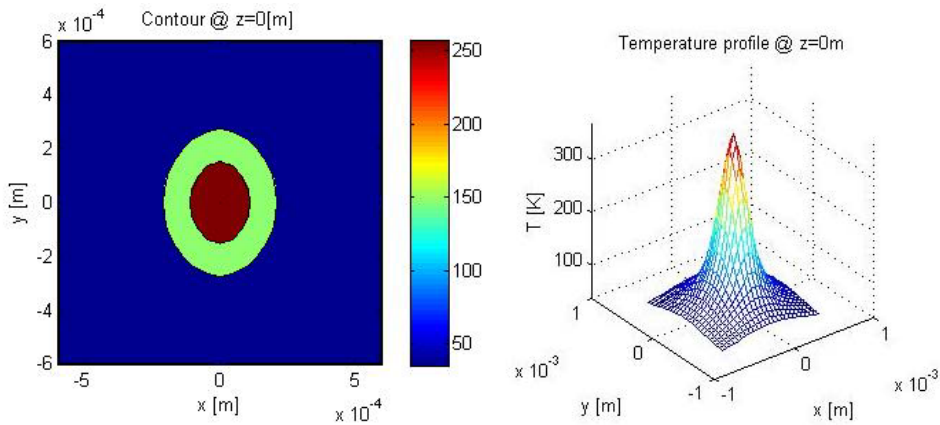


Figure 7. Plot of the temperature field induced in an Al 5068 sample by a gaussian beam powered at 20 W

It is important to observe that it is possible to achieve an increase in temperature of 276 K in correspondence of a 15 W absorbed power from a bigaussian laser source with the given characteristics. Due to these findings experimental measurements were performed in correspondence of this level of power. In Fig.8 the experimental trend of relaxation, for the longitudinal stress, is reported for the specimen subjected to three repeated cycle of annealing. At the end of the sequence a 25 % of relaxation with respect to the initial stress level has been observed.

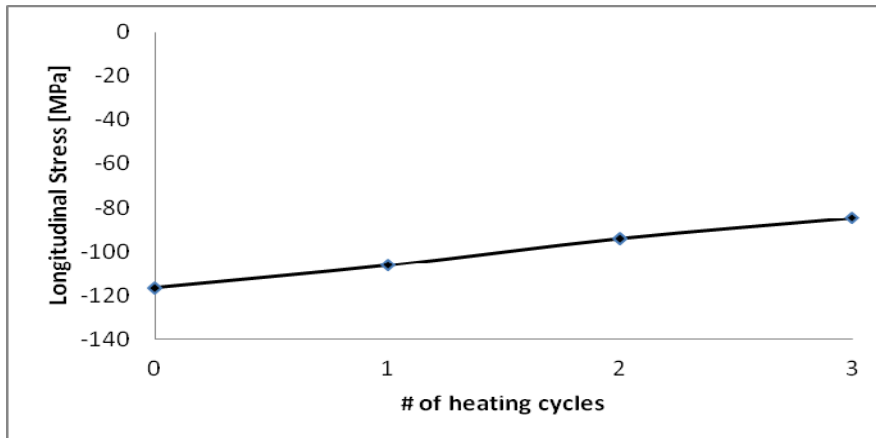


Figure 8. Experimental trend of stress relaxation after annealing treatments

4. CONCLUSIONS

In this work the effects of laser annealing process on residual stresses has been investigated. The procedure implies a substantial localized relaxation in a very short time with respect to the traditional heat treatments. Temperature distribution of different kind of sources were analyzed in correspondence of different process parameters. Based upon results from numerical models an experimental set up was built in order to perform annealing treatment and diffractometric measurements confirmed the effectiveness of the process in obtaining local stress relaxation.

REFERENCES

1. H. Holzapfel, V. Schulze, O. Vohringer and E. Macherauch. Residual stress relaxation in an AISI 4140 steel due to quasistatic and cyclic loading at higher temperatures. *Materials Science and Engineering A*, 248(1):9–18, 1998.
2. H. Liu, R.X. Guo, F. Viejo and Z. Liu. Comparison of microstructure and residual stress characteristics of electroless ni-w-p coatings annealed with a laser and a furnace. *Surface & Coatings Technology*, 206(8-9):2380-2387, 2012.
3. I. Nikitin and M. Besel. Residual stress relaxation of deep-rolled austenitic steel. *Scripta Materialia*, 58(3):239-242, 2008.
4. B. Du, W. Zhu, B. Ma and L. Li. Prolonging fatigue life of a damaged steel by annealing. *International Journal of Fatigue*, 26(9):1017-1023, 2004.
5. E. Seker, J. T. Gaskins, H. Bart-Smith, J. Zhu, M. L. Reed, G. Zangari, R. Kelly and M. R. Begley. The effects of annealing prior to dealloying on to the mechanical properties of nanoporous gold microbeams. *Acta Materialia*, 56(3):324-332, 2008.
6. Y.D. Wang, R. Lin Peng, X.L. Wang and R.L. McGreevy. Grain-orientation-dependent residual stress and the effect of annealing in cold-rolled stainless steel. *Acta Materialia*, 50(7):1717-1734, 2002.
7. B.D. Cullity. Elements of X-ray diffraction, 2nd ed., *Addison-Wesley*, 1980.
8. Determination of Residual Stresses by X-ray Diffraction - Issue 2 Measurement Good Practice Guide No. 52, edited by Tony Fry, Crown, 2005.
9. G.R.B.E. Römer. Matlab Laser Toolbox User Manual. Version 0.1 beta. University of Twente, Faculty of Engineering Technology, 2010.

10. G.R.B.E. Römer and R.F. de Graaf. Direct calculation of optimized laser power density profiles for laser heating. *Proceedings of the 15th meeting on modeling of material processing with lasers*, Austria, 2000.
11. G.R.B.E. Römer and A.J.Huis in't Veld. Matlab Laser Toolbox. *Physics Procedia*, 5(0): 413-419.
12. G.R.B.E. Römer and A.J.Huis in't Veld. Matlab Laser Toolbox. *Proceedings of the 29th International Congress on Applications of Lasers & ElectroOptics (ICALEO)*, Anaheim(CA), 2010.
13. <http://www.keytometals.com/Article139.htm>.

APPLICATIONS TO SCRAPERS OF RAILWAY MACHINES

Cr. Besleaga, R.M. Negriu, I.C. Popescu, S.G. Badea

* *ECONET PROD SRL, Bucharest, Romania*
cristibesleaga@yahoo.com

Abstract: In the frameworks of railway infrastructure, the various forms of wear phenomena have a significant share. The objects of this paper are the scrapers from the ballast cleaning railway machines. These scrapers work in an intensive stress and wear regime. FEM simulations were performed on the models and also experimental research was done (on site) in various work conditions. We established the optimal shapes of the scrapers and of the zones and a new type of scraper.

Key words: Railway machine, wear, scrapers, F.E.M

1. INTRODUCTION

To maintain elasticity for damping requests (including overload, shock) resulting from the dynamic rolling of the railway material (locomotives, coaches and freight, rail cars for railway maintenance) and the draining capacity for atmospheric precipitation (drainage from rainfall, from melting snow) of the ballast prism, specific maintenance work is carried out [1, 2]. These works consist in raising and excavating crushed stone prism (Fig.1), the transport of the resulting material to the cleaning facility, sorting and

separating of the adequate crushed stone from inappropriate crushed stone and waste.



Figure 1: Raising and excavating crushed stone

Finally, the crushed stone is recovered and reintroduced in the rail (normally between 55% - 65% of the initial amount) and the inadequate crushed stone and waste are discharged. The work is performed mechanically by cleaning machines that riddle the ballast prism [3], as the one shown in Fig. 2.

Due to local conditions, specific to the ground (infiltration of water, lower consistency of the land etc.), local deformations of the track geometry (plain), successive freeze-thaw phenomena, wear and appearance of big races in the clamping and fastening system of rails, deformations or superficial defects of rails, joints for joining the end of the rails and so on, combined phenomena of intense stress and wear of the crushed stone (which is gets grinded, crumbled) and excessive compaction of the crushed stone prism due to repeated wetting and drying conditions appear, phenomena that cause local effects of excessive clogging ($>> 30\%$) of the crushed stone prism and forming of very hard portions (conglomerates) (Fig. 3). These conglomerates can have equivalent hardness of broken stone, considering that the movement of loosening

(scarification) occurs crushing it (Fig.3).



Figure 2: Ballast cleaning machine



Figure 3: The local effects of excessive clogging (>> 30%) of the crushed stone prism- the emergence of very harsh portions (conglomerates).

2. WORKING AND SOLICITATION CONDITIONS OF SCRAPERS

The working movements of the excavation installation (excavator chain) and scrapers are:

- the auxiliary movement, free travel, without solicitation, in oblique rectilinear motion, lowering the excavator chain on the descent guide (chute) Fig. 4, Item 6;

- the main working movement of raising, digging and chopping, of pulling and dislocation of crushed stone from the clogged ballast prism, materialized by the horizontal movement on the front cross bar (Fig.4, item 2), from right to left in respect to the direction of advancement of the vehicle, characterized by a complex stress system, due to the contact with the clogged ballast prism, which manifests in high dynamic stress of bending, shearing, crushing, high speed (shock) and intense abrasion wear due to rubbing with the crushed stone;

- the secondary working movement of transporting material (crushed stone and waste) resulting from rising, digging and crumbling the clogged crushed stone prism, towards the installation for screening, cleaning and sorting of crushed stone depending on varieties and selecting of crushed stone proper for waste. It is materialized by an oblique rectilinear movement, of raising the excavator chain on the climbing guide (chute) (Fig. 4, item 10). This phase is characterized by a system of reduced demand, mainly due to friction with excavated material which has a natural tendency to flow back to the guide (trough) under gravitational effect.

In Fig. 4 is shown the excavation installation: 1 – clogged crushed stone prism; 2 - front cross bar of the installation (raising and excavation area); 3 – sleeper; 4 - cleaned crushed stone prism; 5 – rail; 6 – chain lowering guide (gutter); 7 - chain excavator; 8 – the chain's direction of work movement; 9 - chain wheel drive; 10 – the chain's climbing guide (gutter) (transportation of excavated material); 11 - the direction of advancement.

In Fig. 5 are shown the main components of the excavator chain: 1 – joint bolt; 2 – connecting chain link; 3 – scraper shovel; 4 – classic scraper.

The demands on the elements of the excavator chain (Fig. 5) during the work movements are complex (repeated dynamic demands of traction, bending, shearing, crushing, with high speed) and have high intensity [4], as evidenced by the stress analysis performed on a section of the chain (a scraper shovel with 2 connecting chain links, joining bolts and the classic scraper) using CAD with F.E.M. - Fig. 5a and 5b.

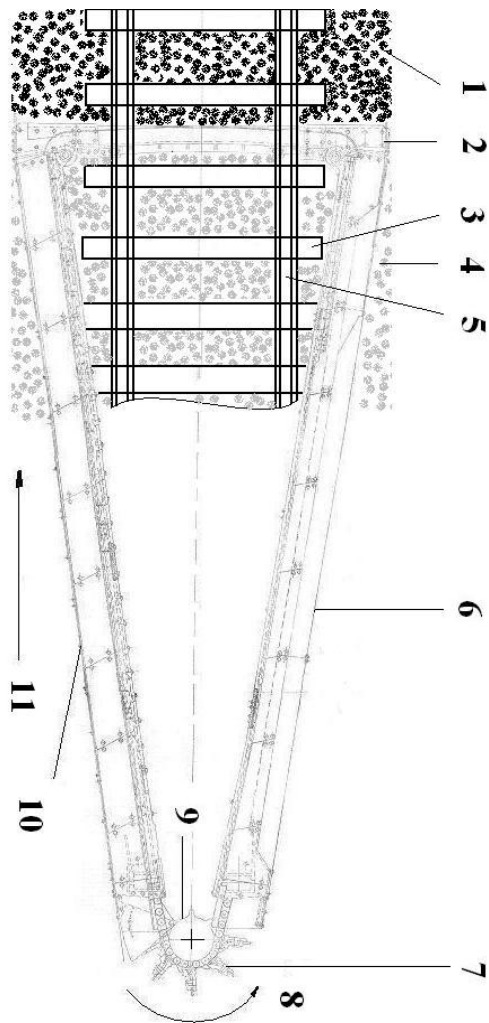


Figure 4: Excavation installation

Several critical areas in the section of the chain can be seen, of which the most critical is the active (top) part of the scraper, where tensions state approaches the flow limit $\sigma_{0,2}$ ($R_{p0,2}$) of heat treated steel alloys (~ 500 MPa). Considering the dynamic effect of demands (variable demands), fatigue also occurs, both in the materials' structure but also in the superficial layer of the

contact surfaces, such that the tensions state is coming dangerously close to the fatigue limit σ_{-1} of heat treated steel alloys (~ 400 MPa).

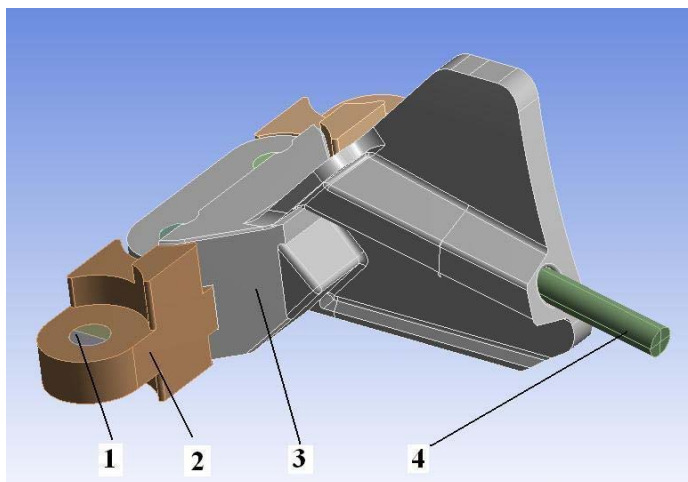


Figure 5: The main components of the excavator chain

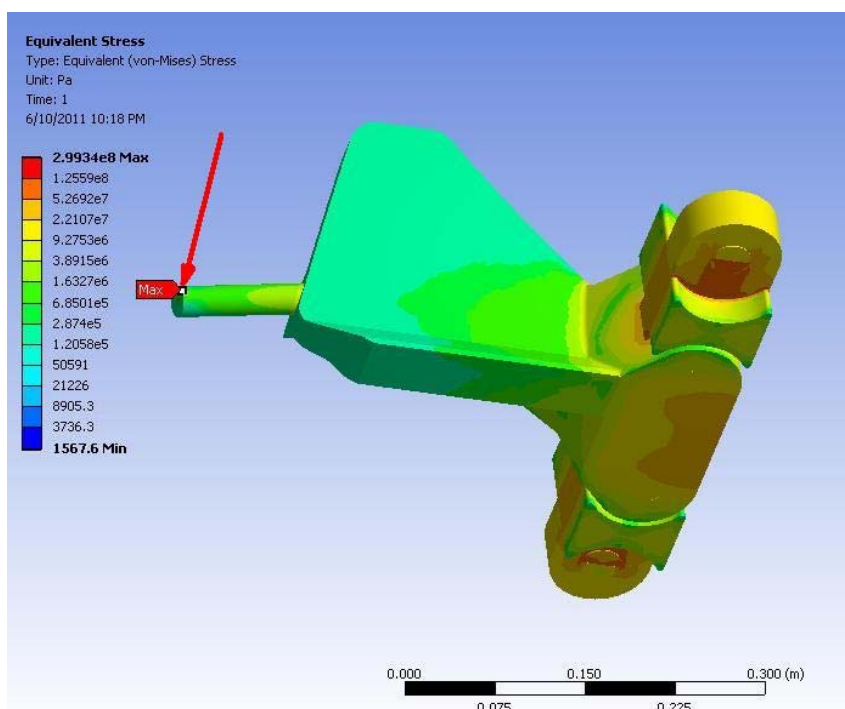


Figure 6 (a): Equivalent tension state (von Mises criterion) in a section of the

chain

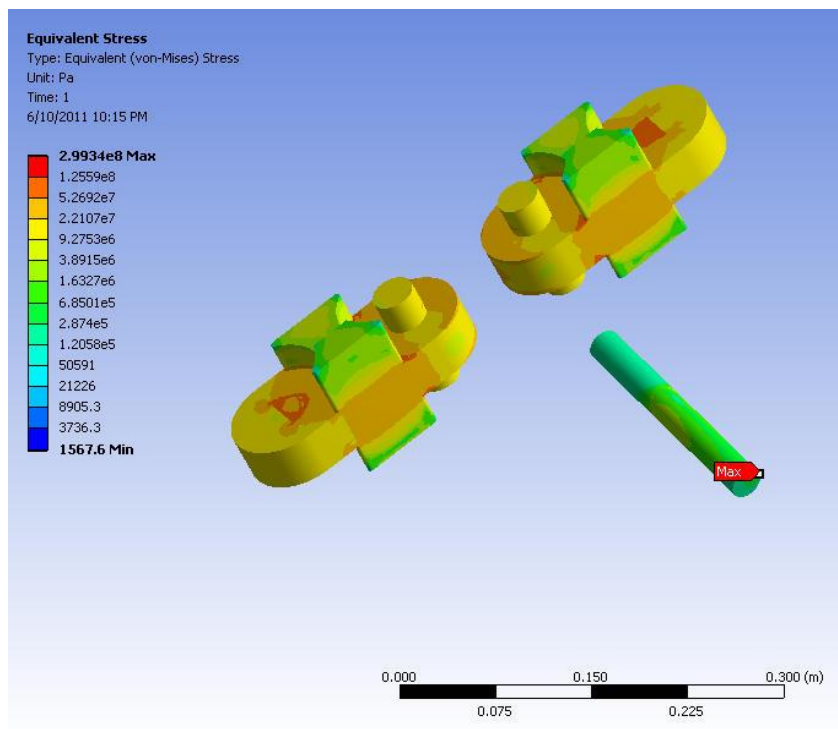


Figure 6 (b): Equivalent tension state (von Mises criterion) in a section of the chain

3. WEAR PHENOMENA OF SCRAPERS

Repeated complex dynamic requests lead to phenomena of intensive abrasion wear, fatigue and impact (shock) in the main elements of the excavating chain (scraper shovel, connecting chain links, joint bolts, scrapers). For scrapers, the wear phenomena and their effects are shown in Fig. 7 and 8.

In Fig.8 is shown the classic scrapper for excavator chain type MCB 450: 1 – new piece (L = 220 [mm]) 2 – used piece (L = 145 [mm]); 3 – used piece (L = 165 [mm]).



Figure 7: Scrapper at the maximum wear limit in mounted on scraper shovel state.



Figure 8: Classic scrapper for excavator chain type MCB 450.

From the analysis of using the classic scraper made of heat treated alloy steel (18MoCr11; 13CrNi30; 42MoCr11; 60Si15A a.s.o., with $\sigma_r \sim 800$ [MPa]), it was found that they had a reduced durability, approx. 1-3 [km] of scarification (rising) and excavation, depending on the degree of clogging and hardness of the ballast prism. Consumption of expensive materials (heat treated alloy steel) is high and a significant part of it, between 66% - 75% is converted into waste.

One of the solutions to reduce the intensity of the wear on the active part of the scrapers was the development of hard materials based on PM technology for making and assembling hard bodies and mounting them in the active part of the scrapers [5]. Experimental research in real conditions, on work sites [6], with these constructive scrapers solutions have demonstrated improved wear behavior of the active part and the value of materials and PM technology to achieve these outcomes (durability increased by 100%, from 2 to 6 [km] of ripping-rising and excavation, depending on the degree of clogging and hardness of the ballast prism).



Figure 9: Wear forms of the active part of fixed scrapers with sintered metallic carbide.

During experimental research, a new form of wear of the active part of scrapers was observed (Fig. 9), both in the CMS tough body but especially in

the scraper's body (support) on which the body of sintered metallic carbide is mounted. There was a more intense wear on the active part (body from sintered metallic carbide and support body of the scraper), part that come first in contact with the clogged crushed stone hard prism. Through wear a new surface is created, inclined at approx. 45 ° to the direction of work (ripping-rising-excavating). On the other hand, on the back-side of the active part no wear effects are found, showing unused technical reserves, fact being used in the following.

4. NEW TYPES OF SCRAPERS WITH SINTERED METALLIC CARBIDES

To resolve problems of wear observed during experimental research (see chap. 3), we have developed new types of scrapers with CMS that will lead to improved wear resistance and increased durability. A new type of scraper is shown in Fig.10.



Figure 10: Improved version of the scraper for the excavation chain type MCB-450.

The new type scraper in Fig. 10 has an improved active part shape, through the excess material added and shaped accordingly to the wear shape, leading

to a geometric form close to a cone. Additionally this type of scraper can rotate on its axis to allow the entire surface of the active part to work in contact with rising material (dislocated), using the whole reserve of material existent on the active part. Experimental research carried out in real conditions, on the site of the railway infrastructure maintenance works have shown an improvement in the wear behavior of the active part compared to the previous type (Fig. 9).

Additionally, to increase the wear resistance of the surface layers the scrapers' active part, extremely tough alloy powders were loaded experimentally through laser melting in the area adjacent to the active part (support), to reduce the wear intensity Fig.11.



Figure 11: Scraper type MCB-450 loaded with extremely tough alloy powders through laser melting

During the experimental research in real conditions, it was found that the assurance and retention system of the scraper in scraper shovel mounting position, system that allows at the same time the rotation around the scraper's axis (for uniform wear) and scraper control in different working positions, is affected by non-compliance results from the technological manufacturing process (manufacturing deviations), both of the scraper and of the insurance and maintenance in working position bolt (safety bolt), and human errors

during installation. To correct the nonconformity, a new type of scraper was developed, like the one in Fig.12, the scarification bolt, mobile (rotating) and interchangeable being shown in Fig.13.

In Fig.12 is shown the new type of scraper for the excavation chain type MCB-450: 1 – body of the scraper; 2 - bush support; 3 – scraper bolt, mobile (rotating) and interchangeable; 4 - brazing material; 5 – extremely tough insert from CW-Ni and (CW-(W, Ti) C)-Ni composite material with structural material gradient; 6 - extremely tough alloy cords through laser melting; 7 – elastic pin; 8 - Insurance bush; 9 - releases for securing and retaining the scraper in the mounting position on the chain's scraper shovel.

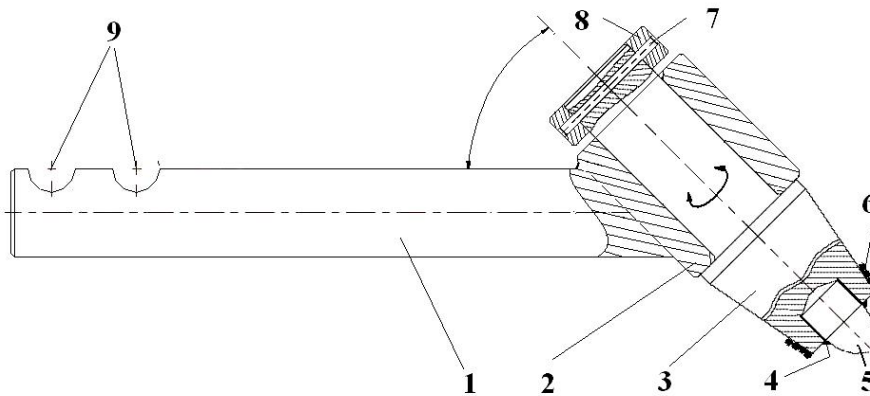


Figure 12: New type of scraper for the excavation chain type MCB-450



Figure 13: Scraper bolt, mobile (rotating) and interchangeable (see Fig.12, Item 3)

5. ANALYSIS OF THE NEW SCRAPERS WITH CAD- FEM METHOD

The simulation of the tension state was made using Autodesk Inventor for the model (Fig.14a and b) and Ansys Workbench Model for the simulation itself. The model was imported from Autodesk Inventor into Ansys Workbench (Fig.15). For all elements, except the part from sintered metallic carbides, the physical and mechanical properties of steel were introduced in the simulation. For the part from sintered metallic carbides, specific sintered metallic carbides characteristics were introduced [7, 8]. It was considered that the maximum load (140 kN) acts point-wise on the top of the element from sintered metallic carbides. To obtain a simulation as simple as possible, but that also approximates as well as possible the real situation, only a subset consisting of two links and a left scraper shovel were analyzed.



Figure 14 (a): A new chain section with the new type of scraper with sintered metallic carbide – the front side



Figure 14 (b): A new chain section with the new type of scraper with sintered metallic carbide – the rear side

Mesh used in finite element model was smooth and all model surfaces were refined to obtain the best possible solution. The meshed model is shown in Fig. 16.

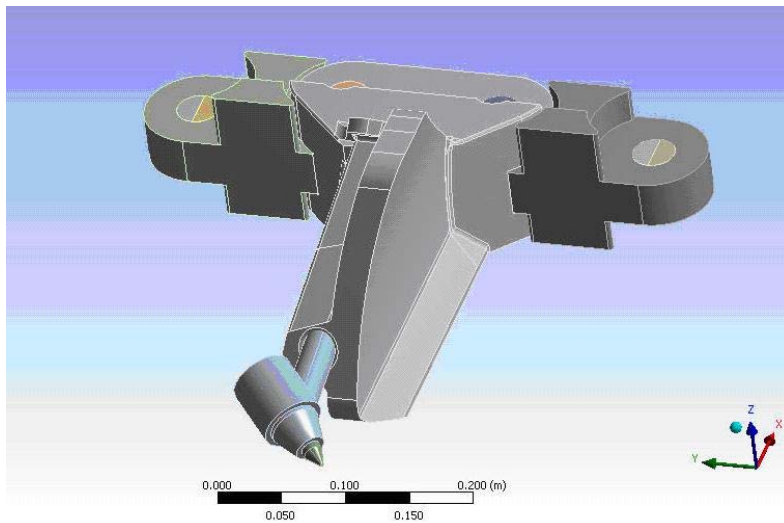


Figure 15: Modeling a new chain section with the new type of scraper with sintered metallic carbide

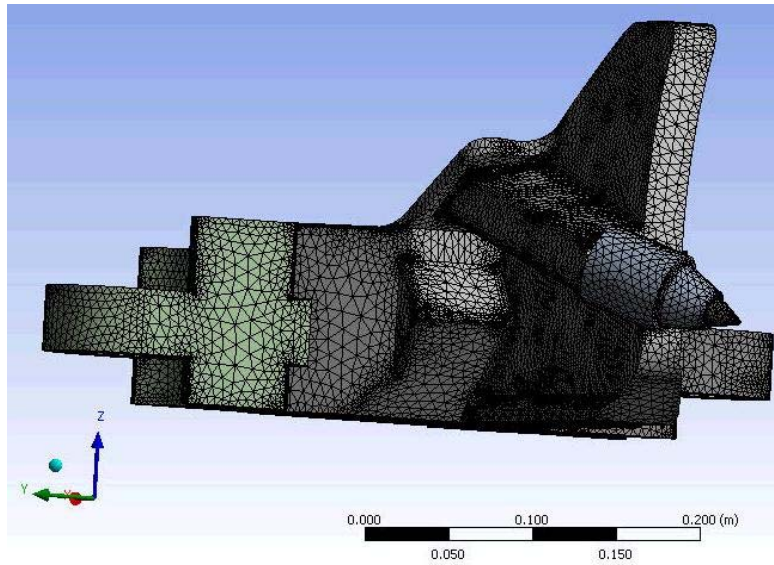


Figure 16: Meshing the new chain section with the new type of scraper with sintered metallic carbide

Equivalent stress simulation results are shown in Fig. 17a and b. In Fig.17 b, the scraper shovel is invisible to highlight the equivalent tension state on the surfaces that normally are covered by it.

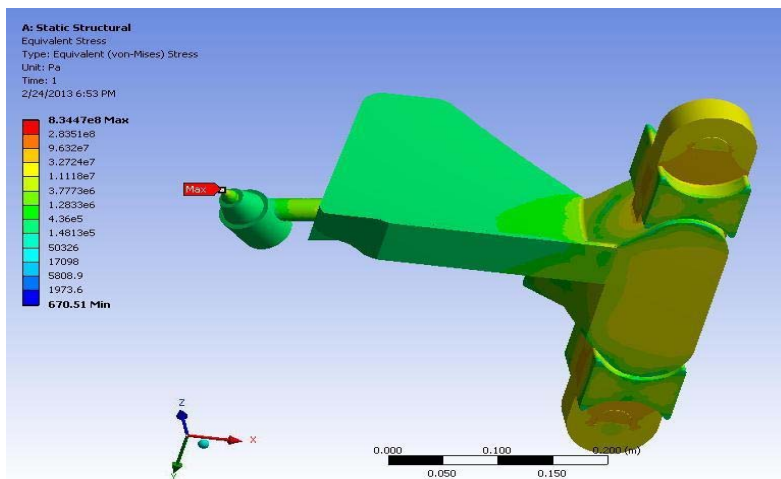


Figure 17 (a): Equivalent tensions state (von Mises) in the chain section

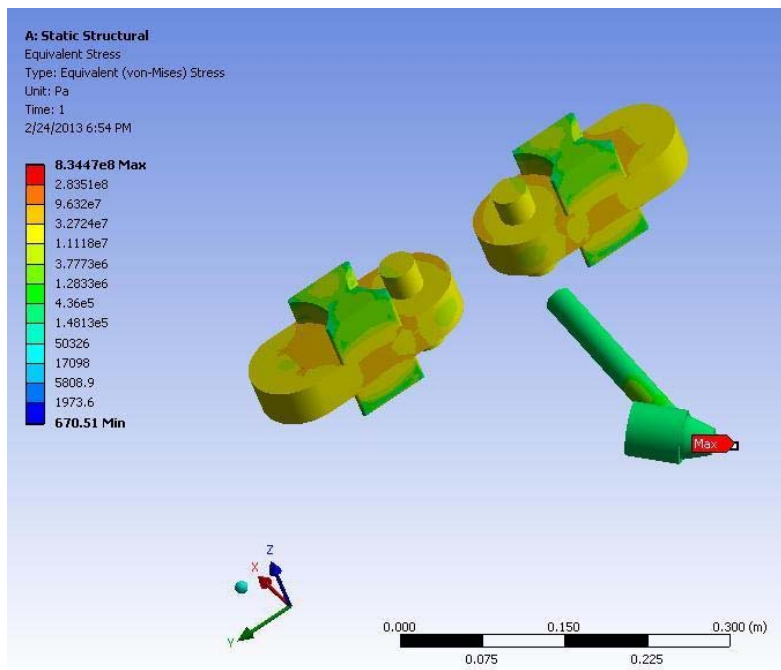


Figure 17 (b): Equivalent tensions state (von Mises) in the chain section

6. CONCLUSION

Application of new materials and methods for increasing the sustainability of scrapers from technological installations of railway machines for cleaning and screening ballast used for railway infrastructure maintenance are found to be of constant current to increase productivity and reduce costs.

Analyzing the simulation results shows that the maximum stress state in elements of the chain made of steel leads to an equivalent tension state below the flow of steel and therefore the chain defects (breakage, premature wear) that appear in its elements (connecting chain links, scraper shovel, joint bolts, scrapers) were caused by defective materials, treatment of a non-compliant exploitation of the system or other accidental causes. The hertzian contact area between chain elements (especially the top of the scrapers) and clogged crushed stone prism (crushed stone, scrap metal etc.) shows the high tension level in that area; there is damage by "cutting" the sintered metallic carbides body.

Developing new types of wear parts (scrapers) with forms, textures and structural and functional geometry optimized according to the working regime and conditions, with working parts encompassing PM materials and technology, lead to substantial increases in durability (> 100 %).

REFERENCES

1. *Instruction for execution radical maintenance railway*, no. 302, SNCFR, Railway Publishing, Bucharest, 1997;
2. *Instructions for capital maintenance of railway*, no. 303, MTCT, CNCF"CFR"SA, Railway Publishing, Bucharest, 2003;
Turcanu C., *Heavy railway machines*, Matrix ROM Publishing, Bucharest, 2006, ISBN (10) 973-755-029-3; ISBN (13) 978-973-755-029-3;
3. Popescu I.C., Negriu R.M., Besleaga C., Badea S.G., Stefanescu M., "Case Study of the Chain Excavator", Structural Integrity and Life, Vol. 12, no. 2, page 87÷92, Journal of the Society for Structural Integrity and Life (DIVK) and Institute for Material Testing (IMS), Beograd, Serbia, 2012, ISSN 1451-3749
4. Besleaga C, Negriu R.M., Popescu I.C., Badea S.G., Stefanescu M.,

“Applications of PM the Chain Excavator of a Railway Machine”, Euro PM2011 Congress Proceedings, vol.3, pag. 427-432, Barcelona, Spain, 9-12 October 2011, ISBN 978-1-899072-22-4;

5. Besleaga C., Negriu R.M., Popescu I.C., Badea S.G., “Case Study Regarding the Tamping Tool Type BNRI 85”, Structural Integrity and Life, Vol. 11, no. 2, page 109÷114, Journal of the Society for Structural Integrity and Life (DIVK) and Institute for Material Testing (IMS), Beograd, Serbia, 2011, ISSN 1451-3749;

6. I.C. Popescu, *Introduction in computer aided analysis of the process equipments*, Printech Publisher, ISBN 973- 652- 951- 7, Bucharest, 2004;

7. I.C. Popescu, T. Prisecaru, B. *Finite elements Analysis of Pressure Equipment, Computer Aided Engineering Solutions for Design, Analysis and Innovation*, (ANSYS & FLUENT User Group Meeting), Sinaia, 26-27 Aprilie 2007

THE STATISTICAL ANALYSIS OF EMERGENCE REASONS AND DEVELOPMENT OF ACCIDENTS ON THE DANGEROUS OBJECTS WORKING AT LOW TEMPERATURES BY METHOD OF FT AND ET

Bolshakov A.M., Zakharova M.I.

Affiliation Larionov Institute of the Physical-Technical Problems of the North of the Siberian Branch of the RAS

marine3@yandex.ru

Abstract: Currently the probability method is considered one of the most perspective. Accidents and experience statistics registrations of previous risk analysis can provide a useful contribution to process of hazard identification. In this article the main attention is paid to scenario approach to the solution of hazards identification problems and emergencies probabilities assessment on the basis of statistical data analysis and systematization on tanks and gas pipelines accidents at low environment temperatures – by event and fault tree method. The main value of event and fault tree method is connected with possibility to find the most critical development option of events and to estimate expected risk of accidents. Generally, faults trees and events trees are only visual illustration to the simple probabilistic models. However they represent considerable interest for the experts connected with exploitation, service and supervision of technical objects.

Key words: Risk analysis, danger, scenarios, probability.

Any system is operated in certain environmental conditions; it is affected by environment factors (climatic, dynamic, etc.). These factors can lead to change of parameters and a functioning state of separate elements and system

as a whole. For elements of the technical systems located in the conditions of the North, defining external factor are low temperatures of atmospheric air which worsen the main physicomachanical properties of constructional materials, raise possibility of brittle fracture. [1]

At low temperatures physical properties of oil products change. For many grades of oil and oil products the minimum air temperature is lower than the congelation temperature therefore there is an inspissated oil. Also explosion hazard of some hydrocarbons changes, for example, methane becomes explosive at low temperatures of air (lower minus of 40 °C), that takes place in the conditions of the North. Gasolines of all brands belong to the most dangerous products because of low value of flash point in the closed crucible. It is noticed that often explosions happen at ambient temperature lower than a 0 C.

Uncontrollable development of emergencies on objects of an oil and gas complex connected with explosions and fires can lead to considerable destructions and to death of people.

For the purpose of overcoming of negative tendencies with accident rate in the industry the law "About Industrial Safety of Dangerous Production Objects" in which need of preparation of the special document - "Declarations of industrial safety of hazardous production facilities" is established is adopted.

The most significant and responsible section of the declaration is the risk analysis, i.e. justification for frequency of occurrence and specifics of different development of accidents, and also definition of the quantitative index connected with it of social, material, ecological damages.

Basic element of the risk analysis - danger identification (detection of possible violations) which can lead to negative consequences.

Danger is the situation which is constantly present at environment and capable in certain conditions to lead to realization in environment of an undesirable event - to occurrence of a dangerous factor.

The main objectives of a stage of danger identification – identification and the accurate description of all sources of dangers and ways (scenarios of their realization). [2]

The essence of the risk analysis consists in selection and processing of all available information for danger identification and an assessment of its possible consequences. Generalization of accident probabilities according to various scenarios it is most convenient to carry out by logiko-probabilistic methods (fault trees and event trees). Wide use of the FT/ET methods is

caused by simplicity and clarity of the initial idea used at a problem setting of modeling.

Creation of event trees allows to track consequences of each possible initial event and to calculate the maximum probability of the main event from each of such initial events. But the main value of a method of event trees is connected with opportunity at design level to reveal various sequences of the events leading to the main event and by that to define possible consequences of each initial events. The method of event trees is simple in a form and is easily interpreted. Generally, both fault trees and event trees are only evident illustration to the elementary probabilistic models. However they represent considerable interest for the experts connected with exploitation, service and supervision of technical objects. Having such scheme, the expert, at all without possessing thorough knowledge of probability theory, can not only find the most critical option of succession of events, but also estimate expected risk if the corresponding event tree or fault tree is added with statistical data.

By results of accident analysis of the tanks and the pipelines which have occurred at low temperatures, the main reasons influencing frequency of accidents are received (tables 1 - 3), fault tree of brittle fracture of the tank is constructed (figure 1).

Table 1. The main causes of accidents on oil pipelines at low temperatures

The causes influencing frequency of accidents on oil pipelines	Probability of realization this event
Rupture of elements of the pipeline (latches)	0,08
Leak through fistula, corrosion opening, crack, depressurization on a welded joint	0,16
Diversion	0,3
Violations of technological process	0,14
Pipeline wear	0,14
Human factor	0,05
Oil pipeline damage	0,11

Table 2. The main causes of gas leakage on gas pipelines at low temperatures

The causes	Probability
Crack in the gas pipeline	0,09
Corrosion	0,27
Pipeline wear	0,18
Pipeline deformation at metal fatigue	0,09

Pipeline deformation from difference of ambient temperatures	0,09
The causes influencing frequency of explosion of the tank with oil product	Probability of realization of this event
The tank with oil product got to the seat of fire	0,18
Effect of static electricity on the tank with oil product	0,09
Violation of the rules of technical and fire safety	0,45
Diversion	0,09
Effect of sharp fluctuation of temperature of atmospheric air	0,09
Causes of explosions of the empty tank from the remains of vapors of oil product	
Violation of the rules of technical and fire safety	1
Causes of explosions of the high pressure tank	
Violation of technological process	0,5
Latent defects	0,5
Latch failure, destruction of the spherical crane, depressurization	0,14
butt between IFJ and a flange of the feed gas pipeline	
Pipe damage	0,14

Table 3. The main causes of accidents connected with tank explosion at low temperatures

The analysis of fracture of tanks at low temperatures (lower than -50 °C) exploitation shows that the limit state of a construction is defined as the brittle fracture having sudden character and the events at a low temperature. Accidents are accompanied by emission of a significant amount of oil products and constitute serious ecological danger.

The most common cause of accidents are:

- for tanks with oil products:
 - violation of the rules of technical and fire safety;
 - use staly poor quality;
 - the welded connections having technological defects;
 - increase of local tension;
- for tanks of a high pressure:
 - violation of technological process;
 - latent defects;
- for oil pipelines:
 - pipeline wear;
 - violations of technological process;
 - leak through fistula, corrosion opening, crack, depressurization on a welded joint;

- oil pipeline damage;
- for gas pipelines:
 - gas pipeline wear , defects , metal fatigue, influence of low climatic temperatures.

As a result of the analysis and systematization of data on accidents of the tanks and pipelines at low temperatures of exploitation " event trees " are constructed (figures 2-4).

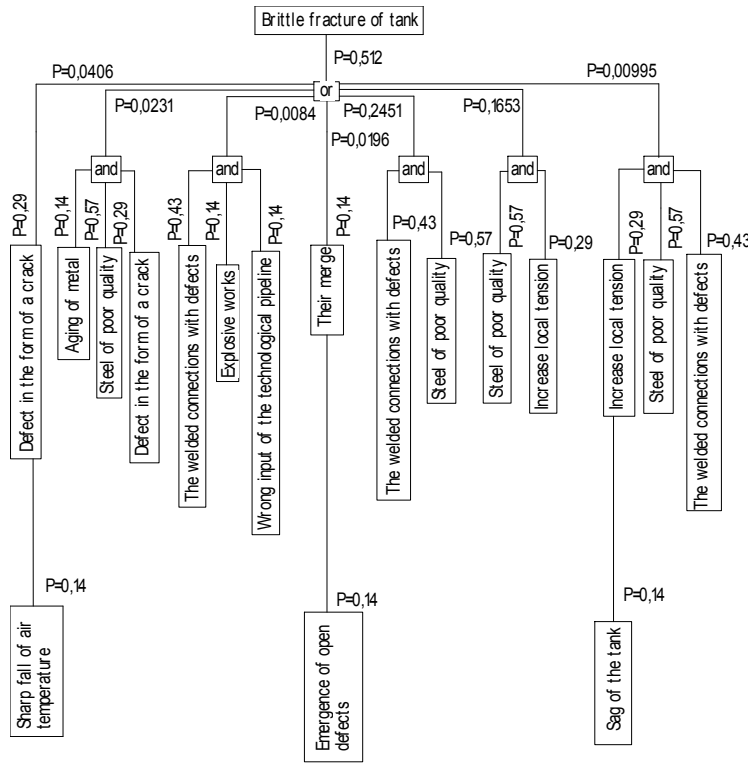


Figure 1. Fault tree of brittle fracture of the tank at low temperatures (lower than -50 °C)

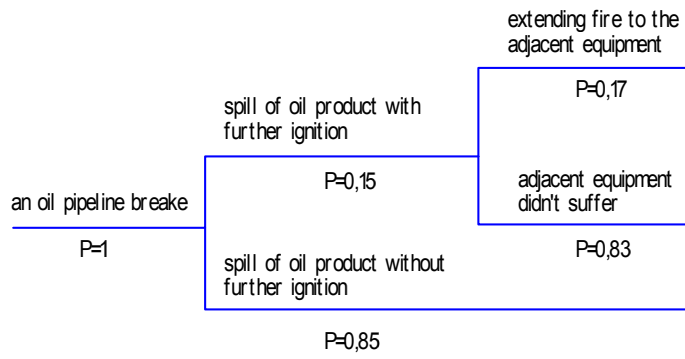


Figure 2. Event tree at an oil pipeline break at low temperatures of exploitation

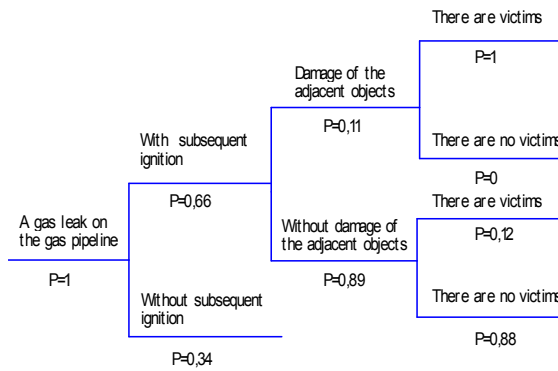


Figure 3. Event tree at a gas leak on the gas pipeline at low temperatures of exploitation

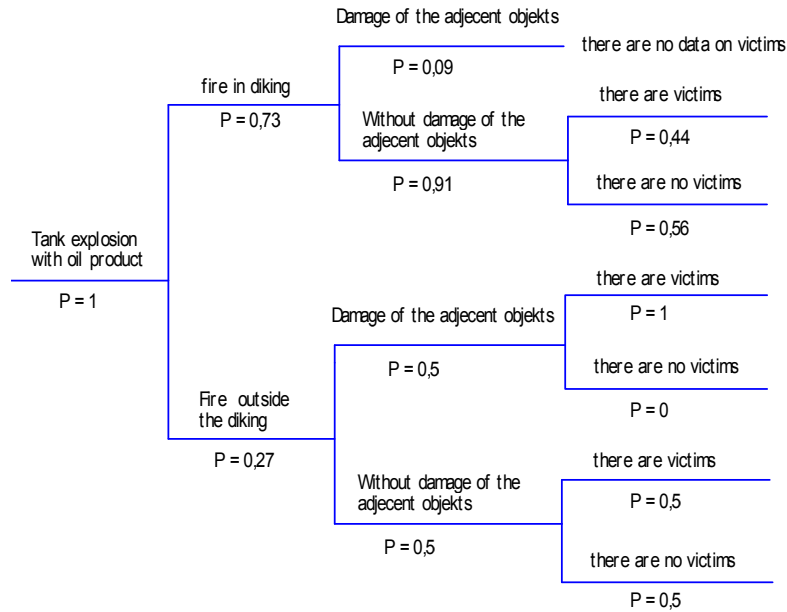


Figure 4. Event tree at tank explosion with oil product at low temperatures of exploitation

Relative probabilities of development of emergencies situations determined by data systematization results on development accidents of tanks and pipelines at low temperatures of exploitation.

CONCLUSION:

Danger identification is a responsible stage of risk analysis, as undetected dangers at this stage aren't exposed to further consideration and drop out of sight. Here the preliminary estimate of dangers for the purpose of a choice of further activity directions is given:

- to stop the further analysis in view of insignificance of dangers;
- to carry out a more detailed risk analysis;
- to develop recommendations about reduction of dangers.

If necessary, after danger identification pass to risk assessment stage. Risk assessment - a stage at which the identified dangers have to be estimated on the basis of criteria of acceptable risk with the purpose to mark out dangers with an unacceptable risk level, and this step will form a basis for development of recommendations and measures for reduction of dangers.

REFERENCES

1. Акимов В.А., Лапин В.Л., Попов В.М., Пучков В.А., Томаков В.И., Фалеев М.И. Надежность технических систем и техногенный риск. – М.: ЗАО ФИД «Деловой экспресс», 2002 – 368 с.
2. РД 03-418-01 Методические указания по проведению анализа риска опасных производственных объектов. Утверждено Постановлением Госгортехнадзора России от 10 июля 2001 г. №30

EVALUATION OF THE IMPACT RESPONSE OF POLYETHYLENE SANDWICH PANEL

C. Casavola, V. Moramarco, C. Pappalettere

*Dipartimento di Meccanica Matematica e Management, Politecnico di Bari, Viale Japigia
182, 70126 Bari, Italy*

v.moramarco@poliba.it

Abstract: The present work presents a preliminary study to evaluate the impact response of a new sandwich panel, made up of two polyethylene skins separated by lightweight polyethylene foam. The material was built with an innovative manufacturing process called rotational moulding. To characterize the low-velocity impact response of this new material three homogenous polyethylene sandwich panels, 44 ± 1 mm thick, were cut using a belt saw to obtain square specimens with dimensions of 10 ± 0.1 mm \times 10 ± 0.1 mm and absorbed energy and force were recorded during the test. Seven impact test energy levels, from 5J to 70J, were tested. Experimental tests have allowed obtaining absorbed energy and the load-time plot for each impact energy level. Furthermore, a quantitative analysis of the damage due to the impact is presented. Finally a finite element model was implemented to evaluate the damping effect of the core.

Keywords: Polyethylene foam, sandwich panels, low velocity impact test

1. INTRODUCTION

Sandwich panels, made up of two polyethylene skins separated by a lightweight polyethylene foam, could represent a good solution in a lot of technical uses where a high damping impact effect is required (e.g. car bumpers) [1]. The panel studied in the present work was built with an innovative manufacturing process called rotational moulding (or rotomoulding) whose peculiarity is the possibility of creating in a unique step

the entire sandwich component, so to obtain a better adhesion and continuity between the skins and the core. Rotomoulding is the principal process for making hollow shapes. In rotomoulding, polymer in powder form is introduced into a mould, which is then closed and rotated. If the mould temperature is set with appropriate regard to the melting temperature range of the polymer powder, a viscous molten layer is built up next to the mould surface which gradually extends inward [2]. To fill the interior part of the panel, special polymeric beads are introduced into the mould with the powder. These beads have the characteristic to explode and to foam at an higher temperature than polymer melting temperature. This technology should permit a reduction of production time and an increase of material mechanical characteristics.

Sandwich structures are known to be susceptible to impact damage by foreign objects [3,4]. The impact represents, therefore, an indispensable issue to characterize this kind of material [5-8]. This type of damage and, more specifically, the response of composite sandwich panels under low velocity impact is the focus of this study.

The first aim of the present work is to characterize the low-velocity impact response of this new material. For this purpose the load-time and absorbed energy for different impact energy levels will be recorded and analysed.

Some authors have tried to define a quantitative characterization of the damage related with impact [9-10]. To evaluate the damage, the average indentation angles and the upper and bottom skin indentation diameter will be measure. To this purpose, the tested samples will be then sectioned into two halves and photographed using a digital camera to take the digital image of the fracture surfaces to evaluate the damage area and failure patterns.

Finally a finite element model of the complete panel will be presented and the comparison between the numerical and experimental model under the same condition will be shown. The influence of the damping effect to simulate as well as possible the mechanical behaviour of the model will be shown.

2. MATERIALS AND METHODS

2.1 Experimental analysis

Three homogenous polyethylene sandwich panels, 44 ± 1 mm thick, was cut using a belt saw to obtain square specimen with dimension of 10 ± 0.1 mm \times 10 ± 0.1 mm. Thirty-five specimens without macroscopic defects was selected (Figure 1). The specimen's skin was 2.75 ± 0.25 mm thick. The bulk density of the core material is 71.6 kg/m³, while the face sheets density is

756.6 kg/m³. The average bulk density of the selected specimens was 142±5 kg/m³. The core material can be considered as an open cell foam with a porosity $\phi = 0.095$ and a characteristic dimension of the pores of 1 mm (Figure 1b).

The impact tests were carried out using a CEAST model 9350 drop weight impact testing system instrumented with an hemispherical piezoelectric crosshead (maximal force 22 kN) with a diameter of 16 mm, acquisition system DAS 16000 and anti-rebound system (Figure 2). The tests were conducted according to ASTM D3763 – 2006 [11]. During the test the specimens were laid on the machine support but were not clamped to not modify the foam structure. The support had an external diameter of 60 mm and an internal diameter of 40 mm. The tests were conducted with the gravitational mass of 2 kg.

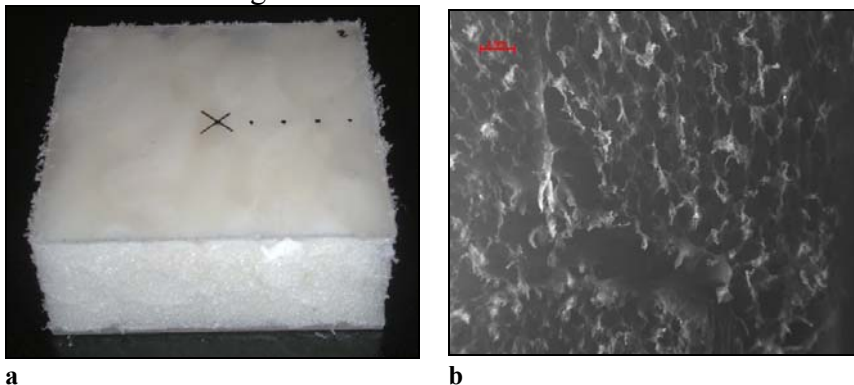


Figure 1. Polyethylene sandwich panel specimen for impact test (a) and micrograph of the foam core (b).

Seven impact test energy levels, 5–10–15–20–30–50–70 J, were tested, corresponding to drop-heights of 253, 509, 763, 1014, 1525, 2592 and 3555 mm. For each energy level five specimens were used. The impact force and the absorbed energy histories were recorded during the tests.

2.2 Numerical Model

Finite element model was built using Abaqus 6.8 in order to reproduce the impact test and the material response at 5 J, 10 J and 15J. Due to the great stiffness of crosshead with respect to the specimen materials, surface rigid elements 'R3D4' were chosen to mesh the crosshead whose radius was 16 mm. The gravitational masses of the testing machine impact tool were reproduced by means of a concentrated mass element 'MASS' located in the centre of the top surface of the specimen. The tested specimen (100 mm

length and 45 mm high) was discretized using 42332 hexahedral 8-nodes elements C3D8 (Figure 3).

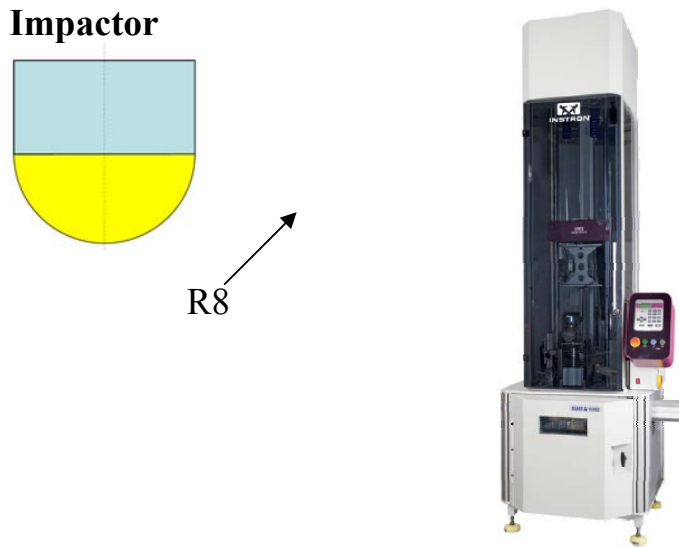


Figure 2. CEAST model 9350 drop weight impact testing system

Table 1: Finite element model constants [12].

	Material Behaviour Model	Elastic Constants	Density [kg/m ³]	Geometric Dimensions [mm]
Skins	Elasto-plastic	E = 110 [MPa] ν = 0.3 σ _{sn} = 7.4 [MPa] E _{pl} = 1.0 [MPa]	756.6	L = 100 H = 3 (x2)
Core	Hyperfoam (N=2) with Mullin effect	μ ₁ = 1.55 [MPa] μ ₂ = 0.17 [MPa] α ₁ = 13.8 α ₂ = -0.437 β = 1.63	71.6	L = 100 H = 38
Crosshead	Rigid Body	--	--	Ø=16

To distinguish the mechanical behaviour of the skins from the foam core, the specimen mesh was divided in two different zones. The skins, 3 mm thick, were modelled using a continuum elasto-plastic model, while the core was modelled using a hyperfoam material model with damping effect [13-15].

The material model behaviour was fitted to previous experimental data obtained on the same material. The comparison between the axial tension behaviour of the polyethylene skins and elasto-plastic numerical model response and between the axial compressive behaviour of the foam and

hyperfoam numerical model response were plotted in Figure 4. All the material constants adopted in the model are summarized in Table 1

The friction coefficient between the crosshead and superior skin of the specimen model was set equal to 0.2 as the steel-polyethylene coefficient [16]

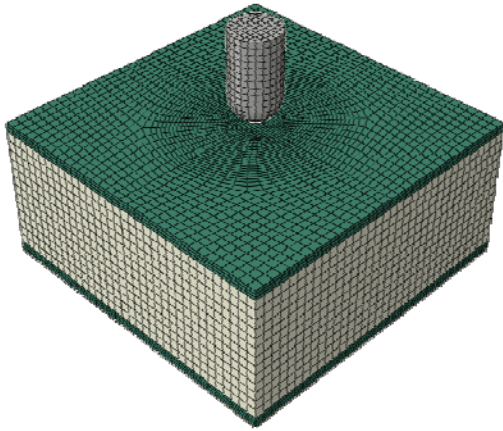


Figure 3. Finite element model mesh

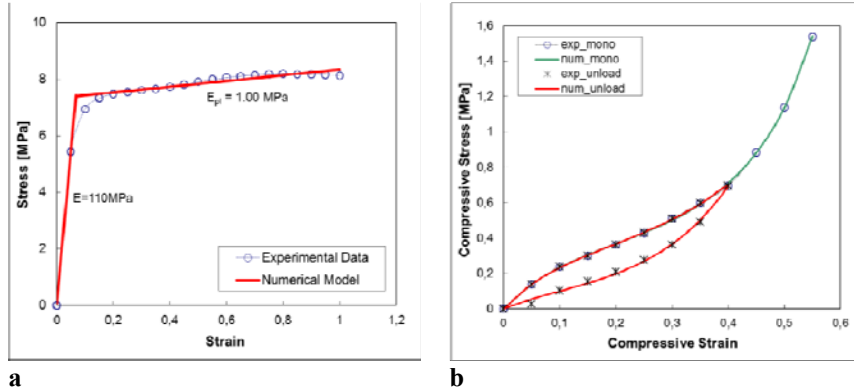


Figure 4 Comparison between the axial tension behaviour of the polyethylene skins and elasto-plastic numerical model response (a) and between the axial compressive behaviour of the foam and hyperfoam numerical model response (b)

3. RESULTS

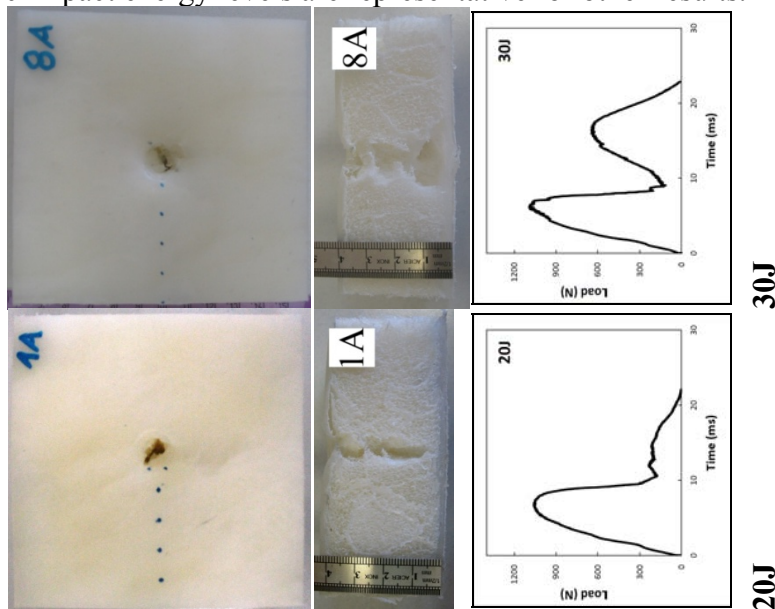
2.1 Experimental results

The load-time plots and the pictures of impact surface and cross-sectional view for the through-thickness foam sandwich composites at 5 - 70 J energy levels can be seen in Figure 5.

The results show that from 5 to 15 J there is no penetration of upper skin and the only visible damage is the local plastic deformation of the skin. The

maximal residual penetration at 15 J is 3.2 mm at the centre of the specimen. Furthermore, further damage is not visible through the foam section, for these levels of impact energy. The penetration of upper skin starts at 20 J. The image shows that the foam core provides low resistance to penetration and in fact is completely traversed by the dart. The load-time histories show that peak force increases from 750 N at 5 J to 1050 N at 20 J and it remains almost constant for higher levels of impact energy. For a level of impact energy of 30 J also the lower skin is penetrated. The penetration of the bottom skin is highlighted in the load-time diagrams by the presence of a second peak. The maximum force of the second peak is between 600 and 700 N. It is lower in comparison to the first peak and it is almost constant for all energy levels. The maximum force of the second peak is about 35% lower than that of the first peak.

In figure Figure 6 the absorbed energy versus time for 5 J, 15 J, 20 J, 30 J and 50 J impact energy levels was plotted. The corresponding energy-time plots at other impact energy levels give almost identical information about the impact response, so the energy-time plots shown at 5 J, 15 J, 20 J, 30 J and 50 J impact energy levels are representative for other results.



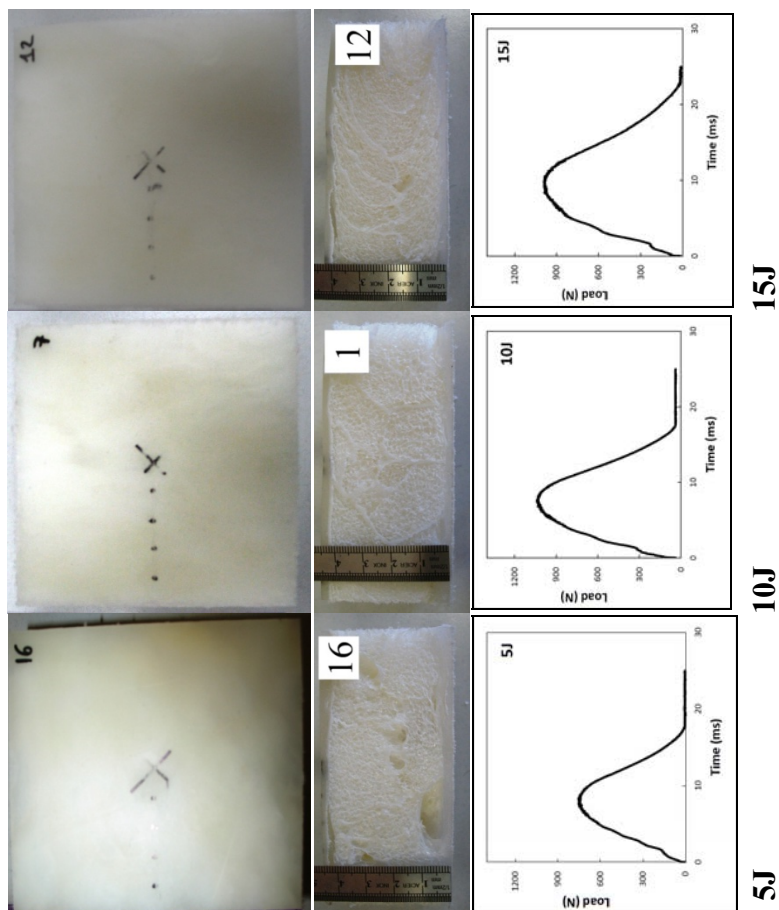
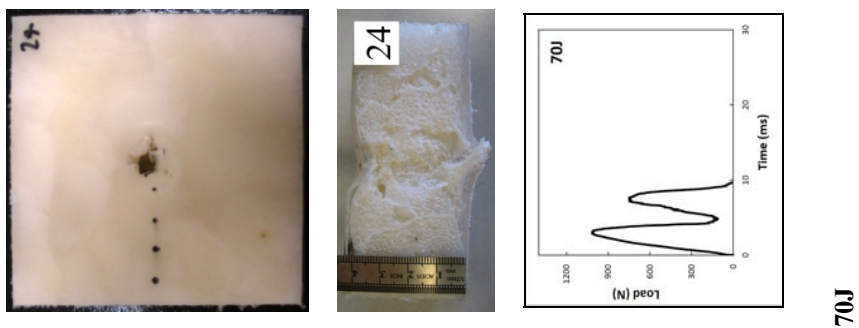


Figure 5. Load-time plots and pictures of impact surface and cross-sectional view for failed samples at 5–70 J energy levels



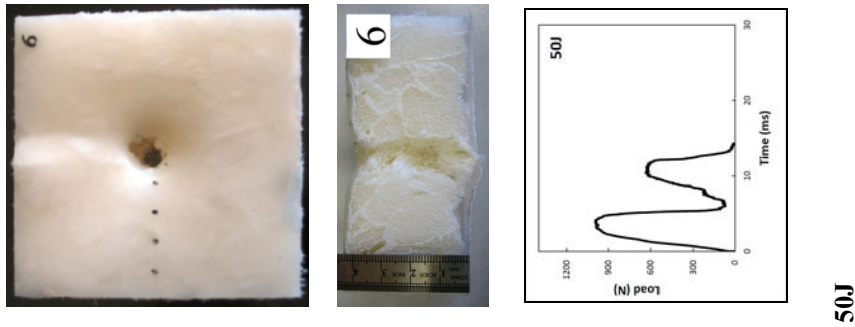


Figure 5. (continued)

The absorbed energy was calculated as prescribed by ASTM D3763-2006 as:

$$E(t) = \frac{1}{2} m(v_i^2 - v(t)^2) + m.g.x(t) \quad (1)$$

where:

- m = mass of falling weight including all attachments;
- v_i = velocity at the point when the specimen is engaged;
- $v(t)$ = velocity of the falling weight;
- g = acceleration of gravity;
- $x(t)$ = displacement.

For 5 J and 15 J energy levels the absorbed energy shows a linear increase with a peak at ~10ms and then a reduction of energy. The value of the peak is equal to the impact energy while the stationary values are respectively 3 J and 9,5 J. For 20 J energy levels, the absorbed energy value displays initially a linear grows up to 20 J, and then the slope of the plot goes to zero. The 30 J impact energy plot shows a first rising section divided in two linear segment separated by a zero slope segment at 24 J and, in the end, a zero slope section at 30 J. Finally, the 50 J energy level plot highlights that the maximum energy absorbed is equal to 46 J.

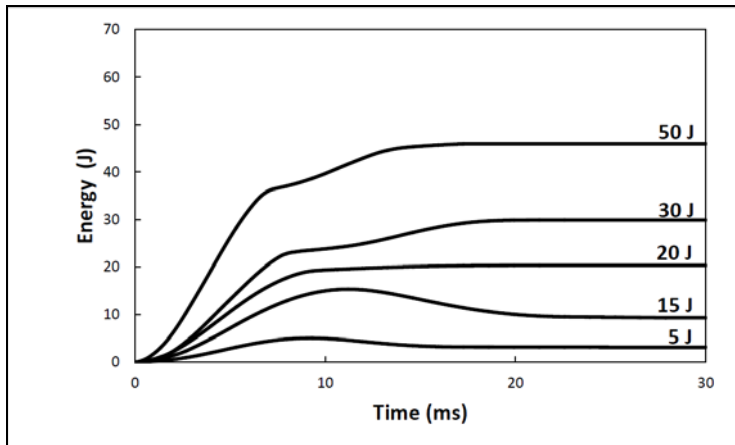


Figure 6. Energy versus time plots for failed sample at 5, 15, 20, 30 and 50 J impact energy level

In order to further understand the impact response and the failure modes in more quantitative manner, it is considered that the damage extent of the failed foam sandwich composites can be characterized by the average indentation angles and the upper and bottom skin indentation diameter (Figure 7).

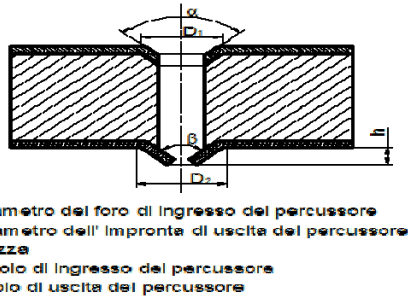


Figure 7. Schematic diagram of cross-section view of failed samples: α upper skin indentation angle; β upper skin indentation angle; D_1 upper skin indentation diameter; D_2 bottom skin indentation diameter.

Initially, for low impact energy, the dart does not have sufficient energy to penetrate the skin and a dent damage shape appears on the impact location. In this cases no damage was identify in the foam due to their hyper-elastic behaviour. When the impact energy increases, the dart produces a cylindrical damage through the entire section of the foam. Finally, for the highest levels of energy, also the bottom surfaces of samples are penetrated through causing a conical crack as shown in Figure 7. The relationship between the damage parameters and impact energy for the foam sandwich panels at different energy levels is seen in Figure 8. The results show that with the impact energy levels increasing (5–70 J) the indentation angle on top surface decrease gradually (171° - 120°) while the indentation diameter initially

increase (14 mm at 10 J) than have a minimum at 20 J (10 mm) and became stable for higher level of impact energy (~14 mm). The indentation damages appear on the bottom surface when impact energy level reaches 30 J. Also in this case the results show that the indentation decrease gradually (160°- 120 °) while the indentation diameter increases (5 – 7.6 mm).

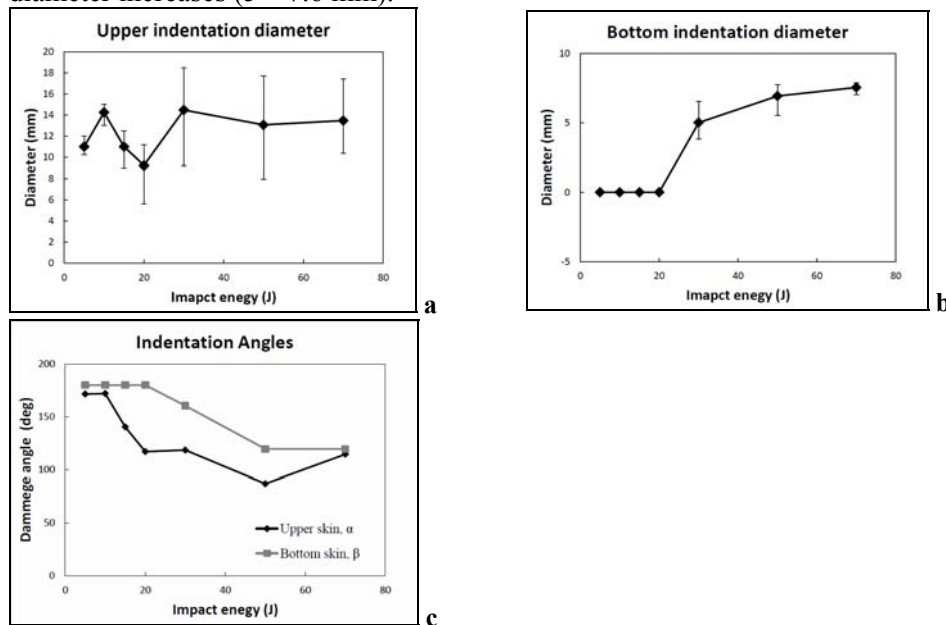


Figure 8. Relationship between impact energy and damage parameters for failed samples: (a) upper skin indentation diameter; (b) bottom skin indentation diameter; and (c) damage angle

3.2 Numerical results

To validate the numerical model the velocity/time curve and the peak forces between the experimental results and numerical models was compared (Figure 9). The comparison between the numerical results and experimental data appears to be in good agreement. The results highlight the importance of introducing the damping effect in the mechanical model of the foam.

For an impact energy of 5 J, the residual velocity obtained implementing the damping effect is -1.18 m/s in comparison with that measured experimentally equal to -1.16 m/s (err = -1.7%), while that obtained without damping effect is -1.86 m/s (err = 86%). For impact energy of 10J, the residual velocity obtained implementing damping effect is -1.56 m/s in comparison with that measured experimentally equal to -1.69 m/s (err = -8.2%), while that obtained without damping effect is -2.61 m/s (err = 54.4%). Finally, for an impact energy of 15 J, the residual velocity obtained implementing Mulling effect is -1.93 m/s in comparison with that measured experimentally equal to -2.12 m/s

(err = -9.0%), while that obtained without damping effect is -3.31 m/s (err = 47.64%).

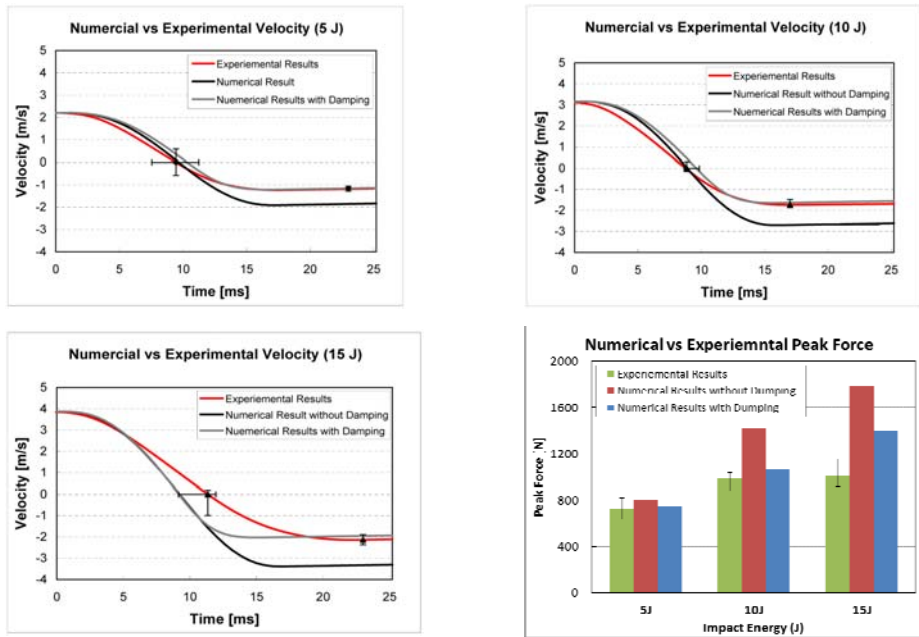


Figure 9. Comparison between the experimental data and numerical models results

The importance of implementation of the damping effect in the constitutive model of the foam is pointed out also by the results obtained for the peak forces. Comparing the experimental measures with the numerical results got with and without damping, it is clear, as the reduction of error obtained with the numerical model is conspicuous. For 5J impact energy, the average experimental peak force is 730,6 N while those obtained with numerical model with and without damping are respectively 741.5 N (err = 1.5%) and 804.7 N (err = 10.1%). The peak force obtained with impact energy of 10J, considering the effects of damping, is 1070.3 N (err = 8.3%), while that calculated without damping effect is 1414.0 N (err = 43.1%), with an average peak force measured experimentally of 988.3 N. The worst results were obtained with impact energy of 15 J. In this case, the numerical model without damping estimates a peak force of 1791.6 N in comparison with that measured experimentally of 1011.3 N (err = 77.2%). Also in this case, the implementation of the damping into the constitutive model of the foam reduces appreciably the value of the peak force, 1399.5 N (err = 38.4%), although it is out of the experimental range.

4. CONCLUSIONS

Rotomoulding is one of the principal techniques to produce sandwich structures made up of two polymeric skins separated by a foam core. This is therefore the ideal solution for structures that combine a low weight with high impact energy absorption. In the present work the impact behaviour of a polyethylene sandwich panel with a polyethylene foam core was studied.

Thirty-five specimens were tested at seven energy levels (5 -70 J). The load and absorbed energy history were recorded during the tests.

The results shown that the average peak force to penetrate the upper skin is about 28% higher in comparison with the peak force on bottom skin. This phenomenon could be related with the foam compressional behaviour, which absorb part of impact energy, but also reduce the plastic deformation of the skin increasing the force necessary to pierce the skin.

The absorbed energy history analysis has highlighted that for low levels of impact energy (under 15 J) the foam absorbs elastically the 30% of impact energy. The 30 J impact energy plot shows, in the first part, a low slope segment between to higher slope segment. This segment represents the energy absorbed by the foam, and it can be estimated in 1-2 J. This result is confirmed for 50 J impact energy level. The 50 J impact energy level points out also that the maximum impact energy level, that this sandwich material can absorb, is 46 J.

The damage analysis has shown that the indentation diameter at 10 J is greater than that to 15 J. This effect can be explained with the plastic behaviour of the skin. These results are in agreement with those shown by Fan and Xiao-quiring [9]. Furthermore the damage analysis has pointed out that the indentation angle after penetration for the upper and lower skins is similar.

Finally, a finite element model was implemented in order to reproduce the experimental test at 5-15J. Higher impact energy levels were not considered because a damage model should be required. The model was geometrically coherent with those that have been tested experimentally. The mechanical behaviour of the skin was modelled as an elasto-plastic material, while two different constitutive models were used to simulate the core behaviour: a hyperfoam with damping effect and a hyperfoam without damping effect.

The results shown that the implementation of the damping effect, into the constitutive model of the foam, is fundamental to simulate as well as possible the mechanical response of this sandwich panel in terms of deceleration and peak force. Although, generally, the numerical results are in agree with the experimental measure, an overestimation of peak force was found for impact

energy of 15J. This could be related with the damage initiation in the materials and it will be the focus of future analysis.

In conclusion this work can be consider a first analysis of the impact behaviour of this material although a more extensive test campaign is necessary. In particular, the comparison between the panels produced using the rotomoulding technique and those obtained by pasting the skins on the foam is required to fully evaluate the advantage of this technology. Also a more sophisticated finite element model, that consider for example the damage behaviour of the materials, could be help to better understand the mechanical response of this kind of sandwich panels.

REFERENCES

1. L.J. Gibson, M. F. Ashby: Cellular solids. Structure and properties – Second edition (Cambridge University Press, UK 1997).
2. S.F. Bush and O.K. Ademsu. Low-density rotomoulded polymer foams. Colloids and Surfaces A: Physicochem. Eng. Aspects Vol. 263 (2005), p. 370-378.
3. Abrate S. Localized impact on sandwich structures with laminated facings. Applied Mechanical Review Vol. 50 (1997), p. 69–82.
4. Abrate S. Impact on composite structures. Cambridge UK: Cambridge Press; 1998.
5. Md. Akil Hazizan and W.J. Cantwell. The low velocity impact response of foam-based sandwich structures. Composite: Part B Vol. 33 (2002), p. 193-204.
6. J.N. Baucom and M.A. Zikry. Low-velocity impact damage progression in woven E-glass composite systems. Composites: Part A Vol. 36 (2005), p. 658–664.
7. F.G. Torres and C.L. Aragon. Final product testing of rotational moulded natural fibre-reinforced polyethylene. Polymer Testing Vol. 25 (2006), p. 568–577.
8. P. M. Schubel, J. Luo, I. M. Daniel. Low velocity impact behavior of composite sandwich panels. Composites Part A: Applied Science and Manufacturing Vol. 36 (2005), p. 1389-1396.

9. X. Fan and W. Xiao-qing. Study on impact properties of through-thickness stitched foam sandwich composites. *Composite Structures* Vol. 92 (2010), p. 412-421.
10. V.I. Rizov. Low velocity localized impact study of cellular foams. *Material and Design* Vol. 28 (2007), p. 2632-2640.
11. USA Standard Association. ASTM D3763-2006. Standard test method for high speed punctures properties of plastics using load and displacement sensor. USA: USA Standards Association International; 2006.
12. C. Casavola, V. Moramarco, C. Pappalettere. Experimental and Numerical Characterization of the Impact Response of Polyethylene Sandwich Panel: A Preliminary Study. *Applied Mechanics and Materials* Vol. 70 (2011), p. 195-200.
13. Hibbit, Karlsson and Sorensen, Inc.: ABAQUS Analysis Users Manual, v. 6.8. (HKS Inc. Pawtucket, RI, USA 2008).
14. Ogden, R.W., 1972. Large deformation isotropic elasticity: on the correlation of theory and experiment for compressible rubberlike solids. *Proceedings of the Royal Society of London A* 328, 567–583.
15. Ogden, R. W., D. G. Roxburgh, 1999. A Pseudo-Elastic Model for the Mullins Effect in Filled Rubber. *Proceedings of the Royal Society of London A* 455, 2861–2877.
16. J. R. Davis: *Concise Metals Engineering Data Book* (ASM International, 1997).

EVOLUTION OF THE DEFORMATION FIELD ON THE SURFACE OF SHEET PLASTIC MATERIALS AT DYNAMIC NONEQUILIBRIUM PROCESSES

Chausov M.G., Berezin V.B., Pylypenko A.P.

National university of life and environmental sciences of Ukraine

mich@nubip.edu.ua, valikb@yandex.ru, andriy3pl@gmail.com

Abstract: Using the original methods of testing and developed software for contactless analysis of the strain field by digital image correlation method, equipped with high-speed camera Phantom v711, authors analyzed the evolution of the strain field on the surface of sheet D16 and 2024 - T3 aluminum alloys, stainless steel at a "pure" static deformation and DNP implementation. It was found that during DNP the kinetics of deformation of studied aluminum alloys has cardinally changed in comparison with the "pure" static deformation.

Key words: dynamic nonequilibrium processes, strain field, digital image correlation, dissipative structures

1. INTRODUCTION

To the present time authors had accumulated the large experimental data set [1-5] which allows making some preliminary conclusions about mechanical behavior of different classes of materials at dynamic nonequilibrium processes (DNP). The DNP is linked with the violent exchange of energy between separate elements of any statically indeterminate design, caused by fracture of one or several elements of a mechanical system. In this case, element wise equilibrium is being violated and potential energy

release triggers an additional impulse load, which is nonlinearly transferred to other active elements of the system.

Based on the results of carried out earlier tests, first of all, it is necessary to pay attention to the formation of thin-strip dissipative structures in materials during DNP, these structures are volumetrically connected on the various scale levels and contribute to plasticization of materials.

At the subsequent static extension these newly formed dissipative structures can essentially alter the mechanical properties of materials, compared with the initial ones.

The reasons of self-organization of materials structure during DNP couldn't be determined from current experimental data array. There is a main question: what leads to the new deformation mechanism which is linked with the self-organization of structure? It is impossible to answer this question without additional detailed physical researches at various scale levels.

Taking into account complexity and laboriousness of such physical researches to understand the processes running in materials during DNP, authors turned to the analysis of strain field kinetics on the surface of sheet metal sample subjected to DNP.

The purpose of this work is to study the evolution of the strain field on the surface of sheet D16 and 2024-T3 aluminum alloys and stainless steel during the DNP using modern high-speed camera Phantom v711 (up to 1.4 million fps).

2. METHODS

A new type of mechanical test, developed by Professor M.G. Chausov with colleagues and described in [1-3] is used to implement the DNP at the present work. Processes of the deformation and fracture of materials during impulse-loading are being investigated in the specialized mechanical system. This system is an elementary statically indeterminate structure, in the form of three parallel elements loaded simultaneously – the central sample, and two symmetrical specimens – satellites ("fragile samples") of different cross-section, made of hardened steel U8A or 65G. During the loading process of this construction the samples - satellites fracture at a given load on the tested sample (or at given strain), which leads to the impulse loading of the tested sample. The developed method of mechanical testing of materials allows to implement the initial conditions and to regulate energy exchange in the closed mechanical system and, thus, to investigate the mechanical behavior of

materials subjected to DNP. One more very important thing is that such system provides the experimental results on different levels of pre-static deformation, at which an impulse-loading is being performed, and it is possible to change the intensity of these loads.

It is obvious that the classical methods of strain measurement during the mechanical tests using extensometers are unable to provide sufficient information on the evolution of the strain field, both in static and dynamic conditions of the deformation. Accordingly, to analyze such a complex process as the DNP is, the tools that allow obtaining information about the kinetics of the strain field should be used.

For this purpose, the authors used the original package [6, 7] for analyzing the strain field by the means of digital image correlation method (DIC) equipped with a high-speed camera Phantom v711.

The tests were carried out on flat specimens with a thickness of 3 mm and with the working zone of 25x75mm. Aluminum alloys D16 and 2024-T3 were specially chosen as the test material, because they show a clear tendency to have the strain-wave process of deformation during static tensile tests, and stainless steel that, is not prone to such kind of strain-wave process. In all experiments, the total load of samples - satellites ("fragile probes") fractured at almost the same load of 87 ± 12 kN. Level values of pre-static deformation at which impulse-loading was performed, were between 1.8 ... 7.0%.

3. RESULTS

Basing on the analysis of experimental results of surface strain evolution in aluminum alloys during and after the DNP authors identified a number of characteristic modes of strain field kinetics. For example and visualization of the obtained results in the present work we give a comparison of one of the identified modes of strain field kinetics during the DNP. During the DNP a band of localized deformation breaks into two bands, which is followed by their interaction and by the formation of a new band which is oriented in different direction. But during a "pure" static deformation there exist no such kind of strain band transformation; it simply runs through sample working area maintaining its direction.

The corresponding results of the evolution of the strain field on the surface of the D16 alloy are on Fig. 1 and 2. Here, Fig. 1 represents a characteristic pattern of the process of deformation of the alloy at a "pure" static

deformation and Fig. 2 represents typical mode of deformation process during the DNP. For comparative purposes these strain fields are calculated from the displacement field corresponding to 6.44% on the 16 mm base.

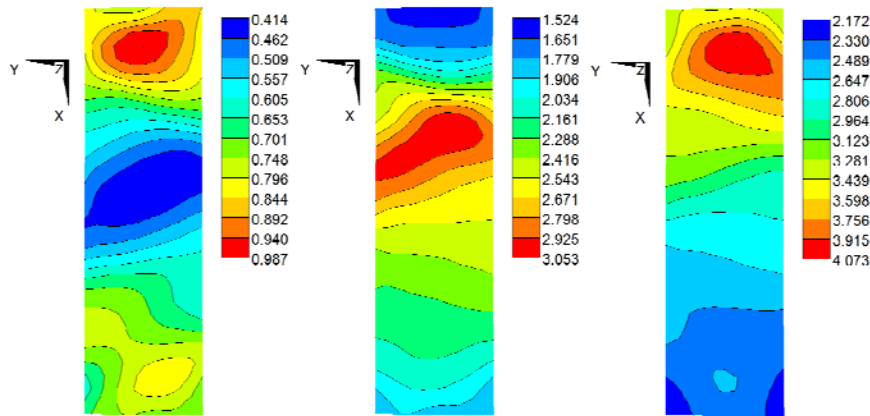


Figure 1. Strain field of aluminium alloy D16 during pure static test

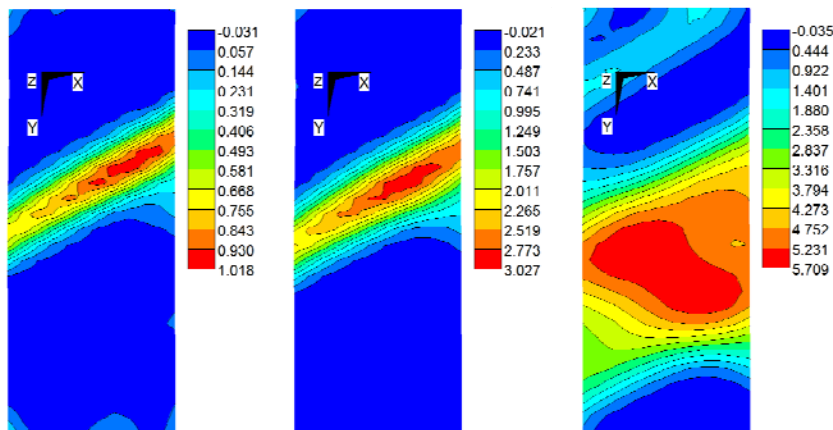


Figure 2. Strain field of aluminium alloy D16 during the DNP

The results of tests on similar samples of stainless steel are on Fig. 3,4. These strain fields are calculated from the displacement field corresponding to 7.48% of local strain in the center of the sample. In contrast to the tested aluminum alloys, the evolution of the strain field on the surface of stainless steel during the DNP (strain field inhomogeneities are caused by the impact

waves) has similar pattern evolution as in statics, which clearly indicates a sensitivity of different classes of materials to DNP.

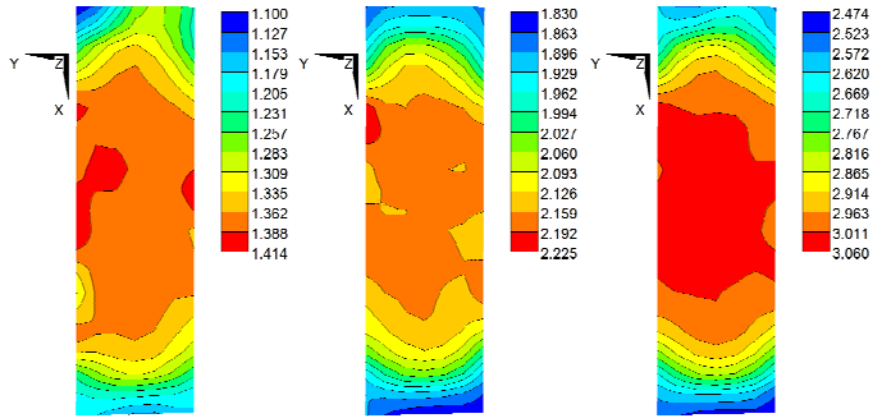


Figure 3. Strain field of stainless steel during pure static test

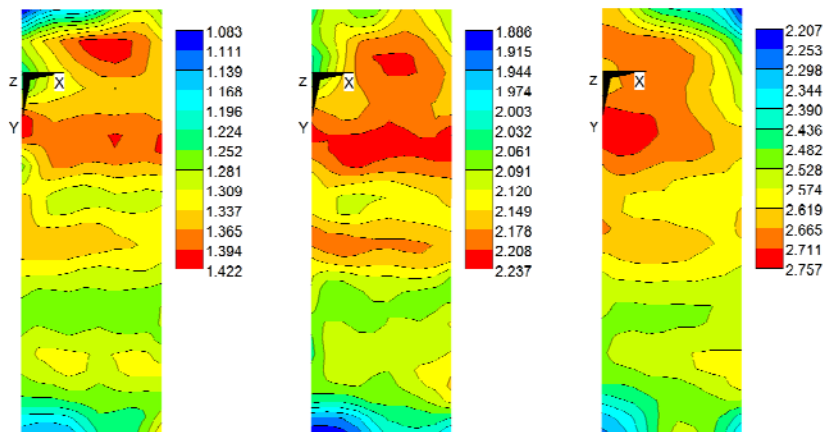


Figure 4. Strain field of stainless steel during the DNP

Originality of the experimental results, presented by the authors, is that for the first time it is shown that the DNP can be implemented at a sufficiently simple test by means of one or more impulse loads on simple statically indeterminate system. The main parameters that specify the process in the element of the mechanical system with a definite stiffness is the load release

rate of sample-satellites (N/s) and their fracture load value. As this kind of testing can be implemented at almost any standard hydraulic testing machine, one of the tasks of the present study was to determine the true values of the load release rate in the used testing machine for the DNP implementation. As a result of specially conducted experiments, using a high-speed camera Phantom v711, it was found that the rate of load release rate in the used test system is 300-500 MN/s, and fracture delay of sample-satellites was as small as 3-4 msec.

The presence of two stages of the process at low and high speed which are responsible for the formation and development of dissipative structures in 2024-T3 and D16 aluminum alloy as well as stainless steel during the DNP were revealed during researches. The average strain rate at the first stage of the formation of dissipative structures in local areas is relatively low, about 2 ... 3 s⁻¹. At the second stage of the process when there exist the propagation of the newly formed dissipative structure over the sample volume the strain rate is significantly higher – up to 50 ... 60 s⁻¹.

4. CONCLUSIONS

1. There exists a significant deviation of strain field kinetics after DNP compared with pure static test. In addition there is a different sensitivity of different classes of materials to the DNP.
2. The materials with temporally non-homogenous strain distribution during plastic deformation (aluminum alloys due to Portevin-Le Chatelier effect) are especially prone to the deviation of strain field kinetics after DNP.
3. We determine two stages of the process, one with low and one with high velocity, responsible for the formation and propagation of dissipative structures in a material during DNP. Average velocity of deformation at the first stage of formation of dissipative structures in local zones is rather low, with an order 2 ... 3 s⁻¹. At the second stage of process when newly formed dissipative structures propagate throughout the volume of investigated sample, deformation velocity reaches up to 50 ... 60 s⁻¹ in local zones.
4. The revealed features of strain field evolution on surface of the sheet plastic materials during DNP explain some aspects of the mechanical behavior of materials at the subsequent static extension.

REFERENCES

1. N.G. Chausov, Y.E. Z asimchuck, L.E. Markashova, V.E. Vildenman, V.E. Turchak, A.P., Pylypenko, et al. Specialty deformation of plastique materials under dynamic non-equalibrium processes. *Factory lab. Material diagnostic*, 75: 52-59, 2009.
2. E.E. Z asimchuk, T.V. Turchak, L.I. Markashova, N.G. Chausov, A.P. Pylypenko, V.N. Paratsa. Peculiarities of structural transformation in plastic materials under abrupt changes in loading conditions. *Phys. Mesomechanics*, 12:175-179, 2009.
3. M.G. Chausov, A.P. Pylypenko. Laws of deformation processes and fracture of plastic steel from the point of view of dynamic overloading. *MECHANIKA*, 4 (54):24-29, 2005.
4. M. Chausov, P. Maruschak, A. Pylypenko, F. Sergejev, O. Student. Effect of high-force impulse loads on the modification of mechanical properties of heat-resistant steel after service. *Estonian Journal of Engineering*, 18(4):251–258, 2012.
5. Z asimchuk, E.E., Gontareva, R.G., Baskova, O.I., Chausov, M.G., Hutsaylyuk, V. On possibility to use single crystal sensors of deformation damage under dynamical loading (2012) *Metallofizika i Noveishie Tekhnologii*, 34 (4):509-520, 2012.
6. V.B. Berezin, M.G. Chausov. Research of deformation field of flat surface material specimens by the method of correlation of digital images. (Statical loading). *Technical diagnostics and non-destructive control*, 2:15-20, 2011.
7. N.G. Chausov, V.B. Berezin. Evolution of deformation field on the surface of the leaf of stailless steel under dynamic non-equalibrium processes. *Monthly of National Technical University of Ukraine "KPI". Series: Machine building*, 63:253-257, 2011.

PHYSICAL PHENOMENA, OCCURRING UNDER PERIODIC STRAINING OF METAL ALLOYS

V.I. Kapustin, K.V. Zakharchenko, E.A. Maksimovskiy

Novosibirsk State Technical University, Novosibirsk

Nikolaev Institute of Inorganic Chemistry SB RAS, Novosibirsk

macler06@mail.ru

Abstract: The paper considers the following physical phenomena from the standpoints of non-equilibrium thermodynamics and local structural transformations: dissipative warming-up, contraction (volume reduction), surface relief formation, disintegration of structural elements and alteration of ultimate composition concentration on the surface of strained specimen.

The tools and methods of the field research are described.

Data, represented in this paper, prove the existence of nonlinear dependence between stress amplitude and researched characteristics of metal alloy condition. The type of nonlinear dependences allows to determine the range of loads, where equilibrium (elastic) or non-equilibrium straining is implemented. It is suggested to use the characteristic stress – stress of transition to non-equilibrium straining as the mechanical feature of metal quality and the condition features: temperature of dissipative warming-up, volume strain, ultimate composition concentration, etc., as the indicator used for the purposes of technical diagnostics of metallic materials and machine component parts.

Key words: fatigue, thermodynamic potential, nonequilibrium straining, dissipative warming-up, change in the transverse strain, surface microrelief, spontaneous transformation of solid solution.

1. INTRODUCTION

Development of a new concept in deformable solid mechanics requires application of physical chemistry's tools and techniques of studying irreversible processes within the frames of the multilevel approach to the problems of fracture and straining [1].

Concerted interdisciplinary experimental studies of the behavior of materials in the field of stress leading to the phenomena of low-cycle and high-cycle fatigue are needed to develop a methodical approach to the problem of fatigue damage in terms of mechanics and non-equilibrium thermodynamics.

This paper tries to find the ways, methods, and some experimental solutions for investigating the nature of materials fatigue due to the positions mentioned above. It being understood that the principles of non-equilibrium thermodynamics here are heuristic in nature and serve to clarify whether the technique under development contradicts the general laws of physics or not.

The paper required to investigate the physical phenomena accompanying the process of periodic straining and fatigue in the transition from the elastic (reversible and equilibrium) to inelastic (irreversible and non-equilibrium) straining and find the relationship between variables (characteristics of state) in the Gibbs equation [2]:

$$dU = TdS - pdV + \sum_1^k \mu_k dN_k,$$

where U - internal energy, p - pressure, V - volume, T - temperature, S - entropy, N_k - number of moles of a substance, μ_k - chemical potential of k^{th} element.

2. TECHNIQUE AND MATERIALS OF THE RESEARCH

It is assumed that the alloy specimen in the initial state represents a heterogeneous closed system, non-isolated from external mechanical impact, in thermodynamic equilibrium.

The specimen is disturbed from thermodynamic equilibrium by periodic loading with gradually increasing amplitude of stress in the cycle so that the moment of the weakly nonequilibrium state can be detected by the change of temperature ΔT of dissipative warming-up.

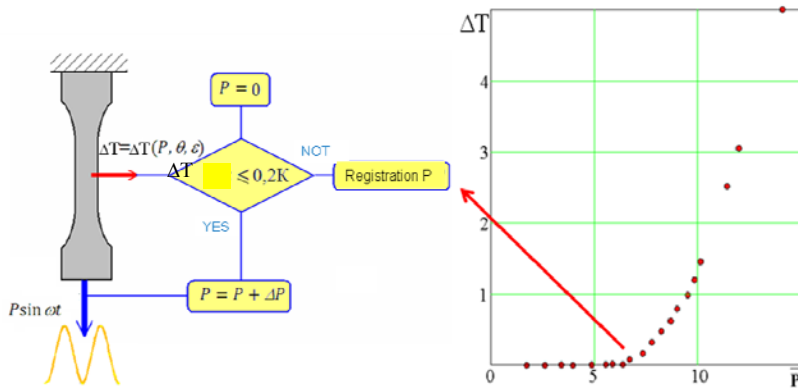


Figure 1. Dissipative warming-up of the specimen.

Fig. 1 shows that there is a critical state of the material and the corresponding critical load and vibration amplitude at which the straining becomes exothermic.

The paper [3] has shown that studied critical stress can be considered as conventional limit of elasticity of the material, if characteristics of the limit stress cycle are measured with the change of temperature of the working part of the specimen by 0.2 K.

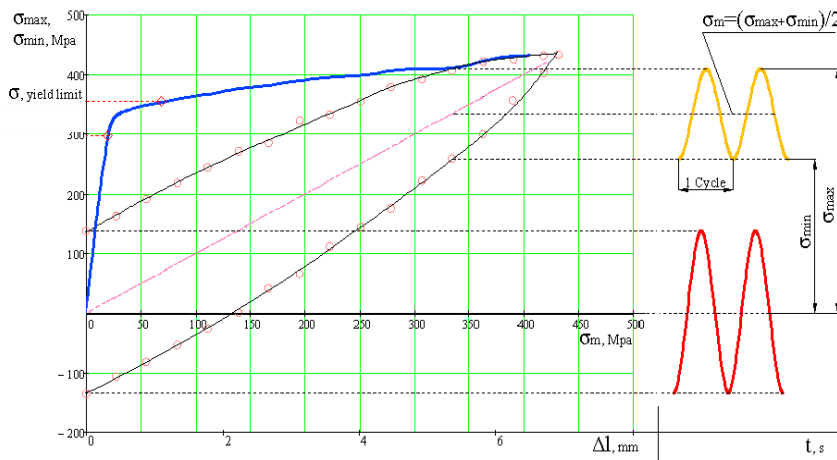


Figure 2. Critical stress and alloy D16AT (Al-Cu-Mg) straining

Comparison of the strain diagram 1 and diagram of the critical stress 2 in Fig. 2 shows that dissipative processes under periodic loading start at a certain critical ratio of mean and amplitude values of the stress cycle characteristics with the stress much lower than the yield strength of the material. Critical ratio obtained within the frames of the discussed experiment on dissipative warming-up reflects a well-known regularity between the characteristics of the limit cycle obtained by destructive check of materials for endurance in the Smith coordinates [4].

Straining of the specimen was carried out by uniaxial loading at the installation "Instron 8801" at room temperature (standard conditions). This equipment provides periodic straining of specimen due to the soft loading scheme. To measure the straining in the axial direction the extensometer № 2620-601 "Dynamic Extensometer" was used with the base of 25 mm. As regards the transverse direction, № WE-404-F "Transverse/Diametral Extensometer" was applied with bases from 6 mm to 12 mm which were mounted on the working part with the length of 50 mm. The specimen were made of the alloys 1163, D16AT, and B95.

The structure of the specimen was studied on the following equipment:

Zygo New View 7300 (USA) - complex for determination of the surface topography; Scanning Electron Microscope JSM 6700F.

The change in temperature of the specimen was studied using thermal imager AGA-680 (Sweden).

It should be emphasized that in this research the maximum stress value in the cycle does not exceed the yield strength of the material.

3. PHENOMENON OF SPONTANEOUS STRAINING

During the research the specimen was disturbed from the metastable equilibrium in accordance with the program of loading shown in figure 3a.

At periodic loading of the specimen it was needed to define the characteristics of the critical stress cycle in which dissipative phenomena occur, ie, in this case - the phenomenon of spontaneous straining-, due to measurements of the components of the strain tensor.

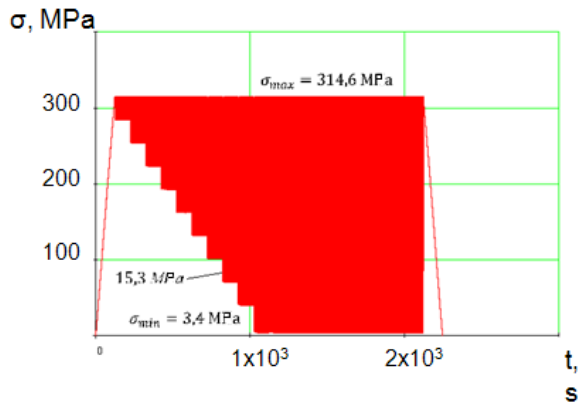


Figure 3a. Test program

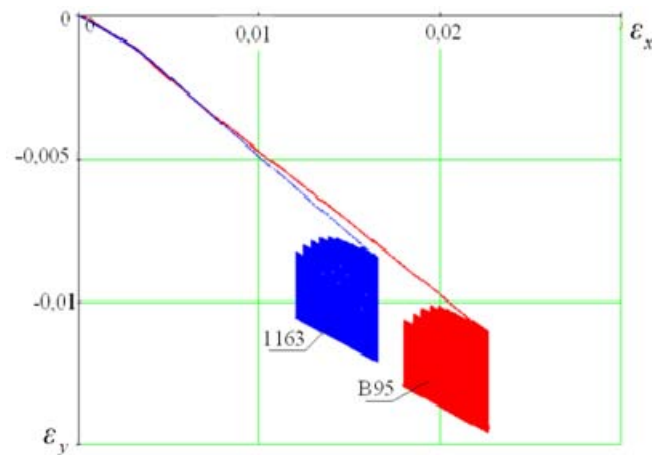


Figure 3b. Test results of specimens of Al-alloys, 1163 (Al-Cu-Mg) and B95 (Al-Zn-Mg-Cu)

Monitoring the change in transverse strain by measuring the volumetric strain while the specimen is deformed, you can see that transversal strain increases starting from the certain stress amplitude with periodic loading. This process (the process of contraction) is monotonous and increases with rising stress amplitude. As the experiment shows, the strain tensor components in real non-equilibrium process changes in time with a finite velocity, and, therefore the number of loading cycles appears as a new variable to describe them.

Thus, these experiments demonstrate that the non-equilibrium process generated by straining beyond the elasticity is accompanied by spontaneous physical processes of warming-up and contraction, which in turn is consistent

with the behavior of the alloy [2].

Due to [2], the alloy which was initially considered to be statistically homogeneous and in the equilibrium metastable state, in transition to the unstable equilibrium state becomes capable of forming dissipative structures and self-organizing of its microstructure. The paper has already mentioned [1] the occurrence of the surface microrelief at periodic straining of model and real alloys. Studying the phenomenon of the alloys' structure self-organization under periodic loading will be continued within the frames of this paper.

4. THE PHENOMENON OF SELF-ORGANIZATION OF STRUCTURE AT PERIODIC STRAINING

The researches in chemistry and biology have collected a lot of examples of the behavior of non-equilibrium systems, where non-equilibrium is a source of the order. Formation of the Benard convection cells has become a striking example of such a behavior.

Studies of the surface microrelief of the working part of the specimen before and after straining also revealed the characteristic element of the structure (Fig. 4), which was obtained by the non-equilibrium periodic straining.

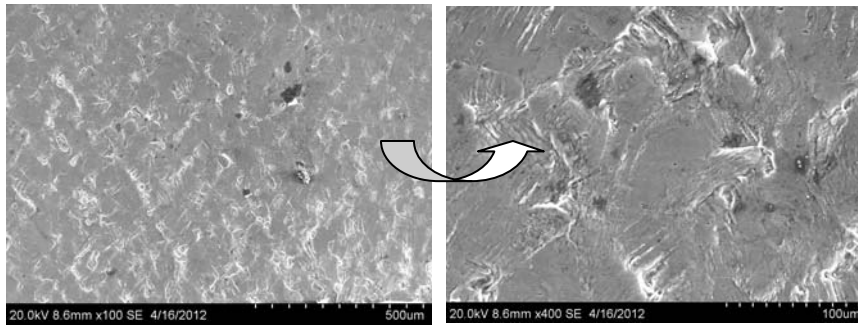


Figure 4. The element of surface microrelief structure of the specimen D16AT. Plating was removed.

This element (mesh [1] or the Benard cell) is found in the specimen after the non-equilibrium straining. It has typical sizes. The diagonal of a cell is oriented along the applied load, and the sides - on the areas of maximum shear stress.

With a scanning electron microscope JSM 6700F the grain structure before

and after straining has been studied. As a result of the periodic straining, the structure of the D16AT alloy's grains was much smaller than before the loading (Figure 5.)

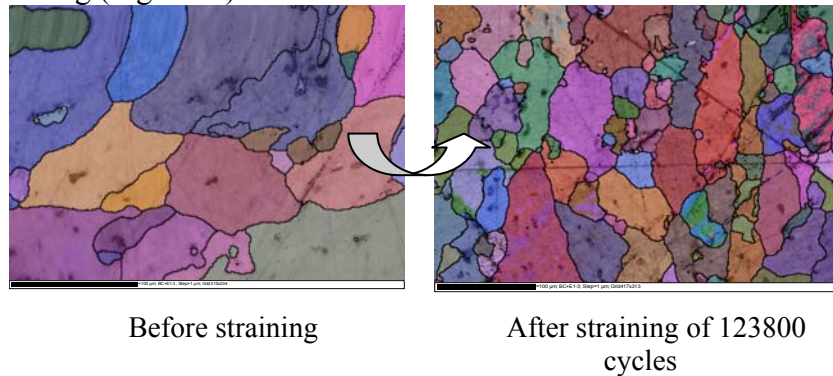


Figure 5. Fragmentation of the grained structure of the alloy after periodic straining. (D16AT)

5. CONCLUSION

It is concluded that the observed processes of the material warming-up, and laws of accumulation of macro - and micro strainings are generated by non-equilibrium process of straining beyond the elastic limit, occur on the surface of the working part of the specimen and are interdependent.

Experimentally it has been shown that the alloy, which initially was considered to be statistically homogeneous and in an equilibrium metastable state, has become capable of forming dissipative structures and self-organizing its microstructure in transition across the unstable equilibrium which is defined by the critical ratio of loading cycle characteristics.

In addition, the characteristics of the state: temperature of dissipative warming-up, components of the strain tensor, change of the grain structure, etc., can be seen as indicators and used for technical diagnostics of metal materials and machine parts.

REFERENCES

1. V.E. Panin, V.E. Egorushkin, A.V. Panin, Nonlinear wave processes in the strained solid as in the hierarchically organized system.// Physical Mesomechanics, 2012, V. 15., № 1. - p. 7-22.
2. I. Prigogin, A.D. Kondepudi. Modern Thermodynamics. From heat engines to dissipative structures. - Academic Press, 2002. – p. 461.
3. V.I. Kapustin, V.P. Gileta, E.A. Tereshin On determining the limits of elasticity of dissipative heating materials // PMTF 2010.T.51, № 3. p. 112-117.
4. V.T. Troshchenko Fatigue and inelasticity of metals. - Kiev: Naukova Dumka, 1971. – p.268.

A MODEL FOR FATIGUE CRACK GROWTH WITH A VARIABLE STRESS. DESCRIPTION IN TERMS OF CRACK MECHANICS

V. M. Kornev

Lavrentyev Institute of Hydrodynamics SB RAS, Novosibirsk, 630090, Russia

kornev@hydro.nsc.ru

Abstract: Stepwise extension of a crack in quasi-brittle materials under low-cycle loading conditions is considered. Both steady and unsteady loadings at pulsating loading mode are studied. It is proposed to use quasi-brittle fracture diagrams for solids under cyclic loading conditions. When diagrams are plotted, both necessary and sufficient fracture criteria by Neuber-Novozhikov are used. A specific implementation is made on the base of the Leonov-Panasyuk-Dugdale model for mode I cracks when the pre-fracture zone width coincides with the plasticity zone width near the crack tip. Curves divide the plane “loading versus crack length” into three subareas. The condition of a stepwise crack tip extension has been derived. A crack extends only in the embrittled material of the pre-fracture zone. The number of cycles between jumps of the crack tip is calculated by the Coffin equation, when damage accumulation in material in the pre-fracture zone is taken into account. Critical fracture parameters under low-cyclic loading conditions have been obtained in a closed form. Estimates of the average dimensionless rate of crack tip advance for a single loading cycle at stepwise crack extension have been obtained. The derived expressions for the average rate can be considered as structural relations for plotting Paris curves under steady loading conditions.

Key words: brittle and quasi-brittle fractures; fracture diagram; low-cyclic fatigue; damage accumulation; Paris curves.

1. INTRODUCTION

In order to obtain estimates for the number of cycles, the diagram of quasi-brittle fracture under low-cycle fatigue is used [1, 2].

2 .DIAGRAMS OF QUASI-BRITTLE FRACTURE UNDER SINGLE LOADING

Apply the simplest approximation of the $\sigma - \varepsilon$ diagram for elastic-plastic material when the diagram is approximated by a double-link straight line. The parameters of this approximation are as follows: E is the modulus of elasticity, σ_Y is the yield strength of material, and σ_Y is constant stress acting in accordance with the modified Leonov-Panasyuk-Dugdale model [3, 4], ε_0 is the maximum elastic material elongation ($\sigma_Y = E\varepsilon_0$), ε_1 is the maximum material elongation. Let r be the grain diameter for a granulated material with the regular structure. The Neuber-Novozhilov approach [5, 6] makes it possible to use solutions having a function of singularity for structured media.

Now consider an internal I mode crack. Let an internal plane I mode crack extends rectilinearly. In addition to the internal rectilinear crack-cut of length $2l_0$, model crack-cuts of length $2l = 2l_0 + 2\Delta$, each of pre-fracture zones Δ being located on the continuation of a real crack ($2l$ and Δ are lengths of model cracks and pre-fracture zones) are introduced into consideration. The problem of fatigue fracture has two linear scales: if a grain diameter is defined by a material structure, then the second linear size is governed by the system itself. Under low-cycle fatigue conditions, the second linear scales serve as pre-fracture zone lengths Δ , which change in accordance with changing i) the length of a real stepwise extending crack, and ii) the intensity of loading conditions. Emphasize that under single loading conditions, the critical pre-fracture zone length Δ^* is a completely definite parameter [7, 8] and $2l^* = 2l_0 + 2\Delta^*$ is the critical macrocrack length, that is $\Delta^* / l_0 \ll 1$ for quasi-brittle materials.

When diagrams of quasi-brittle fracture under conditions of low-cycle loading are plotted in [1, 2], sufficient fracture criteria are used when the mode I cracks are considered

$$\frac{1}{r} \int_0^r \sigma_y(x, 0) dx = \sigma_Y, \quad 2\nu(x, 0) = \delta^* \quad (1)$$

Here $\sigma_y(x, 0)$ are normal stresses on the crack continuation; Oxy are the rectangular coordinate systems oriented about right crack sides (the coordinate

origin coincides with the model crack tip in the modified Leonov-Panasyuk-Dugdale model [1, 2, 8]); $2\nu = 2\nu(x, 0)$ is crack opening ($x < 0$), δ^* is the critical crack opening displacement.

The field of normal stresses $\sigma_y(x, 0)$ on the model crack continuation $x > 0$ can be represented as a sum of two summands

$$\sigma_y(x, 0) \cong K_I / (2\pi x)^{1/2} + O(1), \quad K_I = K_{I\infty} + K_{I\Delta}, \quad K_{I\infty} > 0, \quad K_{I\Delta} < 0, \quad (2)$$

where $K_I = K_I(l, \Delta)$ are total stress intensity factors (SIFs) at the tips of model cracks, $K_{I\infty}$ are SIFs generated by stresses σ_∞ specified at infinity, $K_{I\Delta}$ are SIFs generated by constant stresses σ_Y . The first and second summands in relation (2) are singular and smooth parts of solution, respectively. The first equality in criterion (1) controls stresses on the model crack continuation after averaging, these stresses being coincident with the yield strength σ_Y , and the second equality in criterion (1) describes real crack blunting at its tip.

The first equality of the sufficient criterion (1) is a typical strength fracture criterion [9], and the second equality of this criterion is a deformation criterion [9]. The sufficient fracture criterion (1) simultaneously takes into consideration both strength and deformation fracture criteria at specific points of a pre-fracture zone. Selected specific points of the pre-fracture zone are well-adapted to description of stepwise crack tip advance and accumulation of damages in the pre-fracture zone material under fatigue conditions [1, 2].

The simplest analytical representation of the field of stresses $\sigma_y(x, 0)$ on the model crack continuation has the following form [8]

$$\sigma_y(x, 0) = \frac{K_{I\infty} + K_{I\Delta}}{\sqrt{2\pi x}} + \sigma_\infty = \frac{\sigma_\infty}{\sqrt{x}} \sqrt{\frac{l}{2}} + \frac{2\sigma_Y \sqrt{\Delta}}{\pi \sqrt{x}} + \sigma_\infty. \quad (3)$$

Introduce into consideration critical stresses calculated via the necessary fracture criterion σ_∞^0 and sufficient one σ_∞^* . In the view of the study of low-cycle fatigue, the most interesting loading area is $\sigma_\infty^0 \leq \sigma_\infty \leq \sigma_\infty^*$. After system (1) is solved, critical fracture parameters for quasi-brittle materials [1, 8] are as follows

$$\sigma_\infty^* = \sigma_\infty^* \left[l^*, \sigma_Y, (\varepsilon_1 - \varepsilon_0) / \varepsilon_0 \right], \quad \Delta^* = \Delta^* \left[l^*, \sigma_Y, (\varepsilon_1 - \varepsilon_0) / \varepsilon_0 \right];$$

$$\sigma_\infty^0 = \sigma_\infty^0(l_0, \sigma_Y), \quad \Delta \equiv 0. \quad (4)$$

Fracture diagrams for quasi-brittle materials are pairs of curves $\sigma_\infty^0 = \sigma_\infty^0(l_0, \sigma_Y)$, $\sigma_\infty^* = \sigma_\infty^* \left[l^*, \sigma_Y, (\varepsilon_1 - \varepsilon_0) / \varepsilon_0, \sigma_\Delta / \sigma_Y \right]$. Analytical representations of critical fracture parameters for quasi-brittle materials with account for solution representation (4) has the form [1]

$$\frac{\sigma_{\infty}^*}{\sigma_Y} = \left[\left(1 - \frac{5}{8\pi} \frac{\varepsilon_1 - \varepsilon_0}{\varepsilon_0} \right) \sqrt{\frac{2l^*}{r}} + 1 \right]^{-1}, \Delta^* = \frac{5^2}{2^9} \left(\frac{\varepsilon_1 - \varepsilon_0}{\varepsilon_0} \right)^2 \left(\frac{\sigma_{\infty}^*}{\sigma_Y} \right)^2 l^*,$$

$$\frac{\sigma_{\infty}^0}{\sigma_Y} = \left(\sqrt{\frac{2l_0}{r}} + 1 \right)^{-1}. \quad (5)$$

Expressions (5) make sense if $1 - (5/8\pi)[(\varepsilon_1 - \varepsilon_0)/\varepsilon_0] > 0$. For a plain specimen of the finite width, the critical fracture parameters can be written in the form [7]

$$\frac{\sigma_{\infty w}^*}{\sigma_Y} = \left[\left(1 - \frac{5}{8\pi} \frac{\varepsilon_1 - \varepsilon_0}{\varepsilon_0} \right) Y^* \sqrt{\frac{2l^*}{r}} + \frac{1}{1 - 2l^*/w} \right]^{-1},$$

$$\frac{\sigma_{\infty w}^0}{\sigma_Y} = \left(Y^0 \sqrt{\frac{2l_0}{r}} + \frac{1}{1 - 2l_0/w} \right)^{-1}. \quad (6)$$

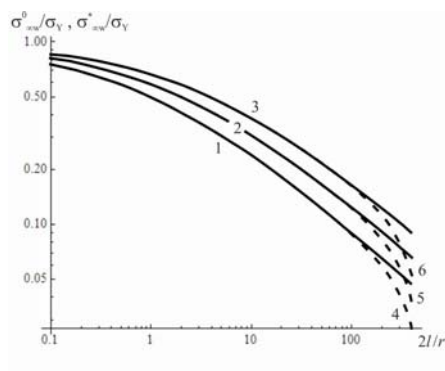


Fig. 1. Diagrams of quasi-brittle fracture for plain specimens

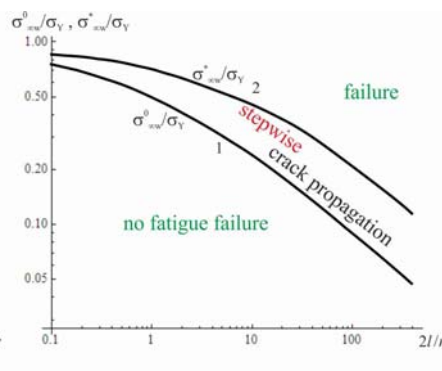


Fig. 2. Diagram of fatigue fracture

Here $w < \infty$ is the plain specimen width, $Y^0 = Y^0(l_0/w)$ and $Y^* = Y^*(l^*/w)$ are coefficients such that $K_{lw} = YK_l = Y\sigma_{\infty}\sqrt{\pi l}$. Values of the coefficient $Y^0 = Y^0(l_0/w)$ for various ratios l_0/w and loading conditions can be found in handbooks [10]. For calculations, the approximate relationship $Y^* \approx Y^0$ is used for quasi-brittle materials when $\Delta^*/l_0 \ll 1$. The finite specimen width effects upon critical fracture curves on the plane “crack length–internal load”. The calculation results are given in Fig. 1 in the log-log coordinates, when $w/r = 500$. In this Figure, the solid curve 1 and the dashed curve 4 are plotted via relation (5) for σ_{∞}^0

and via relation (6) для $\sigma_{\infty w}^0$, respectively; solid curves 2 and 3, and dashed lines 5 and 6 are plotted via relation (5) for σ_{∞}^* and via relation (6) for $\sigma_{\infty w}^*$, respectively, for $(\varepsilon_1 - \varepsilon_0) / \varepsilon_0 = 1.5; 2.5$. Pairs of curves 1-2, 1-3, and 4-5, 4-6 in Fig. 1 are diagrams of quasi-brittle fracture for plain specimens of infinite and finite width, respectively. Under cyclic loading conditions the subareas between curves $\sigma_{\infty}^0 / \sigma_Y$ and $\sigma_{\infty}^* / \sigma_Y$ are areas, in which damage accumulation in pre-fracture zone material takes place.

3. DIAGRAM OF QUASI-BRITTLE FRACTURE UNDER FATIGUE CONDITIONS

The original diagram of quasi-brittle fracture under fatigue conditions coincides with the diagram of quasi-brittle fracture under single loading if a single-frequency pulsating loading regime with the constant amplitude [1] is considered. Below, as it is in work [1], a cyclically stable material is considered, i.e., the yield strength $\sigma_Y = const$ is independent of the cycle number. One of curves of quasi-brittle fracture diagrams is changed with regard to damage accumulation in the pre-fracture zone for subsequent loading cycles up to the first crack tip advance because the material of this zone is embrittled.

When the proposed diagram at low-cycle fatigue [1] is plotted, there is no need to use SIFs. It can be plotted depending on both elastic-plastic material properties and a crack length. This diagram in Fig. 2 consisting of a pair of curves divides the plane of “crack length vs. external load amplitude” ($2l/r, \sigma_{\infty} / \sigma_Y$) into three subareas: 1. the subarea where fatigue fracture is not observed is located to the left and lower the curve $\sigma_{\infty}^0 / \sigma_Y$; 2. the subarea of fracture at single loading is located to the right and above the curve $\sigma_{\infty}^* / \sigma_Y$; 3. the subarea of stepwise crack propagation due to embrittlement of material under cyclic loading conditions is located between curves $\sigma_{\infty}^0 / \sigma_Y$ and $\sigma_{\infty}^* / \sigma_Y$. When repeated loads are applied, the curve $\sigma_{\infty}^* / \sigma_Y$ is transformed, embrittlement of the pre-fracture zone material being considered. The proposed diagram has two threshold values $\sigma_{\infty}^0 / \sigma_Y$ and $\sigma_{\infty}^* / \sigma_Y$ in relation (6).

Consider limitations typical for one-frequency loading with variable amplitude

$$\sigma_{\infty}^0 / \sigma_Y < \sigma_{\infty}^{+-} / \sigma_Y < \sigma_{\infty}^+ / \sigma_Y < \sigma_{\infty}^{++} / \sigma_Y < \sigma_{\infty}^* / \sigma_Y. \quad (7)$$

Here $\sigma_{\infty}^+ = const, \sigma_{\infty}^{+-} = const, \sigma_{\infty}^{++} = const$ are amplitudes corresponding to the normal loading, underloading, and overloading. When limitations (7) are obeyed, we have the low-cycle fatigue for three different loading regimes.

Changes in the subarea of the diagram of quasi-brittle fracture with account for damage accumulation are described by inequalities (7) for the normal loading regime $\sigma_{\infty}^+ / \sigma_Y$

$$\frac{\sigma_{\infty}^0}{\sigma_Y} < \frac{\sigma_{\infty}^+}{\sigma_Y} < \frac{\sigma_{\infty}^{*(s)}}{\sigma_Y}, 1 \leq s_j \leq N_j - 1, j = 1, 2, \dots, j^* - 1, \sigma_{\infty}^0 < \sigma_{\infty}^{*(s)} < \dots < \sigma_{\infty}^{*(2)} < \sigma_{\infty}^{*(1)} = \sigma_{\infty}^*; \\ \sigma_{\infty}^+ / \sigma_Y \geq \sigma_{\infty}^{*(s)} / \sigma_Y, s_j = N_j, j = 1, 2, \dots, j^*, \sigma_{\infty}^0 < \sigma_{\infty}^{*(s)}, \quad (8)$$

when the critical number of loading cycles N^* is calculated in such a way

$$N^* = 1 + \sum_1^{j^*-1} N_j, N_j \geq 2, j = 1, 2, \dots, j^* - 1, N_{j^*} = 1. \quad (9)$$

Here $\sigma_{\infty}^{*(s)}$ is the critical load obtained via the sufficient fracture criterion in s -th loading cycle up to $j = 1, 2, \dots, j^* - 1$ crack tip advance, s_j is number of cycle between $j-1$ and j crack tip advances, $s_j = 1$ corresponds to the state of original material after each crack tip advance, N_j is the number (group) of cycles between $(j-1)$ and j crack tip advances, N^* is the critical number of loading cycles (9).

For the loading level $\sigma_{\infty}^+ / \sigma_Y$ of a real crack of length $2l_{j-1}$, we have for specimens of finite width (6)

$$\frac{\sigma_{\infty w}^+}{\sigma_Y} = \left[\left(1 - \frac{5}{8\pi} \frac{\varepsilon_{j-1,w}^+ - \varepsilon_0}{\varepsilon_0} \right) Y^+ \left(\frac{l_{j-1}}{w} \right) \sqrt{\frac{2l_{j-1}}{r} + \frac{1}{1 - 2l_{j-1}/w}} \right]^{-1}, \quad (10)$$

$$\Delta_{j,w}^+ = \frac{5^2}{2^9} \left(\frac{\varepsilon_{j-1,w}^+ - \varepsilon_0}{\varepsilon_0} \right)^2 \left[Y^+ \left(\frac{l_{j-1}}{w} \right) \frac{\sigma_{\infty w}^+}{\sigma_Y} \right]^2 l_{j-1}, 2l_j = 2l_{j-1} + 2\Delta_j, j = 1, 2, \dots, j^*.$$

The number of cycles N_j between $j-1$ and j crack tip advances at the loading level $\sigma_{\infty}^+ / \sigma_Y$ is calculated as follows

$$(N_j)^C = (\varepsilon_1 - \varepsilon_0) / (\varepsilon_{j-1}^+ - \varepsilon_0), j = 1, 2, \dots, j^* - 1. \quad (11)$$

Here $0.2 \leq C \leq 1$ are Coffin's constants [11] numerical values of which depend on material properties. Parameter of original material $(\varepsilon_1 - \varepsilon_0)$ and inelastic elongations $(\varepsilon_{j-1}^+ - \varepsilon_0)$ at the appropriate loading regime enter Coffin's equation [11]. In fatigue failure, it is reasonable to obtain estimates of average dimensionless

rate $V = (\Delta_j^+ / r) / N_j$ of crack advance per one loading cycle for plain specimens of finite width (10) and (11) ($j = 1, 2, \dots, j^* - 1$)

$$V = \frac{\Delta_j^+ / r}{N_j} = \frac{5^2}{2^9} \left(\frac{\varepsilon_0}{\varepsilon_1 - \varepsilon_0} \right)^{1/C} \left(\frac{\varepsilon_{j-1}^+ - \varepsilon_0}{\varepsilon_0} \right)^{2+1/C} \left(\frac{\sigma_\infty^+}{\sigma_Y} \right)^2 \frac{l_{j-1}}{r}. \quad (12)$$

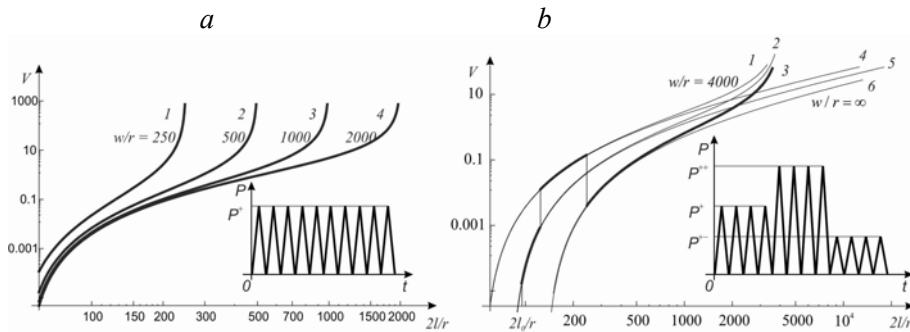


Fig. 3. The average rate of crack tip advance (Paris curves) in plain specimens of finite length for nonlinear summation $C = 0,5$ of damages under steady-state loading (a) and unsteady loading (b).

In considered loading regimes, the derived relationships (laws) describing crack growth (12) do not reduced to simple laws of fatigue crack growth. In the general case, these laws are not self-similar processes.

REFERENCES

1. V.M. Kornev. Quasi-brittle fracture diagrams of solids with structural hierarchy under low-cycle loading. *Physical. Mesomech.*, 14(5):31-45, 2011 (in Russian).
2. V.M. Kornev. Diagrams of quasi-brittle fatigue fracture (two-frequency loading). *Physical. Mesomech.*, 15(6):45-58, 2012 (in Russian).
3. M.Ya. Leonov and V.V. Pansyuk. Development of smallest cracks in a solid. *Prikl. Mekh.*, 5(4):391-401, 1959 (in Russian).
4. D.S. Dugdale. Yielding of steel sheets containing slits. *J. Mech. Phys. Sol.*, 8:100-108, 1960.
5. H. Neuber. *Kerbspannungslehre: Grunlagen fur Genaue Spannungsrechnung*. Springer-Verlag, 1937.
6. V.V. Novozhilov. About the necessary and sufficient brittle strength criteria. *Prikl. Mat. Mekh.*, 33(2):212-222, 1969 (in Russian).
7. V.M. Kornev and A.G. Demeshkin. Quasi-brittle fracture diagram of

- structured bodies in the presence of edge cracks. *J. Appl. Mech. Techn. Phys.*, 52(6):975-985, 2011.
8. V.M. Kornev. Evaluation diagram for quasi-brittle fracture of solids with structural hierarchy. Necessary and sufficient multiscale fracture criteria *Physical. Mesomech.*, 13(1):47-59, 2010 (in Russian).
14. I.M. Kershtein, V.D. Klyushnikov, E.V. Lomakin, S.A. Shesterikov. Basis of experimental fracture mechanics. Moscow universitet, Moscow, 1989 (in Russian).
15. Y. Murakami. Stress intensity factors handbook (in 2 vol.). Pergamon Press, Oxford, 1986.
16. L.F. Coffin and N.Y. Schenectady. A study of the effects of cyclic thermal stresses on a ductile metal. *Trans. of the ASME*, 76(6):931-950, 1954.

DETERMINATION OF H_{PL} FACTORS FOR PIPE – RING SPECIMENS USING FINITE ELEMENT ANALYSIS

Andrej Likeb¹, Nenad Gubelj¹, Jožef Predan¹, Yury G. Matvienko²

¹ *University of Maribor, Faculty of Mechanical Engineering, Smetanova 17, Maribor, Slovenia*

² *Mechanical Engineering Research Institute of the Russian Academy of Science, 4, M. Kharitonievsky Per., 101990 Moscow, Russia*

andrej.likeb@um.si, nenad.gubelj@um.si, jozef.predan@um.si,
ygmtatvienko@gmail.com

Abstract: The aim of this paper is to determine the plastic correction factors called η_{pl}^{LLD} and η_{pl}^{CMOD} for non – standard Pipe – Ring specimens to calculate J – Integral and analyze the elastic – plastic behavior of tested material regarding to shape of specimen. The analysis of evaluating η factor based on load separation concept. Therefore the research, realized by Finite Element Analysis of load displacement qof bending behaviour was performed on Pipe – Ring specimens with outer radius of $R=70\text{mm}$ and wall thickness of $t = 4.25\text{mm}$. Specimens with through thickness notch with three aspect ratios $a/W = 0.55; 0.5; 0.45$ and different notch tip radius $R_n = 0.1; 0.25; 0.5; 0.75; 1.25; 1.5$ and 2mm were considered in this analysis. The goal of this paper is find out relationship between notch tip radius of the notched non–standard specimens and plastic η factors.

Key words: CMOD-Crack Mouth Opening Displacement, LLD-Load Line Displacement, Plastic Correction Factors ($\eta_{pl}^{CMOD}, \eta_{pl}^{LLD}$), Pipe – Ring Specimens, FEM-Finite Element Method

1 INTRODUCTION

Structure integrity assessment of pipeline based on quality of input data, especially materials data. Often is quite difficult to measure fracture toughness of pipeline material by using specimen according to standards ASTM E-1820 or BS 7440 [1,2]. In order to find alternative technique for measurement fracture toughness of already delivered pipe-line segment, the new pipe-ring specimen has been proposed by Matvienko. Specimen contains cracks or machine notch with standard aspect ratio a/W . Since the fracture behavior of ductile material depends on geometry and loading manner of specimen, the relevant calibration curve between fracture toughness measured using standard specimens and pipe-ring specimens should be determined. Test method for measurement of elastic-plastic fracture toughness JIC are based on the single specimen technique and require a load versus load line displacement record or crack mouth opening displacement record in the calculation of J-integral. The elastic component of J-integral is the Griffith energy release rate G . The plastic component of the J-integral is usually measured from the area under a load versus load line displacement curve, where η_{pl} the plastic correction factor is used.

With load separation method approach, successfully analyzed J – Integral and elastic – plastic fracture mechanics behavior of structure components for standard and non – standard specimens under pure mode I loading, can be done using only numerical approach. [3, 4]

In this paper determination of η_{pl} factors for Pipe – Ring non – standard specimens based on Finite Element Analysis because standard – experimentally approach terms on required time of production specimens and makes costly consuming procedure.

2. LOAD SEPARATION METHOD

Load separation method is the theoretical approach that has been developed to experimentally estimate J – Integral and used it to calculate η_{pl} factors

for standard and non – standard specimen with certain crack and notch size of different materials and specimen configurations. [3-11]

A method is suggested by Paris and colleagues and is based on separate for the load P in plastic region [3]. Load P is represented as a product of two functions. Load separation concept introduces a separation parameter S_{ij} as the ratio of loads $P(a, v_{pl})$ of same specimen but with two different crack lengths a_i and a_j over the entire region of the plastic displacement v_{pl} . [2] So if the load is in the next separable expression:

$$P = G\left(\frac{b}{W}\right)H\left(\frac{v_{pl}}{W}\right) \quad (1)$$

where G is specimen geometry function and H is the material deformation function. Then the load separation concept is noted as the following Equation (2) presents:

$$S_{ij} = \frac{P(a_i, v_{pl})}{P(a_j, v_{pl})} \Big|_{v_{pl}=const.} = \frac{G\left(\frac{b_i}{W}\right)H\left(\frac{v_{pl}}{W}\right)}{G\left(\frac{b_j}{W}\right)H\left(\frac{v_{pl}}{W}\right)} = \frac{G\left(\frac{b_i}{W}\right)}{G\left(\frac{b_j}{W}\right)} = const \quad (2)$$

a_i and a_j from Equation (2) are two different crack lengths, v_{pl} is plastic displacement. The average separation constants S_{ij} versus uncracked ligament b_i/W on logarithmic plot $\log(S_{ij}) - \log(b_i/W)$ made points. Through these points the fitted straight line gives the slope which is actually the η_{pl} factor. It is important that the η_{pl} factors are estimated for at least three specimens with different crack aspect ratios. [2]

3. ESTIMATION OF η_{pl}^{LLD} AND η_{pl}^{CMOD} FACTORS FOR PIPE - RING SPECIMEN USING FEA

The determination of η_{pl} correction factors for non – standard Pipe – Ring specimen shape were performed on three point bending experiment with Simulia Abaqus 6.11–3 finite element analysis software. Three point bended experiments was used to acquire concentrated force under the center loading point and to got premature failure of material. Pipe – Ring specimens with outer radius of $R = 70\text{mm}$ and wall thickness of $t = 4.25\text{mm}$ were notched through wall thickness with initial aspect ratio $a/W = 0.55; 0.5; 0.45$ and blunt notched with notch tip radius $R_n = 0.1; 0.25; 0.5; 0.75; 1.25; 1.5$ and 2mm . There were also maded three analyzes for Cracked only specimens through wall thickness with different crack aspect ratios a/W to compare and evaluate suitability of solutions. Geometry, scheme of testing and specimens characterizations are displayed on *Figure 1*.

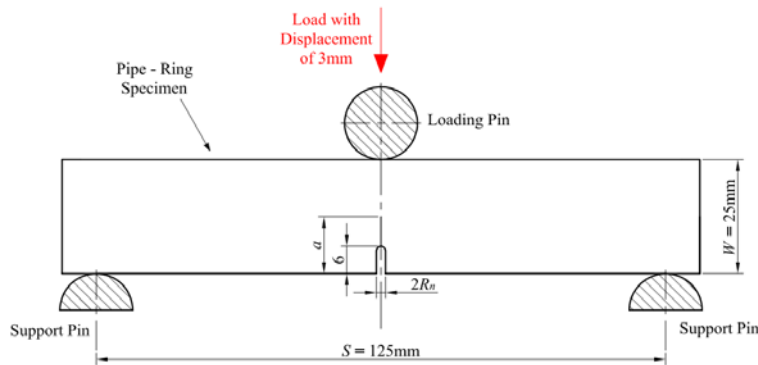


Figure 1. Side view scheme of a three point bended Pipe – Ring specimen with $a/W = 0.5$ and 6mm of notch depth with notch radius $R_n = 1.5\text{mm}$.

The specimens with crack aspect ratio of $a/W = 0.45$ and 0.5 were notched only up to 6mm of depth *Figure 1*, except the reference specimens which were fully notched up to $a/W = 0.55$.

The η_{pl}^{LLD} and η_{pl}^{CMOD} correction factors for non – standard Pipe – Ring specimen were determined under linearly increased force up to 3mm of load line displacement. Analyze of fracture toughness behavior for structure

Steel based on material with yield stress of $\sigma_y = 220\text{MPa}$ and true ultimate stress $\sigma_u = 500\text{MPa}$.

Input material data for the analyses were Young's modulus $E = 210000\text{MPa}$, Poisson ratio 0.3 and true stress – strain curve with $\sigma_y = 220\text{MPa}$. But because the simulations were solved using Dynamic Implicit solver to avoid divergence of solution of nonlinear solved problem, it was also necessary to add material density in Abaqus default unit $\rho = 7.85 \cdot 10^{-9} \text{ tonne/mm}^3$.

The analyses were performed on specimen half models, because specimens were symmetric through half. That gave us better options to determine boundary conditions and it's also decreased time of computation.

Loading and boundary conditions are displayed of *Figure 2 and 3* for Pipe – Ring specimen with $a/W = 0.5$ and 6mm of notch depth with notch radius $R_n = 1.5\text{mm}$. The tags U1, U2 and U3 signify directions in x, y and z – axis. UR1, UR2 and UR3 signify rotations in x, y and z – axis.

For all other cases of tested specimens, analyses were same according to load, supports and so allowed displacement in vertical z - axis.

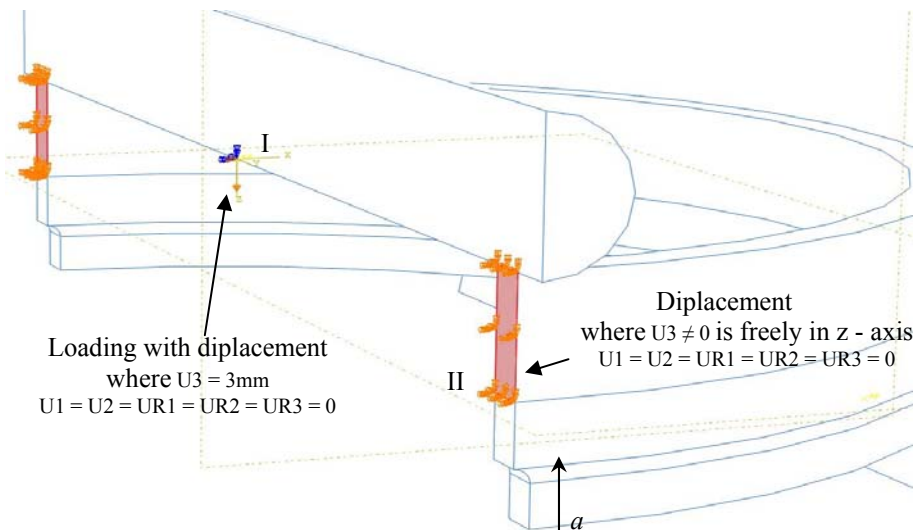


Figure 2. Boundary conditions. I) Loading with $U_3 = 3\text{mm}$ of displacement on reference point of half loading pin. II) Free in vertical z – axis, $U_3 \neq 0$.

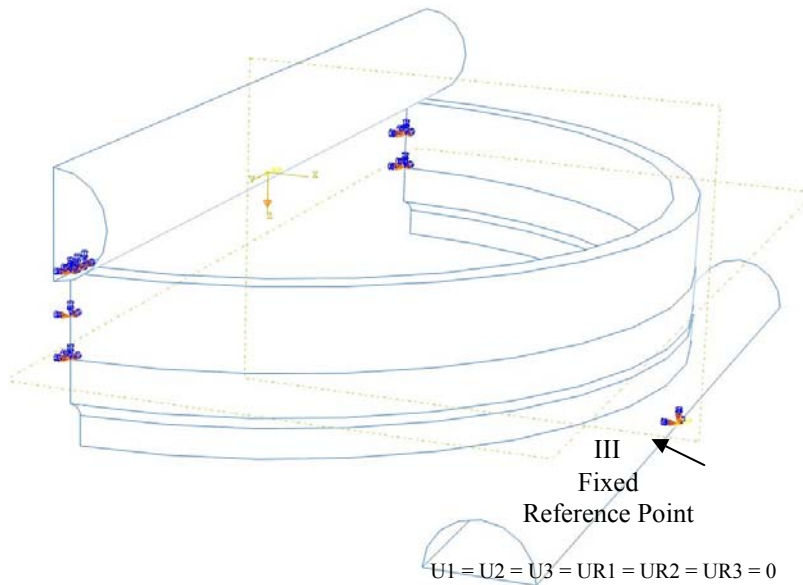


Figure 3. III) Fixed reference point with no allowed directions and rotations to fix supports and balanced whole system.

CAD models always presents a lot of attention on meshing if we want to get accurate and well corresponded solutions. Meshing of Pipe – Ring model was done manually by using Seed Edge option to refine mesh on most important places where expected results were. Method of edge meshing based on size of element from min 0.15 to max 0.5. Meanwhile other edges of model were meshed by number of elements 100 and bias ratio of 75.

Between loading pin and specimen and also between support pin and specimen are required interaction properties. Discretization method was surface to surface contact with no adjustments for surfaces. Contact properties were described as normal component with not allowed separation, and as tangential component with friction coefficient of 0.1. It was also assumed that on the contact places small sliding behavior occurred during loading.

As it was mentioned, solving of analyses were done using Dynamic implicit procedure with step time period 1 and Nlgeom option on ON.

Incrementation was set to automatic with maximum number of increments 1000. Initial and maximum increment size were set to 0.01, and minimum size was set to $1 \cdot 10^{-10}$. All other options and settings were set on default as full Newton solution technique and default equation solver.

4. RESULTS AND DISCUSSION

When all analyses were done, next data (Force vs. time, total Load Line Displacement vs. time and total Crack Mouth Opening Displacement vs. time) has been carried out and saved for each analysis separately. Because the first thirty to forty increments of full step for single analysis nothing happened, only time was running without increasing force or displacement and solution was diverging, all data must be adjusted to removed zero and negative values.

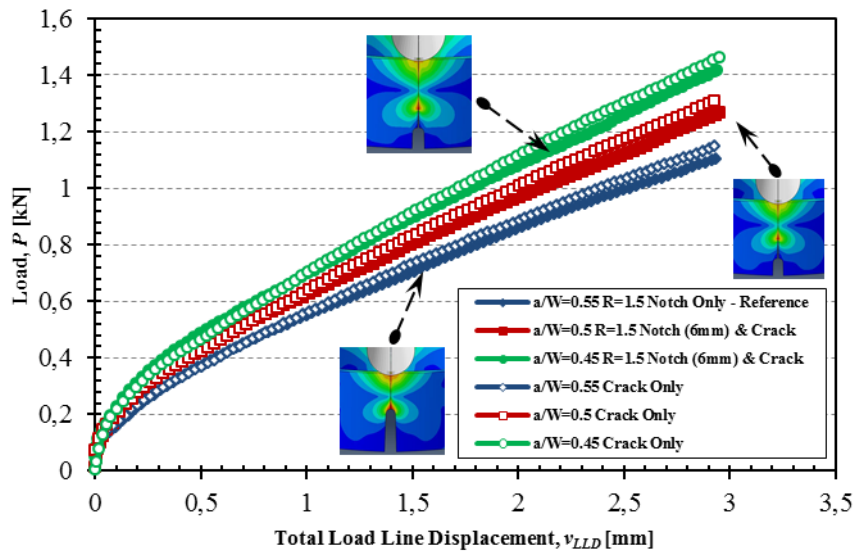


Figure 4. Load versus total Load Line Displacement curves for different a/W and with notch radius $R_n = 1.5\text{mm}$.

After that load vs. displacement curves for each notch radius R_n , were been plotted on Load vs. total Crack Mouth Opening Displacement and Load vs. total Load Line Displacement plots. *Figures 4* shows dependence 4

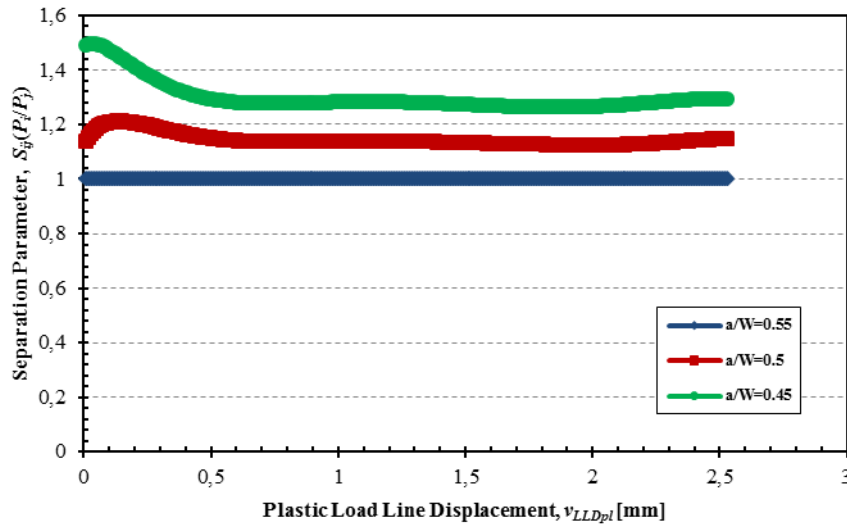


Figure 5. Separation parameters S_{ij} for notch radius $R_n = 1.5\text{mm}$ with different crack aspect ratios a/W versus plastic Load Line Displacement.

The next Figures 5 shows separation parameters S_{ij} for each point considered v_{LLDP_l} displacements. It is obvious that proves unstable increased force in proportionality of linearly ramped loading displacement for first fifty increments, because of very differently growth of the plastic zone through wall thickness. And then after a certain time at some point of loading, the force increasing gets lined with increased displacement and started linearly growth.

The average values of separation constants S_{ij} from Figure 5 are versus the uncracked ligaments b_i/W for single specimen gave points from which the slope of the $\log(S_{ij}) - \log(b_i/W)$ curves are η_{pl} factors.

Table 1: Results of estimated η_{pl} factors in dependence of notch radius

η_{pl}	Notch (6mm) and Crack							Crack Only
	$R_n = 0.1$	$R_n = 0.25$	$R_n = 0.5$	$R_n = 0.75$	$R_n = 1.25$	$R_n = 1.5$	$R_n = 2$	
CMOD	1.7974	1.6088	1.6373	2.0436	2.0179	2.2502	2.706	2.0683
LLD	0.8809	1.2159	1.0886	1.3188	1.352	1.2981	1.6744	1.4289

Generally values of η_{pl} factors should increase with increased notch radius R_n but that it's not true. It has to be mentioned that because of non – standard geometry of Pipe – Ring specimens, deformations are not uniformed through thickness of specimens and causes that the η_{pl}^{LLD} factors did not increase continuously with increased notch radius.

5. SUMMARY

As it is presented in several listed references, the load separation method is very effective approach to analyze plastic behavior and measure the η_{pl} factors for non – standard shape of specimens like Pipe – Ring is. η_{pl}^{CMOD} factors Pipe – Ring specimens increase with the increased notch radius continuously as normal, but that is not the same with η_{pl}^{LLD} factors where is exhibited greater impact of plastic zone.

That makes a lot of attention on further research work, that will include experimental and FEA testing of several different Pipe – Ring specimen geometries to determine both η_{pl}^{CMOD} and η_{pl}^{LLD} factors. Also to calculate changing of fracture toughness between standard and non – standard Pipe – Ring specimens and after all find their necessary correlation.

REFERENCES

1. ASTM E-1820: Standard test method for measurement of fracture toughness, Annual Book of ASTM Standards, Vol. 03.01, 2013
2. BS 7448: "Fracture mechanics toughness test, Part 1 published in 1991, Part 2: Method for determination of KIC, critical CTOD and critical J Values of Welds in Metallic Materials", TWI Abingdon Hall, Cambridge, December 1995.
3. Yu. G. Matvienko. Separable functions in load separation for the η_{pl} and η_{pl}^{CMOD} plastic factors estimation. *Int Journal of Fracture*, (2004). **129**:265–278.
4. Yu. G. Matvienko and Muravin E. L. Numerical Estimation of Plastic J-Integral by the Load Separation Method for Inclined Cracks under Tension. *Int Journal of Fracture*, (2011). **168**:251–257.

5. Y. S. Kim, Yu. G. Matvineko and H. C. Jeong. Development of Experimental Procedure based on the Load Separation Method to measure the Fracture toughness of Zr-2.5Nb Tubes. *Key Engineering Materials Vols. 345-346*, (2007). pp. 449-452
6. M. H. Sharobeam and J. D. Landes. The load separation criterion and methodology in ductile fracture mechanics. *Int Journal of Fracture*, (1991). **47**:81-104.
7. M. H. Sharobeam and J. D. Landes. A simplified approach for ductile failure analysis of semi – elliptical surface cracks. *Int Journal of Fracture*, (1993). **61**:379-395.
8. M. H. Sharobeam and J. D. Landes. Numerical solution for ductile behavior of semi – elliptical surface crack. *Int Journal of Fracture*, (1999). **63**:131-145.
9. A. N. Cassanelli, R. Cocco, L. A. de Vedia. Separability property and η_{pl} factor in ASTM A387-Gr22 steel plate. *Eng Fracture Mechanics*, (2003). **70**:1131-1142.
10. J. Capelle, J. Gilgert, Yu. G. Matvienko and G. Pluinage. Measurement of the resistance to fracture emanating from scratches in gas pipes using non-standard curved specimens. In: Security and Reliability of Damaged Structures and Defective materials/ eds.: G. Pluinage and A. Sedmak, *Springer Netherlands*, (2009). 157-174.
11. P. C. Paris, H. Ernst and C. E. Turner. A J – Integral approach to development of η factors. In Fracture Mechanics: Twelfth Conference, ASTM STP 700. American Society for Testing and Materials. Philadelphia, (1980). pp. 338-351.

ANALYSIS OF LARGE-SCALE CATASTROPHES IN COMPLEX ENGINEERING SAFETY

Nikolay A. Makhutov, Dmitry O. Reznikov

*Mechanical Engineering Research Institute of the Russian Academy of Sciences. 10199 0, 4,
M.Kharitonievsky Lane, Moscow, Russia*

kei51@mail.ru, imashreznikoff@yandex.ru

Abstract: The paper presents the current status of research activity as well as regulatory and legislative basis in the field of ensuring engineering safety. Most of the currently available safety methods have been developed on the assumption that engineering systems are tractable. As this assumption is not valid for complex engineering systems (CES), there is a need to develop methods to deal with intractable systems. This could be done based on resilience and robustness engineering approach. The proposed approach should not be considered as a substitute rather a supplement to the traditional one. Adopting this view creates a need to move beyond traditional “threat-vulnerability-consequence” models that are limited to analyzing design-basis events and deal with beyond design-basis impacts (and impact combinations) on CTSs. This new approach is based on such concepts as robustness and resilience that allows one to provide more comprehensive explanations of accidents as wells as identify ways to reduce risks caused by beyond design-basis impacts. The new safety paradigm for complex engineering systems should focus the efforts not only on development of protection barriers and safeguards against design-basis accidents but also on increasing the CES’s robustness and resilience towards beyond design-basis impacts.

Key words: Engineering safety, risk, robustness, resilience, beyond design-basis impact.

1. INTRODUCTION

Modern society cannot exist without stable and reliable engineering systems, whose operation is vital for any national economy and constituent the back-bone of the modern industry and society. These systems include electric power transmission and distribution; rail and road transportation systems; oil, gas, and water processing, storage and delivery; telecommunication and information networks. Their performance is commensurate with storing and processing huge amounts of information, energy and hazardous substances.

Complex engineering systems (*CES*) are critical in terms of life support of population and ensuring sustainable development of the economy. The functioning *CES* is related to storing and conversion of huge amounts of energy. The unauthorized release of the energy at *CES* may cause disastrous consequences and trigger cascading failures in interrelated infrastructures.

An extensive bank of knowledge has been created by scientists of different countries for analysis and classification of natural and man-made emergencies, and in-depth study of the processes of their initiation and propagation in order to reduce vulnerability of *CES* in case of natural or manmade catastrophes.

2. FUNDAMENTALS OF SAFETY ANALYSIS FOR COMPLEX SYSTEMS

Complex engineering systems are referred to the group of high risk critical facilities. The failure to provide for basic characteristics of strength, reliability, resilience and robustness with regard to a range of criteria leads to the possibility of accidents and catastrophic situations arising and developing at all stages of the life cycle of high risk facilities. Over the past decade, institutes of the Russian Academy of Sciences, the Russian Ministry of Emergency Situations, the Russian Ministry of Education and Science, have synthesized a substantial volume of fundamental information on accidents and catastrophes of an industrial and natural character as part of the State Scientific-Technical Program for *Safety for the Population and Economic Objects Considering the Risk of Natural and Manmade Disasters* (“SSTP Safety”). These efforts were continued in the frame of the Federal Research Program *Reduction of Risks and Mitigation of Consequences of Natural and Manmade Emergencies in the Russian Federation*. In carrying

out these programs, participants analyzed and generalized information on the basic characteristics, conditions, and scenarios for the outbreak of accidents and catastrophes in the natural and industrial spheres engendered by complex dangerous phenomena and processes in various regions of the world. Hazardous components of high risk facilities (atomic power stations, petroleum chemical plants, hydropower engineering facilities, etc.) might create catastrophes in the following classes (from 7 to 1): planetary, global, national, regional, local, facility-level, and localized (Figure 1). The potential losses and periodicity of occurrence were evaluated depending on the class of accidents and catastrophes (beginning from the global and ending with the localized) [1].

Official documents in the Russian Federation use six classes of catastrophes (from 6 to 1): transborder (equivalent to global), federal (equivalent to national), regional, local, facility-level, and localized. Based on the results of this summary analysis, a classification of catastrophes was constructed, taking into account the losses U and the periodicity ΔT of their occurrence (see Table 1). Here the magnitude U for each catastrophe decreases from $10^{10} \div 10^{11}$ to $10^3 \div 10^4$ dollars, while the periodicity of their occurrence declines from $(3 \div 5) \cdot 10^1$ to 10^{-1} years. Thus, the variation in losses (dollars per catastrophe) for various types of disasters could reach seven orders of magnitude, while that of the probability of occurrence $P=1/\Delta T$ (1/year) could reach three orders of magnitude.

The concept of risk is the key one in resolving problems related to ensuring safety. Risk is defined by means of the functional F_R of the probability that a catastrophe will occur and the magnitude of loss inflicted.

$$R = F_R \{P, U\} = \sum_{i=1}^n R_i = \sum_{i=1}^n P_i \cdot U_i = \int U(P) \cdot P dP = \int P(U) \cdot U dU \quad (1)$$

where R represents the risk associated with a natural or manmade catastrophe, P is its probability, and U is loss (1).

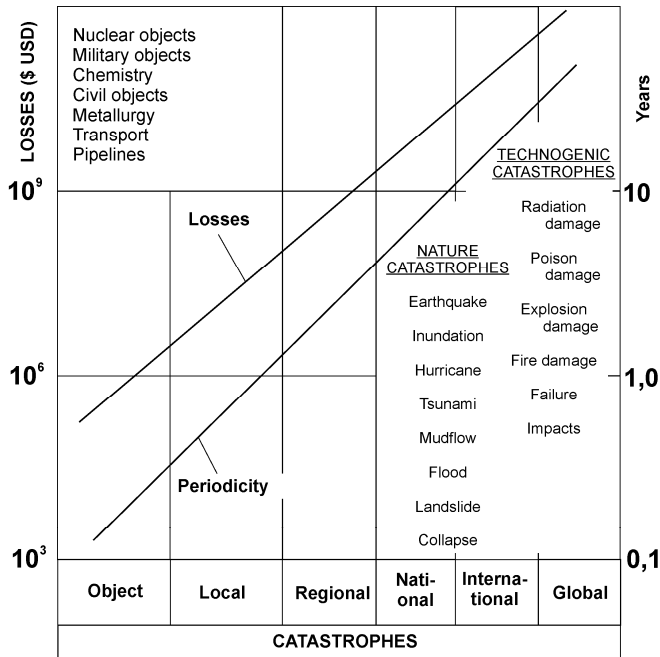


Figure 1. Losses and periodicity of natural and manmade catastrophes

Table 1. Risks of accidents and catastrophes

No	Class of accidents and catastrophes	P (1/year)	U (dollars)	R (dollars/year)
1	Localized	$5.0 \cdot 10^0$	$5.0 \cdot 10^3$	$2.5 \cdot 10^4$
2	Facility-level	$1.2 \cdot 10^0$	$4.0 \cdot 10^5$	$4.8 \cdot 10^5$
3	Local	$5.0 \cdot 10^{-1}$	$7.0 \cdot 10^6$	$3.5 \cdot 10^6$
4	Regional	$1.6 \cdot 10^{-1}$	$1.0 \cdot 10^8$	$1.6 \cdot 10^7$
5	National	$1.2 \cdot 10^{-1}$	$1.5 \cdot 10^9$	$1.8 \cdot 10^8$
6	Global	$8.0 \cdot 10^{-2}$	$1.0 \cdot 10^{10}$	$8.0 \cdot 10^8$

The risks vary within the bounds of four orders of magnitude. For Russia, the probability of the occurrence of national and regional natural-manmade extreme situations differ by 1.4 times and are approximately on the order of

magnitude lower than the risk for local situations; the likelihood of local and facility-level accidents differ by 5 times.

The assessment of the probability P , losses U , and risks R of accidents and catastrophic situations involves a group of risk identification methods, including various methods for analyzing statistical information on natural and manmade catastrophes of a particular type in the region being studied, as well as methods for analyzing the reliability of equipment and technological processes and the effectiveness of management and control. Methods for calculating the magnitude of loss substantially differ for various technical facilities and natural systems. Therefore, specialists in Russia and other countries have developed a group of special methods aimed at analyzing natural-manmade processes capable of leading to accidents and catastrophic situations at engineering infrastructures.

These methods are based on special graph models called scenario trees. The system is designed to fulfill a so called success scenario S_0 (i.e. a transition from its initial state IS to the designed end state ES_0). Since any failure scenario S_i presents a deviation from the success scenario S_0 that corresponds to the successful functioning of the CES , the scenario S_i must have a disturbance point at which an extreme event (load regime) A_i ($i = 1, 2, \dots, m$), occurs (Figure. 2). Each attack gives rise to a branch of a scenario tree that has a corresponding scenario S_j ($j = 1, 2, \dots, n$) that ends with an end state ES_j .

In this case one can get a risk index using the following matrix expression:

$$R = \underbrace{\{P(A_1); P(A_2); \dots; P(A_n)\}}_{\text{Threat } T} \times \underbrace{\begin{bmatrix} P[ES_1 | A_1] & P[ES_2 | A_1] & \dots & P[ES_m | A_1] \\ P[ES_1 | A_2] & P[ES_2 | A_2] & \dots & P[ES_m | A_2] \\ \dots & \dots & \dots & \dots \\ P[ES_1 | A_n] & P[ES_2 | A_n] & \dots & P[ES_m | A_n] \end{bmatrix}}_{\text{Vulnerability } V} \times \underbrace{\begin{Bmatrix} U_{ES_1} \\ U_{ES_2} \\ \dots \\ U_{ES_m} \end{Bmatrix}}_{\text{Consequences } C} \quad (2)$$

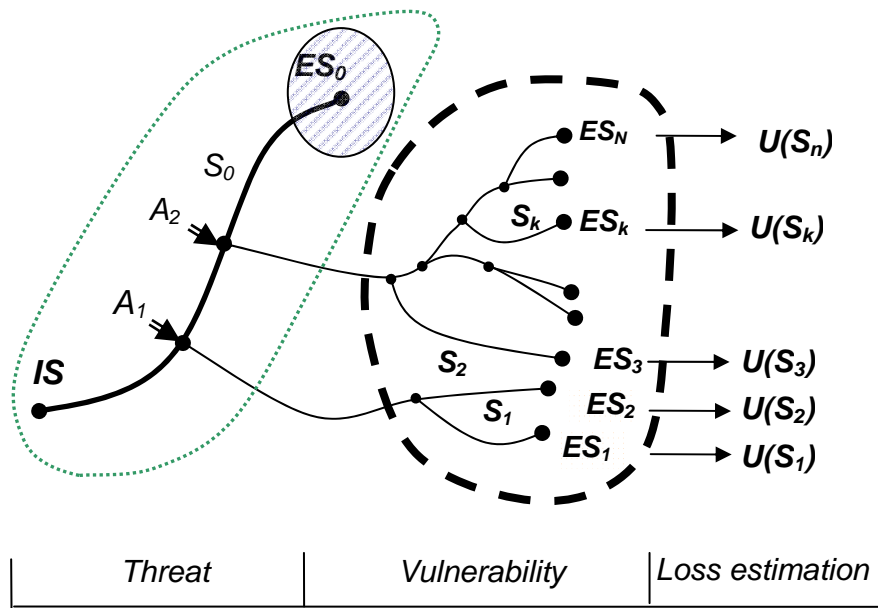


Figure 2. General risk assessment framework

3. NEW SAFETY PARADIGM: MOVING FROM “PROTECTION” TO “PROTECTION + RESILIENCE”

The complexity of modern engineering systems and their interdependence with other systems makes them vulnerable to emergency situations triggered by natural and manmade catastrophes or terrorist attacks.

These complexities largely stem from the vast functional and spatial dependencies and nonlinear interactions between the components of CES as well as from interdependencies that exist among the CESs, which enable failures to cascade within one system and from a system to other system.

Different historical, economical, political, social as well as cultural traditions have formed different approaches to ensuring safety of CES. Contemporary CESs, i.e. power, transport, and telecommunication networks, are becoming transboundary. Their significant spatial extension makes their functioning dependent on many factors and events in different parts of the world. The ensuring of complex engineering system safety is a complex interdisciplinary problem. It is impossible to solve this problem

without joining efforts of experts in different fields and taking into account technical, social, psychological, and cultural-historical aspects.

Analysis of major disasters at CES in different countries shows that high-risk systems in many cases are being designed and constructed according to traditional design codes and norms that are based on common and quite simple linear ‘sequential’ risk assessment models and employ traditional design, diagnostics and protection methods and procedures. This is being done in the assumption that a bounding set of credible (design-basis) impacts and subsequent failure scenarios could be determined for the CES thus allowing one to create a system of protection barriers and safeguards that could secure the CES from the identified impacts with required substantially high probability. This bundling set of impacts referred to as design-basis impacts includes normal operation events as well as abnormal events (components failures, human errors, extreme environmental loads, intentional unauthorized impacts on CES) that are expected to occur or might occur at least once during the lifetime of the CES.

In this approach a number of low probability impacts of extreme intensity are neglected as being practically incredible. Other impacts or impact combinations are not identified and, consequently, not analyzed. Such impacts and impact combinations of different types are classified as beyond design-basis impacts. Thus the issue of protection of CES from beyond design-basis impacts has not been addressed in a proper manner. These impacts however can cause large-scale disasters of extreme severity and induce tremendous property losses and a great number of victims. Such disasters are referred to as beyond design-bases accidents.

A typical example of a beyond design-basis accident is the recent accident at the Fukushima NPP where the height of the Tsunami wave exceeded the designed level. Another example is the Chernobyl catastrophe that was caused by a combination of technical failures, operator’s errors and organizational violations.

It should be noted that the efforts on protection of CES has been traditionally focused on technical issues. All this allows one to substantially increase reliability of the technical components of CESs. This approach however is close to its exhaustion. This is due to the fact that CESs are no longer predominantly technical but socio-technical systems. The

performance of CES is becoming more and more dependable on human and organizations factors. The statistics of accidents at CES reads that from 70 to 90% of accidents at complex engineering systems are caused by human errors made at the stage of design, construction, maintenance and operation of complex engineering systems. It means that these accidents can not be prevented by technical measures only. Some of the emergencies are typical and predictable but others are not. The latter are classified as beyond design-basis events. Some of human errors should also be classified as beyond design-basis impacts on CES.

The traditional approach to modeling socio-technical systems implies decomposition into technical, human and organizational subsystems (levels) that are then studied within different disciplines. Thus the interdependencies between subsystems and their influences on the system's safety are not considered properly.

It should be noted that design, construction and operation of complex engineering systems are being done in competitive environment. There is always a temptation to increase effectiveness by means of reducing investments in safety related activity. In order to justify such reduction organizations operating CESs may intentionally underestimate safety and security risks. The easiest way to do it is to unfoundly reduce the set of design-basis impacts and design-basis accidents or in other words to extend the list of beyond design-basis impacts in order not to consider them. The question "How to assess risks resulted from beyond design-basis events?" requires a special detailed investigation.

Currently available methodologies of risk assessment and CESs design codes have been developed without accounting for risks of beyond design-basis accidents. It means that these methodologies and codes should be revised to include into consideration risks of beyond design-basis impacts on complex engineering systems.

Complex engineering systems are becoming global networks. Protection of complex engineering systems requires pulling the efforts of specialist from different countries. The currently available methodologies of risk assessment and reliability engineering were developed for complicated technological systems with fixed boundaries, well-specified targets of hazards and for systems for which exists historical and/or actuarial data on

accidents initiation events, components failure rates and accidents' consequences which allow one quantify and verify models taking into account uncertainties deriving from both natural variations of the systems parameters (and performance conditions) as well as from lack of knowledge of the system itself.

The current accident models and risk assessment techniques such as fault and event tree analysis are not adequate to account for the complexity of complex engineering systems. The performance of complex engineering systems (as socio-technical systems) depends on the interaction between technical, human and organizational factors. Due to rapid technological and societal developments of the recent decades complex engineering systems are becoming steadily more complex. It means that (1) in safety assessments for CES there are too many details to be considered and (2) some modes of CES's operation may be incompletely known due to complex nonlinear interactions between components of CES, tight couplings among different systems and because CES and its environment may change faster than they can be described. As a result complex engineering systems are becoming underspecified and therefore intractable. Thus for CES it is not possible to describe its performance in every detail, and their performance must therefore be flexible and adaptive rather than rigid.

The distinction between tractable and intractable systems is very important in development safety management systems for CESs. Intractable systems cannot be completely described or specified. In other words for complex engineering systems it is practically impossible to define a bounding set of design-basis impacts that are expected to occur or might occur at least once during the lifetime of the CES.

Most current safety methods however have been developed on the assumption that systems are tractable. As this assumption is not valid for CESs, there is a need to develop methods to deal with intractable systems. This could be done based on Resilience and Robustness Engineering approach. The proposed approach should not be considered as a substitute rather a supplement to the traditional one.

Adopting this view creates a need to move beyond traditional “threat-vulnerability-consequence” models that are limited to analyzing design-basis events and deal with beyond design-basis impacts (and impact

combinations). This new approach will be based on such concepts as robustness and resilience to provide more comprehensive explanations of accidents as well as identify ways to reduce risks caused by beyond design-basis impacts.

In other words the new safety paradigm for complex engineering systems and other complex socio technical systems should focus the efforts not only on development of protection barriers and safeguards against design-basis accidents but also on increasing the CES's robustness and resilience towards beyond design-basis impacts.

Traditionally, accidents at CES have been viewed as resulting from a chain of failure events, each related to its "causal" event or events. It means that currently available risk assessment techniques are based on this linear notion of causality, which have severe limitations in the modeling and analysis of modern complex socio-technical systems that include nonlinear interactions between components, feedback loops, multiple source of failure, etc. Thus traditional accident modeling approaches are not adequate to analyze accidents that occur in complex engineering systems where accidents do not occur due to a single technical failure or human error; rather they arise from the interconnection of several causal factors originating at many levels in a system: hardware failures, human errors (mistakes and/or procedural violations committed by CES operators), latent conditions (arising from such aspects as management decision practices, or cultural influences), local triggering events (such as extreme weather conditions).

Thus, the study of complex engineering systems (being socio-technical systems) requires an understanding of the interactions and interrelationships between the technical, human, social and organizational aspects of systems. These interactions and interrelationships are complex and non-linear, and traditional modeling approaches cannot fully analyze the behaviors and failure modes of such systems.

Thus each complex engineering systems should be treated as an integrated whole, and the emphasis will be made on the simultaneous consideration of technical and social aspects of systems, including engineering design and maintenance strategies of CESs as well as social structures and cultures, social interaction processes, and individual factors such as capability and

motivation of operators. Interdisciplinary research should be applied to capture the complexity of complex engineering systems from a broad systemic view for understanding the multi-dimensional aspects of safety and modeling accidents in socio-technical systems.

As previously stated due to the complexity of complex engineering systems and their potential to large-scale catastrophes in order to ensure safety of such systems one needs to move beyond traditional design-basis risk assessment framework. Here a new paradigm is needed that is focused on increasing CES's robustness and resilience (Figure.3). That means that if the beyond design-basis accidents are to be considered the scope of the analysis should be widened. Safety related efforts should be focused not only on development of protection barriers and safeguards from predetermined (postulated) set of maximal credible accidents but also on increasing complex engineering system robustness and resilience that would prevent catastrophic failure and long-term disfunctioning of CESs in case of beyond design-basis accident.

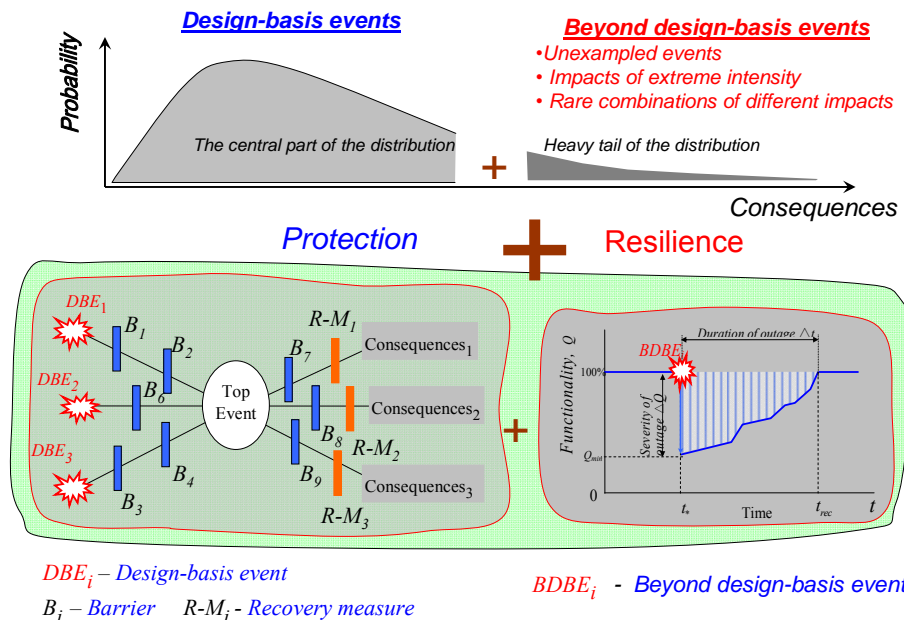


Figure 3. A new paradigm of CES safety: transition from “Protection” to “Protection + Resilience”

Quantitative measures of robustness (based on energy absorption, the ratio between direct and indirect risks and others) and resilience (based on shape of the CES's recovery curve) should be developed as well as a set of measures to increase CES's robustness and resilience will be identified.

4. CONCLUSIONS

Complex engineering systems should be considered as *techno-social* systems whose performance depends on tightly coupled technical, human and organizational functions. A new approach to ensuring CES's safety will be developed to address the new safety concerns that arise from the use of increasingly complex socio-technical systems. This approach should be based on the following premises:

1. Complex engineering systems should be considered as socio-technical systems whose performance is determined by interaction of technical, human and organizational factors.

2. Performance conditions for CES are always underspecified because the work environment is too complex to be described in every detail and because it is not stable and fixed. Thus it is impossible to characterize the CES's performance by analyzing its response to a bounding set of design-basis impacts.

3. Low probability–high consequences (beyond design-basis) events should be included into the scope of CES risk assessment and management framework. This requires development of additional measures aimed at increasing CES's robustness and resilience in case of beyond design-basis impacts.

4. Many adverse events in CES can not be attributed to a single failure or malfunctioning of components. They result from unexpected combinations of various adverse factors. Occurrences of accidents in CES may be due to a combination of performance variability, malfunctions, human errors, adverse unauthorized impacts. Safety management must therefore be not only reactive but also proactive as well.

5. Risk assessment and management models for complex engineering systems should include several levels ranging from legislators over managers and system operators to hardware components.

6. Impacts of technological and intelligent terrorism should be included in the framework of CES risk assessment. This requires that a number of

specific features of terrorist impacts (feedbacks between vulnerability and consequences) be accounted for.

REFERENCES

1. N. Makhutov, D.Reznikov, V. Petrov. “Engineering Infrastructures: Problems of Safety and Security” in Proceedings of the international Workshop “European prospective on security research”, pp. 93-106. Acatech, Gemany. 2010.
2. N. Makhutov, R. Khaziakhmetov, D. Reznikov. Basic Scenarios of Terrorist Attacks at Hydropower Engineering Facilities, in Risk Analysis, Dam Safety, Dam Security, and Critical Infrastructure Management. Proceedings of the 3IWRDD-FORUM Ignacio Eskuder Bueno (ed). 389-395 CRC Press/Balkema. Taylor & Francis Group. 2011.
3. Epstein, S. Unexampled events, resilience and PRA. In E. Hollnagel & E. Rigaud (Eds.). In E. Hollnagel & E. Rigaud (Eds.), Proceedings of the Second. 2006. Resilience Engineering Symposium, Antibes, Juan-les-Pins, France, 8-10 Nov. pp. 105-116.
4. Lundberg, J. & Johansson, B. Resilience, stability and requisite interpretation in accident investigations. In E. Hollnagel & E. Rigaud (Eds.), Proceedings of the Second Resilience Engineering Symposium (pp. 191-198), Antibes, Juan-les-Pins, France, 8-10 Nov. 2006.
5. McDonald, N. Organizational resilience and industrial risk. In E. Hollnagel, D. D. Woods & N. Leveson (Eds.), Resilience engineering: Concepts and precepts, pp. 155-179. Aldershot, UK: Ashgate. 2006.

APPLICATION OF THE EQUIVALENT NOTCH STRESS INTENSITY FACTOR ON THE BRAZILIAN DISK WITH U AND V-NOTCHES

M. Hadj Meliani^{1,2}, Z. Azari², G.Pluinage², Y.G. Matvienko³

¹ LTPM, FS, Hassiba Benbouali University of Chlef 02000, Algeria.

² Laboratoire de Mécanique, Biomécanique, Polymère, Structures (LaBPS) ENIM, 1 Route d'Ars Laquenexy, 57070 Metz.

³ Laboratory of Modelling Damage and Fracture, Mechanical Engineering Research Institute of the Russian Academy of Sciences, 4 M. Kharitonievsky Per.101990 Moscow, Russia.

hadjmeliani@univ-metz.fr azari@enim.fr

Abstract: Mixed mode fracture emanating from notch has recently received increasing attention. The criterions based on the maximum tangential stress (MTS) criterion for crack are developed for notch problems. The critical tangential stress, expressed in terms of mode I and II notch stress intensity factors, has proposed to an approach based on Equivalent Notch Stress Intensity Factor (ENSIF). This paper is focus on initiation point on fracture emanating from notch using MTS criterion for Brazilian disk made in bio-ceramics. A comparison between U and V notches is made..

Key words: mixed mode, ENSIF, Brazilian disk, MTS criterion

1. INTRODUCTION

Recently, authors and research groups takes more discussed and observations an increasing number of papers, were working on the topic of characterization of crack tip stresses using more than one fracture mechanics parameter in mixed mode. Risk of mixed-mode fracture appears when a preexisting defect is load by a multiaxial loading or uniaxial load in a

direction different to the normal direction to defect line. Prediction of this risk needs to answer to the following questions :

- i) what is the fracture load knowing fracture toughness according to each elementary fracture mode ?,
- ii) what is the direction of fracture path?
- iii) for a blunt notch what is the fracture initiation point?

For a crack like defect, the problem of mixed mode of fracture has received a large attention. Several criteria are proposed in literature and can be classified in several families: local stress criteria, local strain energy density, equivalent notch stress intensity factor, local strain criteria, maximum energy release rate in local direction or local crack opening displacement criterion. A review of these different criteria is given in [1]. Validity of these criteria depends on fracture behavior of materials (brittle or ductile), level of mode mixity ratio M^e (predominant opening mode or not) and constraint.

$$M^e = (2/\pi) \cdot \tan^{-1}(K_I/K_{II}) \quad (1)$$

When restricting our interest to brittle materials and low mode mixity ratio, the maximum tangential stress (MTS) criterion, originally proposed by Erdogan and Sih [2] and the strain energy density factor by Sih [3]. Mixed mode fracture emanating from notch has recently received increasing attention [4,5]. El minor et al.[6] have proposed an approach based on equivalent notch stress intensity factor. Ayatollahi et al.[7] have developed a criterion based on the maximum tangential stress (MTS) criterion. The critical tangential stress is expressed in terms of mode I and II notch stress intensity factors. Berto et al have [8] have proposed two fracture criteria and applied to blunt-notched components made of brittle materials loaded under mixed mode; the former is based on the averaged strain energy density over a given control volume, the latter on the cohesive crack zone model. These authors have studied brittle materials and received some success when using the maximum tangential stress (MTS) criterion and the strain energy density factor by Sih.

However for mixed mode of fracture emanating from notch, initiation point and influence of constraint needs particular attention. In mode I, fracture systematically initiates from the notch tip located on the notch bisector line; this is the point where the main principal stress is at a maximum, as well as the maximum shear stress and the strain energy density. Conversely, the point where fracture starts in mixed mode varies from case to case, because

it depends on the geometry of the notch and loading mode mixicity ratio. Ayatollahi et al.[9] have taken into account the constraint in mixed mode of fracture emanating from notch by introducing the biaxiality ratio B and found that the mode mixicity ratio is affected by B

$$B = T.(\pi.a)^{0.5}/(K_I^2 + K_{II}^2)^{0.5} \quad (2)$$

Kim et al.[10] have shown that the biaxiality ratio B have some influence on bifurcation angle. This paper is focus on initiation point on fracture emanating from notch using MTS criterion. A comparison between U and V notches is made. Influence of T-stress on fracture load for Brazilian disc made in bio-ceramics is also study.

2. MATERIAL AND SPECIMEN

One of the key differences between metals and bioceramics is the "brittle" character of bioceramics. They may have to adapt to a deformation of more than a few microns. Unlike metals, bioceramics have no plasticity. They are characterized by a purely elastic behavior with a high Young's modulus (Table 1) and until the failure stress is reached. Although bioceramics have a brittle fracture type, some of them can withstand very high compressive stresses, is the case of Zirconia, even if their total lack of plasticity does not allow them to accommodate deformation under the effect of stress concentrations.

Table 1: Mechanic's characterization of material study

Mechanics characterization	Alumina (Al_2O_3)	Zirconia (ZrO_2)
Compression strength (MPa)	4000	6000
Bending strength (MPa)	550	2200
Young Modulus (GPa)	380	220
Poisson Coefficient (ν)	0.18	0.31
average grain size (μm)	1.3	0.35
Hardness HV (MPa)	2017	1750
Density (g/cm^3)	3.9	6.1
Statique Toughness, K_{Ic} (MP.m ^{0.5})	3.5	6

The study of compression behavior of bioceramics was performed on disk Brazilian loaded in mode I ($\beta = 0^\circ$), mode II ($\beta = 90^\circ$), and mixed mode (I + II). Two notches in V and U have been chosen. Dimensions are in millimeters, Figure 1, for more details see Ref. [1]. The specimen thickness (t) is 4mm and the values of length notch for U and

V are 12mm. Eleven different notch inclination $\theta = 10^\circ - 20^\circ - 30^\circ - 40^\circ - 50^\circ - 60^\circ - 70^\circ - 80^\circ - 90^\circ$, were considered. Figure 2 represent some numerical results about Brazilian disk in compression loading (mixed mode). We present two types of notches: U and V in different angles from 0° (pure mode I) to 90° (pure mode II).

Two different materials are used, Alumina and Zirconia. The specimens were loaded diametrically using a 100 kN capacity universal testing machine with a crosshead speed of 0.02 mm/min at ambient air. At first, loading was continued till failure at the different notch (U and V) and different inclination angle from (pure mode I) to pure mode II with respect to the loading direction to confirm a fracture load for each notch angle condition. Results of the maximum values of loading, for each shape and inclination on the two specimen, are presented in the Table 3.

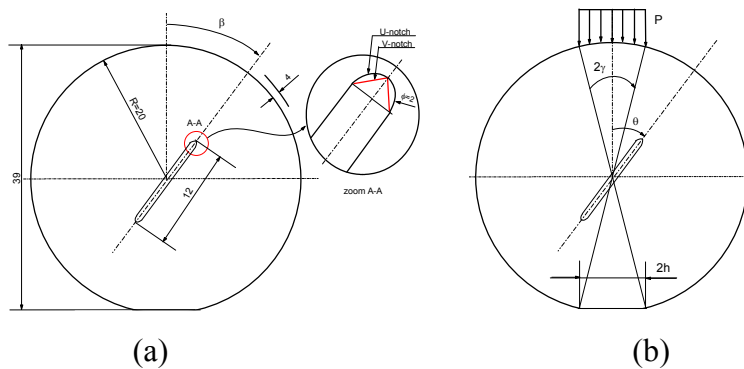


Figure 1. (a) dimensions of the Brazilian disk specimen with U and V-notch and (b) the applied loading position, all dimensions are in mm.

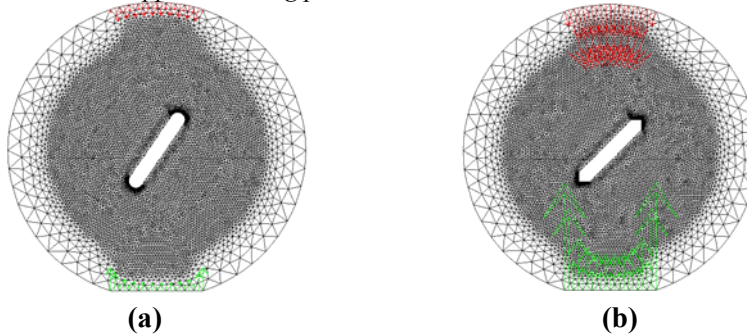


Figure 2. Example Meshing of the Brazilian disk in compression with the action forces (red color) and reaction forces in (green color) contain (a) U-notch at 30° (b) V-notch, at 45° .

Isoperimetric triangular elements were used with six nodes with a dense network in the vicinity of notches. The same mesh style was retained for all samples of Alumina and Zirconia in mode I and mode I + II to eliminate any influence of change of the mesh on the results. The material is assumed to have a isotropic elastic behavior. The Brazilian disk, before and after loading, presented in Figure 3.a with red and blue color, respectively. Zoom of the affected zone are detailed in the Fig 3.b. The distributions of the principal stresses are given in the lines (L6+ L5) (see Fig.3.c).

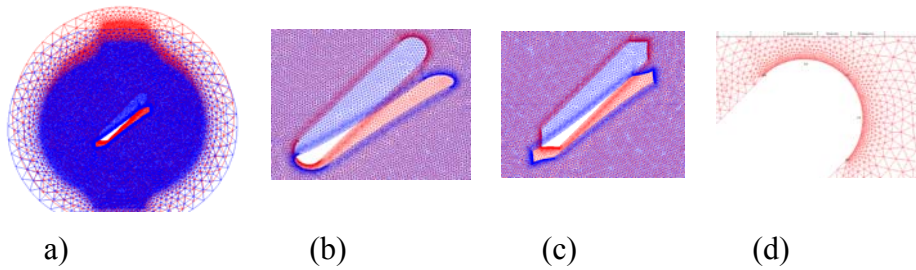


Figure 3. (a) Deformation of the disk before and after loading and (b) zoom of the U-notch deformation and (c) the V-notch (d) mesh near the notch-tip and the contour of stresses (L6+L5).

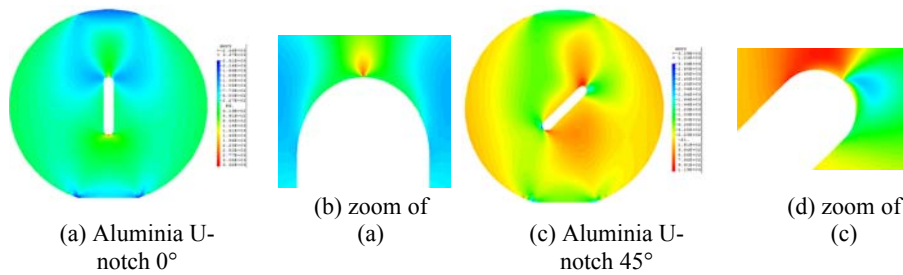


Figure 4. Some results of tangential stress with U-notch for Alumina and Zirconia specimen for mode I (0°) and mixed mode (I+II) (45°)

Examples the tangential stress distributions for pure mode I (0°), pure mode II (90°) and mixed mode I-II (45°) are showed in Figure 4. The tangential stress was formed along the notch line and was concentrated at the notch tip regardless of the notch inclination angle. Although the applied load for the pure mode I (212 N) was less than that for the mixed mode I+II (606 N), the tangential stress was much lower under the mixed mode I+II loading than the pure mode I loading. The pure mode II ($\theta = 0^\circ$) gives the higher values of loading for the two specimens with U and V notches.

3. DETERMINATION OF BIRFURCATION ANGLE

The calculations of numerical results are based on the maximum tangential stress (MTS) criterion was first proposed by Erdogan and Sih (1963) for brittle fracture in mixed mode I/II crack problems. This criterion will be extended to the notches problems. According to this, crack growth from notch, initiates radially from the notch tip along the direction of maximum tangential stress $\sigma_{\theta\theta,max}$. The tangential stresses distribution along the contour (P₆P₇P₈) are presented in the Figure 5, for different angle, from pure mode I in compression ($\theta = 0^\circ$) to the pure mode II ($\theta = 90^\circ$). the contour (P₆P₇P₈) is represented in radius. Figure 6 shows the principal stress distribution $\sigma_{\theta\theta}$, $\sigma_{\phi\phi}$ and $\sigma_{\theta\phi}$ along of the contour P₆P₇P₈ for Alumina specimen with U-notch. Important difference on the tangential stress is observed for inclination angles θ and the two notches U and V. We assume that the mixed-mode (I+II) notch-initiated fracture is governed by the tangential stress (while $\sigma_{\theta\theta}$ plays the major role in the cracking process). Further, we have studied this stress distribution according to the maximum tangential stress direction.

In the Figure 7, the determination of the point of the bifurcation are focus on the contour P₆P₇P₈ in the aim to identified and localized the condition of failure of structure emaning from U and V notches. The different situations of bifurcation are determined for the two materials Alumina and Zirconia for different orientation angle. The criterion assumes that in mixed-mode (I+II) fracture crack initiation from notches is governed by the tangential stress, is proposed, so called the Equivalent Notch Stress Intensity Factor, ENSIF. For the two materials with U and V notches shape, Alumina and zirconia, and inclination angles we have determined the maximum tangential stress points over the notch contour, Figure 8. The distributions of tangential stresses at the notch tip are analyzed according to this approach. The curves of maximum tangential stress distribution gives a minimum values in an orientation of $\theta = 20^\circ$ for the U-notches and $\theta = 30^\circ$ for the V-notches. Figure 9.a represent the numerical results of the maximum tangential stress for different orientation of loading (θ^*) on the Alumina Brazilian disk with V-notch, coupled with the bifurcation orientation β^* . A sudden drop of the maximum tangential stress is noticed for a $\theta = 30^\circ$, orientation with the change in deviation propagation is taken from 90° to 0° . The predicted directions of initial crack propagation are compared in Figure 9.b at the notch tip for U and V shape using the MTS fracture criteria.

Numerical tests have shown that the series term has significant influence on the prediction of initial crack propagation direction β^* with different shape of the notch. For the both shapes U and V notches, and in the margin of 0° - 20° , they are deflected in the same way at the point P_7 . On the other side, when to move in the direction between 30° - 60° , the U-shaped deflected quickly compared to the V shape. The two notches returns to point P_7 guidelines that exceed 70° .

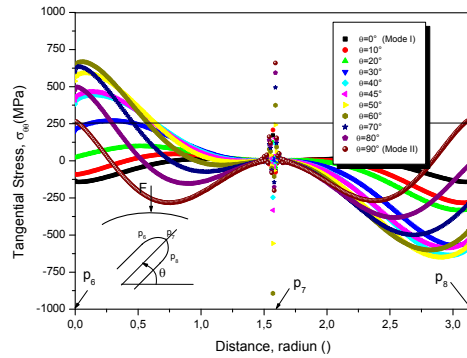


Figure 5. Tangential stress evolution along of ligament ($P_6P_7P_8$)

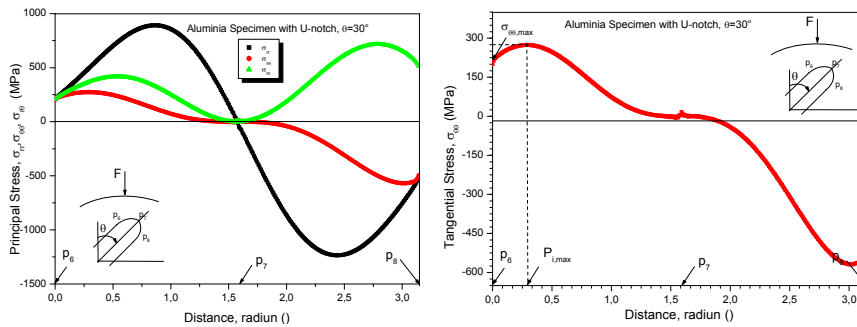


Figure 6. Example of **(a)** the principal stress distribution for Alumina with U-notch on the 30° of orientation and **(b)** determination of the distance with the maximum tangential stress.

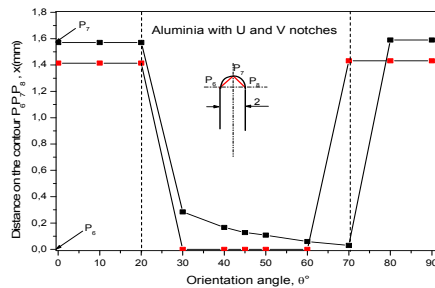


Figure 7. Determination of the point of bifurcation along the contour P₆P₇P₈ for U and V notches

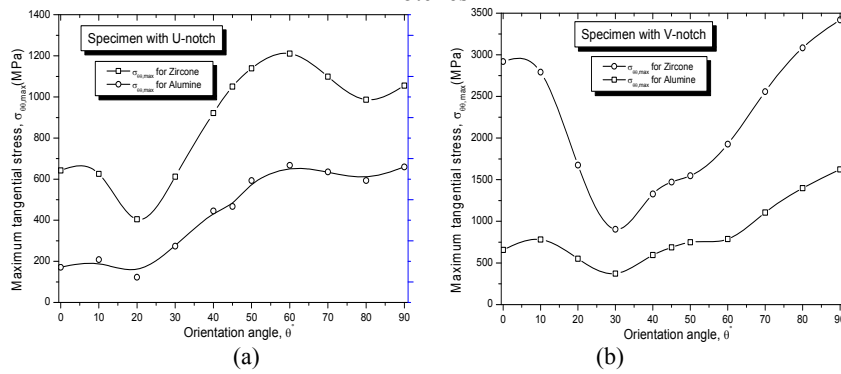


Figure 8. Evolution of the maximum tangential stress for different inclination angle on Alumina and Zirconia specimens with (a) U-notches and (b) V-notches.

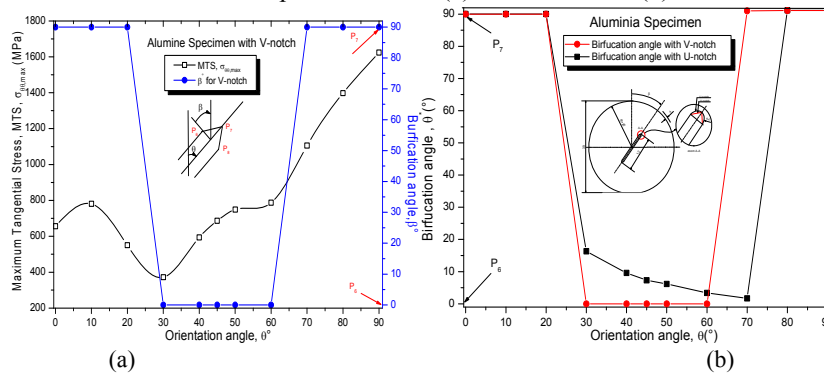


Figure 9. Bifurcation angle on the Alumina specimen (a) for the V-notch with the maximum tangential stress and (b) U-and V-notch.

4. DETERMINATION OF THE EQUIVALENT NOTCH STRESS INTENSITY FACTOR

In the local mode I criterion, the magnitude of the elastic stress field can be described by a single parameter, K_{eq} , designated the Equivalent Notch Stress Intensity factor, ENSIF. The applied stress, the crack shape, size, and orientation, and the structural configuration of structural components subjected to this type of deformation affect the value of the NSIF. This allows translating laboratory results directly into practical design information. The Equivalent Toughness, or the Equivalent Notch Stress

Intensity Factor in mixed mode, ENSIF, is described and defines as a function of effective distance and effective stress given by relationship

$$K_{eq,\rho} = \sigma_{eq} \sqrt{2\pi X_{ef}} \quad (3)$$

the ENSIF is considered as a value of fracture toughness in the mixed mode, with units $MPa \cdot m^{0.5}$, and the minimum effective distance corresponds to the abscissa of the upper limit of zone II and its distance from notch rot was suggested to be the effective distance X_{ef} . It is a principle of fracture mechanics that unstable fracture occurs when the notch stress intensity factor at the notch tip reaches a critical value $K_{n,c}$. For the local mode I deformation and for small crack tip plastic deformation, i.e. plane strain conditions, the critical notch stress intensity factor for fracture instability is $K_{eq,\rho,c}$. The value $K_{eq,\rho,c}$ represents the fracture toughness of the material. A simple fracture criterion is obtain by using the critical notch stress intensity factor $K_{eq,\rho,c}$ and write

$$K_{eq,\rho} = K_{eq,\rho,c} \quad (4)$$

The critical equivalent notch stress intensity factor is a fracture toughness values with units $MPa\sqrt{m}$, if the notch has parallel side (notch angle equal to zero) and for elastic behaviour.

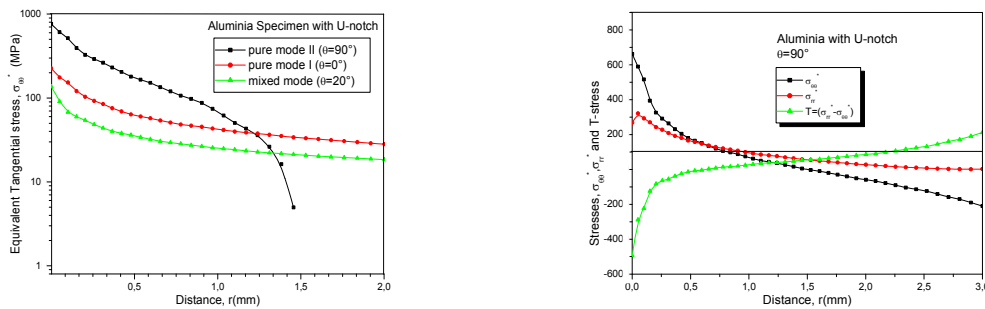


Figure 12. Equivalent tangential stress distribution along of the ligament r for $\theta = 0^\circ, 60^\circ$ and 90° for U-notch

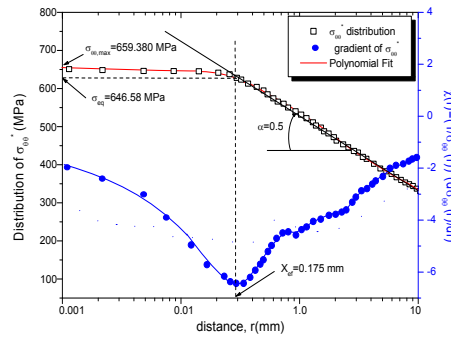


Figure 13. Tangential stress distribution at the notch tip. Relative tangential stress gradient versus the distance. Determination of the effective tangential distance.

The tangential stress component value occurring along the notch-tip is plotted in Figure 12 as a function of the distance r . The inclined path is perpendicular to the notch-tip and starts from the point of the maximum of $(P_6P_7P_8)$ stress component along the notch profile. The finite element results are compared with the pure mode I ($\theta = 0^\circ$), pure mode II ($\theta = 90^\circ$) and mixed mode (I+II) ($\theta = 20^\circ$). By definition, the effective tangential distance is the diameter of the process volume assuming it has a cylindrical shape. A typical example of the tangential stress distribution is presented in Fig. 13. The relative tangential stress has also been plotted versus distance r for Alumina with U-notch at $\theta = 90^\circ$. All results for different notches and orientation of the two materials are recapitulated in the Table 2.

Table 2. Recapitulative of the different results for Alumina and Zirconia specimen with U and V notch

θ	Alumina with U-notch					Zirconia with U-notch				
	Pc	$\sigma_{\theta\theta max}$	$\sigma_{\theta\theta}$	x_{eff}	K_{eff}	Pc	$\sigma_{\theta\theta max}$	$\sigma_{\theta\theta}$	x_{eff}	K_{eff}
0	2.12	171,38	160,00	0,120	4,392	7.94	641,91	629,587	0,208	22,754
10	2.35	208,20	198,54	0,138	5,845	8.10	625,38	610,654	0,201	21,696
20	2.85	122,66	112,69	0,157	3,538	8.40	404,58	489,654	0,182	16,554
30	4.79	273,79	265,00	0,180	8,910	10.70	611,99	596,547	0,193	20,768
40	5.60	445,50	437,56	0,195	15,312	11.58	921,42	912,65	0,225	34,306
45	6.06	466,67	456,40	0,210	16,574	12.04	1050,30	1 042,15	0,230	39,607
50	6.48	593,03	580,24	0,228	21,956	12.43	1139,20	1 130,86	0,245	44,358
60	7.39	667,65	667,12	0,240	25,899	13.40	1210,50	1 204,96	0,254	48,125
70	8.23	635,20	628,40	0,210	22,821	14.22	1098,80	1 079,24	0,234	41,372
80	9.11	593,39	575,45	0,209	20,848	15.15	986,75	872,56	0,228	33,017
90	10.	659,38	646,58	0,175	21,435	16.00	1055,00	1038,67	0,231	39,561
θ	Alumina with V-notch					Zirconia with V-notch				
0		656,21	647,21	0,185	22,060		2919,00	2 900,00	0,430	150,700
10		780,71	772,56	0,207	27,855		2791,40	2 781,00	0,384	136,567
20		550,31	539,45	0,175	17,883		1674,50	1 662,58	0,300	72,164
30		371,93	363,45	0,161	11,557		903,86	895,32	0,235	34,395
40		594,02	579,18	0,198	20,423		1328,40	1 319,67	0,261	53,428
45		686,32	675,45	0,190	23,332		1471,60	1 463,47	0,269	60,151
50		748,94	738,12	0,199	26,094		1547,50	1 536,95	0,278	64,219
60		786,87	777,67	0,201	27,630		1927,60	1 912,62	0,323	86,141

70	1 105,30	1 091,64	0,241	42,469	2557,90	2 536,64	0,364	121,280
80	1 397,60	1 375,65	0,273	56,960	3083,40	3 062,45	0,448	162,438
90	1 623,70	1 608,98	0,294	69,136	3419,40	3 398,54	0,486	187,754

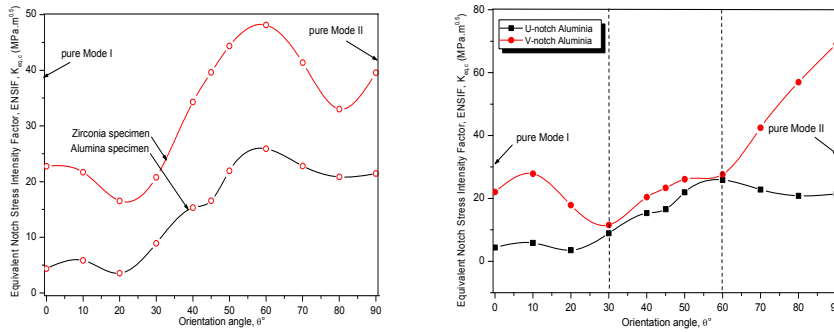


Figure 14 : Evolution of the equivalent notch stress intensity factor for (a) Alumina and Zirconia specimen with U- notch and (b) comparison between U and V notches for Alumina.

Figure 14.a shows typical equivalent notch stress intensity factor curves for various notch inclination angles for Alumina and Zirconia. The ENSIF values decreased as the notch inclination angle increased in the range of $0^\circ < \theta \leq 20^\circ$. The Zirconia material gives the high values. The dependence of the fracture toughness on the notch inclination angle in the mixed mode loading condition can be understood by examining the stress distribution of notch tip formulated by Atkinson. For pure mode I ($\theta = 0^\circ$), the maximum tangential stress is in tension but the shear stress tend to zero so that the crack propagates only under the influence of the tangential stress. However, for mixed mode I-II ($0^\circ < \theta < 20^\circ$), the shear stress increase with increasing on θ , take positive value with a maximum at around $\theta = 20^\circ$, the tangential stress is decreasing and tend to minimum value on tensile. In this range, crack initiated from notch by the shear deformation at the notch tip might intensify the tangential stress so that the crack could be propagated at relatively low fracture toughness with increasing the notch inclination angle. Chandra Rao et al.[11] shows, for modified compact tension specimen, the total fracture toughness remains more or less unchanged when the inclination of θ increases from 0° to 30° and subsequently increases when θ increases from 30° to 45° .

5. CONCLUSION

Mixed mode of fracture criteria predict generally loading conditions of fracture and direction of bifurcation. In this paper, using the maximum tangential stress (MTS) criterion, in addition we are looking for position of fracture initiation emanating from notches. The criterion assumes crack initiation from notches is governed by the maximum tangential stress, introduced in the Equivalent Notch Stress Intensity Factor, ENSIF. This problem has been studied for the two ceramics (alumina and zircona) on Brazilian disks with U and V notches shape. Numerical results indicate that in fracture initiation location move by discrete values from center of the notch for low and high loading angle values to end of notch for intermediate values corresponding to some seldom experimental results in steel specimens. Evolution of computed equivalent notch stress intensity factor confirms existence of these three domains of fracture behavior with limits independent of notch geometry and material behavior.

REFERENCES

1. M. Louah. Fissuration en Fatigue en mode mixte I + II à l'aide du disque brésilien. Thèse de doctorat, Université de Metz (1986).
2. Erdogan F., Sih G.C. On the crack extension in plates under plane loading and transverse shear. J Basic Engng Trans 1963; ASME 85:525-7.
3. Sih GC (1974) Strain-energy-density factor applied to mixed mode crack problems. Int J Fract 10:305–321
4. Papadopoulos G.A, Paniridis P.I, Crack initiation from blunt notches under biaxial loading. Eng Fract Mech, 31,(1),pp 65–78, (1988).
5. Priel. E, Bussiba. A, Gilad .I, Yosibash .Z “Mixed mode failure criteria for brittle elastic V-notched structures”. Int. J Fract 144, pp 247–265,(2007).
6. H. El Minor, M. Louah, Z. Azari, G. Pluvinage and A. Kifani, “Brittle Mixed Mode Fracture I+II-Application of Equivalent Notch Stress Intensity Factor to the Cracks Emanating From Notches”, Problems of strenght, N°6, pp 61-71, Décembre; (2002).
7. M.R. Ayatollahi, A.R. Torabi “Investigation of mixed mode brittle fracture in rounded-tip V-notched components” Engineering Fracture Mechanics.

8. Berto. F, Lazzarin. P, Gómez. F. J, Elices, M. Mixed mode loading.” two procedures based on the equivalent local mode I concept” . Int J Fract, 148, pp415–433, (2007).
9. Smith D.J., Ayatollahi M. R., Pavier M. J. The role of T-stress in brittle fracture for linear elastic materials under mixed-mode loading 2001; Fatigue Fract Engng Mater Struct.24 :137-50.
10. Kim, J.H. and Paulino, G.H. (2003) T- stress, mixed mode stress intensity factors, and crack initiation angles in functionally graded materials: a unified approach using the interaction integral method. Comp. Meth. Appl. Mech. Eng.,**192**, 1463-1494.
11. B.S.S. Chandra Rao et al. Materials Science and Engineering A 476 (2008) 162–168

RETARDATION OF MICRO-CRACK INITIATION AT MECHANICAL COMPONENTS SUBJECTED TO TORSION LOADING, USING A DISCRETE DISLOCATION TECHNIQUE

V. Močilnik¹, N. Gubeljak², J. Predan²

¹*ERD d.o.o., Črneče 186, 2370 Dravograd, Slovenia*

²*University of Maribor, Faculty of Mechanical Engineering, Smetanova ul. 17, 2000 Maribor, Slovenia*

vinko.mocilnik@siol.net, nenad.gubeljak@um.si, jozef.predan@um.si

Abstract: The presented contribution summarizes the contents and findings from current articles covering field of numerically-modelling initiations and the propagation of micro-cracks within a crystalline material using discrete dislocations method. The discrete nature of the crack initiation phenomenon was investigated within a crystal grain lattice. Namely, the fatigue crack propagation within the crystalline grains and any influence of the grain boundary's vicinity on its propagation and arrest, respectively. In the following, in accordance with the method of discrete dislocations, an explanation is provided for the increase in lifetimes of torsion-subjected specimens. The lifetimes of the specimens were increased by means of compressed pre-stress in the axial direction.

Key words: Micro-crack, Initiation, Lifetime, Discrete dislocation, Pre-stress

1. INTRODUCTION

The main purpose of this article is to present those causes leading to irreversible processes within this material, discussion of the micro-crack formation mechanisms, and on assessment of the stress level required for the crack-initiation and its propagation. The topics covered by this

contribution are summaries of more recent articles from this area [1, 2, 8, 9, 10, 16, 17, 19, 20 and 21]. These papers resulted from studying the initiation and spreading of micro cracks, as part of creating a doctoral thesis [12], in order to explain the process of initiation fatigue micro-cracks on the surface and within the metallic material of a smooth specimen, without the pre-planned macro-notch effect.

Tests were carried out on full and hollow pre-stressed specimens of spring material, loaded with unidirectional or alternating torsion loads without those incisions made on the surfaces that are normally seen as crack initiators. A cylindrical specimen, containing of full spring material was preloaded within the plastic field of a material in torsion direction, which had to increase the torsion elastic limit. This type of pre-stress is often used when making torsion-springs, as it can significantly increase the elastic applied angle. Therefore, the pre-stress consequently reduces operating stress on the surface of the torsion specimen [12]. Reduced operating stress has a positive influence on the lifetime and retard initiations of micro-cracks on the surface, because a maximum principal stress is crucial for the initiating of micro-cracks. Due to surface-rolling, compressive residual stresses were introduced on the surface of the specimen. Both contributions for reducing the operating stress on the surfaces of the specimens during torsion loading led to the fact that the initiation of micro-cracks occurred inside the material and not on the surface as is customary. This survey was conducted in order to determine how the intensity of pre-stress affects the lifetimes of metallic materials when subjected to torsion fatigue [12]

Another method of dealing with the influence of pre-stress on the lifetime of torsion fatigue regarding mechanical parts was carried out on a hollow tubular specimen. Pre-stress was done in such a way that the hollow specimen was compression pre-loaded in the axial direction. The compressive load in the axial direction was present throughout the execution of the alternating torsion fatigue [4, 5, 6, 11, 12, 22, 23, 24, 25 and 26]. Any increase in the service-life of the axial pre-stressed mechanical parts, fatigued by torsion or a combination of torsion and bending could be explained by the method of discrete dislocations. This is discussed in detail during presentation.

2. SIMULATION OF CRACK GROWTH USING DISCRETE DISLOCATION TECHNIQUE

Several numerical methods have been developed for the purpose of modelling and simulating aspects of crack formation and propagation. It is necessary to take into account the eventual influence of the microstructure, because the size of the plastic zone increases when the crack occurs within a crystal grain, and then spreads through other crystal grains. One of these is a method for modelling short fatigue crack-growth using a discrete dislocation formulation, the authors [10, 17 and 19].

2.1 DISLOCATION DIPOLE

The simulation of a crack opening provides for the distribution of infinitesimal edge-dislocations along the crack [1, 16, 8, 2 and 3]. The principle of superposition has been used in given references. Dislocation dipole consists of two edge dislocations of the same size and the opposite orientation of the Burger's vectors, Figure 1. Using dislocation dipoles has the advantage that the size of the Burger's vector of the dipole corresponds exactly to the crack surface displacement at the dipole-midpoint (collocation point). During simulation, the singularity is avoided by introducing finite-length dipole elements.

A dislocation dipole with an opening character is used, Figure 1a), for a description of a short crack-growth. The dislocation dipole causes a stress-field within the material, which must be in equilibrium with the external load and all other discrete dislocations within the system.

During computer simulation the loading-cycle which fatigues the crack, is divided into several load increments within which the steady-state is calculated by means of an iterative process. Calculation of the balance is repeated until all dislocations take an equilibrium position. It is assumed that during each simulation the dislocation dipole maintains a constant displacement.

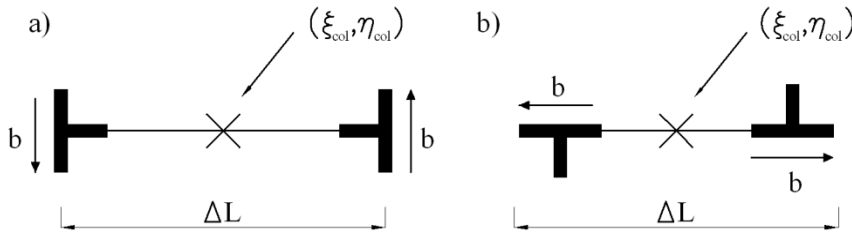


Figure 1. Dislocation dipole: a) Opening character b) Sliding character

2.2 FORMULATION OF THE PROBLEM

A plain problem is modelled, edge dislocations are used and linear elastic material is assumed. The formulation of the problem is based on any influence on the stress that comes from the dislocation dipoles, and the discrete dislocations within the material. The stress tensor formed by the dislocations and Burger's vector $\mathbf{b}=(b_x, b_y)$, in the point (ξ, η) of the given Cartesian coordinate system (x, y) , has the following form:

$$\sigma_{ij}(x, y) = \frac{2 \cdot G}{\pi(k+1)} \sum_{k=x, y} C_{ij}^k(x, y; \xi, \eta) \cdot b_k(\xi, \eta), \quad i, j = x, y, \quad (1)$$

here G is the shear modulus, k the Kolosov constant, and C_{ij}^k the influence function. For the plane stress state: $k=3+4\nu$.

By using the principle of super-positioning a balance has to be found between the stress field, which is caused by dislocations along the crack, the stresses due to external loads, and the stresses due to the dislocations which form the plastic zone:

$$\bar{S}_{ij}^0 = \tilde{S}_{ij} + \sum_{k=x, y} \Delta C_{ij}^k \bar{U}_k, \quad i, j = xy, xy \quad (2)$$

where \bar{S}_{ij}^0 is a vector containing the boundary conditions, \tilde{S}_{ij} a vector that contains the stresses of the external loads and individual dislocations,

and ΔC_{ij}^k the matrix which contains influence functions of all the dipole elements.

When the crack progresses, new dipoles nucleate along the crack and the system of equations is increased. In the case of crack-closure, the relevant elements are exempt from the system because the compression load is not possible as a boundary condition during simulation. On the other hand, when the crack is opening some elements are re-added to the system.

Movement of discrete dislocations along slip bands causes local plastification. A loading history is very important when forming the plastic zone. Load increments should be properly sized to achieve a steady-state.

During cyclical loading, many dislocations that form the plastic zone nucleate during the first loading-cycle. In subsequent load-cycles, some dislocations annihilate and nucleate new ones. The crack spreads in a repeated pattern and leaves behind a plastic track.

Analysis was performed for the edge-crack in a BCC steel lattice subjected to fatigue. The global coordinate system was considered starting from your half-space plane, Figure 2, with crack-front parallel to the global z axis. A plane strain and linear elastic material was assumed.

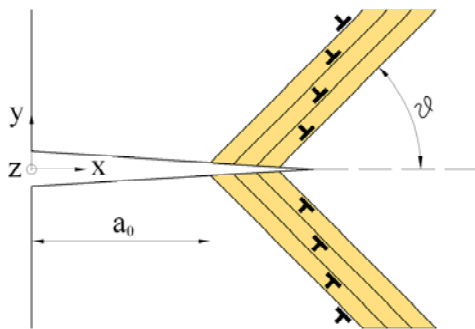


Figure 2. Geometry of the crack and slip bands.

a_0 - Initial crack-length

ϑ - Slip-system angle

The crack propagation accelerates and retards over discrete stages due to the competition between the shielding effect of the plastic zone as a result of discrete dislocations, and the increasing global stress intensity factor. Prior to crack arrest, the increase of the crack is greater within the vicinity of the grain boundary than when the grain boundary is very further away. The

shorter the distance to the grain boundary, the less loading - cycles are needed to arrest the crack, which occurs as approximately 20% - 30% of the initial distance to the grain boundary. The computation model simulates the crack-arrest by blocking of the plastic deformation, before spreading into the neighbouring crystal grain.

3. CRACK INITIATION OF AN AXIAL PRE-STRESSED SPECIMEN WITH AN ALTERNATING TORSION

The lifetime of pre-stressed hollow specimen made from spring steel had increased. It had been loaded by an alternating torsion fatigue ($R=-1$) and pre-stressed by static axial compress force at the same time. Biaxial stress state had appeared in the material of the specimen [14]. The increase of the lifetime of this compressed pre-stressed specimen has already been discovered by other authors, [6, 11, 22, 24, 25 and 26]. The principal stresses σ_1 and σ_3 are decisive for the propagation of macro- cracks in hollow specimens. In the cases of those specimens without any pre-stress, they are the same size and have an orientation at an angle of 45° with respect to the longitudinal axis of the specimens. The principal stress σ_1 has a tensile character, σ_3 a compressive one. During the loading-cycle their sizes increase steadily over time to the amplitude, and then decreases in the opposite direction back to zero. In the case of alternating torsion load there is also a negative part of the loading-cycle that follows it. Although during the loading- cycle the sizes of the principal stresses constantly change, their directions remain unchanged throughout the whole loading-cycle. Therefore, the macro- crack at torsion loading $R=0$ propagates in the directions of the principal stresses [13].

The case is somewhat different when the axial static compressive pre-stress acts together with an alternating torsion fatigue. The compressive principal stress σ_3 increases but the tensile one σ_1 , decreases. In addition to changing sizes during the loading-cycle, their direction also changes. So in this case, the principal stresses change constantly during the loading-cycle in terms of their sizes as well as their direction [13].

The question can be partly answered from the above as to why the pre-stressed specimens have a longer lifetime than usual. External loading, causing activated slip-planes in the crystal grain of the material, according to the slip mechanism, affects the initial crack. The shear stress affects the

slip-planes and when it reaches the critical value (Figure 3), the dislocation-dipole nucleates on the surface of the micro-crack.

The crack blunts, the negative dislocation remains on the crack-surface, but the positive discrete dislocation moves via the corresponding slip-band inside the material, in accordance with the size of the shear-stress and the vicinities of the neighbouring dislocations, which thus retards or accelerates the movements of the other dislocations. The vicinity of the crystal grain has a strong influence on the movements of the dislocations. During the positive part of the loading-cycle, new slip planes are activated, are to the loaded crack-tension the new dislocation dipoles then nucleate and discrete dislocations travel away from the crack- surface inside the material. When the loading begins to ease, the negative shear- stress and discrete dislocations on the slip-bands travel back to the crack-surface. Some of them reach the crack-surface, some do not. Those dislocations that return to the crack-surface join those negative dislocations which have remained on the surface during the nucleation, or they annihilate. When a discrete dislocation returns to the crack-surface and annihilates there, the crack reshapes and extends for a Burgers' vector. During alternating loading there is also the negative part of the loading-cycle which, due to the stress in the opposite direction, literally "sucks" the dislocations onto the crack-surface, thus making the crack grow faster. The crack growth is retarded by the vicinity of the grain-boundary, because the dislocations there are piled-up and arrested. The dislocations, when returning to the crack-surface, form a cyclical plastic zone, however those which are arrested on the grain boundary and cannot return to the crack surface form a static plastic-zone in front of the crack-tip. The static plastic zone retards the micro-crack growth; furthermore, it could even stop it. In this way, the cracks propagate in the case of torsion-loading without any axial pre-stressing.

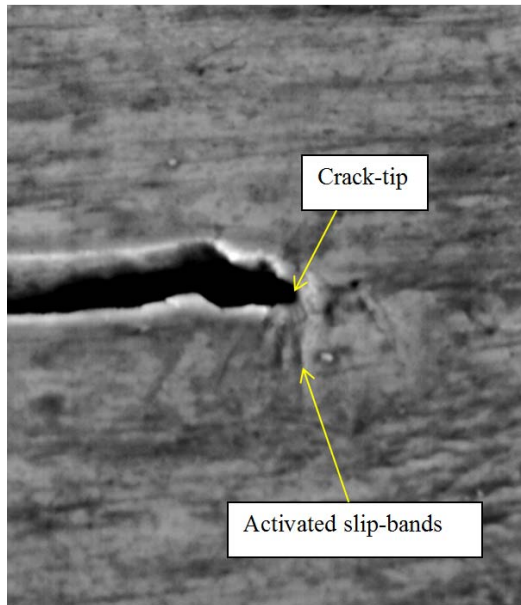


Figure 3. A micro crack on the surface of the specimen at a magnitude of the 5000x

In the case of torsion-loading and axial pre-stressing, the pre-stressing increases the critical shear-stress on the slip-bands, which consequently retards the nucleation of new dislocations and the movement of existing ones along the slip-planes. Therefore more load cycles are required for the propagation of micro-cracks and for the return of discrete dislocations to the crack-surface. The second contribution to any increase of the lifetime, in the case of the pre-stressing, appears as a result of continuous changing of the principal stress- direction during the loading-cycle. When during a specific moment the shear stress on the activated slip-band reaches the critical value and the dislocation dipole is formed, then the loading direction changes. In response to the changed loading-direction, new active slip-planes appear, and according to them, new dislocation dipoles nucleate. A momentary load acts on the dislocations and on the slip-planes from the previous moment only as a component which no longer has such an effect on the movement of dislocations as when the load direction was adequate for the corresponding slip-planes. This process occurs, continuously throughout the whole loading-cycle and, for the dislocations to return onto the crack-surface, more loading cycles are required due to the constant directional changes. Several more slip-planes are activated on which discrete dislocations occur. They

are very poorly movable and form the so-called static plastic-zone, which spreads from the crack tip and retards or even stops crack-propagation.

Theoretically, it would be possible to increase the lifetimes of mechanical components by means of pre-stress, until reaching the fatigue limits. Due to the specific shapes of the specimens, there were differences in the surface compression stresses, which led to the fact that their lifetimes began to fall when increasing the pre-stress level.

The lifetimes of those mechanical parts with smooth surfaces are greater because the formation of gaps and their intensifications need more loading cycles. They also have a significant influence on gap-direction, with respect to the direction of loading on the surface. Crack-initiation is further retarded when the load is applied perpendicular to the orientation of the initial surface scratches.

The principle of increasing the lifetime and level of safety regarding a hollow specimen, by means of axial pre-stressing or multi-axial stress-state, can be generalized and used within other dynamically-loaded mechanical parts. The same principle can be used for the design of dynamically-loaded shafts and axles.

4. CONCLUSIONS

The review of fatigue crack initiation as a consequence of dislocation generating has been presented in case of bi axially-loading a hollow bar subjected to torsion-loading. The hollow bar was subjected to constant compression and alternate torsion loads. The fatigue micro-crack initiation process is not only the consequence of a dislocation phenomena within crystal material, as other inclusions should be taken in account like stress concentration spots on the free surface. The process of voids' generation is actually a local plastified dislocation slip around the non-metallic inclusion. Higher stress around the inclusions accelerates further dislocation-slips and generates fatigue micro-crack initiation between the voids. A macro-crack appeared as a coalescence of voids during biaxial loading. Therefore, the initiation of a fatigue-crack during bi-axial loading is governed by inclusions, and the dislocation process. However, the theoretical consideration of the fatigue process actually explained how it is possible to extend the lifetimes of mechanical parts loaded with cyclical torsion fatigue, by using compressed pre-stress in the axial direction. A method of discrete dislocations was introduced in order to explain the process within the

crystalline material lattice. This process can lead to increases in the lifetimes of compressed pre-stressed mechanical parts subjected to alternate torsion fatigue-loading.

REFERENCES

1. C. Bjerken, & S. Melin. A tool to model short crack fatigue growth using a discrete dislocation formulation. *Int. Jnl. of Fatigue*, vol.25, No.6, p.p. 559-566, 2003.
2. C. Bjerken & S. Melin. A study of the influence of grain boundaries on short crack growth during varying load using a dislocation technique. *Engineering Fracture Mechanics*, vol.71, No.15, p.p. 2215-2227, 2004.
3. C. Bjerken. The discrete nature of the growth and arrest of micro structurally short fatigue cracks modeled by a dislocation technique. *Paper E*, Department of Mechanical Engineering, Lund University, P.O. Box 118, S-221 00 Lund, Sweden.
4. K. Dang-Van. Macro-Micro Approach in High-Cycle Multiaxial Fatigue, in *Advances in Multiaxial Fatigue, ASTM STP 1191, D.L., McDowell and R.Ellis, Eds.*, ASTM, Philadelphia, 120-130, 1993.
5. W.N. Findley. A Theory for the Effect of Mean Stress on Fatigue of Materials Under Combined Torsion and Axial Load or Bending. *Journal of Engineering for Industry*, pp. 301-306, 1959.
6. M. A. Fonte, & M. M. Freitas. Semi- elliptical under rotating or reversed bending combined with steady torsion. *Fatigue Fract. Eng. Mater. Struct.*, No. 20, p.p. 895-906, 1997.
7. N. Gubeljak, V. Močilnik, & J. Predan. Measurements of mode I and mode III fracture toughness of spring's steel. *Key eng. Mater., cop. 2012*, vols. 488-489, p.p. 468-471, 2011.
8. P.Hansson, S. Melin & C. Persson. Dislocation modelling of short fatigue crack growth through shingle shear. *Licentiate Dissertation*, Department of Mechanical Engineering, Lund University, Sweden, 2004.
9. D. Hull & D.J. Bacon. Introduction to Dislocations, *Butterworth-Heinemann*, Oxford, UK, 4th edition, 2001.
10. I.-H. Lin & R. Thomson Cleavage dislocation emission and shielding for cracks under general loading. *Acta metall.*, No. 34(2), p.p. 187-206, 1986.

11. C. Makabe & D. F. Socie. (2001). Crack growth mechanisms in precracked torsion fatigue specimens. *Fatigue Fract. Eng. Mater. Struct.* 24, pp 607-615, 2001.
12. V. Močilnik. The influence of pre-stress on dynamic capacity of the torsion springs. *Doctoral thesis*, University in Maribor, Faculty of Mechanical Engineering, 2009.
13. V. Močilnik, N. Gubelj, J. Predan & J. Flašker. The influence of constant axial compression pre-stress on the fatigue failure of torsion loaded tube springs. *Eng. fract. mech.*, vol. 77, issue 16, p.p. 3132-3142, 2010.
14. V. Močilnik, N. Gubelj, J. Predan & J. Flašker. Compression pre-stress of tubular torsion springs. *Tehnički vijesnik*, vol. 17, no. 3, p.p. 307-315, 2010.
15. V. Močilnik, N. Gubelj & J. Predan. Model for fatigue lifetime prediction of torsion bars subjected to plastic pre-setting. *Tehnički vijesnik*, vol.18, no. 4, p.p. 537-546, 2011.
16. S. Pearson. Initiation of fatigue crack in commercial aluminium alloys and the subsequent propagation of very short cracks. *Eng. Fract. Mech.*, No. 7, p.p. 235-247, 1975.
17. R. Pippan. Dislocation emission and fatigue crack growth threshold, *Acta metall. mater.* Nr.39(3), p.p. 255-262, 1991.
18. F.O. Riemelmoser, R. Pippan & O. Kolednik. Cyclic crack growth in elastic plastic solids. A description in terms of dislocation theory, *Comp. Mech.* Nr. 20, p.p.139-144, 1997.
19. F.O. Riemelmoser, R. Pippan & H.P. Stüwe. A comparison of a discrete dislocation model and a continuous description of cyclic crack tip plasticity. *Int. J. Fracture*, No.85, p.p. 157-168, 1997.
20. F.O. Riemelmoser, R. Pippan & H.P. Stüwe. An argumentation for a cyclic- by cyclic propagation of fatigue cracks at small stress intensity ranges. *Acta mater.*, No. 46(5), p.p. 1793-1799, 1998.
21. F.O. Riemelmoser & R. Pippan. Intrinsic material behavior in the near threshold regime, In X.R. Wu in Z.G. Wang, editors, Fatigu '99, Proc. 7th Int. *Fatigue Congress*, vol. ¼, , Beijing, P.R. China, Higher Education Press, p.p. 387-392, 1999.
22. K. Tanaka, Y. Iwata & Y. Akiniwa. Fatigue Crack Propagation in Lead - Free Solder under Mode I and II Loadings. *17th European Conference on Fracture*, 2 – 5 September, Brno, Czech Republic, 2008.
23. K. Tanaka, T. Kato & Y. Akinawa. Prediction of fatigue crack

- propagation behavior from a precrack under combined torsion and axial loadings. *Proceedings of International conference on fatigue crack paths*, Sept. 18-20, Parma Italy, 2003.
24. E.K. Tschegg. A contribution to mode III fatigue crack propagation. *Mater. Sci. Eng.*, No. 54, p.p. 127-136, 1982.
 25. F.P. Yang & Z.B. Kuang. Fatigue crack growth for a surface crack in a round bar under multi-axial loading condition, *Fatigue Fract. Eng. Mater. Struct.* 28, p.p. 963-970, 2005.
 26. W. Zang & R. Akid. Mechanisms and fatigue performance of two steels in cyclic torsion with axial static torsion/ compression. *Fatigue and Fracture of Eng. Mater. and Struct.* 20, p.p. 547-557, 1997.

REGIMES OF FRACTURE INITIATION IN A PLANE WITH SQUARE LATTICE OF CIRCULAR HOLES UNDER UNIAXIAL COMPRESSION

Mokryakov V.

Ishlinsky Institute for Problems in Mechanics RAS, Moscow, Russia

mokr@ipmnet.ru

Abstract: The article considers modes of initiation of fracture in elastic perforated plates (lattices) under external uniaxial compression. Special attention is paid to the internal mode of initiation (i.e., to the case of fracture nucleation inside the material, and not on the edges of the holes). We consider the parametric region of the internal mode, the region depends on the angle of the applied external loads and the structural lattice parameter; the size of the region (extreme values) is calculated. A particular point of the region is found; it is shown that at this point there are three possibilities of fracture initiation.

Key words: elasticity, perforated plates, lattice of circular holes, fracture initiation, uniaxial compression.

1. INTRODUCTION

The article considers different modes of fracture initiation in elastic perforated plates both on the hole contours and inside the material.

Lattices of circular holes in an elastic plane have been studied since the 1930s (V.Ya. Natanzon, 1935 [1]; R. Howland, 1935 [2]). Over the years different lattice geometries were studied: square (G. Horvay, 1952 [3]; R. Bailey, R. Hicks, 1960 [4]; G. Wang Fo Fi, 1965 [5]; G.N. Savin, 1968 [6]), rectangular (H. Saito, 1957 [7]), rhombic (M. Ishida, H. Igava, 1991

[8]; K. Ting et al, 1999 [9]; S.G. Mogilevskaya et al, 2003 [10]), hexagonal (D. O'Donnell, B. Langer, 1962 [11]; J. Goldberg, K. Jabbour, 1965 [12]). E.I. Grigolyuk and L.A. Filshtinsky [13] in 1970 published a fundamental monograph on perforated plates and shells, considering methods of calculation (based on Kolosov-Muskhelishvili complex potentials [14]), and solutions of specific problems. Development of these methods led to the method of singular boundary integral equation (SBIE), which description can be found in M.P. Savruk [15], A.M. Linkov [16], etc.

In many of these works the problem of stress concentration in the lattice was posed. Usually the lattices were considered under conditions of tension or shear; and the external load was applied only along the axes of the lattice, or diagonally. Obviously, the lack of numerical capacities was not allowed at that time to consider the problem in the whole range of external loads, and the researchers had to limit themselves with certain important cases.

In previous work [17], the author tried to partially fill the gap: stress fields of three essentially different square lattices were considered under uniaxial tension, shear, and uniaxial compression, in the entire range of load direction (from 0° to 45°). Also, stress concentrations were considered in detail in both direct and diagonal loading (both tensile and compression). It was found that the concentration of the first principal stress σ_1 can occur not only on contours of the lattice holes but also at points of the plane away from the contours. Moreover, the value of σ_1 at the "inner" points of concentrations can exceed the values at the "boundary" points, i. e. construction fracture under certain conditions can start inside the medium but not at the holes contours.

This work continues the previous study in order to determine under what parameters one or another mode of fracture initiation is possible.

2. PROBLEM STATEMENT

An infinite elastic plane weakened by a square lattice of circular holes is considered (Fig. 1). Hole radius is R , the gap between the holes is d . Further, a dimensionless structural parameter $\delta = d/R$ is used. It is assumed that the plane is exposed to an average uniaxial compression at an angle α ($\alpha = 0^\circ$ corresponds to the load is directing along the axes of the lattice).

Here, the method of multipole expansions (MME) is used [18-20]: the sought stress field is represented as a linear combination of multipoles, i.e. basic solutions, automatically satisfying the laws of equilibrium, elasticity,

and compatibility. A single multipole has the physical meaning as a point defect. So, in order to solve a problem, one needs to find the best linear combination coefficients meeting the boundary conditions.

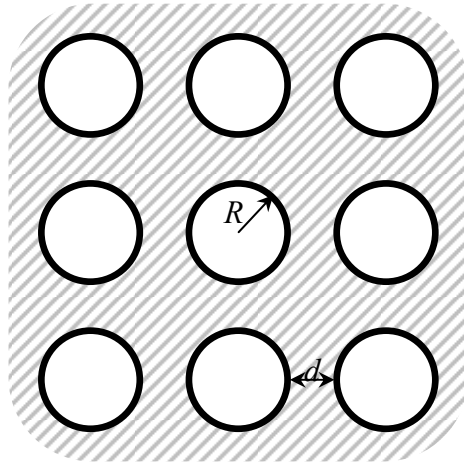


Figure. 1. Problem statement

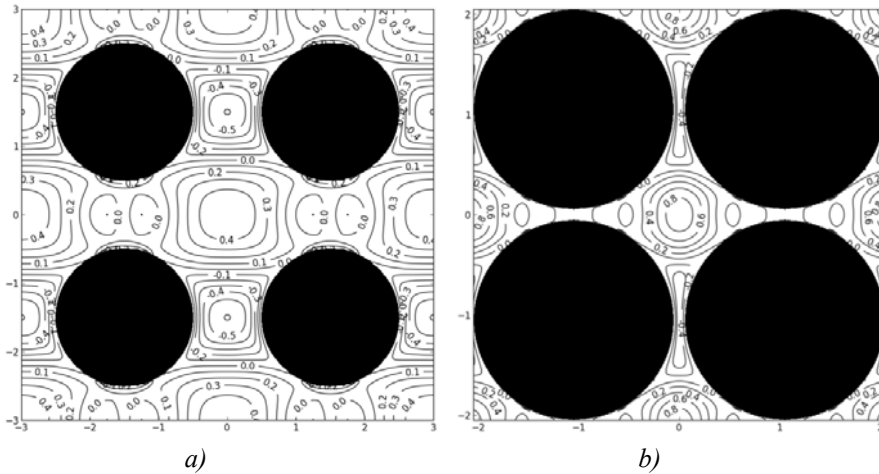


Figure. 2. Stress σ_1 in the lattices (with the parameter *a*) $\delta = 1$, *b*) $\delta = 0.1$) under vertical unite uniaxial pressure.

In [17], MME was used to calculate stress states of the lattices to determine the maximum values of the first principal stress. It was found that at direct ($\alpha = 0^\circ$) uniaxial compression the maximum can occur not only on the contours of the holes, but also in the material (see Fig. 2). Moreover, as it is shown in Fig. 3, at $\delta < 1.355$ the inner maximum exceeds the contour ones, i.e. destruction will begin within the material, but not at the holes contours.

The current work aim is to find a region of the parameters values (α , δ) where the inner fracture initiation mode exists.

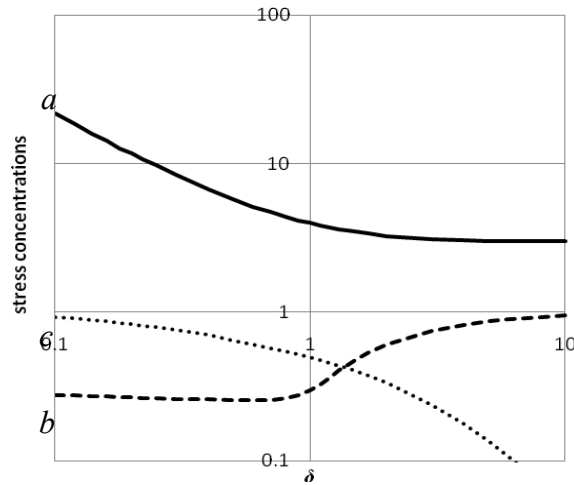


Figure 3. The concentrations dependences on the parameter δ [17]:
a) boundary (tension); b) boundary (compression); c) inner (compression)

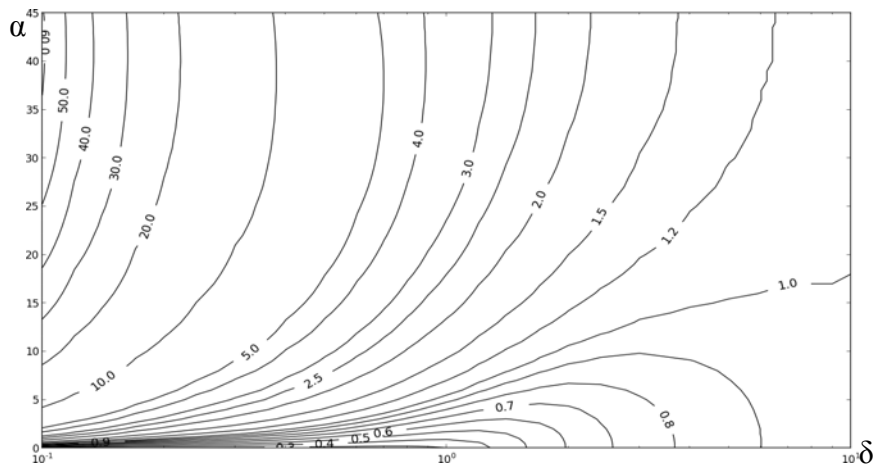


Figure 4. Maximal σ_1 at holes contours

3. OBTAINED RESULTS

Results of the study of a parameter region ($0.1 \leq \delta \leq 10$, $0^\circ \leq \alpha \leq 45^\circ$) are presented in the following plots: maximal σ_1 at holes contours (fig. 4), and the value of σ_1 inside the lattice material, at the farthest point from holes (fig. 5). The maximal σ_1 along the whole bulk of the lattice (fig. 6) and

location of maximal σ_1 at holes contours (fig. 7) are considered in an area ($0.02 \leq \delta \leq 2$, $0^\circ \leq \alpha \leq 2^\circ$). In the plots, the horizontal axis of δ is logarithmic; the vertical axis of α is linear; the dotted line marks the region of the internal mode of the fracture initiation.

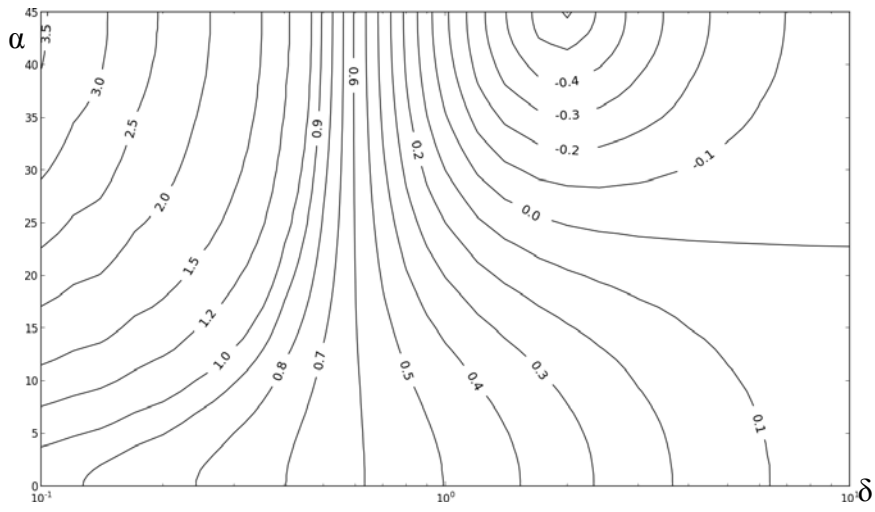


Figure 5. Value σ_1 inside the lattice material, at the farthest point from holes

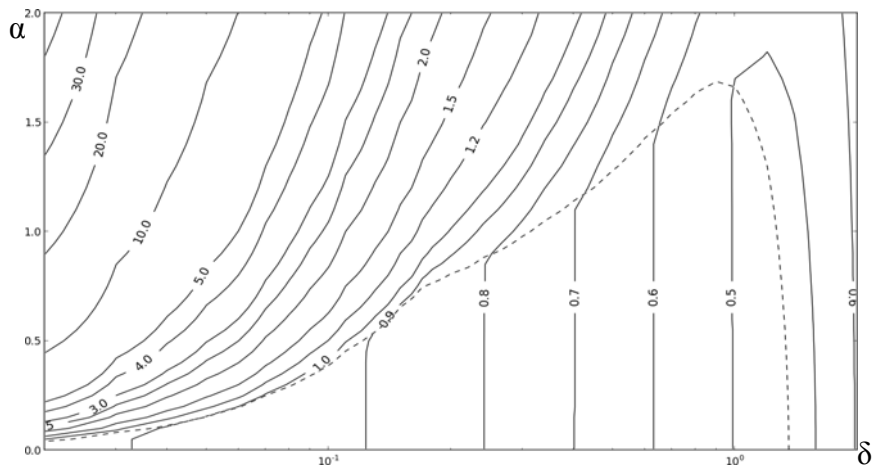


Figure 6. Maximal σ_1 along the whole bulk of the lattice and the region of the internal mode of the fracture initiation (dotted line)

4. RESULTS ANALYSIS

First of all, we note that the region of the internal mode of fracture initiation is limited by the conditions $\delta < 1.355$, $\alpha < 1.7^\circ$. As one can see, the region is narrow enough: the internal mode exists only at compression along one of the axes of the lattice. At a deviation more than 1.7° , the maximum on the contour increases rapidly and exceeds inner maximum that means a change of the internal fracture initiation mode to the boundary mode.

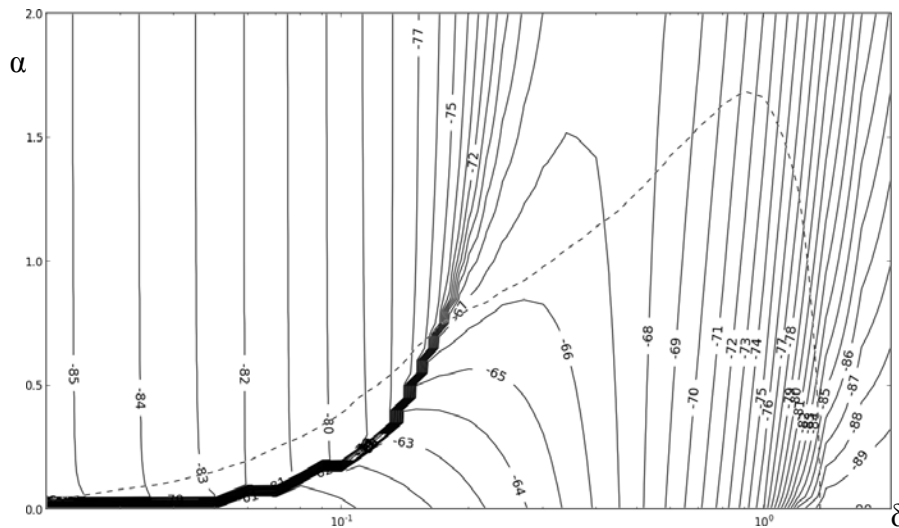


Figure. 7. Location of maximal σ_1 at holes contours
(in degrees, 0° corresponds the right point of the contour)

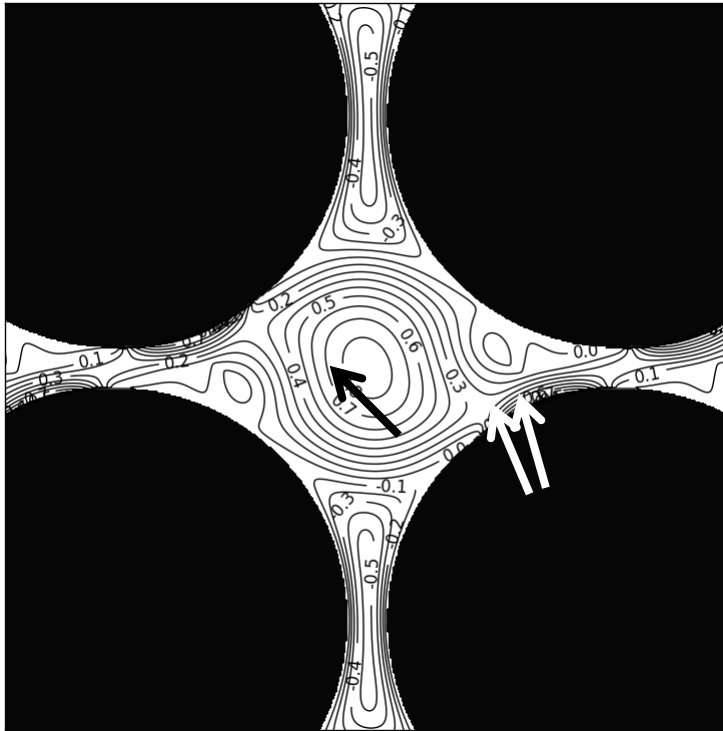


Figure. 8. Field of the first principal stress σ_1 at the special point; the arrows show positions of the concentrations

The studied region has the maximal width along α at $\delta \approx 0.9 \div 1$. With decreasing $\delta < 0.9$, the region width along α also decreases. At point $\delta \approx 0.17$, $\alpha \approx 0.745^\circ$ (stress concentration σ_1 equals 0.857) the region boundary undergoes a break. The fact is that at this place there is a gap of location of the boundary maximum σ_1 (fig. 7). The reason is that in dense lattices two closely located boundary maxima can appear. As is evident in fig. 7, the boundary maxima can diverge up to 20° (see the values on the opposite sides of the gap). On the break the boundary maxima are equal, but at the right or left side of the gap one of the maxima is greater than the other, that also affects fracture form. At the point of the break location of the two points of the boundary concentrations are 67° and 74° . Thus, the break point of the boundary of the inner mode region is a special point: under this condition the fracture can begin at any of the three different locations, and one of them is interior.

The stress field σ_1 at the special point is shown in fig. 8.

5. CONCLUSION

So, perforated plates under an external pressure load have two types of tensile fracture. In most cases, the crack emerges at the hole contour. However, at a certain combination of the lattice structural parameter with an external load, there appears conditions for the tensile crack initiation in the material, not at the hole contour.

The parameter region (δ, α) of the internal initiation modes of fracture is calculated. At points (δ, α) belonging to the boundary region, the inner maximum and the boundary maximum are equal. This means, in a given lattice with the structural parameter δ and the load angle α , any of the fracture initiation modes can be realized. Moreover, the study of the stress field of dense lattices has shown that the boundary maxima at $\alpha \leq 1.5^\circ$ bifurcate. It is shown that at the point $(\delta \approx 0.17, \alpha \approx 0.745^\circ)$ the inner maximum and both boundary maxima are equal, i.e. in this situation, the fracture can arise in any of these three different points, in other words any of the three modes of fracture initiation can be realized.

One can conclude that fracture scenarios of some of the structures under certain extreme conditions are unpredictable. On the other hand, in this case, it is enough to slightly change the direction of the applied load to realize a required scenario.

Nevertheless, it can be assumed that one of the boundary maxima (at the special point) gets an advantage due to the high gradient of σ_1 (gradient at the internal maximum is zero); this hypothesis can be verified experimentally.

It should be noted that the conclusions are valid only if it is assumed that fracture occurs at a critical value of σ_1 . If the material is better described by other criteria then the possible initiation fracture modes may be quite different.

The author thanks the Corresponding Member of the Russian Academy of Sciences, prof. R.V. Goldstein, and Senior Researcher, Dr. N.M. Osipenko for his valuable consultations, and the research assistant, Dr. P.S. Shushpannikov for the results verifications.

This work was supported by RFBR (Project № 11-01-00358-a), and the grant of the President of the Russian Federation for support of leading scientific schools (NSh-3842.2012.1).

6. REFERENCES

1. V.Ya. Natanzon. On stresses in a stretchable plate, weakened by identical holes, as on a chess-board. *Math. coll.*, 42(5):616–636, 1935, in Russian.
2. R.C.J. Howland. Stress in a plate containing an infinite row of holes. *Proc Roy Soc of London. Ser. A*, 148:471–491, 1935.
3. G. Horvay. The plain-strain problem of perforated plates. *J App Mech*, 19: 355–360, 1952.
4. R. Bailey, R. Hicks. Behaviour of perforated plates under plane stress. *J Mech Engng Sci*, 2(2):143–165, 1960.
5. G.A. Van Fo Fi. On one solutions of the bi-axial problem of elasticity theory. *DAN USSR*, 9:1152–1155, 1965, in Ukrainian.
6. G.N. Savin. Stress distribution near holes. Naukova Dumka, Kiev, 1968, in Russian.
7. H. Saito. Stress in a plate containing infinite parallel rows of holes. *ZAMM*, 37(3-4):111–115, 1957.
8. M. Isida, H. Igawa. Analysis of a zig-zag array of circular holes in an infinite solid under uniaxial tension. *Int J Solids Struct*, 27(7):849–864, 1991.
9. K. Ting, K.T. Chen, W.S. Yang. Stress analysis of the multiple circular holes with the rhombic array using alternating method. *Int J Pressure Vessels Piping*, 76:503–514, 1999.
10. S.G. Mogilevskaya, S.L. Crouch, J. Wang. A complex boundary integral method for multiple circular holes in an infinite plane. *Engng Anal Bound Elem*, 27:789–802, 2003.
11. W.J. O'Donnell, B.F. Langer. Design of perforated plates. *J Engng Ind*, 84:1–13, 1962.
12. J.E. Goldberg, K.N. Jabbour. Stresses and displacements in perforated plates. *Nuclear Struct Engng*, 2:360–381, 1965.
13. E.I. Grigolyuk, L.A. Fil'shtinsky Perforated plates and shells. Nauka, Moscow, 1970, in Russian.
14. N.I. Muskhelishvili. Some fundamental problems of mathematical elasticity theory. Nauka, Moscow, 1966, in Russian.
15. M.P. Savruk. Two-dimensional problems of elasticity for bodies with cracks. Naukova Dumka, Kiev, 1981, in Russian.
16. A.M. Lin'kov. Complex method of boundary integral equations in elasticity. Nauka, St. Petersburg, 1999, in Russian.
17. V. Mokryakov. Study of the strength of an elastic plane with a square

- lattice of circular holes under external loading. *Preprint of IPMech RAS № 1023*, Moscow, 2012. in Russian.
18. V. Mokryakov. Application of the multipole method to the problem on two close holes. *Mech Solids*, 42(5):771–785, 2007.
 19. V. Mokryakov. Study of the dependence of effective compliances of a plane with an array of circular holes on array parameters. *Comp Cont Mech*, 3(3):90-101, 2010, in Russian.
 20. V. Mokryakov. Application of the multipole expansion method to evaluation of the stress state of an infinite elastic plane containing several circular holes. *Comp Cont Mech*, 5(2):168-177, 2012, in Russian.

FRACTURE TOUGHNESS FOR CRACK TIP STRESS FIELDS WITH NON SQUARE ROOT SINGULARITY

E.M. Morozov

*Department of Strength Physics, National Research Nuclear University MEPhI, , Moscow
115409, Kashirskoe sh., 31, Russia*

evgeny-morozov@mtu-net.ru

Abstract: We consider the stress field near the crack tip in the plane problem when the singularity power of the elastic field is different from the usual inverse square root one. Such field exists in the vicinity of the curved crack front in three-dimensional problems. In this case, the stress intensity factor in the plane perpendicular to the crack front is measured in units that are different from usually used in determining the fracture toughness. We propose the model for restoring fracture toughness units.

Key words: singularity of the crack tip stress field; stress intensity factor; fracture toughness.

1. INTRODUCTION

The traditional solution of the plane elasticity problem at the crack tip region leads to the asymptotic solution for stresses with the inverse square root singularity. The coefficient of this singular field is called the stress intensity factor with units $\text{MPa m}^{0.5}$. Existing standards for fracture toughness determination in different loading conditions use such units.

Commercial software systems for fracture mechanics analysis also base their computational modeling on the inverse square root stress singularity near the crack tip. However, there are tasks in which the singularity of stress state at the crack tip is different from the inverse square root [1-4]. Here is given of conversion of the fracture toughness in a traditional dimensionality.

2. THE STRESS INTENSITY FACTOR

Sometimes, stress fields in the vicinity of the crack tip (or front in the three-dimensional case) are described by mathematical solutions with singularity that is different from the inverse square root. In this case, the first term in the expansion of the stress in powers of the distance from the crack front is given by

$$\sigma_{\theta} = \frac{K_{\lambda}}{(2\pi r)^{\lambda}}.$$

Here (r, θ) is the polar coordinate system with its origin at the crack tip. It is assumed that the crack deformation follows the opening mode. The stress σ_{θ} corresponds to $\theta = 0$ and terms with positive powers of coordinate r are neglected. In classical elastic problem, singularity exponent λ is equal to 0.5, with the stress intensity factor further denoted by $K_{0,5}$. If the singularity differs from the inverse square root, the stress intensity factor is referred as K_{λ} with units MPa m^{λ} .

To be able to use and compare the characteristics of materials with the square root singularity accumulated in large databases with the characteristics of materials having different singularity ($\lambda \neq 0,5$), we propose a method based on the specific fracture work. Indeed, the specific fracture work (crack driving force G , fracture toughness G_{IC}) should have units which are independent of the exponent λ , namely N / m . This fact can be used to relate the stress intensity factors K_{λ} and $K_{0,5}$. We show how this can be done [5].

3. SOLUTIONS OF THE PROBLEM

Stresses have a singularity λ , that is circumferential stress is proportional to $\sigma_{\theta} \sim \frac{1}{r^{\lambda}}$. The strain singularity can be found from the condition of bounded strain energy in a small neighborhood of the crack tip $\int_{\Omega} \sigma_{ij} \varepsilon_{ij} r d\theta dr \sim \int \frac{r}{r^{\lambda}} \frac{1}{r^x} dr d\theta$. From the last integral it follows that $\lambda + x = 1$ and the asymptotic dependence of the strain on distance from the crack tip is $\varepsilon_{\theta} \sim \frac{1}{r^{1-\lambda}}$. We do not discuss here why Hooke's law deviates from linearity.

The displacement at the upper crack surface is approximately equal to the accumulated circumferential strain over the upper semicircle around the crack tip. Since the angular dependence of the strain is not known, we take it constant (this is not essential for singularity determination). Then the displacement can be expressed as follows: $u \sim \int_0^{\pi} \varepsilon_{\theta} r d\theta = \int_0^{\pi} r^{\lambda} d\theta = \pi r^{\lambda}$.

However, the displacement must have units of length. In the formula for the displacement the proportionality coefficient for r^{λ} does not have to be equal to the stress intensity factor in the formula for stress. So the proportionality coefficient for r^{λ} is $K_{1-\lambda}$ with units MPa m^{1-λ}. Young's modulus E should be present in the denominator of the asymptotic relation for displacements.

Now let us write an expression for the energy flow to the crack tip. By definition the energy flow is $G = \lim_{\Delta l \rightarrow 0} \frac{1}{2 \Delta l} \int_0^{\Delta l} \sigma_{\theta} 2u_{\theta} dr$. To get rid of the

limit the crack length increment is formally set to unit. We get the following energy flow value (up to a constant factor which is defined from solution of a particular problem)

$$G = \int_0^1 \frac{K_{\lambda}}{(2\pi r)^{\lambda}} \frac{K_{1-\lambda} \pi (1-r)^{\lambda}}{E} dr = \frac{\pi K_{\lambda} K_{1-\lambda}}{(2\pi)^{\lambda} E} \int_0^1 \left(\frac{1-r}{r} \right)^{\lambda} dr =$$

$$= \frac{\pi^2 K_\lambda K_{1-\lambda}}{(2\pi)^\lambda E} \frac{\lambda}{\sin(\pi\lambda)}.$$

Units of G in the resulting formula is N / m. This provides possibility of conversion to the ordinary stress intensity factor $K_{0,5}$ using the well-known relation $EG = (1 - \nu^2)K_{0,5}^2$.

4. CONCLUSION

Thus, the solution of the problem with non-square root singularity (in the form of the stress intensity factor K_λ and the displacement parameter $K_{1-\lambda}$) can be transformed into the ordinary stress intensity factor with further structural integrity analysis based on the traditional rules of linear fracture mechanics.

REFERENCES

1. G.B. Sinclair. Stress singularities in classical elasticity. I - Removal, interpretation, and analysis. *Applied Mech. Rev.* - Trans ASME, 57(4): 251–297, 2004.
2. G.B. Sinclair. Stress singularities in classical elasticity. II – Asymptotic identification. *Applied Mech. Rev.* - Trans ASME, 57(5): 385-439. 2004.
3. Carpinteri A. Stress-singularity and generalized fracture toughness at the vertex of the re-entrant corners // *Engng. Fract. Mech.* 26: 143-155. 1987.
4. Аминян А., Андреев А.В. Метод анализа условий равновесия трещины, достигающей границы раздела двух сред // *Вестник МЭИ.* №5: 83-89. 2011.
5. Морозов Е.М. Вязкость разрушения при некорневой особенности напряженного состояния у вершины трещины // *Заводская лаборатория. Диагностика материалов.* № 12. 2012. 65-66.

A ROLE OF HYDROGEN IN THE DEGRADATION OF PIPELINE STEELS

V.V. Panasyuk, H.M. Nykyforchyn

Karpenko Physico-Mechanical Institute of the NAS of Ukraine, Ukraine

panasyuk@ipm.lviv.ua

Abstract. An evaluation of the technical state of long-term exploited structures and calculation their residual life time is impossible without an account of the change of the material physical and mechanical properties, which appear during service. It is concerns, in particular, pipeline steels of hydrocarbon transportation. It is necessary to consider in the last case the hydrogenating ability of transported environment when the degradation process occurs during simultaneous action of stresses and hydrogen. The pipeline steels degradation is considered in the paper just from such positions. The investigation subject: steels of oil and gas pipelines and pipelines of heat power stations.

Long-term service of the steels causes the essential deterioration of its as-received properties, especially the parameters of brittle fracture, the crack growth resistance first of all. The sensitivity of steels to hydrogen embrittlement increases, therefore, for the evaluation of its in-service degradation, it is recommended to test metal in the hydrogenation conditions, best of all – for the crack growth resistance under action of hydrogenating environment.

Two stages of in-service the properties degradation of pipeline steels are considered: deformation aging and dispersed damaging. The role of hydrogen is revealed in the intensification of the stage of dispersed damaging. The main regularities of steels properties degradation for the different stages of service are given.

Keywords: pipeline steel, degradation of properties, deformation aging, dissipated damaging, crack growth resistance, corrosion, hydrogen cracking.

1. INTRODUCTION

An evaluation of the technical state of long-term exploited structures and calculation of their residual life time is impossible without an account of the change of the material physical and mechanical properties, which appear during service. Really these properties are changed mainly in worse direction, so “in-bulk” material degradation should be considered [1]. It concerns, in particular, pipeline steels exploited at ambient and elevated temperatures. It is evident that diffusion factor can play a dominant role in high temperature degradation of steel properties. It causes changes of the metal microstructure which worsen its resistance to fracture. In particular, the main change for ferrite-pearlite microstructure of power steam pipeline steels consists in dissolution of pearlite and formation of grain boundary carbides [2]. For usual service temperatures change of steel structure is not so pronounced but, for example, for main gas pipeline steels, the changes on the dislocation substructure level, coagulation of grains, grain boundary carbide formation on nanoscale are considered [3].

The peculiarity of pipelines is in their use for transportation of environments which can serve as a source of hydrogen and, correspondingly, to hydrogenate the pipe wall. Then the degradation process occurs during simultaneous action of stresses and hydrogen. The role of hydrogen in the acceleration of macrocrack initiation and propagation is well known but additionally the intensification of in-bulk material degradation (degradation of properties) is considered. In this connection there are two ways of hydrogen effect on nano- and microscale: hydrogen intensifies diffusion [4] and therefore accelerates structure changes [5]; hydrogen facilitates in-bulk dissipated damaging [5, 6]. The pipeline steels degradation is considered in the paper just from such positions. The analysis consists of properties comparison in the as-received state (spare pipes) and after 28–40 years of service [5–10].

2. HYDROGENATION ABILITY OF TRANSPORTED HYDROCARBONS

The 0.10C-1.6Mn-0.30Si steel of main oil pipeline in as-received state and cut from the upper *up* and lower *bottom* parts of a pipe being in service for 28 years were tested. Residual water deposited from the oil on the pipe bottom was considered as an aggressive environment causing possible in-bulk pipe wall hydrogenation from the internal surface of the pipe. It is confirmed by more intensive internal corrosion damaging the *bottom* part of

the pipe (Fig. 1). The tests in simulated residual water showed that the corrosion rate of specimens cut from a middle part of pipe wall was 200% higher for the *bottom* and 170% higher for the *top* parts than for the spare pipe. Thus, the results provided evidence that the changes in the properties of material occur due to long time contact with the residual water as a source of hydrogen absorbed by the exploited metal.

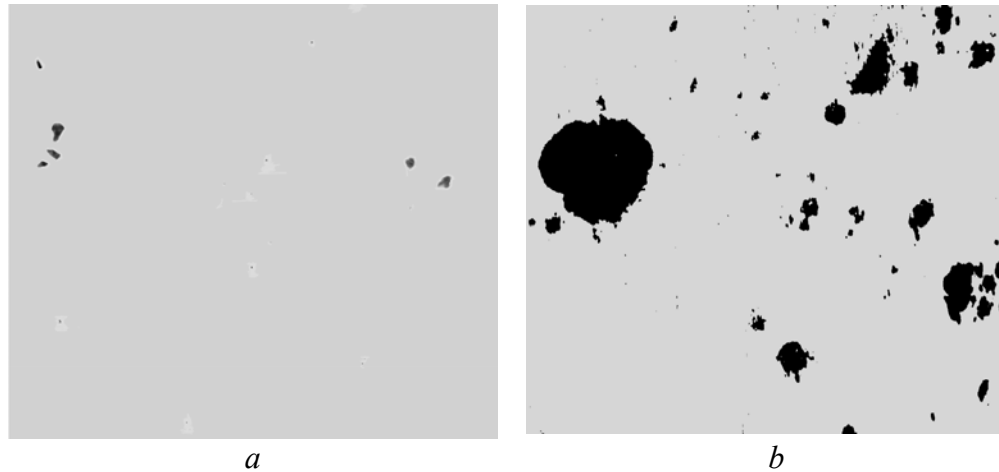


Fig. 1. The inner surface of the *up* (a) and the *bottom* (b) parts of the pipe after 28 years of service.

The results of Charpy tests show that virgin steel exhibits the highest value of KCV (180 J/cm^2). The toughness of the material from the *bottom* part is about half of it (95 J/cm^2). Such a dramatic drop in the toughness indicates the degradation of mechanical properties of the steels exploited in oil transport lines. In the case of the *bottom* part of the pipe being in operation, it was not possible to evaluate the impact toughness, because of the formation of cracks parallel to the pipe surface.

Sensitivity of the pipe materials to stress corrosion cracking has been evaluated by slow strain rate (10^{-7} s^{-1}) tensile tests under moderate cathodic polarization (0.5 A/m^2) in water deposited in the oil storage tank. The relative elongation ($K_\varepsilon = \delta^c/\delta$ 100%) and relative reduction in area $K_{RA} = RA^c/RA$ 100%,) of specimens tensile tested in the air (δ , RA) and those tested in corrosion environment (δ^c , RA^c) were compared. The *bottom* part of the material exhibited lower strength and elongation than the virgin part, either tested in air or in the aggressive environment (Table 1).

Table 1. Plastic properties of tensile tested materials

Material	Test environment	δ [%]	RA [%]	K_E [%]	K_{RA} [%]
As received	air	36	77	39	55
	water	14	42		
Being in service	air	28	56	25	5
	water	7	3		

As it is seen the values of K_{RA} are 55% and 5% respectively for the virgin specimens and cut out from a bottom section of the pipe. The drastic decrease in the K_{RA} and RA values for virgin specimens from the *bottom* part of in-service pipe measured in the air comparing with the virgin ones indicates the possibility of drastic decrease in resistance to brittle fracture of the metal during exploitation.

The next example is a model for demonstrating the role of hydrogen in degradation of steels. Properties of St3sp (0.2C) oil storage tank steel specimen cut off the high-capacity oil storage tank after 30 years of operation were investigated. Specimens cut off from different areas of the structure were tested: the *upper* part of the wall of the reservoir with air and condensed water during operation (I), areas of the wall that were in permanent contact only with oil (II); areas of the wall near the *bottom* of the reservoir (III), and the *bottom* of the reservoir (IV). Note that areas III and IV were in permanent contact only with residual water.

Table 2. Corrosion current density j_{corr} of St3sp steel from different areas of the storage tank (I– IV) in residual water taken from two refineries (conventionally, 1 and 2)

Area Residual water	$j_{corr} \cdot 10^6$ [A/cm ²]			
	I	II	III	IV
1	3,8	1,7	5,1	4,0
2	6,7	3,3	8,6	7,3

Among the standard mechanical characteristics, the impact toughness appeared to be the most sensitive to the in-service degradation of the steel; the steel from the area II is characterized by the highest mean impact toughness ($KCV = 153 \text{ J/cm}^2$), and area III is characterized by its lowest value (62 J/cm^2) due to the joint influence of the aggressive medium and the most intensive loading. For the metal from areas I and IV, which also contacted with the hydrogenating medium, the impact toughness was 72 and

84 J/cm² respectively. Note that the metal of the *upper* part of the reservoir is practically not subjected to mechanical loading, and, hence, the low level of *KCV* is obviously connected only with the action of hydrogen from the condensed water, i.e., the hydrogenation of the metal is accompanied by the initiation of substantial internal stresses. Thus, for the degradation of steels “in the volume,” external load is not mandatory, and only intensive hydrogenation of the metal is sufficient. Correspondingly, corrosion resistance of the metal from different areas of the reservoir determined from the results of electrochemical measurements of the corrosion current (Table 1), also differ, namely, j_{corr} is minimum for area II and maximum for area III. Predicting the corrosion rate of the steels in long operation, this feature should be taken into account.

The steels 17G1S (0.17C-Mn-Si) and API 5L X52 of main gas pipelines in as-received state (spare pipes) and after 28–40 years of service were studied. The API 5L X52 steel (code X52 for as-received state) was in service for 30 years (code X52-10 and X52-12 for wall thickness 10 and 12 mm respectively). Upper *up* and lower *down* parts of the exploited pipes were distinguished and in some cases specimens were cut out closer to inside *in* and outside *out* parts of the pipe wall. Such separateness of the different parts of exploited pipe is explained by the fact that in the case of wet gas pipelines the condensed water accumulates at the pipe bottom [11].

As it is seen in Fig. 2 the internal surface of the pipes being in service revealed the deposits of corrosion products. In the case of the *down* surface, non uniform and pitting corrosion was observed (Fig. 2*b*).

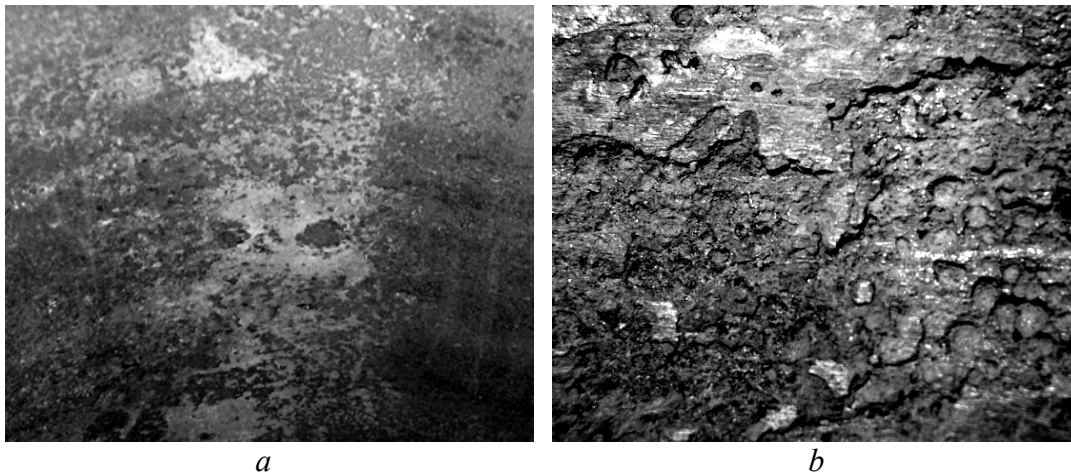


Fig. 2. The inner surface of pipe X52-10-*up* (a) and X52-10-*down* (b).

The investigations revealed a number of effects of changes in the physical and mechanical properties after their long operation in comparison with the same steels of spare pipes. In particular, the strength, the hardness (HRB), and the plasticity (RA) of the steels decrease, the plateau of yield appears on tension diagrams, and, in this case, the strain hardening coefficient n increases (Table 3). An abrupt decrease in the yield strength for 17G1S steel and an abrupt increase in the characteristic RA were registered for all steels. However, the influence of operation on the percentage elongation δ is ambiguous: for X52-10 and 17G1S steels its increase was observed. The hardness of the lower areas of the operated steels is smaller than that of the upper regions.

Table 3. Mechanical properties of the studied gas pipeline steels

Steel code	Service time [years]	Pipe part	σ_y [MPa]	σ_{UTS} [MPa]	RA [%]	δ [%]	n	$J_i/J_{0.2}$, [kJ/m]
X52	0	-	355	475	72.9	22.7	0.59	86/412
X52-12	30	bottom	268	451	64.4	20.8	0.74	50/127
		up	255	460	62.5	22.9		
X52-10		bottom	362	536	54.6	29.7	0.82	37/79
		up	335	538	55.0	28.8		
17G1S	0	-	378	595	79.0	20.2	0.58	203/315
	28		403	590	68.2	20.5		
	29		345	547	71.1	19.6	0.76	
	31		419	574	73.8	21.8		87/201
	38		357	520	73.1	25.4	0.97	
	40		302	515	69.2	26.3	0.75	

As a result of the pipes operation, the characteristics of resistance to brittle fracture of the steel, namely the impact toughness KCV and the crack resistance (the critical value of the J -integral $J_{0.2}$ for an increase in the length of the crack of 0.2 mm), also decrease. The resistance to brittle fracture of the metal of a spare pipe correlates well with its hardness: the harder material from the external surface is characterized by the smaller impact toughness. The operated metal has another dependence: KCV and $J_{0.2}$ of the material are higher from the external surface of the pipe than those from the internal surface indicating that in the latter case it degrades more severely. This also confirms the determining role of hydrogen here because

its content in the metal near the internal wall of the pipe, where it evolves as a result of the corrosion interaction of the steel with the components of transported natural gas, is higher [12].

The impact toughness of X52 steel in the initial state somewhat decreases (by 15–20%) with the decrease of the test temperature due to the energy A of propagation of a crack, which enters into the total energy of deformation and fracture (Fig. 3). At the same time, the low-temperature impact toughness of the operated steel is the one-third than that for the nonoperated steel, and the energy of propagation of a crack is the one-fourth than that for the nonoperated steel.

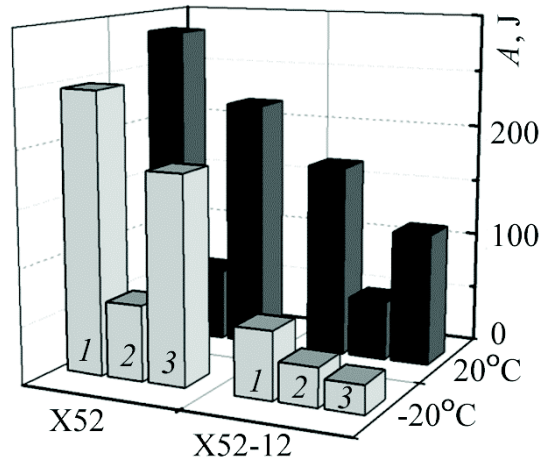


Fig. 3. Total fracture energy (1) and its components: energy of crack initiation (2) and propagation (3) during Charpy tests of API 5L X52 steel.

The stress corrosion cracking in an environment modelled by an aqueous condensate inside the gas pipeline was investigated on smooth specimens and specimens with preliminarily formed cracks. Some experiments were accompanied by moderate cathodic polarization (0.1 A/m^2), which simulated the possible hydrogenation of pipes as a result of cathodic protection. Tests of smooth specimens did not detect the susceptibility to corrosion cracking of the steel in all states at the corrosion potential, but registered it during experiments on cracked specimens (Fig. 4, the threshold of corrosion crack resistance J_{sc} was compared with the value of the J -integral J_i of the crack start under intensive loading in the air).

The steel in the initial state is characterized by a maximum resistance to stress corrosion cracking, and cathodic polarization reduced additionally the

threshold J_{scc} . This means that the degradation of properties of the pipelines steels manifest itself as a substantial decrease not only in the impact toughness and crack resistance but also in the corrosion resistance and resistance to hydrogen cracking. Moreover, it can be assumed that precisely these parameters of fracture mechanics most sensitive to brittle fracture resistance are also most sensitive to in-service degradation of steel. The embrittlement factors, specifically, decrease of the test temperature and hydrogenation of the metal, enhance this property, and, therefore, the comparison investigations of operated and nonoperated steels under precisely these conditions should be carried out.

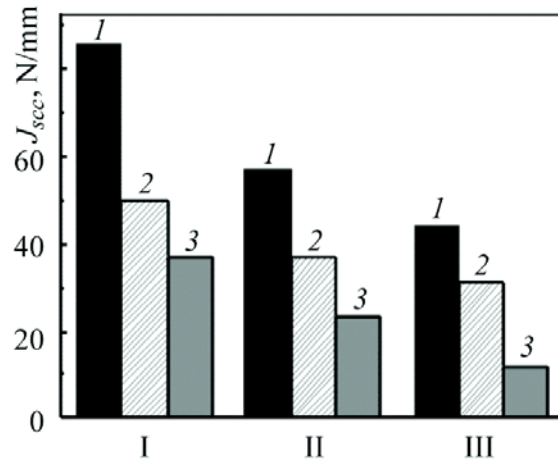


Fig. 4. Crack growth resistance of X52 (I), X52-12 (II) and X52-10 (III) steels in the air (J_i , 1), in the corrosion environment under corrosion potential (2) and cathodic polarisation (3).

Moreover, the detected high susceptibility to hydrogen cracking of the metal operated for a long time, despite its low strength, should be taken into account using electrochemical protection of pipelines. Since it is known the electrochemical protection must be used carefully for high-strength steels for the reason that under the metal hydrogenation by cathodic polarization, hydrogen cracking of the pipe is possible. A similar situation is also observed after in-service degradation of a low-strength steel.

3. TWO STAGES OF IN-SERVICE DEGRADATION OF STEELS

According to the widespread opinion, the main factor of degradation of the main pipelines steels is their deformation aging, which increases the

strength and decreases the plasticity and impact toughness (stage I in Fig. 5). However, if the operation time of the metal approaches about 20–30 years, the intensive damage develops, which levels the hardening of the material by deformation aging and simultaneously decreases the hardness and brittle fracture resistance (stage II). Another feature is the change in the plasticity characteristics of the operated steels, namely, the decrease in RA and the increase in δ .

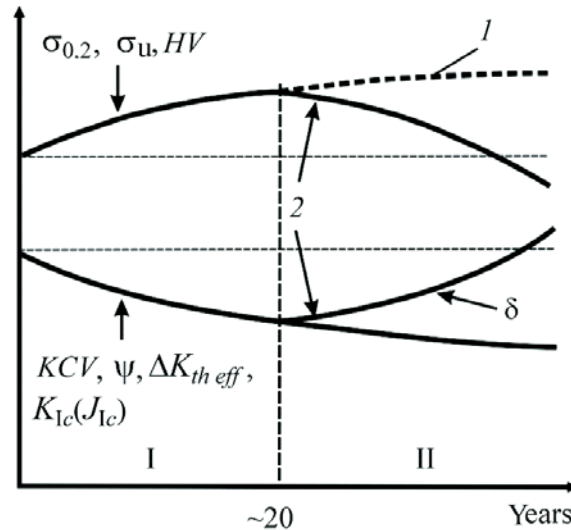


Fig. 5. Changes in steels properties that determine their in-service degradation: (1) without hydrogen effect; (2) in the presence of hydrogen. The proposed hypothesis that the microdamage of the operated steel is the main factor of degradation of pipes after their long operation is consistent with the results of investigations of the hydrogen behaviour in the metal obtained by assessing the hydrogen permeability and temperature dependences of the hydrogen extraction from the metal in different states [5–9]. The concentration of hydrogen in the metal and its diffusion coefficient, as a rule, are determined predicting its influence on the decrease of the structural strength because hydrogen may accumulate in the prefracture zone. However, in recent years, known methods of investigating of hydrogen behaviour in metals have been used to assess their possible damage taking into account that hydrogen is predominantly located in defects, which are considered as its traps [13]. During the determination of hydrogen amount in the metal by vacuum extraction, temperature was increased stepwise with some hold in each step. Then, at a relatively low temperature, “low-energy” hydrogen, i.e.,

hydrogen located in low-energy (taking into account its interaction with defects) traps, leaves the metal. Among such traps are dislocations, for example. At the same time, the “high-energy” hydrogen is located in “deeper” traps (pores, nano-, or microcracks) and, therefore, can leave the metal only at higher temperatures. This is the base of the metal defectiveness analysis [5–9].

The electrochemical method for the determination of hydrogen diffusion coefficient in the metal assumes using a membrane specimen between two electrochemical cells. One side of the membrane (inlet) is polarized cathodically in a potentiostatic mode, and the opposite side is polarized anodically. Hydrogen formed during discharge on the surface of the membrane cathode in the polarization cell partially penetrates into the metal and approaches diffusively the anode side contacting with an alkali solution. Hydrogen atoms from the outlet side of the membrane are almost completely ionized by an applied potential and provide an ionization current proportional to the instantaneous desorption rate of hydrogen. On the whole, the physical (lattice) D and effective D^* (with regard to trapping) diffusion hydrogen coefficients can be determined and, hence, the ratio $D/D^* = 1 + N(k/p)$ can be calculated, where N is the density of traps, k and p are the kinetic constants of trapping and release of hydrogen from traps, and $N(k/p)$ is the efficiency of hydrogen trapping.

4. CONCLUSIONS

1. Transport of hydrogen containing environments causes the pipe wall hydrogenation therefore the degradation of the in-bulk material occurs under simultaneous effect of mechanical stresses and hydrogen absorbed by metal.
2. A number of features in the degradation of the mechanical and corrosion-mechanical properties of oil and gas main pipelines and oil storage reservoirs operated for 28–40 years are detected. These are: the decrease in the resistance to brittle fracture, expressed in the terms of the impact toughness drop, reduction in area, crack resistance, corrosion resistance, and resistance to hydrogen cracking; anomalies in the mechanical behaviour of the operated metal, namely, the decrease of the resistance to brittle fracture is accompanied with the decrease of the hardness, and the decrease of the reduction in area is accompanied by an increase in elongation; the high sensitivity of the impact toughness to the degradation of steels is caused by the decrease of the propagation energy of cracks, i.e., the parameter of fracture mechanics.

3. The main factor of the degradation of durable pipes is microdamage, which is indirectly substantiated by the intensification of trapping of hydrogen, the increase of the fraction of deep hydrogen traps, the increase of the elongation, and the decrease of the hardness. Two stages of degradation of steels, namely, deformation hardening and development of defectiveness are proposed.

REFERENCES

- [1] V.V. Panasyuk, H.M. Nykyforchyn: Proc. of the 19th European Conference on Fracture «Fracture Mechanics for Durability, Reliability and Safety», Kazan, Russia, 26 - 31 August, 2012. – Paper 77 (CD).
- [2] H.M. Nykyforchyn, O.Z. Student, H.V. Krechkovs'ka, A.D. Markov: Mat. Sci., N 2 (2010), p. 177.
- [3] Yu. S. Nechaev: Uspekhi Fizicheskikh Nauk, N 7. (2008), p. 681.
- [4] V.A. Goltsov: Int. J. of Hydrogen Energy, N 2/3 (1997), p. 119.
- [5] H.M. Nykyforchyn, K.-J. Kurzydowski, E. Lunarska, in: Prediction, Industrial Developments and Evaluations, volume 2 of *Environment-induced cracking of materials*, Edited by S.A. Shipilov, R.H. Jones,, J.-M. Olive and R.B. Rebak, Elsevier, (2008), p. 349.
- [6] H.M. Nykyforchyn, E. Lunarska, P. Zonta: Proc. of the NATO advanced research workshop on corrosion protection of pipelines transporting hydrocarbons, Dordrecht, Springer (2011), p. 59.
- [7] H. Nykyforchyn, E. Lunarska, O. Tsyulnyk et al.: Mat. and Corr., N 9 (2009), p. 716.
- [8] H. Nykyforchyn, E. Lunarska, O.T Tsyulnyk et al.: Eng. Failure Analysis, N 4 (2010), p. 624.
- [9] E.I. Kryzhaniv'skyi, H.M. Nykyforchyn: Mat. Sci., N 2 (2011), p. 127.
- [10] A. Zagórski, H. Matysiak, O.T. Tsyulnyk et al.: Ibid, N 3 (2004), p. 421.
- [11] G. Gabetta, M. Margarone: NACE Corrosion Conference Expo Paper 07522, Nashville, USA (2007), 13 p.
- [12] O.T. Tsyulnyk, Z.V. Slobodyan, O.I. Zvirko et al.: Mat. Sci., N 5 (2008), p. 619.
- [13] E.Lunarska: Proc. of Int. Conf. Environmental Degradation of Engineering Materials, 1999, Gdańsk, Poland, p. 32.

FATIGUE DAMAGE SUMMATION IN VERY HIGH LOADING CYCLE DOMAIN AND UNDER NATURAL AGEING

I.M. Petrova, I.V. Gadolina

Mechanical Engineering Research Institute of the Russian Academy of Sciences. 101990, 4, M.Kharitonievsky Lane, Moscow, Russia

impetr@mail.ru

Abstract: At the present time a large amount of the technical systems works under dynamic loading and in longevity domain, which significantly exceeds the guaranteed resource, which was estimated on the basis of the fatigue resistance characteristics, estimated by the tests on 10^7 loading cycles. Investigations on the basis $10^8 \dots 10^9$ have shown that the fatigue limit decreases, but in varied rate for the varied construction material. For the investigation of the damage accumulation under random loading laws the tests under programmed loading were carried out. The programmed blocks were built by step-wise approximation of the uniform, normal and exponent laws of the stress amplitude distribution. The tests on the basis of $5 \cdot 10^8$ have shown the fatigue limit decrease.

On the other hand, the reason of the failure in exploitation might be the initial fatigue resistance characteristics change during material natural ageing, which takes place without exploitation loads. The investigation of steel 45 fatigue resistance characteristics after its storage during 50 years at room temperature and low humidity has been done. No surface corrosion was observed. The mechanical characteristics of steel 45 by producing were as follows: yield stress $\sigma_y = 398\text{MPa}$, ultimate stress $\sigma_u = 660\text{MPa}$, specific elongation 22%. After ageing they were as follows: yield stress $\sigma_y = 374\text{MPa}$, ultimate stress $\sigma_u = 641\text{MPa}$, specific elongation 26%. The surface hardness did not change and constitute 172HB. That is the mechanical properties did not change much: by 6% and 3% accordingly.

Key words: fatigue resistance characteristics, natural ageing, programmed block

At the present time a large amount of the technical systems works under dynamic loading and in longevity domain, which significantly exceeds the guaranteed resource, which was estimated on the basis of the fatigue resistance characteristics, estimated by the tests on 10^7 loading cycles. The experiment results under regular loading have shown that the fatigue limit in very high cycle domain decreases, but in varied rate for the varied construction material. For the investigation of the damage accumulation under random loading dependences the tests under programmed loading were carried out on the base more than $5 \cdot 10^8$. The programmed blocks were built by step-wise approximation of the uniform, normal and exponent laws of the stress amplitude distribution. For all specimen types the basic fatigue curves were estimated on the same equipment with the programming device switched off. On the picture 1 the experimental and calculated fatigue curves, corresponding to the normal distribution law, obtained by regular and random loading are shown. For the calculation the proposed by S.V.Serensen and V.P.Kogaev equation was used. It allows carrying out the life estimation by the working exploitation stress only slightly exceeding the fatigue limit estimated on the base 10^7 cycles.

$$\sigma_{-1i} = \sigma_{-1i-1} [1 - k m_i / N_i (\sigma_{ai} / \sigma_{-1i-1} - 1)] \quad (1)$$

Here σ_{-1i} is the fatigue limit of the initial material corresponding the base 10^7 cycles, never previously loaded; k is the parameter, which characterize decrease intensity because of preliminary loading; N_i - is the number of cycles by the fatigue curve of the initial material corresponding the loading amplitude σ_{ai} . By the calculation by the formula (1) some assumptions are accepted, namely that the cycle loading of already defective because of preliminary loading specimens will lead to new fatigue limit decrease and that the amplitudes are arranged in descending order. The equation (1) is good for calculation in the very high cycle domain, because here only current fatigue limit value is used, which depends on accumulated damage. The calculation algorithm with using formula (1) is described in [1].

From Fig.1 it is seen, that the calculated and experimental life estimation coincide satisfactory. The damage is accumulated also under stress amplitude below fatigue limit. Under very high experimental bases, which correspond to low stress levels, the failures take place.

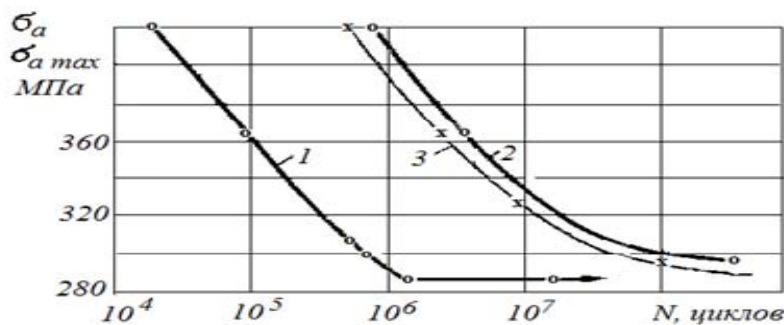


Fig.1 Calculated and experimental fatigue curves under regular and random loading for the normal distribution; 1- fatigue curves under regular loading, 2- under random loading (dependence N from σ_{amax}), 3 – calculated by the equation (1).

On the other hand, the reason of the failure in exploitation might be the initial fatigue resistance characteristics change during material natural ageing, which takes place without exploitation loads. The investigation of steel 45 fatigue resistance characteristics after its storage during 50 years at room temperature and low humidity has been done. No surface corrosion was observed. The mechanical characteristics of steel 45 by producing were as follows: yield stress $\sigma_y = 398\text{MPa}$, ultimate stress $\sigma_u = 660\text{MPa}$, specific elongation 22%. After ageing they were as follows: yield stress $\sigma_y = 374\text{MPa}$, ultimate stress $\sigma_u = 641\text{MPa}$, specific elongation 26%. The surface hardness did not change and constitute 172HB. That is the mechanical properties under tension did not change much: by 6% and 3% accordingly.

For the estimation of the fatigue resistance characteristics the testing under bending with rotation with frequency 47 Hz had been carried out. The initial fatigue curve (line 1 on Fig.2) was estimated on the basis of wide range experiment on 4 stress levels, and on each of them 22-23 specimens were tested (the testing was performed by M. Galperin). The endurance limit medium value at initial state on the basis $2 \cdot 10^6$ cycles was 318 MPa. Lines 1a and 1b represent the limits of fatigue curves parameters scatter, corresponding to fracture probability of 5% and 95%. Coefficient of fatigue limit variation, corresponding to testing bases from $4 \cdot 10^5$ to 10^7 cycles of dynamical loading is in the limit $v_{\sigma-1} 0,06 \dots 0,04$.

After long-term ageing 11 specimens were tested at the same testing machines at the varied amplitude stresses. The endurance limit medium value on the basis $2 \cdot 10^6$ cycles was 178 MPa. It means that it decreased by 44 %. The fatigue curve of after long-term ageing specimens is shown on Fig.2

(line 2). The limits of scatter of fatigue curves parameters of ageing specimens are represented by lines 2a and 2b. They were estimated by the method proposed in [2]. According to this method to each specimen corresponds its own fatigue curve; this lets estimate fatigue characteristics scatter for the given life by the results of testing the limited number of specimens. Fatigue limit variation coefficient for the testing bases from 10^5 to 10^8 was about $v_{\sigma-1} = 0,24$. The analysis of the fatigue curves 1 and 2 (Fig.2) has shown, that the scatter bands do not intersect. It means it can be regarded that they belong to varied sets describing the varied materials.

Carried out in IMET RAN under Botvina L.R. leadership analysis of micro relief of ageing specimen fatigue fracture has shown, that the decrease of endurance limit after long-term ageing was caused apparently by the material structure state change, which does not influence much on the mechanical characteristics during tension, but influences significantly on fatigue resistance characteristics.

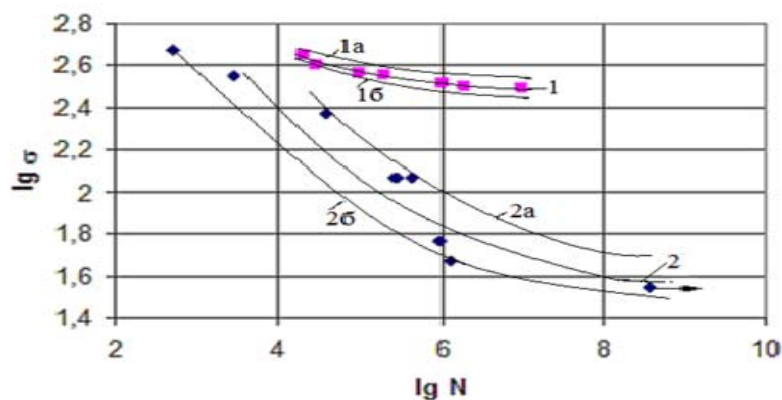


Fig. 2. Smooth steel 45 specimens fatigue curves in initial (1) and ageing (2) state. Curves 1 a,b and 2 a,b represent the scatter band of the fatigue curves, with probabilities 5% and 95% correspondingly.

REFERENCES

1. Fatigue machine part design in probabilistic point of view. Metodicheskie ukazaniya. Moskva. Mejtstraslevoi nauchno-tehnicheskii complex "Nadejnost' mashin". 1996. 85p.
2. Petrova I.M., Gadolina I.V. Fatigue characteristics scatter estimation by the limited number of specimens tested. // Zavodskaja laboratorija 2009, #11. V. 75. c. 50-51

APPLICATION OF THE RECIPROCITY GAP FUNCTIONAL METHOD FOR IDENTIFICATION OF SMALL WELL-SEPARATED DEFECTS IN AN ISOTROPIC ELASTIC BODY USING THE RESULTS OF ONE STATIC TEST

E.I. Shifrin, P.S. Shushpannikov

*A. Yu. Ishlinsky Institute for Problems in Mechanics, Russian Academy of Sciences,
prosp. Vernadskogo 101-1, Moscow 119526, Russia*

shifrin@ipmnet.ru, shushpan@ipmnet.ru

Abstract: An inverse problem of identification of a finite number of small, well-separated defects in an isotropic linear elastic body is considered. It is supposed that the defects are cavities or inclusions (rigid or linear elastic). If the defects are cavities then their boundaries are supposed unloaded. If the defects are inclusions it is supposed complete bonding between the matrix and inclusions. It is assumed also that as a result of static test the loads and displacements are measured on the external boundary of the body. A method for determination of centers of the defects projections on an arbitrary plane is developed. If the defects are ellipsoids their geometrical parameters (directions and magnitudes of the ellipsoids axes) are determined also. Numerical examples illustrating efficiency of the developed method are considered.

Key words: elastostatic inverse problem, multiple defects, reciprocity gap functional

1 INTRODUCTION

The problems of defects identification in an elastic body using results of static tests were studied very intensively during last two decades. Several groups of methods were developed for solving the problem. The most commonly used group of methods is based on constructing of an error function and application of one of the optimization methods for the function minimization (see for example [1-4]). Asymptotic expansion of the far field was used in [5-8]. Estimations of a defect volume were obtained in [9,10]. The reciprocity gap functional (RGF) method enabled to develop an analytical approach for solving some inverse problems [11-19]. The most of the methods were applied to the problem of identification of a single defect. The methods for identification multiple defects are much less developed. It is possible to mention [20] where a method for identification of a cluster of small elastic inclusions was developed on the base of the results obtained in [5] and the papers [21-23] where the methods for identification multiple defects for inverse 2d problems for Laplace equation were developed.

Below we propose a new simple method for identification of small, well-separated defects in 3d elastic body using results of one static test. The method is based on the use of RGF. The problem is reduced to the problem of identification of the projections of the defects on an arbitrary plane due to the use of the regular elastic fields of specific type. The obtained 2d problem is turned out similar to the problem of determination of simple poles of a meromorphic function. It enabled to use in the considered problem the methods developed for the determination of simple poles.

The statement of the problems is given in the Section 2. Reduction of the initial 3d problem to 2d problem for determination of the defects projections on an arbitrary plane is presented in the Section 3. The used method for determination the number of defects and coordinates of their centers is described in the Section 3 also. An algorithm for determination of the geometrical parameters of the ellipsoidal defects is presented in the Section 4. Numerical examples illustrating efficiency of the proposed method are considered in the Section 5.

2 STATEMENT OF THE PROBLEM

Let $V \subset R^3$ be a bounded domain with a boundary ∂V . $G_k \subset V$, $k=1,2,\dots,n$ are small, simply connected subdomains. We suppose that

$\bar{G}_i \cap \bar{G}_j = \emptyset, i \neq j, \bar{G} = \bigcup_{k=1}^n \bar{G}_k \subset V$, where \bar{G}_k is a closure of the subdomain G_k . Let us suppose that an isotropic linear elastic body with a shear modulus μ_M and Poisson ratio ν_M occupies the domain $\Omega = V \setminus \bar{G}$. The defects G_k can be cavities or inclusions (rigid or linear elastic). If G_k is a cavity we suppose that its boundary ∂G_k is unloaded. If G_k is an inclusion, it is supposed complete bonding between the matrix and inclusion. We assume that typical sizes of the defects have the same order. Denote the typical size l . Assume also that the typical distances between the defects have the same order and denote the typical distance L . We assume that the defects are small in the following sense

$$l \ll L \quad (1)$$

Let us introduce Cartesian coordinates $Ox_1x_2x_3$. We suppose that the loads $\mathbf{t}^d = (t_1^d, t_2^d, t_3^d)$ and displacements $\mathbf{u}^d = (u_1^d, u_2^d, u_3^d)$ are measured on ∂V in a static test. We will mark with the superscript d the stress-strain state in the body Ω : σ_{ij}^d is the stress tensor, e_{ij}^d is the strain tensor and \mathbf{u}^d is the displacement vector, $t_i^d = \sigma_{ij}^d n_j$, where $\mathbf{n} = (n_1, n_2, n_3)$ is a unit outward normal to the boundary ∂V and convention of summation for repeated indices is used. Below we will suppose that the defects are linear elastic inclusions. The cases of cavities and rigid inclusions can be considered as limit cases when the elastic moduli tend to zero or infinity, respectively. The stress-strain state in the inclusion G_k we will mark with the superscript Ik ($\sigma_{ij}^{Ik}, e_{ij}^{Ik}, \mathbf{u}^{Ik} = (u_1^{Ik}, u_2^{Ik}, u_3^{Ik})$ are the stress tensor, the strain tensor and the displacement vector, respectively). The shear modulus and Poisson ratio of the inclusion G_k we denote by μ_k and ν_k , respectively.

According to our suppositions the following equalities are valid for $\mathbf{x} = (x_1, x_2, x_3) \in \Omega$:

$$\begin{aligned} e_{ij}^d &= \frac{1}{2}(u_{i,j}^d + u_{j,i}^d), \quad (i=1,2,3; j=1,2,3) \\ \sigma_{ij}^d &= 2\mu_M \left(\frac{\nu_M}{1-2\nu_M} \theta^d \delta_{ij} + e_{ij}^d \right), \quad \theta^d = \sum_{k=1}^3 e_{kk}^d \\ \sigma_{ij,j}^d &= 0 \end{aligned} \quad (2)$$

Here δ_{ij} is the Kronecker delta.

The elastic field with the superscript lk satisfies in the domain G_k the equations analogical to Eq. (2) with the replacement of the values μ_M and ν_M by the values μ_k and ν_k , respectively. The conditions of complete bonding between the matrix and inclusion G_k have the following form:

$$\mathbf{u}^{lk}(x) = \mathbf{u}^d(x), \quad \sigma_{ij}^{lk}(x)N_j(x) = \sigma_{ij}^d(x)N_j(x), \quad x \in \partial G_k \quad (3)$$

Here $\mathbf{N}(x) = (N_1(x), N_2(x), N_3(x))$ is a unit normal to the boundary ∂G_k at the point x .

We will call the elastic fields in the body V without defects as regular elastic fields and mark by a superscript r ($\sigma_{ij}^r, e_{ij}^r, \mathbf{u}^r = (u_1^r, u_2^r, u_3^r)$ are the stress tensor, the strain tensor and the displacement vector, respectively). The regular elastic fields satisfy the Eq. (2) in the domain V .

The RGF, depending on two stress states with superscripts d and r , is defined as follows:

$$RG(d, r) = \int_{\partial V} (t_i^d u_i^r - t_i^r u_i^d) dS \quad (4)$$

where $t_i^r = \sigma_{ij}^r n_j$.

The problem is to reconstruct the defects G_k using the known loads \mathbf{t}^d and displacements \mathbf{u}^d on the boundary ∂V . Because the vector-functions \mathbf{t}^d and \mathbf{u}^d are known, the values $RG(d, r)$ can be calculated for all regular elastic fields r . So, the problem will be solved if we express the parameters of the domains G_k by means of the values $RG(d, r)$. It was shown in [16,17] that the expression (4) can be written in one of the following forms:

$$RG(d, r) = \sum_{k=1}^n \int_{G_k} \Delta e_{ij}^{lk} \sigma_{ij}^r dx \quad (5)$$

$$RG(d, r) = \sum_{k=1}^n \int_{G_k} \Delta \sigma_{ij}^{lk} e_{ij}^r dx \quad (6)$$

where $\Delta e_{ij}^{lk} = \bar{e}_{ij}^{lk} - e_{ij}^{lk}$, $\Delta \sigma_{ij}^{lk} = \sigma_{ij}^{lk} - \bar{\sigma}_{ij}^{lk}$, \bar{e}_{ij}^{lk} are the strains corresponding to the stresses σ_{ij}^{lk} and $\bar{\sigma}_{ij}^{lk}$ are the stresses corresponding to the strains e_{ij}^{lk} in the material with the shear modulus μ_M and Poisson ratio ν_M .

3. REDUCTION OF THE PROBLEM TO 2D PROBLEM OF THE DEFECTS PROJECTIONS IDENTIFICATION

Let us denote the centers of the defects G_k by $x^k = (x_1^k, x_2^k, x_3^k)$ and the volumes of the domains G_k by $|G_k|$. Let us remind that we suppose that the diameters of the defects are small and the defects are well-separated. It follows from our suppositions that in this case Eq. (6) can be rewritten in the form:

$$RG(d, r) \approx \sum_{k=1}^n \Delta \sigma_{ij}^{lk}(x^k) e_{ij}^r(x^k) |G_k| \quad (7)$$

Consider, for example, projections of the defects on the plane x_1x_2 . To determine projections of the defects centers on the plane x_1x_2 we will use the regular elastic fields corresponding to plane strain states. According to [24] the displacements $\mathbf{u} = (u_1, u_2, 0)$, strains e_{ij} and stresses σ_{ij} of a plane strain field can be expressed by means of two holomorphic functions $\varphi(z)$ and $\psi(z)$, $z = x_1 + ix_2$

$$2\mu_M(u_1 + iu_2) = \kappa\varphi(z) - z\overline{\varphi'(z)} - \overline{\psi(z)}, \quad \kappa = 3 - 4\nu_M \quad (8)$$

$$\sigma_{11} + \sigma_{22} = 4\text{Re}[\Phi(z)],$$

$$\sigma_{22} - \sigma_{11} + 2i\sigma_{12} = 2[\overline{z}\Phi'(z) + \Psi(z)], \quad (9)$$

$$\sigma_{13} = \sigma_{23} = 0, \quad \sigma_{33} = \nu_M(\sigma_{11} + \sigma_{22})$$

$$e_{11} + e_{22} = \frac{2(1 - 2\nu_M)}{\mu_M} \text{Re}[\Phi(z)],$$

$$e_{22} - e_{11} + 2ie_{12} = \frac{1}{\mu_M} [\overline{z}\Phi'(z) + \Psi(z)], \quad (10)$$

$$e_{13} = e_{23} = e_{33} = 0$$

where $\Phi(z) = \varphi'(z)$, $\Psi(z) = \psi'(z)$, the overbar denotes the complex conjugation.

Let us mark with a superscript r a regular elastic field corresponding to a plane strain state determined by the following holomorphic functions:

$$\Phi(z) = 0, \quad \Psi(z) = -2\mu_M H(z) \quad (11)$$

It follows from the Eqs. (7), (10) and (11)

$$\begin{aligned}
 RG(d, r) &\approx \\
 &\approx \sum_{k=1}^n \left[\left(\Delta\sigma_{11}^{lk}(x^k) - \Delta\sigma_{22}^{lk}(x^k) \right) \operatorname{Re} H(z_k) - 2\Delta\sigma_{12}^{lk}(x^k) \operatorname{Im} H(z_k) \right] |G_k|
 \end{aligned} \tag{12}$$

where $z_k = x_1^k + ix_2^k$.

Let us mark with a superscript ρ a regular elastic field corresponding to a plane strain state determined by the holomorphic functions:

$$\Phi(z) = 0, \quad \Psi(z) = -2\mu_M iH(z) \tag{13}$$

It follows from the Eqs. (7), (10) and (13)

$$\begin{aligned}
 RG(d, \rho) &\approx \\
 &\approx \sum_{k=1}^n \left[-\left(\Delta\sigma_{11}^{lk}(x^k) - \Delta\sigma_{22}^{lk}(x^k) \right) \operatorname{Im} H(z_k) - 2\Delta\sigma_{12}^{lk}(x^k) \operatorname{Re} H(z_k) \right] |G_k|
 \end{aligned} \tag{14}$$

From the Eqs. (12) and (14) one has

$$\begin{aligned}
 RG(d, r) - iRG(d, \rho) &\approx \\
 &\approx \sum_{k=1}^n \left[\left(\Delta\sigma_{11}^{lk}(x^k) - \Delta\sigma_{22}^{lk}(x^k) \right) + 2i\Delta\sigma_{12}^{lk}(x^k) \right] H(z_k) |G_k|
 \end{aligned} \tag{15}$$

Let us take $H(z) = H_m(z) = (z/L)^m = w^m$, $m = 0, 1, 2, \dots$, where L was introduced in (1). In this case Eq. (15) for various $H_m(z)$ have the following form:

$$\sum_{k=1}^n A_k w_k^m = b_m, \quad m = 0, 1, 2, \dots \tag{16}$$

where $A_k = \left[\left(\Delta\sigma_{11}^{lk}(x^k) - \Delta\sigma_{22}^{lk}(x^k) \right) + 2i\Delta\sigma_{12}^{lk}(x^k) \right] |G_k|$, $b_m = RG(d, r_m) - iRG(d, \rho_m)$, $w_k = z_k / L$, r_m and ρ_m are regular elastic fields corresponding to the holomorphic function $H_m(z)$.

Eq. (16) coincide with the equations arising in the problem of simple poles of a meromorphic function identification, see for example [25,26]. There are several methods to determine the locations of the defects projections w_k and the coefficients A_k from the Eq. (16). We have used the method developed in [26]. Let us remind briefly the main ideas of the method. Let us first suppose that we know the number of the defects n . Consider a polynomial

$$P_n(w) = \prod_{k=1}^n (w - w_k) = w^n + \sum_{m=0}^{n-1} q_m w^m \tag{17}$$

Here $\deg P_n(w) = n$ and $w_k, k = 1, 2, \dots, n$ are the roots of the polynomial $P_n(w)$, q_m are unknown coefficients.

Using Eq. (16) it is possible to obtain a system of linear algebraic equations relative to the coefficients q_m . It follows from the Eqs. (16), (17)

$$b_{p+n} + \sum_{m=0}^{n-1} b_{p+m} q_m = 0, \quad p = 0, 1, 2, \dots, n-1 \quad (18)$$

Eq. (18) is a system of linear algebraic equations relative to unknowns $q_m, m = 0, 1, 2, \dots, n-1$. After determination of the values q_m it is possible to construct the polynomial $P_n(w)$ and to find its roots. Thus, the projections of the defects on the plane $x_1 x_2$ are found. After determination of the values w_k we consider a system of equations (16) for $m = 0, 1, 2, \dots, n-1$. It is a system of linear algebraic equations relative to A_k . So, the values w_k and A_k are determined. Here we suppose that $A_k \neq 0$.

Usually we do not know the number of defects n , but we can suppose that we know an upper bound of the number. Let us suppose that we know that $n \leq N$. In this case applying the considered procedure for a polynomial $P_N(w)$, constructed according to Eq. (17), we obtain the roots of the polynomial w_k and coefficients $A_k, k = 1, 2, \dots, N$. Among the obtained values w_k there are some roots corresponding to the defects projections and some spurious roots. The spurious roots can be excluded using the following criteria:

1. Some of spurious roots are located outside of the body projection.
2. The values $|A_k|$ corresponding to spurious roots w_k are small relative to the values $|A_k|$ corresponding to projections of real defects.
3. The spurious roots w_k are not stable relative to the chosen value of the upper bound N and can change significantly when various values N are considered.
4. If projections on several planes are considered then it is possible to see that spurious roots are not projections of some points in R^3 .

If one of the criteria is satisfied for a considered root then the root does not correspond to any defect.

Let us suppose that the spurious roots are excluded. The number of remaining roots can exceed the number of projections of real defects because several roots can correspond to one defect, see for example [23]. To

determine the exact number of defects projections it is possible to use the supposition that typical sizes of defects is much less than the distances between the defects. So, if we obtain, for example, three roots 1, 2 and 3 and the distance between the roots 1 and 2 is much less than the distances between the roots 1, 3 and 2, 3 then we can suppose that the roots 1 and 2 correspond to the projection of the same defect. After determination of the number of defects we repeat the described above procedure for the obtained number of defects. As a result, we obtain roots located close enough to the projections of defects centers. Numerical examples confirming that the use of the proposed algorithm enables to determine the number of defects and their centers are considered in the Section 5.

Let us make few remarks regarding to the proposed method for the defects number determination.

Remark 1. Note that there are the planes that the projections of several defects on these planes are close to each other. In this case, the defects are separated by considering of the projections on the other planes.

Remark 2. In the case of certain types of combinations of applied load, the size and orientation of the defect the value of A_k for the defect projection on some plane can be close to zero (for example, plane x_1x_2 in case of uniaxial tension (compression) load along the axis x_3 and spherical defect). In this case, the defect can be detected and identified by considering the projections on other planes.

Remark 3. In some exceptional cases (for example, in the case of a hydrostatic compression (tension) and spherical defect) the values of A_k for the projections of the defect are close to zero for any plane. In these cases, to identify the defect it is necessary to perform an additional experiment. Such a situation in the case of a single defect was discussed in [17].

In the Section 4 we suppose that the defects have an ellipsoidal shape and the number of defects and their centers are known. A method for determination of the magnitudes and directions of the ellipsoid semiaxes is developed.

4. IDENTIFICATION OF SMALL ELLIPSOIDAL DEFECTS

4.1 Identification of spherical cavities and spherical rigid inclusions

First, we consider a special case. Suppose that there are grounds to assume that defects are spherical linear elastic inclusions. Consider a regular elastic field in the body V without defects subjected to the loads \mathbf{t}^d on the boundary ∂V . The elastic field we will mark by a superscript dr . Because the defects are small, the stress state in the defect G_k is approximately constant and close to the stress state in the sphere G_k located in an infinite elastic solid and subjected to the stresses $\sigma_{ij}^{dr}(x^k)$ at the infinity. Using an analytical solution of the direct problem for a spherical inclusion located in an infinite elastic solid, see [27], it is possible to obtain the following equality:

$$\begin{aligned} & (\Delta\sigma_{11}^{lk} - \Delta\sigma_{22}^{lk}) + 2i\Delta\sigma_{12}^{lk} = \\ & = -120\mu_M(1-\nu_M)B\left[\left(\sigma_{11}^{dr}(x^k) - \sigma_{22}^{dr}(x^k)\right) + 2i\sigma_{12}^{dr}(x^k)\right] = C_k \end{aligned} \quad (19)$$

Here the value B depends in a general case on the elastic moduli of the matrix and inclusion. If the defect is a spherical cavity, then

$$B = \frac{1}{8\mu_M(7-5\nu_M)} \quad (20)$$

If the defect is a rigid spherical inclusion, then

$$B = -\frac{1}{16\mu_M(4-5\nu_M)} \quad (21)$$

Thus, if the defects are spherical cavities or rigid spherical inclusions their radii can be calculated directly from the values A_k and Eqs. (19) – (21)

$$r_k = \sqrt[3]{\frac{3A_k}{4\pi C_k}} \quad (22)$$

Here r_k is a radius of the sphere G_k .

4.2 General case of ellipsoidal inclusions

Let us suppose now that the defects G_k are ellipsoidal inclusions. To determine the geometrical parameters of the inclusions (the magnitudes and directions of their axes) we will use an approach developed in [14-18] for determination of a single ellipsoidal defect. Similarly to the case of spherical inclusions, due to the smallness of defects the stress state in the defect G_k is approximately constant and close to the stress state in the ellipsoidal inclusion G_k located in an infinite elastic solid and subjected to the stresses $\sigma_{ij}^{dr}(x^k)$ at the infinity. For definiteness, let us find the geometrical parameters of the defect G_1 . To determine the geometrical parameters of the defect G_1 , we construct a regular elastic field so that the contribution of the first term in the sum on the right side of the Eq. (6) was significantly greater than that of the remaining terms. First introduce Cartesian coordinates with the origin in the center of the defect G_1

$$x_i = \xi_i + x_i^1, \quad i = 1, 2, 3 \quad (23)$$

Denote coordinates of other defects centers in the coordinate system by $(\xi_1^k, \xi_2^k, \xi_3^k)$, $k = 2, 3, \dots, n$. Define holomorphic functions $\chi_m(\zeta)$, $\zeta = \xi_1 + i\xi_2$

$$\chi_m(\zeta) = \frac{1}{L^{m(n-1)}} \prod_{k=2}^n (\zeta - \zeta_k)^m, \quad m \geq 3, \quad \zeta_k = \xi_1^k + i\xi_2^k \quad (24)$$

Consider a holomorphic function $H_m(\zeta)$

$$H_m(\zeta) = \left(\frac{\zeta}{L} \right)^2 \chi_m(\zeta) \quad (25)$$

Consider regular elastic fields \mathbf{u}_m^r and \mathbf{u}_m^p corresponding the holomorphic functions $\Phi(\zeta)$ and $\Psi(\zeta)$ determined by means of the holomorphic function $H_m(\zeta)$ according to Eqs. (11), (13). It follows from the Eqs. (6), (10), (11), (13) and from supposition that tensors σ_{ij}^{lk} are approximately constant inside G_k

$$\begin{aligned} & RG(d, r_m) - iRG(d, \rho_m) \approx \\ & \approx \sum_{k=1}^n \left[(\Delta\sigma_{11}^{lk} - \Delta\sigma_{22}^{lk}) + 2i\Delta\sigma_{12}^{lk} \right] \int_{G_k} H_m(\zeta) d\xi \end{aligned} \quad (26)$$

where $d\xi = d\xi_1 d\xi_2 d\xi_3$.

We suppose that the values $\Delta\sigma^k = (\Delta\sigma_{11}^{lk} - \Delta\sigma_{22}^{lk}) + 2i\Delta\sigma_{12}^{lk}$ for different defects G_k have the same order which we denote by $\Delta\sigma$. According to our suppositions, the contribution of the first term, corresponding to the defect G_1 , to the sum in the right hand side of the Eq. (26) has an order S_1^m

$$S_1^m = \Delta\sigma l^5 L^{-2} \quad (27)$$

The order of the sum of other terms is as follows:

$$S_+^m = (n-1)\Delta\sigma l^{m+3} L^{-m} \quad (28)$$

It follows from the Eqs. (27) and (28)

$$\frac{S_+^m}{S_1^m} = (n-1)\left(\frac{l}{L}\right)^{m-2} \quad (29)$$

It follows from Eq. (29) and our supposition (1)

$$\lim_{m \rightarrow \infty} \frac{S_+^m}{S_1^m} = 0 \quad (30)$$

It follows from Eqs. (26) and (30) that for big values of m

$$\begin{aligned} RG(d, r_m) - iRG(d, \rho_m) &\approx \\ &\approx \left[(\Delta\sigma_{11}^{l1} - \Delta\sigma_{22}^{l1}) + 2i\Delta\sigma_{12}^{l1} \right] \int_{G_1} H_m(\zeta) d\zeta \end{aligned} \quad (31)$$

It follows from the definition of the function $H_m(\zeta)$ given in (24), (25) that the main term of asymptotic expansion of the function in the domain G_1 has the form:

$$H_m(\zeta) \approx \left(\frac{\zeta}{L}\right)^2 P_m, \quad P_m = \chi_m(0) = \prod_{k=2}^n \left(-\frac{\zeta_k}{L}\right)^m \quad (32)$$

From the Eqs. (31) and (32) one has

$$\begin{aligned} RG(d, r_m) - iRG(d, \rho_m) &\approx \\ &\approx \left[(\Delta\sigma_{11}^{l1} - \Delta\sigma_{22}^{l1}) + 2i\Delta\sigma_{12}^{l1} \right] P_m L^{-2} \int_{G_1} \left[(\zeta_1^2 - \zeta_2^2) + 2i\zeta_1 \zeta_2 \right] d\zeta \end{aligned} \quad (33)$$

It follows from the Eq. (33) and expression for A_1 obtained from the Eq. (16)

$$\frac{L^2 [RG(d, r_m) - iRG(d, \rho_m)]}{A_1 P_m} \approx \frac{\int_{G_1} \left[(\zeta_1^2 - \zeta_2^2) + 2i\zeta_1 \zeta_2 \right] d\zeta_1 d\zeta_2 d\zeta_3}{|G_1|} \quad (34)$$

Consider now regular plane strain states corresponding to holomorphic function $\Psi(\zeta) = 0$.

Let us mark with a superscript s_m a regular elastic field corresponding to the holomorphic functions

$$\Phi(\zeta) = \Phi_m(\zeta) = \mu_M \bar{P}_m \chi_m(\zeta), \quad \Psi(\zeta) = 0 \quad (35)$$

It is possible to show that for big enough m Eq. (6) is reduced to the equation

$$RG(d, s_m) \approx \int_{G_1} (\Delta \sigma_{11}^{I1} e_{11}^{s_m} + \Delta \sigma_{22}^{I1} e_{22}^{s_m} + 2\Delta \sigma_{12}^{I1} e_{12}^{s_m}) d\xi \quad (36)$$

It follows from the Eqs. (24), (32), (35) and the supposition of smallness of the domain G_1 that inside the domain the following approximation is valid

$$\Phi_m(\zeta) \approx \mu_M |P_m|^2 \quad (37)$$

Denote $\chi'_m(0) = D_m$. The derivative of the function $\Phi_m(\zeta)$ can be approximated inside the domain G_1 by the following expression

$$\Phi'_m(\zeta) \approx \mu_M \bar{P}_m D_m \quad (38)$$

It follows from the Eqs. (10), (37) and (38)

$$e_{11}^{s_m} + e_{22}^{s_m} \approx 2(1 - 2\nu_M) |P_m|^2, \quad e_{22}^{s_m} - e_{11}^{s_m} + 2ie_{12}^{s_m} \approx 0 \quad (39)$$

From the Eqs. (36) and (39) one has

$$RG(d, s_m) = (1 - 2\nu_M) |P_m|^2 (\Delta \sigma_{11}^{I1} + \Delta \sigma_{22}^{I1}) |G_1| \quad (40)$$

Using the value A_1 and equation (40) it is possible to calculate the values

$$\Gamma_{\alpha\beta} = \Delta \sigma_{\alpha\beta}^{I1} |G_1|, \quad \alpha = 1, 2, \quad \beta = 1, 2 \quad (41)$$

Let us mark with a superscript h_m a regular elastic field corresponding to the holomorphic functions

$$\Phi(\zeta) = \Phi_m(\zeta) = \mu_M \bar{P}_m H_m(\zeta), \quad \Psi(\zeta) = 0 \quad (42)$$

where the function $H_m(\zeta)$ was defined in Eqs. (24), (25).

Let us assume again that the value m is big enough such that Eq. (6) is reduced to equation analogical to Eq. (36). It follows from the Eqs. (32) and (42) that inside the domain G_1 the main terms of asymptotical expansions of the functions $\Phi_m(\zeta)$ and $\Phi'_m(\zeta)$ have the form:

$$\Phi_m(\zeta) \approx \mu_M |P_m|^2 \zeta^2 L^{-2}, \quad \Phi'_m(\zeta) \approx 2\mu_M |P_m|^2 \zeta L^{-2} \quad (43)$$

From the Eqs. (10), (42) and (43) one has

$$\begin{aligned} e_{11}^{h_m} + e_{22}^{h_m} &= 2(1 - 2\nu_M) |P_m|^2 L^{-2} (\xi_1^2 - \xi_2^2), \\ e_{22}^{h_m} - e_{11}^{h_m} &= 2 |P_m|^2 L^{-2} (\xi_1^2 + \xi_2^2), \quad e_{12}^{h_m} = 0 \end{aligned} \quad (44)$$

It follows from the Eqs. (41), (44) and Eq. (36) where the superscript s_m is substituted with a superscript h_m

$$\begin{aligned} RG(d, h_m) &= \frac{2|P_m|^2}{L^2|G_1|} \left\{ \left[(1 - \nu_M)\Gamma_{22} - \nu_M\Gamma_{11} \right] \int_{G_1} \xi_1^2 d\xi + \right. \\ &\quad \left. + \left[\nu_M\Gamma_{22} - (1 - \nu_M)\Gamma_{11} \right] \int_{G_1} \xi_2^2 d\xi \right\} \end{aligned} \quad (45)$$

Consider now a regular elastic field marked with superscript κ_m and determined by the following holomorphic functions:

$$\Phi(\zeta) = \Phi_m(\zeta) = i\mu_M \bar{P}_m H_m(\zeta), \quad \Psi(\zeta) = 0 \quad (46)$$

Using the same reasoning as above one obtains

$$\begin{aligned} RG(d, \kappa_m) &= \frac{2|P_m|^2}{L^2|G_1|} \left\{ -(1 - 2\nu_m)(\Gamma_{11} + \Gamma_{22}) \int_{G_1} \xi_1 \xi_2 d\xi + \right. \\ &\quad \left. + \Gamma_{12} \int_{G_1} (\xi_1^2 + \xi_2^2) d\xi \right\} \end{aligned} \quad (47)$$

Using Eqs. (34), (41), (45), (47) and supposition $A_i \neq 0$ it is possible to calculate values

$$Z_{\alpha\beta}^1 = \frac{5}{|G_1|} \int_{G_1} \xi_\alpha \xi_\beta d\xi, \quad \alpha = 1, 2, \quad \beta = 1, 2 \quad (48)$$

Considering projections on the planes x_2x_3 and x_3x_1 one can calculate all the values

$$Z_{ij}^1 = \frac{5}{|G_1|} \int_{G_1} \xi_i \xi_j d\xi, \quad i = 1, 2, 3, \quad j = 1, 2, 3 \quad (49)$$

Let us construct a matrix $\mathbf{Z}^1 = (Z_{ij}^1)$. As it was shown in [14], the eigenvalues of the matrix \mathbf{Z}^1 equal $(a_1^1)^2$, $(a_2^1)^2$ and $(a_3^1)^2$, where a_j^1 ,

$j=1,2,3$ are the semiaxes of the ellipsoid G_1 . The corresponding eigenvectors are directed along the axes of the ellipsoid.

In a similar way it is possible to identify the geometrical parameters of other ellipsoidal defects G_k , $k=2,\dots,n$.

5. NUMERICAL EXAMPLES

In all numerical examples considered below the direct Neumann problem for an elastic body V subjected to the loads \mathbf{t}^d is considered and displacements \mathbf{u}^d are calculated on the boundary ∂V using FEM. After that the corresponding values of the RGF are calculated. Using calculated values of the RGF the number of defects and their geometrical parameters are determined using the results obtained in Sections 3, 4.

In all numerical examples the Poisson ratio of the matrix is $\nu_M = 0.25$, the Young's modulus is $E_M = 2\mu_M(1 + \nu_M) = 200 \text{ GPa}$. The load parameter is $\sigma = 200 \text{ MPa}$.

5.1 Determination of the number of defects and coordinates of their centers

An approach for determination of the number of defects was described in Section 3. To explore the accuracy of such approach some numerical examples are considered below.

Let us assume in the first example that elastic body V is a cube $\{x: |x_i| < 10, i=1,2,3\}$. The loads \mathbf{t}^d applied to the boundary ∂V are chosen correspond to uniaxial tension in the direction of the axis x_1 (see Figure 1)

$$\mathbf{t}^d(x) = (\sigma n_1(x), 0, 0), x \in \partial V \quad (50)$$

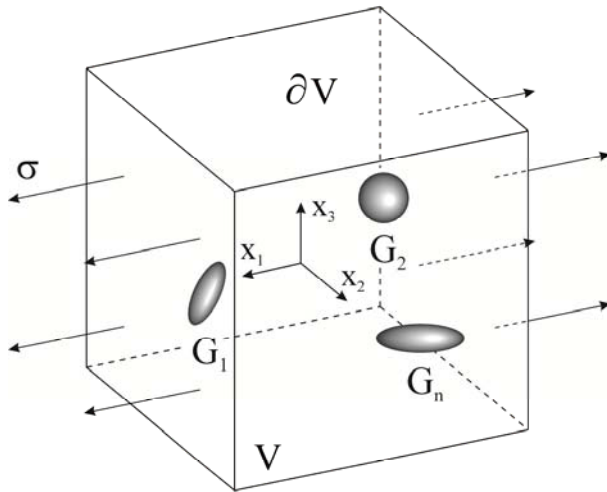


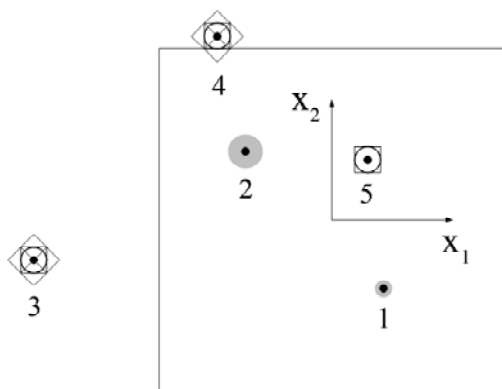
Figure 1. A cube with embedded ellipsoidal defects subjected to uniaxial tension

Let us consider a case of two spherical cavities with the centers at points $x^1 = (3, -4, 5)$, $x^2 = (-5, 4, -3)$ and radii $r_1 = 0.5$, $r_2 = 1.0$ (see Figures 2, 3). Here and below the projections of the given defects on the planes are grey dashed on the figures ((a) – plane x_1x_2 , (b) – plane x_1x_3). The projections of the body V are marked with the solid lines.

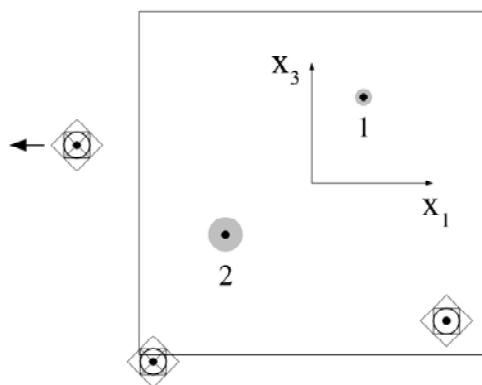
To determine the number of defects n the polynomials $P_N(w)$, defined by Eq. (17), are constructed for different values of the upper bound N in the planes x_1x_2 and x_1x_3 .

The roots of the constructed polynomials $P_5(w)$ and $P_{10}(w)$ are presented on Figure 2 and Figure 3, respectively. The roots w_k , $k = 1, 2, \dots, N$ of the polynomials $P_N(w)$ are marked with the thick points (●) on the figures. The arrows (→) denote the roots located outside the figures bounds.

Among the roots of the polynomials $P_N(w)$ presented on Figures 2, 3 there are some spurious roots which do not correspond to any defects. The spurious roots are excluded using the criteria formulated in Section 3. To illustrate these criteria let us consider for example the roots of polynomial $P_5(w)$ constructed in the plane x_1x_2 (see Figure 2(a)).



(a)



(b)

Figure 2. The roots of polynomials $P_5(w)$ in case of two spherical cavities in a cube

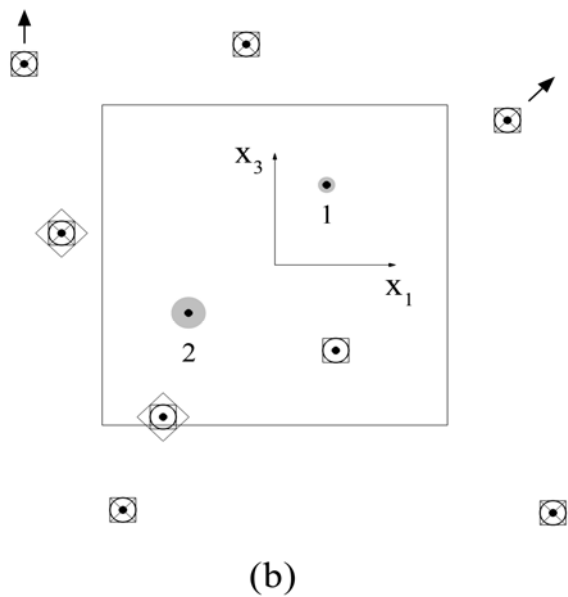
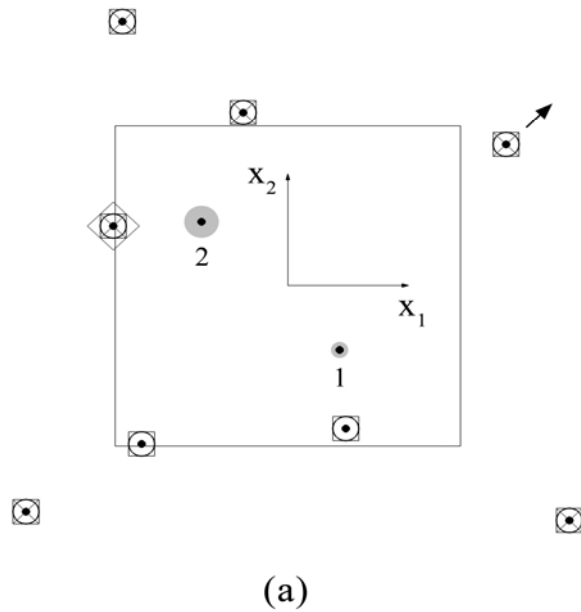


Figure 3. The roots of polynomials $P_{10}(w)$ in case of two spherical cavities in a cube
 The criterion 1 is satisfied for the roots marked with numbers 3, 4 on Figure 2(a) since these roots are located outside of the body projection. We

will mark such roots with the cross symbols (\times) on the figures.

The criterion 2 is satisfied for the roots marked with numbers 3-5 on Figure 2(a) since the values of $|A_k|$ (Eq. (16)) corresponding to these roots are small relative to the values $|A_k|$ corresponding to the roots marked with numbers 1, 2: $A_1 = 0.205 \cdot 10^9$, $A_2 = 0.165 \cdot 10^{10}$, $A_3 = 0.271 \cdot 10^3$, $A_4 = 0.102 \cdot 10^5$, $A_5 = 0.289 \cdot 10^5$. We will mark such roots with the circle symbols (\circ) on the figures.

Comparing the roots of polynomials $P_5(w)$ and $P_{10}(w)$ constructed for $N=5$ and $N=10$ in the plane x_1x_2 (see Figure 2(a) and Figure 3(a)) it is possible to see that the roots marked with the numbers 3-5 on the Figure 2(a) are not stable relative to the chosen value of N . So, the criterion 3 is satisfied for these roots. We will mark such roots with the square symbols (\square) on the figures.

Comparing the roots of polynomials $P_5(w)$ constructed in the planes x_1x_2 and x_1x_3 (see Figure 2(a) and Figure 2(b)) it is possible to see that the roots marked with the numbers 3,4 on Figure 2(a) are not the projections of some points in R^3 (the roots representing a point in R^3 must have the same coordinate x_1 in both considered planes). So, the criterion 4 is satisfied for these roots. We will mark such roots with the rhomb symbols (\diamond) on the figures.

Only the roots of polynomial $P_5(w)$ marked with the numbers 1, 2 on Figure 2(a) do not satisfy any criteria and therefore correspond to the real defects. So, the number of defects $n=2$.

It is shown on the Figure 3 that applying the considered procedure for polynomial $P_{10}(w)$ the same number of defects can be obtained.

Because the number of defects is determined, the centers of the defects projections can be obtained from the roots of the polynomials $P_2(w)$ constructed in planes x_1x_2 and x_1x_3 . In the considered case the roots of these polynomials are almost the same as the roots of polynomials $P_5(w)$ and $P_{10}(w)$ marked with numbers 1, 2 on Figure 2 and Figure 3, respectively, and therefore do not presented on the separate figure. As can be seen, the roots of polynomial $P_2(w)$ are very close to the centers of the given spherical defects projections.

Let us assume in the next example that elastic body V is a hollow cylinder $\{x: 2 < R < 5, |x_3| < 10\}$, where (R, θ, x_3) is the cylindrical coordinates. The loads \mathbf{t}^d applied to the boundary ∂V are chosen correspond to inner pressure in the radial direction (see Figure 4)

$$\mathbf{t}^d(x) = (t_R^d(x), t_\theta^d(x), t_3^d(x)) = \begin{cases} (\sigma, 0, 0), & x \in S_{\text{int}} \\ (0, 0, 0), & x \in \partial V \setminus S_{\text{int}} \end{cases} \quad (51)$$

where S_{int} is the boundary of the hollow $\{x: R = 2, |x_3| < 10\}$. Note, that here and below in the considered example the coordinates of the vectors are given in the cylindrical coordinate system (R, θ, x_3) .

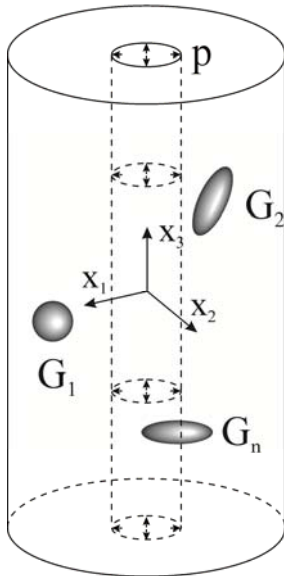


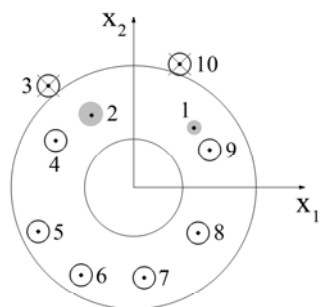
Figure 4. A hollow cylinder with embedded ellipsoidal defects subjected to inner pressure in radial direction

Let us consider as above a case of two spherical cavities with the centers at points $x^1 = (3.5, 45^\circ, 0.0)$, $x^2 = (3.5, 120^\circ, -5.0)$ and radii $r_1 = 0.3$, $r_2 = 0.5$ (see Figure 5).

To determine the number of defects n the polynomials $P_5(w)$ and $P_{10}(w)$ in the planes x_1x_2 and x_1x_3 are constructed. The spurious roots of the polynomials are excluded using the criteria formulated in Section 3.

Let us consider for example the roots of the polynomial $P_{10}(w)$

constructed in the plane x_1x_2 (see Figure 5a).



(a)

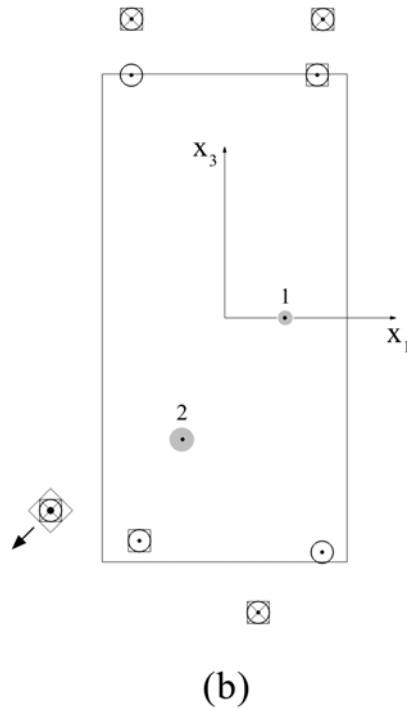


Figure 5. The roots of polynomials $P_{10}(w)$ in case of two spherical cavities in a hollow cylinder

As shown on Figure 5(a), the roots of polynomial $P_{10}(w)$ marked with the numbers 3-10 on the figure satisfy at least one of the formulated criteria and hence are spurious roots. So, the number of defects $n = 2$.

The roots of the polynomials $P_2(w)$ constructed in the considered case are almost the same as the roots of polynomials $P_{10}(w)$ marked with numbers 1, 2 on Figure 5(a) and Figure 5(b) and are very close to the centers of the given spherical defects projections.

Next, let us demonstrate the application of the approach in case of ellipsoidal defects. Assume as in the first example that elastic body V is a cube subjected to uniaxial tension load (50) (see Figure 1). Consider a case of two ellipsoidal cavities with the centers at points $x^1 = (-5, -5, 5)$, $x^2 = (5, 5, -5)$ and volumes $|G_k| = 4\pi/3 \approx 4.189$, $k = 1, 2$ equal to the volume of the unit ball (see Figures 6, 7). Suppose that $\rho_1^1 = 0.25$, $\rho_2^1 = 0.50$ and $\rho_1^2 = 0.50$, $\rho_2^2 = 0.75$, where $\rho_1^k = a_3^k / a_1^k$, $\rho_2^k = a_2^k / a_1^k$ are ellipsoid aspect ratios, a_1^k, a_2^k, a_3^k are semiaxes of the ellipsoid G_k .

Here and below to specify the ellipsoidal defects orientations we will use the Euler angles $(\varphi_k, \theta_k, \psi_k)$, $0 \leq \varphi_k \leq \pi$, $0 \leq \theta_k \leq \pi$, $0 \leq \psi_k \leq \pi$. The definition of used Euler angles $(\varphi_k, \theta_k, \psi_k)$ is given in [16]. Suppose that for considered ellipsoidal cavities $(\varphi_1, \theta_1, \psi_1) = (30^\circ, 45^\circ, 60^\circ)$, $(\varphi_2, \theta_2, \psi_2) = (120^\circ, 135^\circ, 150^\circ)$.

To determine the number of defects n the polynomials $P_5(w)$ and $P_{10}(w)$ in the planes x_1x_2 and x_1x_3 are constructed. The spurious roots of the polynomials are excluded using the criteria formulated in Section 3.

Let us consider for example the roots of the polynomial $P_{10}(w)$ constructed in the plane x_1x_2 (see Figure 6(a)).

As shown on Figure 6(a), the roots of polynomial $P_{10}(w)$ marked with the numbers 5-10 on the figure satisfy at least one of the formulated criteria and hence are spurious roots. Therefore, only the roots marked with the numbers 1-4 should be considered. It can be seen from Figure 6(a) that the distance between the roots 1, 2 is much less than the distances between the roots 1, 3 and 2, 3 (or 1, 4 and 2, 4). Accounting for supposition (1), it can be concluded that the roots 1 and 2 correspond to the projection of the same defect. The same holds for the pair of roots marked with the numbers 3, 4 on Figure 6(a). So, the number of defects $n = 2$.

The roots of polynomials $P_2(w)$ are presented on Figure 7. As can be seen from Figure 7 the obtained roots are very close to the centers of the given ellipsoidal defects projections.

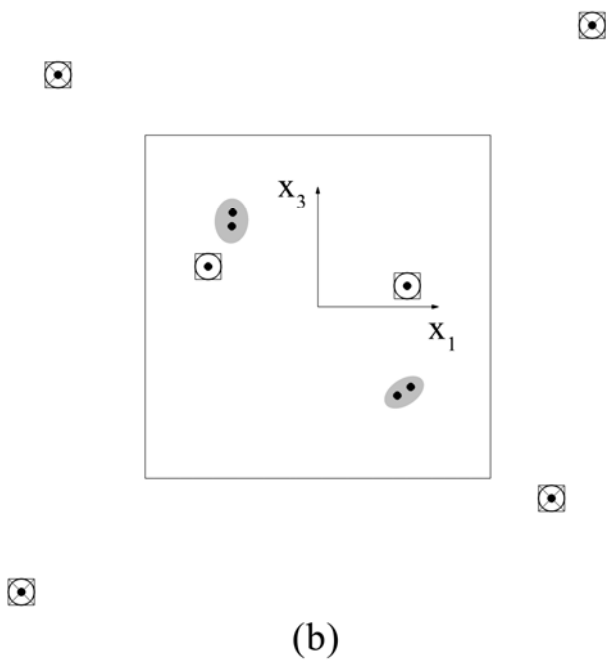
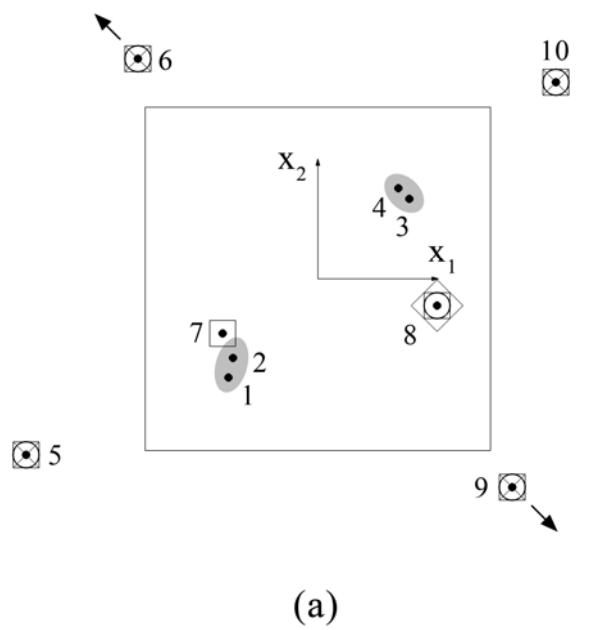
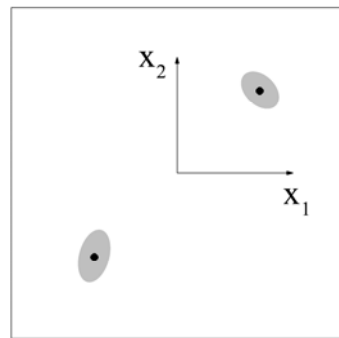
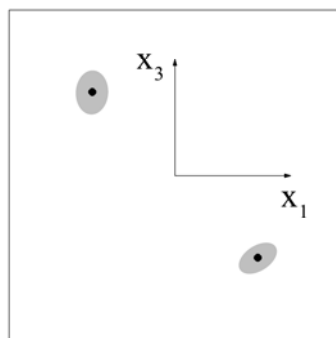


Figure 6. The roots of polynomials $P_{10}(w)$ in case of two ellipsoidal cavities in a cube



(a)



(b)

Figure 7. The roots of polynomials $P_2(w)$ in case of two ellipsoidal cavities in a cube

5.2 Identification of spherical cavities and spherical rigid inclusions

Suppose that the number of spherical defects n and coordinates of their centers

are determined approximately using proposed method. Then the values A_k corresponding to the roots w_k , $k=1,2,\dots,n$ of the polynomials $P_n(w)$ can be calculated from the system of linear equations (16).

It was shown in Section 4 that the radii of spherical cavities and spherical rigid inclusions are calculated directly from the values A_k using Eqs. (19)–(22).

For illustration let us consider the case of two spherical cavities in a cube from Section 5.1 (see Figures 2, 3). The results of identification are presented on Figure 8. Here and below the boundaries of the identified defects projections are marked with the solid lines.

The results presented on Figure 8 demonstrate that the identified defects projections are in exact agreement with the projections of the given spherical defects.

The results of identification presented on Figure 9 demonstrate that the same holds for the case of two spherical cavities in a hollow cylinder from Section 5.1 (see Figure 5).

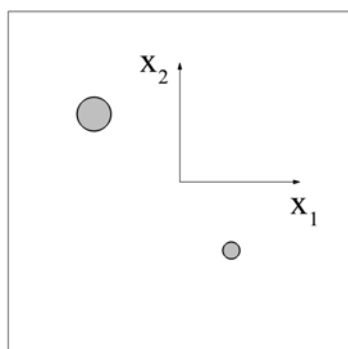
The results of identification of three spherical defects in a cube: two spherical cavities with the same parameters as in the example considered above (see Figure 8) and one spherical rigid inclusion with the center at point $x^3 = (1,1,1)$ and radius $r_3 = 0.25$, are presented on Figure 10.

The results of identification of three spherical defects in a hollow cylinder: two spherical cavities with the same parameters as in the example considered above (see Figure 9) and one spherical rigid inclusion with the center at point $x^3 = (3.5, 240^\circ, 5.0)$ (in the cylindrical coordinate system) and radius $r_3 = 0.4$, are presented on Figure 11.

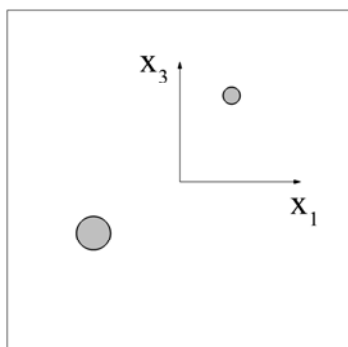
The results presented on Figures 10, 11 demonstrate that in both considered cases the radii of spherical cavities and spherical rigid inclusions are determined with high accuracy using Eqs.(19) – (22).

5.3 Identification of ellipsoidal inclusions

Suppose as above that the number of ellipsoidal defects n and coordinates of their centers are determined approximately using proposed method. Then the magnitudes and directions of the ellipsoids semiaxes can be calculated using the formulas obtained in Section 4.2.

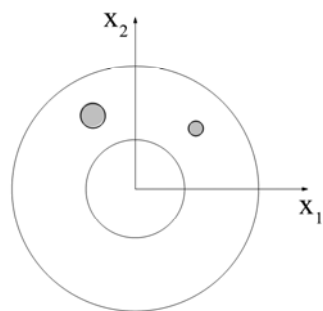


(a)

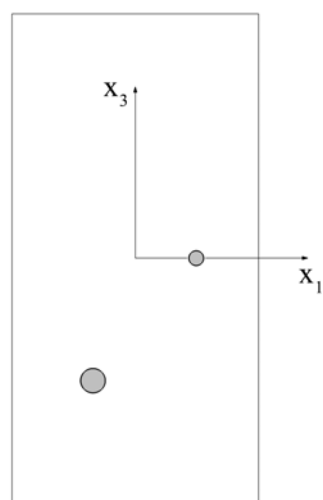


(b)

Figure 8. Identification of two spherical cavities in a cube

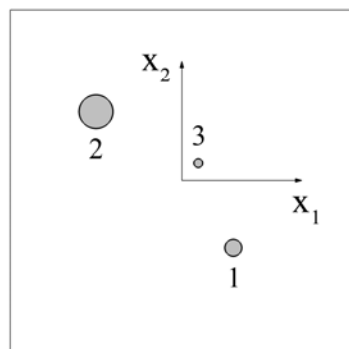


(a)

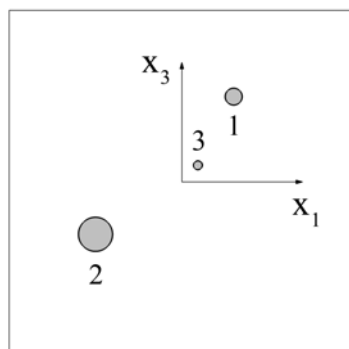


(b)

Figure 9. Identification of two spherical cavities in a hollow cylinder

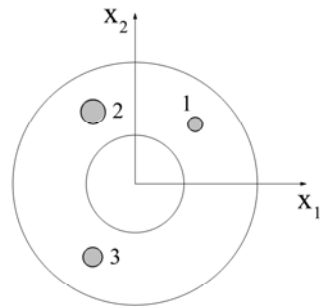


(a)

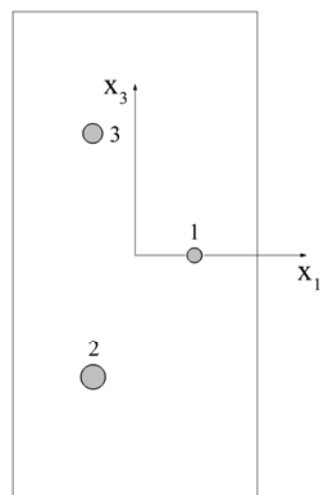


(b)

Figure 10. Identification of three spherical defects in a cube (1, 2 – cavities, 3 – rigid inclusion)

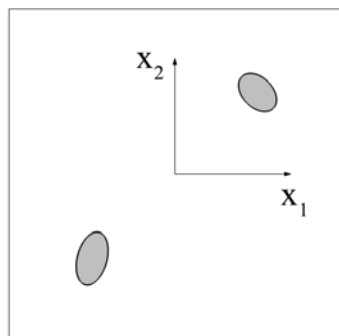


(a)

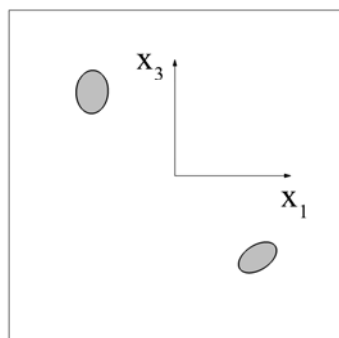


(b)

Figure 11. Identification of three spherical defects in a hollow cylinder (1, 2 – cavities, 3 – rigid inclusion)



(a)



(b)

Figure 12. Identification of two ellipsoidal cavities in a cube

To separate the parameters corresponding to different defects, the polynomial regular elastic fields $r_m, \rho_m, s_m, h_m, \kappa_m$ depending on integer-valued parameter m ($m \geq 3$) are used in the formulas. The values of parameter m are chosen so big as to eliminate the contribution of all terms in the sum on the right side of Eq. (6) except one corresponding to the defect which parameters are determined. It follows from Eq. (29) that the bigger the number of defects n the bigger the value of parameter m should be used to obtain stable identification results.

Let us note that proposed identification method is based on the measurements which are usually subjected to some errors. Increasing the parameter m leads to increasing the degree of the polynomials corresponding to regular elastic fields $r_m, \rho_m, s_m, h_m, \kappa_m$. As consequence, the errors in the calculated values of the RGF corresponding to the fields can also increase. Due to this reason using big values of parameter m for identification of defects requires the measured data with higher accuracy.

In the considered numerical examples the measured data were simulated by FEM. The level of accuracy of such data enabled us to consider only the values of parameter m up to $m = 8$.

For illustration let us consider the case of two ellipsoidal cavities from Section 5.1 (see Figures 6, 7). The identification results obtained for $m = 4$ are presented on Figure 12.

The results presented on Figure 12 demonstrate that for chosen value of parameter m the identified defects projections are in exact agreement with the projections of the given ellipsoidal defects. Using $m = 3$ in the considered case is not enough and leads to big errors in the results of identification.

Let us finally note that the formulas obtained in Section 4.2 are valid not only for ellipsoidal cavities but for inclusions (rigid or linear elastic) also. Moreover, the ellipsoidal defects to be identified can be of different types. The cavities were considered here only as an example.

6. CONCLUSION

A new simple method based on the use of reciprocity gap functional is developed for identification of a finite number of small, well-separated defects (cavities, rigid or linear elastic inclusions) in a 3d isotropic linear elastic body using the results of one static test. The method enables to determine the number of the defects and coordinates of their centers. For

ellipsoidal defects the formulas for determination of the magnitudes and directions of the ellipsoids semiaxes are also obtained. Considered numerical examples demonstrate the efficiency of the developed method.

Acknowledgement

The support of RFBR grant 13-01-00257 is gratefully acknowledged.

REFERENCES

1. H. Ben Ameer, M. Burger, B. Hackl. Cavity identification in linear elasticity and thermoelasticity. *Math. Meth. Appl. Sci.*, 30:625–647, 2007.
2. M. Engelhardt, M. Schanz, G.E. Stavroulakis, H. Antes. Defect identification in 3-D elastostatics using a genetic algorithm. *Optim. Eng.*, 7:63–79, 2006.
3. W.D. Keat, M.C. Larson, M.A. Verges. Inverse method of identification for three-dimensional subsurface cracks in a half-space. *Int. J. Fract.*, 92:253–270, 1998.
4. M. Khoddad, M. Dashti Ardakani. Investigation of effect of different boundary conditions on the identification of a cavity inside solid bodies. *Int. J. Adv. Design Manuf. Technol.*, 4:9–17, 2011.
5. H. Ammari, H. Kang, G. Nakamura, K. Tanuma. Complete asymptotic expansions of solutions of the system of elastostatics in the presence of an inclusion of small diameter and detection of an inclusion. *J. Elasticity.*, 67:97–129, 2002.
6. H. Ammari, H. Kang. *Reconstruction of small inhomogeneities from boundary measurements*. Lecture Notes in Mathematics, 1846, Berlin: Springer-Verlag, 2004.
7. H. Ammari, H. Kang. *Polarization and moment tensors: with applications to inverse problems and effective medium theory*. Applied Mathematical Sciences, 162, New York: Springer-Verlag, 2007.
8. H. Kang, E. Kim, J-Y. Lee. Identification of elastic inclusions and elastic moment tensors by boundary measurements. *Inverse Probl.*, 19:703–724, 2003.
9. G. Alessandrini, A. Bilotta, G. Formica, A. Morassi, E. Rosset, E. Turco. Evaluating the volume of a hidden inclusion in an elastic body. *J. Comput. Appl. Math.*, 198: 288–306, 2007.

10. A. Morassi, E. Rosset. Detecting rigid inclusions, or cavities, in an elastic body. *J. Elasticity*, 73:101–126, 2003.
11. S. Andrieux, A. Ben Abda, H. Bui. Reciprocity principle and crack identification. *Inverse Probl.*, 15:59–65, 1999.
12. P. Steinhorst, A.-M. Sandig. Reciprocity principle for the detection of planar cracks in anisotropic elastic material. *Inverse Probl.*, 28:085010, 2012.
13. R.V. Goldstein, E.I. Shifrin, P.S. Shushpannikov. Application of invariant integrals to the problems of defect identification. *Int. J. Fract.*, 147:45–54, 2007.
14. E.I. Shifrin. Ellipsoidal defect identification in an elastic body from the results of a uniaxial tension (compression) test. *Mech. Solids*, 45:417–426, 2010.
15. E.I. Shifrin, P.S. Shushpannikov. Identification of a spheroidal defect in an elastic solid using a reciprocity gap functional. *Inverse Probl.*, 26:055001, 2010.
16. E.I. Shifrin, P.S. Shushpannikov. Identification of an ellipsoidal defect in an elastic solid using boundary measurements. *Int. J. Solids Struct.*, 48:1154–1163, 2011.
17. E.I. Shifrin, P.S. Shushpannikov. Reconstruction of an ellipsoidal defect in anisotropic elastic solid, using results of one static test. *Inverse Probl. Sci. Eng.*, 2012, <http://dx.doi.org/10.1080/17415977.2012.738677>.
18. E.I. Shifrin, P.S. Shushpannikov. Identification of defects in an elastic body by means of the boundary measurements. *Key Eng. Mater.*, 528:101–110, 2013.
19. A.V. Kaptsov, E.I. Shifrin, P.S. Shushpannikov. Identification of parameters of a plane elliptic crack in an isotropic linearly elastic body from the results of a single uniaxial tension test. *Mech. Solids*, 47:433–447, 2012.
20. H. Kang, E. Kim, J-Y. Lee. Numerical reconstruction of a cluster of small elastic inclusions. *Inverse Probl.*, 23:2311–2324, 2007.
21. L. Baratchart, A. Ben Abda, F. Ben Hassen, J. Leblond. Recovery of pointwise sources and small inclusions in 2D domains and rational approximation. *Inverse Probl.*, 21:51–74, 2005.
22. K. Bryan, R. Krieger, N. Trainor. Imaging of multiple linear cracks using impedance data. *J. Comput. Appl. Math.*, 200:388–407, 2007.
23. M. Hanke, W. Rundell. On rational approximation methods for inverse source problems. *Inverse Probl. Imag.*, 5:185–202, 2011.

24. N.I. Muskhelishvili. *Some basic problems of the mathematical theory of elasticity*. Leyden: Noordhoff, 1977.
25. A. El Badia, T. Ha-Duong. An inverse source problem in potential analysis. *Inverse Probl.*, 16:651–663, 2000.
26. H. Kang, H. Lee. Identification of simple poles via boundary measurements and an application of EIT. *Inverse Probl.*, 20:1853–1863, 2004.
27. J.N. Goodier. Concentration of stress around spherical and cylindrical inclusions and flaws. *J. Appl. Mech. - Trans ASME*, 55:39–44, 1933.

ESTIMATION OF VIBRATING DURABILITY OF ELEMENTS OF HYDRO POWER TURBINES UNDER OPERATING CONDITIONS BY RESULTS OF VIBRATION CONTROL BY STATIONARY SYSTEMS OF VIBRATING MONITORING.

Skvorcov Oleg

Mechanical Engineering Research Institut of the Russian Academy of Science and Diamech 2000 Ltd.

skv@diamech.ru

Abstract: Units and components of the powerful power equipment are exposed to set of the big static and dynamic load. An example of such equipment are turbines hydraulic power plant and, especially, hydroelectric pumped storage power plant. Existing techniques of control of a vibrating condition do not consider: very wide frequency range of vibrating processes, difficult character of such processes in the form of the sum polyharmonic, random and close to shock processes. Such techniques usually do not consider intervals of start-up and stop, and also work on transitive modes when loadings on a construction are maximum. Available techniques of an estimation of admissible level of vibrating influence and tests for vibration durability are not harmonised enough among themselves. Various known interpretations of communication of vibrating characteristics and durability estimations on mechanical pressure at broadband vibrating influence yield ambiguous result. On the basis of the analysis of the published information attempt to formulate the requirement to system of vibrating monitoring of the hydraulic turbine and power motor pumps. System should provide data acquisition and the analysis of the data on a vibrating condition taking into account accumulation of vibrating influences and long term of operation on the basis of estimation methods as low-cycle, and high-cycle (gigacycle) fatigue is made.

Key words: vibrating durability, shock, random, polyharmonic, transitive modes, hydroturbine, acceleration, velocity, displacement, pumped-storage.

It is possible to concern with understanding desire to divide set of processes on separate components for the analysis of the reasons of

occurrence of such components and reaction to them, but it is necessary to consider and that all these components operate simultaneously and probably presence synergy various processes. At the analysis various authors the basic conclusion often is the recognition of that any process is prevailing over others, therefore it is necessary to pay attention to it. Also it is possible to agree with it, but thus it is necessary to take into consideration that cumulative influence of smaller components, or their continuous influence during essentially big intervals of time can appear not less significant.

The estimation of vibrating durability is carried out with use of the data of measurement of vibration on level of acceleration, velocity and moving. All these sizes are interconnected and can be transformed with integration and differentiation use. The measurements equipment forms estimations both average RMS and peak. Such estimations are connected for simple harmonious signals by simple parities. For difficult signals communication between them cannot be presented in simple factor of transformation.

Let's result the short review of methods of an estimation of communication of vibration and stress which are used at carrying out of calculations and tests for vibrating durability.

The classical approach is based on use of the Hook's law connecting pressure and deformations [1,2], fig.1.

$$\sigma = E \cdot \varepsilon = E \cdot \frac{\Delta L}{L} = \frac{E}{L} \cdot \Delta L = k \cdot \Delta L$$

σ - mechanical stress,
 E – Young's modulus (modulus of elasticity),
 ε - relative deformation,
 ΔL – dimensional change.

$$\Delta L(t) = \iint a_1(t)dt - \iint a_2(t)dt = \iint (a_1(t) - a_2(t))dt$$

In [3] for an estimation of the stress:

$$\sigma_{\max}(f) = E \cdot \frac{K(f)}{c_L} \cdot v_{\max}(f)$$

f frequency,
 E Young's modulus,

c_L wave velocity longitudinal wave,
 $v_{max}(f)$ maximum of velocity,
 $K(f) = K'(f) \cdot K_{form}$, a $K'(f)$ - function changing in small limits and defined by the relation private from the maximum stress to the maximum stress in a remote part, to private the maximum velocity in the same areas of the sample, and K_{form} - form factor defined by geometry of the sample.

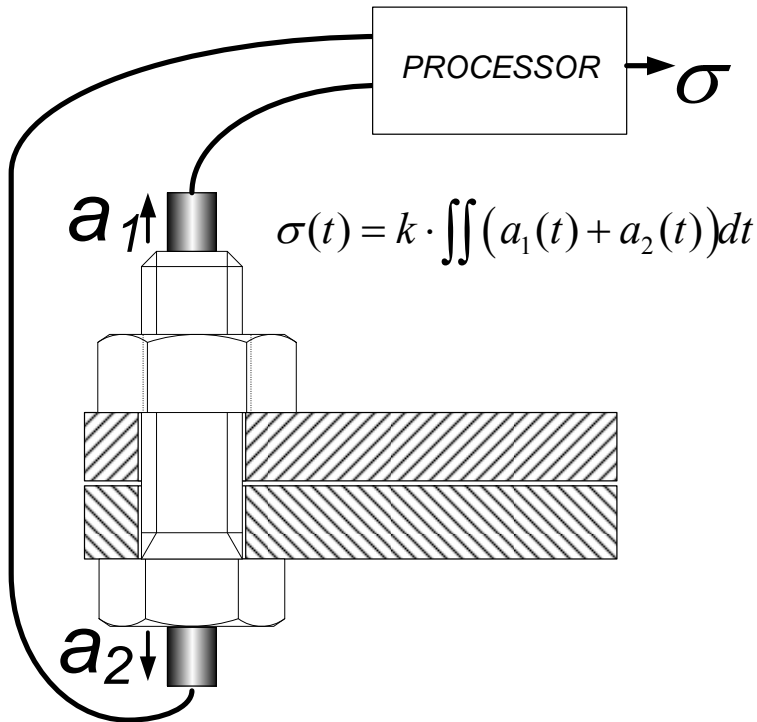


Fig.1.

If vibration is presented by a number of frequencies, the estimation of the general influence corresponds:

$$(\sigma_{max}^2) \leq \sum_{j=1}^{\infty} (\sigma_{max}^2(f))$$

In [3] for an estimation of the maximum stress corresponding to resonant frequencies parities connecting size of static moving $s_{0, max}$ in these

conditions with form factor, good quality Q , speed of a sound also are resulted:

$$\sigma_{n,\max} = \frac{E \cdot K' \cdot K_{form}}{c_L} \cdot 2 \cdot \pi \cdot f_n \cdot Q \cdot s_{0,\max}$$

In [4] the data on change of a limit of fluidity from speed of deformation is cited, it is noticed that faster growth of a limit of fluidity is marked at velocity r when

$$\log_{10}(r) > 4, \text{ and } r \text{ в } I/sec \text{ (Hz)}$$

At high speeds of deformation it is used the $k(N/V)$ calibration r :

$$k = \frac{\int Fdt}{\int Vdt} = \frac{m \cdot \Delta v}{\int Vdt}$$

m - mass,

Δv - velocity variation,

$\int Vdt$ - Integral from voltage from an exit of the gauge of deformation.

That is a direct consequence of the second law of Newton and there is a direct dependence on change of speed i.e. on acceleration.

It is necessary to notice that resulted in [4] data show that at high speeds of deformation, critical values of deformations at which the dependence derivative $\sigma(\epsilon)$ sharply decreases, essentially decreases depending on temperatures in a range $-60 \div +100$ °C, i.e. working temperatures of knots of the hydropower equipment.

In works of Irvin [5] communication of pressure and estimations velocity also is considered. The maximum value of stress at influence on it vibrations depends on its form and for various samples can be presented in a kind:

$$[\sigma]_{MAX} = k \cdot \rho \cdot c \cdot v_{MAX}$$

k – the dimensionless factor, which size is defined by geometry of the sample,

ρ - specific density of a material of the sample,

c – velocity of distribution of waves in a material of the sample,

v_{MAX} – the maximum value of velocity.

At carrying out of tests for vibrating durability the estimation of influence of vibration in the form of acceleration [6] is most widely applied fig.2.

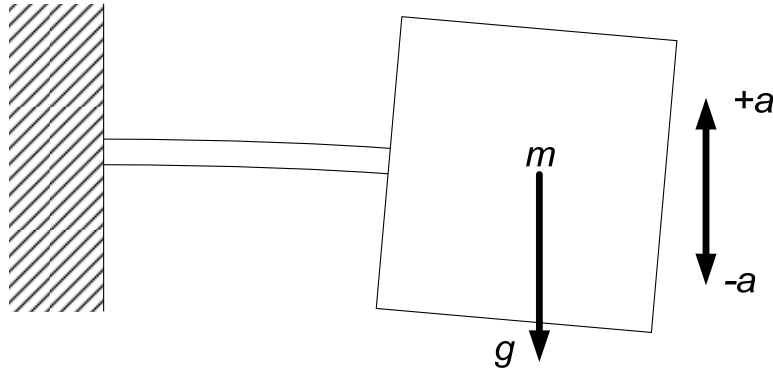


Fig.2.

In this case dynamic stress are defined through the static gravity connected with influence.

$$\sigma = \frac{\sigma_{CT}}{g} \cdot a_M$$

σ - amplitude of mechanical stress,

a_M – absolute acceleration,

g – gravitational acceleration,

σ_{CT} – static mechanical stress from action of static force (gravitation).

Essential advantage of the given approach is possibility to consider simultaneous influence of static and dynamic forces. At influence of dynamic forces transition from typical S-N diagram to analogue with co-ordinates acceleration-number of cycles is possible.

The considered examples show that measurements of essentially different sizes describing vibration are possible. On the one hand control of moving and deformations, and with another of accelerations and connected with

them under Newton's second law of forces. Measurement of velocity is intermediate, but, as appears from the specified references also can be useful.

The basic difference of these approaches to an estimation of level of vibrating influence, at its difficult character is different dependence on frequency. Moving of vibrating character are shown in the field of low frequencies, and in the field of frequencies above several kilohertz of moving are usually smallest. Accelerations, on the contrary, have rather big size in the field of the raised frequencies.

Accelerations of some constructive elements of water-wheels, for example, elements of a cover of the turbine have the considerable levels reaching of several tens g [7].

As moving corresponding to them are rather small, according to representations of the classical analysis of durability connected with deformations or it would seem it is possible to neglect. However in practice at tests for vibrating durability use control in a wide strip of acceleration [8].

Necessity of the account of the high-frequency vibration influencing durability is noted also in [9,10].

In [9] the detailed analysis of the possible reasons of excitation of high-frequency and low-frequency vibration in the field of elements of fastening of a cover of the turbine and results of experimental measuring of dynamic stress in fastening hairpins is resulted. Authors do a conclusion about the greatest contribution to dynamic loadings from high-frequency vibration of the certain frequency connected with influence of vortex of the cavitation von Karman, however it is noticed that the size such dynamic loads is insignificant on absolute size and cannot represent danger from the point of view of development of defects in fastening hairpins. In the given work the detailed analysis of the data about destruction of hairpins of fastening of a cover of the turbine is given also during failure at station Grandee Repids where as a failure principal cause it is specified in possible damage of hairpins during starting-up and adjustment works on the unit when there were raised vibrations. It is important to notice that estimations dynamic stress during the moments of start-up of the unit reach 350 kg/sm^2 that according to the commission investigating failure does not represent danger as total number of such start-up was an order 50000.

Frequency of vortex of the cavitation von Karman:

$$f_K = 0,2 \cdot \frac{v}{t}$$

v - speed motion of vortex,

t - thickness of exit edge.

For the real driving wheel of radially-axial type at $t=0,007$ m, $v = 28,4$ km/s and $f_k = 811$ Hz [10]. Such frequencies are present at a spectrum of vibrations rather low speed water-wheels at measurement on a turbine cover. For more high head and more high-speed turbines essential lifting of level of vibration is observed in a range from 400 Hz to several KHz. As vibration of the hydrodynamic nature connected with vortex flow is casual and its phase continuously changes, on the one hand, lifting on corresponding characteristic frequencies [10] is present at real spectra, and with another corresponding resonant frequencies are not obviously expressed. It does not allow at the analysis of total influence will be limited only to the account of influence of components with certain frequencies.

It is possible to confirm with that in a spectrum each of components does not exceed 0,1g i.e. it is rather small, but the total signal of acceleration taking into account such, enough wide strip has amplitude frequently exceeding 10-15 g. We will notice that according to [10] share high-frequency making pressure in elements of a design of the turbine makes from 40 % to 80 % from size of static pressure which is defined by pressure size. This estimation will well be coordinated with the mentioned experimental data and estimations of a static pressure resulted in table 1 [11].

Table 1.

Hydro power plant	Power for unit, MW	Head, m	Size of runner, m	Mass of unit, metric ton	The pressure force and weight relation
Volga	126	27,0	9,3	1500	1,6
Boguchany	340	69,3	7,5	1250	2,4
Ust-Ilimsk	245	90,0	5,5	800	4,1
Krasnoyarsk	500	100,5	7,5	1250	4,7
Bratsk	255	106,0	5,5	850	4,5
Bureya Dam	333	122,0	6,0	900	5,8
Irganajskaya	205	201,7	4,25	600	8,1
Chirkey	256	207,0	4,5	700	7,7

Sayano– Shushenskaya	650	220	6,77	1400	9,1
Enguri	265	404	4,5	600	19,4
Nurek HEPS	310	275	4,75	850	9,7

Representation of static loading in the form of multiple to weight design rotor parts allows to characterise such estimation in units g, and it simply enough allows to compare it to dynamic loadings, at their estimation on acceleration in units g.

As the remark we will notice that resulted in [9] analysis of possible critical frequencies for hydroelectric power station units Sajano-Shushensky, according to authors, allows not to be afraid of an adverse effect of vortex hydrodynamic influences and corresponds to frequencies above 226 Hz, and gauges used thus, systems of monitoring and a technique of control of a vibrating condition work to frequencies of 200 Hz i.e. if such vibrations and are available actually, regular control devices they cannot be found out.

All it has a direct bearing on the analysis of emergencies and including to failure on Sajano-Shushenskoj of hydroelectric power station, the analysis to which reason causes set of publications [12-16].

Among causes of accident fatigue damages of hairpins of fastening of a cover of the turbine are named. Though the manufacturer assures that прочностные characteristics of such hairpins meet the highest requirements [17]: «High reliability of hairpins of manufacture « Power machines » is confirmed by variety of tests, therefore additional control speaks in a greater degree the psychological factor ...», at other manufacturers can create serious problems as it occurred, for example, at hydrostation Lower Clowhom building in Canada Sechelt, British Columbia [18].

In [9] the way of control of a condition of the fixture, based on comparison velocity for gauges established directly on a hairpin and on a cover about the given hairpin is offered. As such method can be simply enough realised, the given offer represents doubtless practical interest.

As to sizes of the pressure fixed at carrying out of measurements it would be desirable to consider the presented data taking into account following positions:

- Imposings on dynamic loadings of considerable static loadings and the account synergy such influences [27];

- Considering high-frequency character of dynamic loadings and duration of their influence to estimate their influence taking into account positions of behaviour of materials of positions about gycycle durability [28];
- Perform corresponding measurements on start-up of units and on transients.

Operating standard standards on control of admissible level of vibration provide an estimation of current level of scope displacement [19], amplitude or scope displacement [21], and also scope of moving or RMS values velocity [20]. In the publications, levels of maximum permissible vibration concerning a substantiation usually refer to expert methods of admissible level set in standards and what or the account of vibrating history, i.e. accumulation of damages from depending on vibration level is absent. Despite it the analysis of standard base can represent certain interest. Really, as appears from presented to the appendix And [19] schedules depending on frequency of rotation threshold values decrease almost linearly with frequency growth, and it says that that threshold value in a frequency range corresponds to velocity [20], tables of threshold levels of vibration presented in appendix A show that for turbines with greater speed rotation the data displacement reflects vibrating danger less adequately and it is more correct to conduct an estimation of velocity, but also for threshold values of speed for more high-speed turbine is recommended smaller threshold level. In essence it says that that in a wide strip of frequencies dangerous level of vibration is more adequately described in the velocity, and is possible also acceleration.

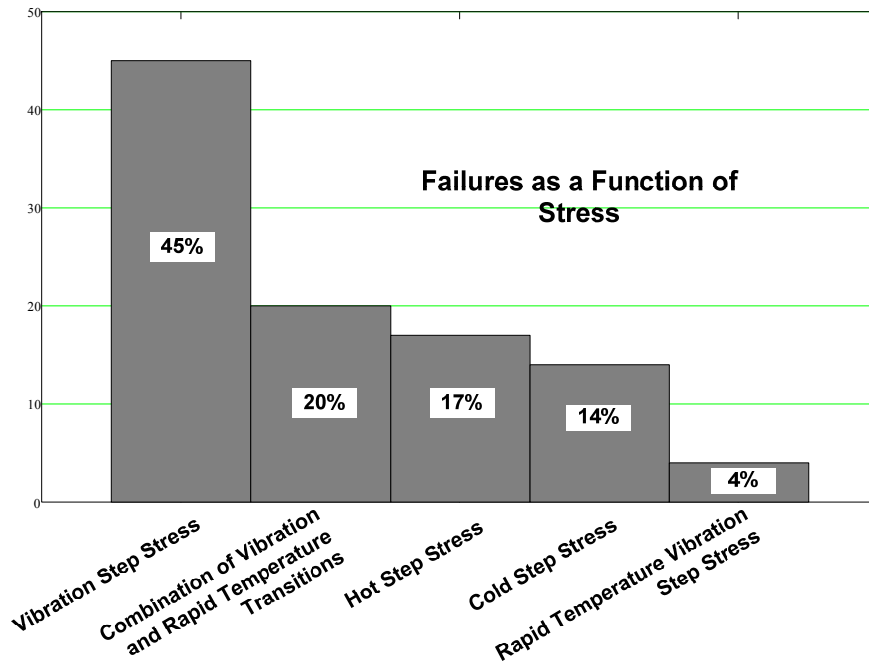


Fig. 3.

In [26] it is recommended for vibration having a frequency spectrum different from one frequency making to use estimations on RMS to value of moving, speed or moving, and for harmonious vibration it is possible as well an estimation of peak value. We will notice that if vibration harmonious peak and RMS values are unequivocally connected among themselves and, hence, the additional estimation of peak value practically loses meaning, and the estimation of peak value is essential to signals with a difficult spectrum when peak value and RMS can strongly differ at a different parity of phases of components summarised in a signal and that is shown at calculation of such important characteristics of a signal as peak-factor, an excess, etc. [7].

Except vibration fatigue durability is influenced also by other reasons, and vibrating influences occupy an important place [29]. On fig.3 the chart distribution cause equipment refusals is presented.

The water hammer phenomenon concerns such processes, in particular. The first has described the given phenomenon Zhukovsky [30].

Overlapping processes penstocks are accompanied by fluctuations of pressure and, accordingly vibrating fluctuations in the form of fading oscillatory processes. The period of fluctuations can is essential will cause a stir from shares of seconds about several seconds, and duration can reach several tens seconds [31,32].

In [33] various examples of behaviour of transients in covers penstocks and a number of emergencies, for example on Oneida Power station in 1984 age are considered. The situation can worsen in connection with formation multiphase water and air mixes, pumping for decrease in probability of formation of cordlike whirlwinds in drainage channels.

A lot of attention in scientific publications [34-37] is constantly given to questions of the analysis of oscillatory processes and shock influence of the current of a liquid connected with changes.

Transients, including the regulations of an operating mode of hydro units connected with process in most cases are shown as the fading oscillatory processes of fading amplitude similar to processes arising at hydro turbine. Amplitudes of fluctuations can reach 20-30 metres of a water column, and frequencies can fall to $\approx 0,1$ Hz.

At an estimation of total influence of various vibrations the rule of linear summation is widely used.

According to a rule of linear summation of damages at influence for i a cycle load with pressure σ_i metal receives damage

$$a_i = \frac{1}{[N]}$$

Where N - average destroying number of cycles at stress σ_i and similar destructions are linearly summarised. In [38] it is noticed that results of calculations received thus do not prove to be true in practice, and received errors can reach 500-1000 % even at a combination only two kinds loads.

Real influences on turbine elements essentially more difficult and thus can not only alternate in time, but also be imposed one on another, for example, static loadings are accompanied dynamic or influence of low-frequency vibration can be combined with high-frequency influence cavitation.

The most critical from the point of view of damages for designs of their metal is development of fatigue cracks at influence of stretching efforts and cyclic loading [39].

Properties of metals essentially change in the course of mechanical influences and a durability estimation strongly depend on "history" loading constructive elements [40].

In [41] it is noticed that the problem of calculation of durability of elements of fastening in water-wheels is actual in connection with numbers of failures on hydroelectric power station of the Dneprovsky cascade (Dneprovsky HAPS-II, the Kiev hydroelectric power station, etc.), but durability calculation is rather difficult and can be spent only at imposing of variety of simplifying restrictions.

The structure of monitoring of high-frequency vibration of the turbine equipment on frequencies 1-100 KHz for the decision of questions of revealing of appearing defects as control on such frequencies allows is typical will get rid of the low-frequency noise masking low vibrations on level, connected with defects [42]. But whether are high-frequency vibrations only convenient means of formation of the diagnostic information or they in itself can have negative destroying influence?

Vibrating process on design elements is generated by operating forces, but it is possible to consider some various cases. In the elementary case of property of a design at its movement also are a direct source of vibration. It for example occurs at presence of a disbalance of a rotating rotor. In the second case exciting force has frequency connected with some processes occurring in the unit. As an example formation of a cordlike current can serve in the drainage channel of the water-wheel. Frequency properties such force can with difficulty depends on a unit operating mode. At last the chance of excitation of fluctuations which can be considered by casual force in some range of frequencies as the white or painted casual noise. Influence of such force on the constructive elements having the certain peak-frequency characteristic generates vibration in the form of narrow-band casual vibration [43]. In the same source in section of the description of testing set broadband vibration in the form of spectral density of acceleration.

On fatigue damages considerable instant loadings which arise on hydro units usual, and even more often hydroelectric pumped storage power plant can be imposed. An example can at hydroelectric pumped storage power plant failure serves in Poland in December 1997 r with destruction water water in the field of directing shovels and connection water water with the spiral chamber [44]. The turbine radially axial with a horizontal arrangement, capacity 1 MW (capacity at the moment of closing of 50 %. The pressure of 13,8 m, the expense of water 22 ^{m³} in second the Machine hall is filled in on 2,5 m the damage Reason – hydro turbine (transitive process at the moment of turn of directing shovels on closing) Is noted low reliability of welded connections in a place of accident connected with poor

quality of welding, long term of operation (more than 70 years) and frequent transients at transitions from pump to a generating mode. During the transition moments - fluctuations with frequency of an order of 2,5 Hz - modelling ADINA. Amplitude of fluctuations of pressure 250-300 KPa, at static pressure to 86 MPa.

At hydro turbine in unit knots there are considerable high-frequency vibrations. High-frequency more than 50 Hz of fluctuation with a delay on 0,2 sek after closing of the channel from 80 to 49 % [45].

Expansion of controllable parameters with inclusion in them of high-frequency accelerations can appear insufficient. Acceleration as controllable size, in particular average quadratic value of acceleration, and also the form of a spectrum of acceleration it is not progressive enough at the decision of problems of an estimation of damages [46].

CONCLUSIONS

1. At carrying out of monitoring of a condition of the difficult equipment which vibrating condition is characterised by vibration in a wide strip of frequencies system of vibrating monitoring should provide control in all such strip of frequencies in a continuous mode with definition of integrated estimations both peak (peak or scope) and statistical (RMS) both, velocity and acceleration.

2. The system of monitoring for the decision of problems of diagnostics and forecasting should provide possibility of the analysis of the information received from primary measuring converters spectral, harmonious, strip, and statistical (the moments of the third and fourth usages), and also the analysis with use of derivatives of the third and fourth usages concerning movings

3. Condition monitoring should be carried out continuously both on stationary modes, and on starting and transitive modes with accumulation of integrated estimations.

4. Working out of primary measuring converters and measuring channels is necessary for maintenance of reliability of the received data providing control in a wide strip of frequencies and in a wide dynamic range with an authentic estimation both polyharmonious, and shock and casual processes.

5. Perfection of methods of an estimation of vibrating durability in the conditions of simultaneous influence static, and also dynamic (and low-frequency and high-frequency) influences of polyharmonious, shock and casual character is necessary.

6. Considering continuous long character of operation of an estimation of vibrating durability should consider features of behaviour of constructional materials and design elements, especially fastening elements in area gygacycle fatigue.

7. As hydroelectric pumped storage power plants in most cases are maintained in with a great number of start-up and остановов, on modes not optimum on capacity and vibration and быстроменяющимся a pressure, and also both in a generation mode, and in a pump mode the expanded monitoring for such units is most actual.

8. Start-up and останов the units, often repeating on storage pumped power plants are often accompanied by shock loadings and modes close to hydro turbines that in turn can generate the response of designs (water waters, drainage pipes, the spiral chamber etc.) on peculiar to them to resonant frequencies in the form of fading oscillatory processes of considerable amplitude. As dynamic loadings in such modes are most considerable it is necessary to be guided by a bottom at fatigue both calculations and forecasting low cycles durabilities.

REFERENCES

1. <http://www.physics.ru/courses/op25part1/content/chapter1/section/paragraph12/theory.html>.

2. A test of Hooke's law. From Walter Lewin (1 October 1999) (in English) (ogg). Hooke's Law, Simple Harmonic Oscillator. MIT Course 8.01: Classical Mechanics, Lecture 10. (videotape). Cambridge, MA USA: MIT OCW. Event occurs at 10:10–16:33. <http://ocw.mit.edu/courses/physics/8-01-physics-i-classical-mechanics-fall-1999/video-lectures/lecture-10/>. Retrieved 23 December 2010.

3. Norton M.P., Karczub D.G. Fundamentals of noise and vibration analysis for engineers. Cambridge university press, 2003, 651 p.

4. Field J. E., Walley S. M., Proud W.G., Goldrein H.T., Siviour C.R. Review of experimental techniques for high rate deformation and shock studies. International journal of impact engineering, 30 (2004), pp.725-775.

5. Irvin Tom. Shock and vibration stress as a function of velocity. 11 december 2012, 68 p. http://www.vibrationdata.com/tutorials2/sv_velocity.pdf

6. A.Lenk, J.Rehnitz. Schwingungsprüftechnik. Veb verlag technik, Berlin, 1974 // Перевод А. Ленк, Ю. Ренитц. Механические испытания приборов и аппаратов., Мир, М., 1976, 272 с.

7. Скворцов О.Б., Трунин Е.С. Автоматизация вибрационной защиты гидроагрегатов. Russia power. HydroVision Russia 2012. 5-7 марта 2012, PennWell, Конференция и выставка. Каталог. Стр.20. <http://pennwell.websds.net/2012/Moscow>

8. Скворцов О.Б. Выбор параметров контроля вибрации для систем непрерывного мониторинга состояния машин и агрегатов. Научные труды II Международной научной конференции "Фундаментальные исследования и инновационные технологии в машиностроении, ИМАШ РАН, 2012, с.412-417.

9. Иванченко И.П., Воеводин С.И. и Прокопко А.Н. Натурные исследования гидродинамических нагрузок, действующих на крепеж крышки турбины. Гидротехника, № 3(28), 2012, с.5-11.

10. Гаврилов С.Н., Георгиевская Е.В., Левина С.М., Смелков Л.Л. Оценка эксплуатационной надежности гидроагрегата с помощью расчетно-экспериментальных исследований на основе сравнительного анализа отечественной и зарубежной литературы. Гидротехника XXI век, №2 (5) 2011, с.28-35

11. Федоров М.П., Елистратов В.В. Авария на Саяно-Шушенской ГЭС и научно-техническое сопровождение ее восстановления. Санкт-Петербургский государственный политехнический университет. <http://www.risk.e-m.ru/10/presentation/fedorov.ppt>. 26 s/

12. Башнин, О. И. Саяно-Шушенская катастрофа - синхронный гидроакустический резонанс / О. И. Башнин // Гидротехническое строительство. - 2012. - № 7. - С. 29-45

13. Берлин, В. В. Исследование резонансных явлений в напорных водоводах и отсасывающих трубах ГЭС / В. В. Берлин, О. А. Муравьев // Гидротехническое строительство. - 2012. - № 7. - С. 46-58

14. Берлин, В. В. О статье В. Н. Тарасова "Гидроупругие колебания агрегатов ГЭС" / В. В. Берлин, О. А. Муравьев // Гидротехническое строительство. - 2012. - № 1. - С. 24-25

15. Лапин, Г. Г. О статьях дискуссионного содержания / Г. Г. Лапин // Гидротехническое строительство. - 2012. - № 1. - С. 2-4

16. Колосов М.А. Надежность направляющего аппарата турбины Саяно-Шушенской ГЭС. Гидротехника XXI век №1 (4) 2011, с.14-17.

17. Денисенко И. Проверили вибрацию и мощность. «Силовые машины» 20 января 2012 года, с. 6.

18. Defective bolts, washers allegedly damage hydro project. Business in Vancouver, June 5, 2012.

19.СТО 17330282.27.140.001-2006 - Методики оценки технического состояния основного оборудования гидроэлектростанций. Некоммерческое Партнерство "Гидроэнергетика России" ОАО "Инженерный центр ЕЭС - Филиал "Фирма ОРГРЭС", М., 2006, 620 с.

20.Международный стандарт ИСО 10816-5:2000 Вибрация. Оценка состояния машин по результатам измерений вибрации на невращающихся частях. Ч. 5. Агрегаты гидроэлектростанций и насосных станций.

21.International standard ISO 7919-5. Second edition, 2005-04-15, Mechanical vibration – Evaluation of machine vibration by measurements on rotating shafts. Part 5: Machine sets in hydraulic power generating and pumping plants. 19 p.

22.СТО РусГидро 02.01.059-2011. Гидроэлектростанции. Мониторинг технического состояния основного оборудования. Нормы и требования. М., 2011, 42 с.

23.ГОСТ ИСО 10816-1-97 Вибрация. Контроль состояния машин по результатам измерений вибрации на невращающихся частях. Часть 1. Общие требования. Минск, 18 с.

24.ГОСТ 28220-89. Испытания. Испытание Fd: Широкополосная случайная вибрация. Общие требования. М., 1989, 17 стр.

25.ГОСТ 26044-83. Вибрация. Аппаратура для эксплуатационного контроля вибрационного состояния энергетических гидротурбинных агрегатов. Общие технические требования.

26.International standard ISO 2954. Second edition, 2012-04-01, Mechanical vibration of rotating and reciprocating machinery – Requirements for instruments for measuring vibration severity. 2012, 14 p.

27.Терентьев В.Ф., Оксогоев А.А. Циклическая прочность металлических материалов. – Новосибирск, Изд-во НГТУ, 2001 г., 61 стр.

28.Claude Bathias, Paul Croce Paris. Gigacycle Fatigue in Mechanical Practice. September 13, 2004 by CRC Press - 328 p.

29.Roy Rivett. N.I.A.R. May 2011. Accelerated Stress Testing. HALT & HASS. 92 p. <http://www.niar.wichita.edu/media/pdf/HALT&HASS-NIAR.pdf>

30.Жуковский Н.Е. О гидравлическом ударе в водопроводных трубах, 1899.

31.Bergant A., Tijsseling A., Vitkovsky J.P., Simpson A.R., Lambert M.F. Discrete vapour cavity model with improved timing of opening and collapse of cavities. 2nd IAHR international meeting of the workgroup on

cavitation and dynamic problems in hydraulic machinery and systems. Timisoara, Romania, October 24-26, 2007, p.117-128

32.Çalamak M., Bozkuş Z. Protective measures against waterhammer in run-of-river hydropower plants/ Digest 2012, December 2012, p. 1623-1636

33.Yadav A., Shaver G. M., Meckl P. Lessons learned : implementing the case teaching method in a mechanical engineering course. Journal of engineering education, 2010, January, p.55-69

34.Bonin C.C. Closure to “Discussions of `Water-Hammer Damage to Oigawa Power Station” (1960, ASME J. Eng. Power, 82, pp. 116–118)

35.Bergant A., Simpson A.R., Tijsseling A.S. Water hammer with column separation^ a historical review. Journal of fluids and structures, 22 (2006) p. 135-171/

36.Adamkowski A., Levandowski M. A New method for numerical prediction of liquid column separation accompanying hydraulic transients in pipelines. Journal of fluids engineering, july 2009, vol.131, 11 p.

37.Simmari N.M.B Modelação numerica de transients hidráulicos em circuitos de usinas hidrelétricas. Porto Alegre, Janeiro, 2006, 129 p.

38.Вереземский В.Г. К II годовщине трагедии на СШ ГЭС. Версия причины и начала аварии. Атомная стратегия XXI. №59, октябрь 2011, с.33.

39.Стрижиус В.Е. Основные положения методов расчета усталостной долговечности элементов авиаконструкций из ПКМ. ООО «Прогрестех». М., 11 с.

40.Багмутов В.П., Савкин А.Н. Сравнительный анализ моделей накопления рассеянных повреждений в металле при нерегулярной переменной нагруженности. Проблемы прочности». 6(402), 2009 г. Стр.95-104.

41.Евдокимов Н.Н., Степченко А.С., Трубаев А.И. Моделирование напряженно-деформированного состояния болтового соединения рабочего колеса гидротурбины на основе 3D модели. Сборник научных трудов «Вестник национального технического университета «ХПИ»» № 49, 2009, Динамика и прочность машин, Харьков. С.48-67.

42.Wattson M., Sheldon J., Amin S. Lee H., Byington C., Begin M. A comprehensive high frequency vibration monitoring system for incipient fault detection and isolation of gear, bearings and shifts/couplings in turbine engines and accessories. Proceedings of GT2007 ASME Turbo Expo 2007, Power for land, sea and air, may 14-17,2007, Montreal, Canada, 10 p.

43. Harris' shock and vibration handbook. Sixth Edition. By: Piersol, Allan G.; Paez, Thomas L. McGraw-Hill, 2010, 1225 p.

44. Adamkowski A. Case study: Lapino powerplant penstock failure. Journal of hydraulic engineering, july, 2001, p.547-555.

45. Sharefi B. R., Zhou W., Glemmestad B., Lie B. The effect of compressibility of water and elasticity of penstock walls on the behavior of a high head hydropower station. SIMS 2011. The 52nd international conference of Scandinavian simulation society, 29-30 september 2011, 31 p.

46. John Van Baren, Philip Van Baren. The third dimensional of random vibration control. Vibration Research Corporation, Jenison, MI, 19 p.
http://www.vibrationresearch.com/public_pdf/The_Third_Dimension_of_Random_Vibration_Control.pdf

CONTINUUM MODELLING OF TRAP-AFFECTED HYDROGEN DIFFUSION IN METALS

Jesús Toribio and Viktor Kharin

University of Salamanca, Campus Viriato, 49022 Zamora, Spain

toribio@usal.es

Abstract: Hydrogen transport by diffusion is a key issue in any environmentally assisted cracking process in metals and alloys since hydrogen may be present in the material due to external sources or because of electrochemical reactions (cathodic discharge) in the vicinity of the crack tip due to local electrochemical conditions promoting acidification and cathodisation in relation to the global (bulk) conditions. In this framework, diffusion is a relevant transport mode to drive hydrogen to the prospective fracture nuclei, thereby producing the damage phenomenon of hydrogen embrittlement in the material. The present paper offers a continuum modelling of trap-affected hydrogen diffusion in metals and alloys, accounting for different physical variables of both macroscopic nature (i.e., related to continuum mechanics, e.g., stress and strain) and microscopic characteristics (material microstructure, traps, etc.). To this end, the model of hydrogen diffusion assisted by the gradients of both hydrostatic stress and cumulative plastic strain, stress-and-strain assisted hydrogen diffusion, proposed and frequently used by the authors of the present paper (Toribio & Kharin) is analysed and compared with other well-known models such as those proposed by (i) McNabb & Foster, (ii) Oriani, (iii) Leblond & Dubois, (iv) Sofronis & McMeeking, (v) Krom & Bakker, showing their mathematical ability to account for different physical variables. Emphasis is placed on the different approaches (implicit and explicit) to formulate the diffusion-with-trapping model, i.e., the consideration of hydrogen traps (both reversible and irreversible) in the different diffusion models. Previous models of hydrogen diffusion are advanced and generalized, so that rigorous and innovative equations are formulated by the authors for the continuum modelling of trap-affected hydrogen diffusion in metals, on the basis of sound mathematical foundations.

Key words: Hydrogen assisted fracture, Hydrogen diffusion, Modelling.

1. INTRODUCTION

Hydrogen is often the key factor in environmentally assisted fracture (EAF) of metals, as it may be present *per se* in the environment or discharge in the vicinity of a crack tip due to a favourable local electrochemistry [1]. Damaging effects of hydrogen on metals (“hydrogen embrittlement”) form the long-standing problem of the mechanics of materials. Hydrogen transport to damage sites is a key component of hydrogen embrittlement, which is rate-limited by hydrogen transport to prospective fracture places. A series of kinetic processes involved in HAF have been identified, among which hydrogen diffusion has been substantiated as the governing mode of hydrogen supply to fracture nuclei [1-3]. Continuum modelling of hydrogen diffusion has been focused as the key issue of HAF studies and their engineering applications [1,3-6].

Concerning hydrogen behaviour in metals, important disconformities [2,7,8] were witnessed between experience and the Fick’s diffusion laws. Various issues have been pointed out as potential causes of these inconsistencies, and several analyses have been performed culminating in continuum mechanics equations of diffusion formulated from microscopic or phenomenological bases [1,4-11]. However, comprehensive consideration of the wide variety of potentially influencing factors is a very complicated task, so that specialised diffusion models, including different microstructural features, have been formulated in the past [8]. This paper goes further in the continuum modelling of hydrogen diffusion in metals, providing rigorous and innovative diffusion equations (including hydrogen trapping) on the basis of sound mathematical foundations

2. HYDROGEN ASSISTED FRACTURE (HAF) THEORY

Hydrogen assisted fracture (HAF) is a result of synergic action of stress, strain and hydrogen amount in material [1,5]. Fracture event takes place in a locus identified by a position vector \mathbf{x} , when hydrogen concentration C accumulated there over time t reaches the critical level C_{cr} dependent on stress-strain state:

$$C(\mathbf{x}, t) = C_{cr}(\boldsymbol{\sigma}(\mathbf{x}, t), \boldsymbol{\varepsilon}_p(\mathbf{x}, t)), \quad (1)$$

where $\boldsymbol{\sigma}$ y $\boldsymbol{\varepsilon}_p$ are, respectively, the tensors of stress and plastic strain.

The condition of contact between the concentration and the critical surfaces, $C(\mathbf{x},t)$ and $C_{cr}(\mathbf{x},t)$, respectively,

$$\partial C(\mathbf{x},t)/\partial \mathbf{x} = C_{cr}(\boldsymbol{\sigma}(\mathbf{x},t), \boldsymbol{\varepsilon}_p(\mathbf{x},t))/\partial \mathbf{x}, \quad (2)$$

accompanies the fracture criterion (1) to form the system of equations to define the location \mathbf{x}_{cr} and time t_{cr} of HAF event [12]. Hydrogen transport towards fracture sites is dominated by diffusion, which defines the left-hand parts of Eqs. (1) and (2).

Material damage is associated with crystal imperfections, and that they act as hydrogen traps (T-sites) for H atoms where their free energies G_T are less than that for ordinary lattice (L-)sites G_L (Fig. 1a). The ratio at.H/at.Me can there substantially exceed that in L-sites [2,3,4,6], as follows from the equilibrium partition of hydrogen between T- and L-sites [2,4,6,13]:

$$\frac{\theta_T}{1-\theta_T} = \frac{\theta_L}{1-\theta_L} K \quad (K = e^{\beta E_b}), \quad (3)$$

where $\theta_X = C_X/N_X$ is hydrogen saturation of X-type sites ($X = L$ or T) defined by volume concentrations of these sites in metal, N_X , and of hydrogen allocated to them, C_X , so that the total concentration $C = \Sigma C_X$, $E_b = G_L - G_T$ is the binding energy of hydrogen to trap, and $\beta = (RT)^{-1}$ is the Boltzmann's factor in terms of the gas constant R and temperature T . Then, e.g., for steels at usual HAF occurrence conditions $T \approx 300$ K and $\theta_L \sim 10^{-6}$ at utmost [3,6], reported values of E_b , being approximately in the range from 0.25 to 1.5 eV [2,14,15] yield $K \geq \sim 10^4$ and $\theta_T/\theta_L \geq \sim 10^4$.

To this end, whenever L/T-partition of hydrogen in volume element $d^3\mathbf{x}$ around a point \mathbf{x} is in equilibrium, all partial concentrations $C_i(\mathbf{x},t)$ ($i = 1,2,\dots$) are related one to another via Eq. (3), so that all them, including the one corresponding to crystal imperfections responsible for HAF micro-mechanism, are biunivocally related to the total one $C(\mathbf{x},t)$. In this case, continuum description of local HAF event by Eqs. (1)-(2) holds, as well as it may be rewritten explicitly in terms of the responsible partial concentration C_X merely by changing there the variable according to Eq. (3). Otherwise,

HAF should be described taking in Eqs. (1)-(2) responsible concentration C_X instead of C , and accounting for L/T-exchange kinetics in analysis of hydrogen transportation.

At any rate, hydrogen delivery to fracture sites proceeds by thermally activated hopping of H atoms between available sites in metal, i.e., by diffusion that turns out to be affected by trapping [2,4,6,7,10,13]. In this context, diffusion modelling is crucial for HAF analysis, prediction and control, as far as, combining with HAF experiments able to reveal fracture initiation time t_{cr} and location x_{cr} , this allows to specify the critical concentration $C_{cr}(\sigma, \epsilon_p)$, i.e., the fracture criterion (1), and to employ this criterion for assessment of fracture time of structures [12,16].

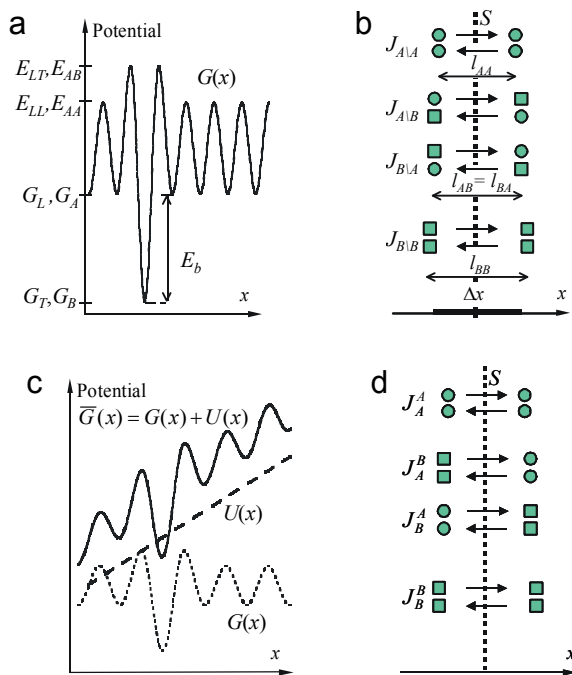


Figure 1. Schematics of (a) potential-position trace $G(x)$ for H in a lattice with different type sites L and T (or A and B); (b) combination of diffusion jumps between sites of different kinds (A – circles, B – quads) to evaluate partial fluxes; (c) distortion of lattice potential $G(x)$ by superposed field U ; (d) combination of hops to establish partial balances.

3. CONTINUUM MODELLING OF TRAP-AFFECTED HYDROGEN DIFFUSION: REVIEW OF PREVIOUS MODELS

Both atomistic and thermodynamic arguments have been used to derive diffusion equations [1,4-11,13,15]. These approaches are not contradictory, but complementary [11] and able to converge into the same field equations with certain insights about specific factors. Concerning traps, they were incorporated into resulting field equations in some cases via plausible postulates [4,6,7,17], but not from background principles (excepting few attempts with limited offspring [10,18,19] for HAF). In this paper, diffusion equations grounding upon diffuser jumps probabilities are revisited.

3.1. Flux Equations

Isothermal diffusion by particles hopping among sites of kinds A and B is considered here by adopting the techniques used elsewhere [11,13,15,18-20]. Concerning the flux of the species through unit surface S normal to x -axis and situated there at position x , eight possible elementary steps can be grouped in pairs as shown in Fig. 1b, where l_{IJ} ($I, J = A$ or B) are jump distances between specified sites, so that each couple renders the net flux J_{AB} by forth and back hops between trans-boundary A and B sites, which are here diffuser releasers and receptors, respectively. The transition frequency Γ_{AB} from A-sites located at x' to B-ones at x'' per unit time depends on attempt frequency Ω_{AB} controlled by particle vibration frequency at given site ω_{0A} and by potential barrier $\Delta E_{AB} = E_{AB} - G_A$, where E_{AB} is the free energy at saddle point of lattice potential $G(x)$ between A and B (Fig. 1a). The frequency of successful hops depends on combined probability Y_B , which merges the probabilities γ_B that encountered receptor sites are the B-type ones and Θ_B that they are empty, that is

$$\Gamma_{AB} = [\Omega_{AB}]_{x'} [Y_B]_{x''} \text{ at } \Omega_{AB} = \omega_{0A}^x \exp(-\beta \Delta E_{AB}),$$

$$Y_B = \gamma_B \Theta_B, \gamma_B = N_B/N, \Theta_B = 1 - \theta_B, \quad (4)$$

where $\omega_{0A}^x = \omega_{0A} f_A^x$ to reckon up the fraction f_A^x of hops contributing to the flux through S having directions towards it, and $N = \sum N_i$ is the volume concentration of all available sites (process parameters f_A , l_{AB} and ΔE_{AB} , according to the crystal symmetry, can depend on the x -axis orientation in

relation to the lattice, thus causing diffusion anisotropy. They are isotropic, e.g., for interstitial sites in cubic lattice, and can be for “spherical” point-wise defects there, yielding $f_A = f = 1/6$ irrespectively of orientation.) Jump probability to any site is assumed to be not conditioned by that to another.

When some imposed potential field $U(x)$ distorts the lattice relief $G(x)$, see Fig. 1c, ΔE_{AB} depends on the jump sense, which biases the hopping probabilities. This implies the modification of the hopping frequency (4) with the factor $\exp(\pm 1/2 \beta \Delta x \nabla_x U)$, where the lower/upper sign corresponds to jumps pro-/counter-wise the x -direction, $\Delta x = x' - x''$, and ∇_x indicates the x -component of the gradient.

Reckoning up the hops of particles from A to B sites through control surface S at position x , using Taylor series expansions of involved variables about x with respect to Δx and truncating them at the second term, the net partial transfer by forth and back A→B jumps can be obtained

$$\mathbf{J}_{AB} = -d_{AB} \{Y_B \nabla C_A - C_A (\nabla Y_B - \beta Y_B \nabla U)\}, \quad (5)$$

where the diffusivity $d_{AB} = \Omega_{AB} l_{AB}^2$ when $\Delta x = l_{AB}$ is taken. The total diffuser flux vector \mathbf{J} is the sum of the net partial ones \mathbf{J}_{AB} over all pairs of site kinds A and B, which reads:

$$\mathbf{J} = \sum_{A,B} \mathbf{J}_{AB} = - \sum_{A,B} d_{AB} Y_B C_A \nabla \ln(e^{\beta U} C_A / Y_B). \quad (6)$$

This holds for arbitrary number m of site types, e.g., the L-sites and $(m - 1)$ kinds of traps T_i ($i=1, \dots, m - 1$). Presented flux equations advance those derived elsewhere [18] in that arbitrary occupation degrees θ_i ($i = 1, \dots, m$) towards saturation are here admitted for all kinds of sites, and that alteration of lattice potential relief by some superposed field $U(x)$ is taken into account.

Description of diffusion in terms of specified partial fluxes can be supplemented with mass-balance relation being now the usual continuity equation in the following form:

$$\frac{C(\mathbf{x}, t)}{\partial t} = -\nabla \cdot \mathbf{J} \left(= \nabla \cdot \sum_{A,B} d_{AB} Y_B [\nabla C_A - C_A \nabla \ln(e^{-\beta U} Y_B)] \right). \quad (7)$$

3.2. Mass Balance

In contrast to the one-level system (single kind of sites), Eq. (7) does not accomplish description of diffusion in terms of concentrations C_i ($i = 1, \dots, m$) for the m -level case ($m > 1$) where a system of m balance equations must be built up. This requires to combine the same diffusion steps as shown in Fig. 1d to gather all forth and back jumps across S that fill/vacate the sites of the sort A in a region Δx around a point x by surmounting saddle points at $x \pm \Delta x/2$. Desired equations are derived here following the random walk theory and its continuum implementation [19,20].

Considering two-level system and addressing the net species supply into A-sites in a domain Δx by overcoming saddle point at $x - \Delta x/2$ from all outer A- and B-sites, involved diffusion steps include the net income flux $J_{A\Delta}$, and the resulting B \rightleftharpoons A-exchange flux, which is as follows:

$$J_A^B = \left\{ e^{-\frac{1}{2}\beta\Delta x\nabla_x U} [C_B l_{AB} \Omega_{BA}]_{x-\Delta x} [Y_A]_x - e^{\frac{1}{2}\beta\Delta x\nabla_x U} [C_A l_{AB} \Omega_{AB}]_x [Y_B]_{x-\Delta x} \right\}. \quad (8)$$

The net exit from A-sites in a domain Δx towards all sites beyond $x + \Delta x/2$ is defined similarly. Then, balancing transitions at both extremes of Δx , using power series expansions and disregarding higher order terms with Δx , mass balance for the species dwelling in A-sites can be derived.

However, calculations in general terms are overly long and tedious, so that now we content ourselves with particular case when the sites characteristics are isotropic and uniform, i.e., jump frequencies $\Omega_{..}$ and lengths $l_{..}$ are constant, for which the following is deduced:

$$\begin{aligned} \frac{\partial C_A}{\partial t} = & d_{AA} \nabla \cdot [Y_A C_A \nabla \ln(e^{\beta U} C_A / Y_A)] + d_{BA} Y_A \nabla \cdot [C_B \nabla \ln(e^{\beta U} C_B)] - \\ & - d_{AB} C_A (\nabla^2 Y_B - \beta \nabla Y_B \cdot \nabla U) + [k_{BA} C_B (N_A - C_A) - k_{AB} C_A (N_B - C_B)], \end{aligned} \quad (9)$$

where $k_{AB} = f^{-1} \Omega_{AB} / N = d_{AB} / (f N l_{AB}^2)$. Similarly, balance for a diffuser dwelling in B-sites can be derived rendering the result that differs from Eq.

(9) by permutation of the site labels A and B. This description is extensible for arbitrary number m of site types by taking in the right-hand part of Eq. (9) the sum over all site kinds from a set $\{B; B \neq A\}$. The last term in brackets in Eq. (9) represents transitions between the nearest neighbour sites of different types in a volume $d^3 \mathbf{x}$ around a point \mathbf{x} .

This way, the system of nonlinear differential equations (9) is derived for partial concentrations C_i ($i=A, B, \dots$ or $1, \dots, m$). Balance in terms of total concentration $C = \sum C_i$ can be obtained summing up the equations of the system (9) over site kinds totality $\{A\}$. After all, the result coincides with that expressed in Eq. (7).

One may notice here the similarity with equations built up by Leblond-Dubois [10] following distinct approach based on construction of Boltzmann type transport equations. Present derivation advances the previous one [19] with respect to the sites saturability, their concentrations non-uniformity, and the contribution of a field U .

3.3. Equilibrium

The chemical potential μ_A of hydrogen residing in metal in sites of whichever type A is [13,15]

$$\mu_A(\theta_A) = \bar{G}_A + RT \ln(\theta_A / (1 - \theta_A)), \quad (10)$$

where \bar{G}_A is the free energy at the site with account for imposed potential U , $\bar{G}_A = G_A + U$ (Fig. 1c). At equilibrium, μ_A must be the same throughout a solid and in equilibrium with the input fugacity of hydrogen imposed by an environment, e.g., H_2 gas at pressure p that has chemical potential of hydrogen $\mu_p = \text{const}$. Then, for all sites at equilibrium $\mu_A = \mu_p$, which yields

$$\left[\frac{\theta_A}{1 - \theta_A} \right]_{eq} = e^{\beta(\mu_p - \bar{G}_A)} = e^{\beta[\mu_p - (G_A + U)]}$$

or

$$\left[\frac{C_A}{(N_A - C_A)S_A} \right]_{eq} = \frac{1}{NS_A} \left[\frac{C_A}{Y_A} \right]_{eq} = e^{\beta\mu_p} \quad (11)$$

where $S_A = \exp(-\beta\bar{G}_A)$ is the solubility factor. From the kinetics point of view, the numbers of forward and backward jumps between the nearest neighbour sites of distinct types in equilibrium are equal to each other in a volume $d^3\mathbf{x}$ around a point \mathbf{x} .

This is expressed by detailed balance relation [20] being nothing else than equilibrium partition Eq. (3), which gets now more forms:

$$C_A \Omega_{AB} Y_B = C_B \Omega_{BA} Y_A$$

or

$$C_A d_{AB} Y_B = C_B d_{BA} Y_A$$

or

$$\theta_B (1 - \theta_A) = \theta_A (1 - \theta_B) \exp[\beta(G_A - G_B)]. \quad (12)$$

One can easily verify that fluxes J_I ($I = A, B, \dots$) are nil at equilibrium by virtue of Eq. (11), and that the sum $J_{AB} + J_{BA}$, $A \neq B$, does the same with the aid of the detailed balance (12). Therefore, the total flux (6) is nil at equilibrium. In addition, Eq. (9) at equilibrium yields $\partial C_A / \partial t = 0$ for all A-s by virtue of Eqs. (11) and (12), the last term in brackets in Eq. (9) being a paraphrase of the detailed balance (12).

4. DERIVATION OF NEW FIELD EQUATIONS AND RETRIEVAL OF PREVIOUS MODELS

4.1. One-level System

In the case of diffusion over identical sites, say L-sites, Eqs. (5), (6), and (9) in the absence of any potential field $U(\mathbf{x})$ render Fick's laws for isothermal diffusion with lattice diffusivity $D_L = d_{LL} = \Omega_{LL} l_{LL}^2$ [11,13,15]. As well, they lead to the equations of uphill diffusion under imposed potential U , e.g., due to lattice dilatation under hydrostatic stress σ , when $U = -V_H \beta \sigma$, V_H is the partial molar volume of H in metal, as they are known both for dilute solutions at $\theta \ll 1$ [1,2,11,21] (hereafter the site type labelling is skipped wherever convenient) and for arbitrary degree of

saturation $\theta = C/N$ [22]. For the latter consideration (a more general case of analysis), the corresponding reduction of Eq. (5) yields:

$$\mathbf{J} = -D_L [\nabla C + \beta C(1-\theta)\nabla U]. \quad (13)$$

The balance equation is established then by common continuity relation, cf. Eq. (7).

4.2. Multi-level System, Implicit Description of Trapping: The Variable Solubility Model

Since the origin of potential $U(\mathbf{x})$ was not relevant in derivations, it can incorporate the intrinsic own lattice potential relief with variable depths of wells at interstitial sites, which yields variable solubility $S(\mathbf{x})$ according to the well bottom $\bar{G}(\mathbf{x})$ at location \mathbf{x} . This can be complemented with variable saddle point energy $E(\mathbf{x})$. Then, skipping site labels that become irrelevant, both Eqs. (5) and (6) can be rewritten in terms of the non-uniform both solubility and diffusivity as follows:

$$\mathbf{J} = -D(1-\theta)C\nabla \ln\left(\frac{C}{(1-\theta)S}\right) = -D(1-\theta)^2 S\nabla\left(\frac{C}{(1-\theta)S}\right), \quad (14)$$

where (cf. expressions (4), (5) and (11))

$$D(\mathbf{x}) = \omega_0(\mathbf{x}) \exp[-\beta(E(\mathbf{x}) - \bar{G}(\mathbf{x}))]^2$$

and

$$S(\mathbf{x}) = \exp(-\beta\bar{G}(\mathbf{x})). \quad (15)$$

With these flux equations, the mass balance is established by usual continuity relation, cf. Eq. (7).

This mode to describe diffusion, named the *non-uniform solubility model* [10], deals with a system where neither interstitial positions nor saddle points are all identical, and so, it treats in effect a multilevel system. Though, specific sites are here indiscernible within each elementary volume $d^3\mathbf{x}$ around a point \mathbf{x} , where the values $\bar{G}(\mathbf{x})$ and $E(\mathbf{x})$ can be interpreted as

effective averages over different sites with account for their amounts in regions, which are small in macroscopic sense, but large enough in microscopic one. Such averaging counts implicitly on equilibrium partition of a diffuser between sites of different kinds in d^3x disregarding traps filling/emptying kinetics.

Anyhow, excepting the term $(1 - \theta)$ that accounts for sites saturability, these equations render fairly the same as established for dilute solutions ($\theta \ll 1$) elsewhere both within the frameworks of microscopic kinetics [10] and macroscopic thermodynamics [1,5,9]. To this end, built up upon phenomenological account of measurable variables, but not relying on specification of atomic mechanisms, the latter approach extends the suitability of hydrogen diffusion description by means of Eq. (14) over much wider range of circumstances, such as non-uniformity of alloy composition, transient external fields (e.g., mechanical stresses), simultaneous (e.g., strain induced) phase transformations, cold working, non-isothermal diffusion (Soret effect), etc. [1,5,9,11]. Till now, these factors could not be incorporated satisfactorily in diffusion models via kinetics considerations. From another side, diffusion modelling accounting for the kinetics of H transitions between different microstructural entities (“sites”) is not feasible on the way of thermodynamics.

4.3. Multi-level System, Explicit Description of Trapping

When conditions of system equilibrium are not fulfilled, it evolves to equilibrium. Various transitions can be discerned there. One of them is rather long-distance transfer that drives to global equilibrium via fluxes represented by respective equations of the previous section. Besides, localised processes of H exchange between the nearest sites of different kinds are there involved, too, which tend to local equilibrium expressed by the detailed balance (12). Corresponding process rates, which may depend on both intrinsic (e.g., vibration frequency and jump length) and extrinsic (such as diffusion distance) factors, may be so distinct, that in the time scale of interest (e.g., for membrane permeation or for hydrogen delivery to fracture locations) some processes may have attained equilibrium while others have not yet.

4.3.1. Diffusion under Traps-Lattice Equilibrium

One possibility of the mentioned partial equilibrium is when detailed balance is quickly reached and maintained during diffusion, e.g., when relatively long diffusion distances x_{cr} with corresponding times $t \sim x_{cr}^2/(4D)$ [23] are of interest. Suggested by Oriani [17] to be kept during diffusion, the hypothesis of local equilibrium assumes that detailed balance (12) holds for all nearest neighbour A and B sites, so that partial balance (9) in the case of multiple B-sites yields the following:

$$\begin{aligned} \frac{\partial C_A}{\partial t} = & d_{AA} \nabla \cdot \left[Y_A C_A \nabla \ln \left(\frac{e^{\beta U} C_A}{Y_A} \right) \right] + \\ & + \sum_B d_{AB} \frac{C_A}{C_B} \nabla \cdot \left[Y_B C_B \nabla \ln \left(\frac{e^{\beta U} C_B}{Y_B} \right) \right] \end{aligned} \quad (16)$$

The global balance (7) for two-level system (for multi-level systems the sum has to be obtained over all site types) under local equilibrium is reduced to the following equation:

$$\begin{aligned} \frac{\partial C}{\partial t} \equiv \frac{\partial (C_A + C_B)}{\partial t} = \\ = \nabla \cdot \left[(d_{AA} Y_A C_A + 2d_{AB} Y_B C_A + d_{BB} Y_B C_B) \nabla \ln \left(\frac{C_A}{S_A Y_A} \right) \right] \end{aligned} \quad (17)$$

Accompanying Eq. (17) with the detailed balance (12), which may be solved with respect to C_B ,

$$C_B = \frac{N_B C_A K / N_A}{1 + C_A (K - 1) / N_A} \quad (K = e^{\beta E_b}, E_b = G_A - G_B) \quad (18)$$

the system of partial-differential equations of diffusion with trapping converts into the system of one partial-differential and a series of algebraic equations (17) and (18) with respect to the partial concentrations C_I ($I = A, B, \dots$). This system transforms into the sole differential equation (17) with respect to C_A by introducing in Eq. (17) the value C_B given by Eq. (18).

It can be verified that, labelling $A \equiv L$ to be lattice sites and $B \equiv T$ traps, at $\theta_L \ll 1$ and $\gamma_T \ll \gamma_L \approx 1$, and so, $Y_T \ll 1$, which are usually met in HAF of engineering alloys [6], and $d_{BX}/d_{AX} \sim \exp(-\beta E_b) < \sim 10^{-4}$ at $E_b > 0.2$ eV

[2,14,15] for $X = L$ or T , Eqs. (17)-(18) convert into the equation of trap-assisted diffusion [4] in the same form as implemented by Oriani in the classical work [17] in which the equilibrium hypothesis was formulated as:

$$\left(1 + \frac{\partial C_T}{\partial C_L}\right) \frac{\partial C_L}{\partial t} = \nabla \cdot [D_L (\nabla C_L - C_L \nabla \ln S_L)]$$

at $C_T = C_L K N_T / (N_L + K C_L)$. (19)

4.3.2. Diffusion Accounting for Lattice/Trap Exchange Kinetics

The system of equations (9), describing hydrogen diffusion affected by traps in general terms, is tough to solve. Taking advantage of circumstances usually met in HAF, it can be reduced to more suitable forms. Namely, $\theta_L \ll 1$, $\gamma_T \ll \gamma_L \approx 1$, and thus $Y_T \ll Y_L \approx 1$, as well as $d_{TX}/d_{LX} \ll 1$ ($X = T$ and L) usually hold in HAF, but the matter of local L/T-equilibrium is not ensured *a priori*. Then, assuming that T→T jumps are fairly improbable, the total flux \mathbf{J} , Eq. (6), and the partial balance for C_T , Eq. (9), can be assessed as follows:

$$\mathbf{J} = \mathbf{J}_{LVL} \left\{ 1 + \frac{d_{TT}}{d_{LL}} \left[Y_T O \left(\frac{|\nabla C_T|}{|\nabla C_L|} \right) + O \left(\frac{C_T}{C_L} \right) \right] + \frac{d_{LT}}{d_{LL}} \left[Y_T O(1) + o(C_L) \right] + \frac{d_{TL}}{d_{LL}} O \left(\frac{|\nabla C_T|}{|\nabla C_L|} \right) \right\}, \quad (20)$$

$$\frac{\partial C_T}{\partial t} = \frac{d_{LT}}{d_{LL}} Y_T \nabla \cdot \mathbf{J}_{LVL} + \frac{1}{f l^2} (d_{LT} Y_T C_L - d_{TL} C_T). \quad (21)$$

Accordingly, if neither ratios of partial concentrations C_T to C_L and their gradients nor the divergence of lattice-hopping flux \mathbf{J}_{LVL} are too large to forbid the disregard of terms with $d_{TX}/d_{LX} \ll 1$ and $Y_T \ll 1$ in Eqs. (20) and (21), then Eqs. (17)-(18) convert into the system of partial- and ordinary-differential equations postulated by McNabb-Foster [7], which is now extended for variable solubility S_L :

$$\frac{\partial}{\partial t} (C_L + C_T) = \nabla \cdot [D_L (\nabla C_L - C_L \nabla \ln S_L)] \quad (22)$$

$$\frac{dC_T}{dt} = (k_{LT}/N)(N_T - C_T)C_L - k_{TL}C_T. \quad (23)$$

Obviously, these specialised equations of trap-affected diffusion are additively extensible for the case of multiple trap kinds T_i ($i = 1, \dots$) in the same form as the antecedent general Eqs. (7) and (9) do.

The system of equations (22)-(23) with respect to a number of concentrations C_i ($i = 1, \dots, m$) may complicate numerical simulations of diffusion making corresponding discrete approximations of the boundary-value problems oversized. However, the equation (23) has the following closed-form solution:

$$C_T = \exp\left(-\int_0^t P_T(\zeta)d\zeta\right) \left[\int_0^t \left(\exp\left(\int_0^\xi P_T(\zeta)d\zeta\right) Q(\xi) \right) d\xi + C_T^0 \right] \quad (24)$$

where:

$$P_T(t) = k_{TL} + k_{LT}C_L(t)/N \quad (25)$$

$$Q(t) = k_{LT}N_T C_L(t)/N \quad (26)$$

$$C_T^0 = C_T|_{t=0} \quad (27)$$

the latter being the initial condition. Substitution of the expression (24) into Eq. (22) reduces the problem to the sole integro-differential-equation with respect to C_L . Its computational implementation, e.g., via available finite element routines [4-6], requires modification only of calculation of concentration capacity matrices.

5. CONCLUSIONS

The rigorous and innovative equations formulated in this paper are adequate for the continuum modelling of trap-affected diffusion of hydrogen in metallic materials and alloys, on the basis of sound kinetics theory foundations and convenient derivations.

The system of equations of diffusion with trapping, derived here from kinetics principles, provides generalisation of pertinent previously-suggested equations, as well as it retrieves special models of hydrogen diffusion, either raised on thermodynamics bases or postulated partially from microscopic considerations and assumptions.

Following this approach, simpler equations of specialised models gain clarification about the involved approximations and about the requisites of their applicability to particular cases. This allows reasoned pondering of their advantages and limitations to select optimal models for analyses of hydrogen assisted fracture (HAF) processes.

Acknowledgements

The authors wish to acknowledge the financial support provided by: (i) the Spanish Ministry for Science and Innovation through Grant BIA2011-27870 and (ii) by the European Union (EU) through the EU 7FP Project “MultiHy”: Multiscale modelling of hydrogen embrittlement in crystalline materials (<http://multihy.eu>) through Grant agreement no. 263335.

REFERENCES

1. J. Toribio and V. Kharin, *Corros. Rev.* 19: 207–252, 2001.
2. J.P. Hirth, *Metall. Trans.* A11: 861-890, 1980.
3. R.P. Gangloff, in: *Comprehensive Structural Integrity. Vol. 6*, Elsevier, 2003, pp. 31–101.
4. P. Sofronis and R. McMeeking, *J. Mech. Phys. Solids* 37: 317-350, 1989.
5. J. Toribio and V. Kharin, *ASTM STP* 1343: 440-458, 1999.
6. A. Krom and A. Bakker, *Metall. Trans.* B31: 1475-1482, 2000.
7. A. McNabb and P. Foster, *Trans. AIME* 227: 618-627, 1963.
8. I. Bekman, in: *Interaction of Hydrogen with Metals*, Moscow, 1987, pp. 143-177.
9. J. Waisman, G. Sines and L. Robinson, *Metall. Trans.* 4: 291-302, 1983.
10. J. Leblond and D. Dubois, *Acta Metall.* 31: 1459-1469, 1983.
11. S. Bokshstein et al, *Thermodynamics and Kinetics of Diffusion in Solids*, Oxonian Press, 1985.
12. V. Kharin, *Sov. Mater. Sci.* 23: 348-357, 1987.
13. R. Kirchheim, *Acta Metall.* 30: 1069-1078, 1982.
14. A. Pisarev and B. Chernikov, in: *Interaction of Hydrogen with Metals*, Moscow, 1987, pp. 233-264.
15. Y. Fukai, *The Metal-Hydrogen System*, Springer, 2005.
16. J. Toribio and V. Kharin, *Mater. Sci.* 42: 263-271, 2006.
17. R. Oriani, *Acta Metall.* 18: 147-157, 1970.
18. R. Barrer, *J. Membrane Sci.* 18: 25-35, 1984.

19. J.M. Hill, *Scripta Metall.* 13: 1027-1031, 1979.
20. A. Allnatt and A. Lidiard, *Atomic Transport in Solids*, Cambridge Univ. Press, 2003.
21. H. Wipf, *Phys. Scripta* T94: 43-51, 2001.
22. R. Fuentes-Samaniego and J. Hirth, *Phys. Stat. Solidi* 106: 359-371, 1981.
23. R. Barrer, *Diffusion in and through Solids*, Cambridge Univ. Press, 1951.

EFFECT OF AGEING ON HARDNESS, CV TOUGHNESS AND FRACTURE OF A Fe-CrNiMo ALLOYS

B. Žužek, F. Vodopivec, R. Celin, M. Godec

Institute of Metals and Technology, Ljubljana, Slovenia

borut.zuzek@imt.si

Abstract: The cast alloys with the microstructure of austenite and different content of δ ferrite were aged in temperature range from 290 °C to 350 °C for up to 2 years. Mechanical properties were determined and fractures of CT specimens were examined. The comparison of increase of hardness and change of CT showed that by alloys with 27 % and 11 % of ferrite, the rapid decrease of CT was limited in a small interval of increase of ferrite hardness. The ferrite hardness increase is due to elastic stresses generated by spinodal decomposition. The calculated chromium diffusion length at ageing temperature 350 °C was about $3.1 \cdot 10^{-10}$ m and about 10^3 to 10^4 times smaller than the size of ferrite grains. It was concluded that the rapid drop of CT was due to ferrite-austenite interfacial elastic stresses due to spinodal decomposition of a thin ferrite layer.

Key words: microstructure, austenite, δ -ferrite, ageing hardness, CV toughness, spinodal decomposition

1 INTRODUCTION

As cast and forged Fe-CrNiMo alloys of appropriate composition are used for essential parts of nuclear power plants. The alloys solidify with a two phases ($\gamma + \delta$) microstructure¹⁻¹⁰ with a different content of alloying elements in both phases. The microstructure of the examined alloy with 27

% δ ferrite is shown in Fig. 1. If the precipitation of carbide and nitride particles in austenite is omitted, as without significant effect on austenite properties, the solid solution in austenite is stable, while the solid solution in ferrite is unstable. With rate depending on diffusion rate at operation temperature, ferrite solid solution decomposes with a spinodal mechanism to two constituents with different chemical composition: one enriched with nickel (α_1) and the other (α_2) enriched with chromium and molybdenum¹⁻¹². Both constituents preserve the ferrite lattice, while, depending on their chemical composition, lattice parameter is changed and the change generates internal and interphase elastic stresses, which increase the hardness and decrease the ductility, Charpy notch toughness (CT) and fracture toughness¹⁻¹⁰.

2. EFFECT OF AGEING ON HARDNESS OF δ FERRITE AND ALLOY CV TOUGHNESS

The change of properties is related to the extent of spinodal decomposition which is faster at higher temperature because of greater diffusion rate and by greater alloy content in ferrite. By aging in temperature range from 290 °C to 350 °C, the hardness of austenite remained virtually unchanged^{1,2}, while, hardness of ferrite increased stronger and faster by aging at higher temperature. Accordingly, at sufficient aging time, CT was decreased stronger at higher content of ferrite and faster at higher temperature^{1,2,3}. In dependence CT versus aging time (Fig. 2),² three periods of CT decrease rate are distinguished: initial period of slow and low, rapid and strong decrease and again low and slow decrease by longer aging time. The careful examination of these dependences for alloys with 27 and 11 % ferrite showed that rapid decrease of Charpy toughness (CT) by ageing at 350 °C (Fig.3) started by apparent average δ -ferrite hardness of about 300HV and ended by about 420HV (Fig. 3). By longer ageing, the hardness increased continuously and faster, while CT decreased much slower.

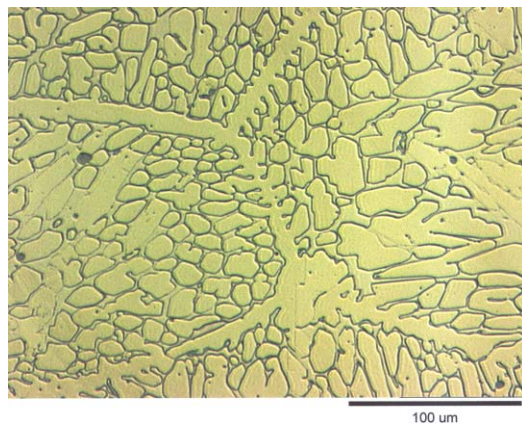


Figure 1. Microstructure of the examined alloy with 27 % of δ ferrite²

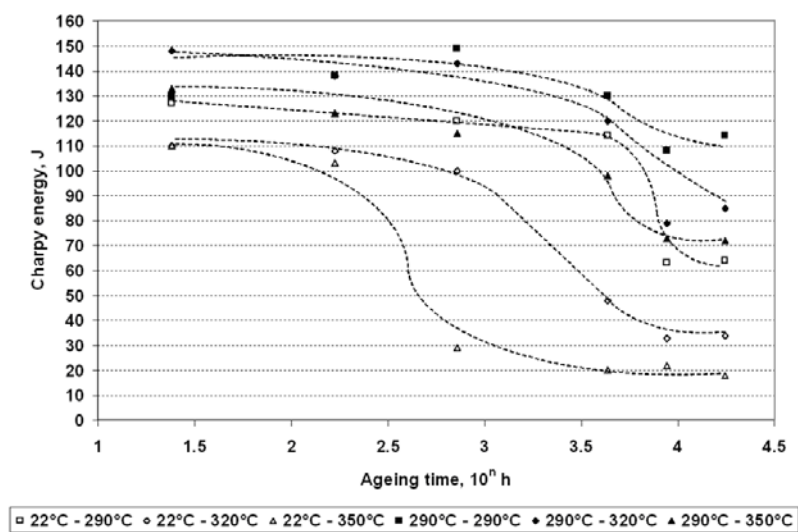


Figure 2. Effect of ageing time at temperatures 290 °C, 320 °C and 350 °C on CT of the alloy with 27 % δ ferrite at ambient temperature²

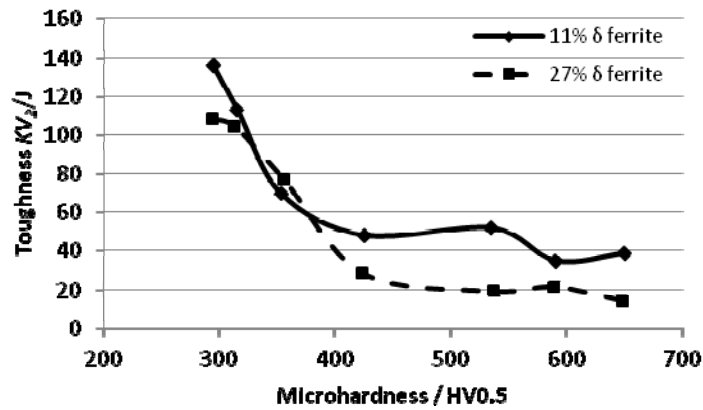


Figure 3. Room temperature log-log dependence of δ ferrite hardness and CT for alloys with 27 % and 11 % δ ferrite

It is evident that the higher rate of decrease of CT by increased ferrite hardness is independent on the content of δ ferrite in the alloy.

3. CT FRACTURE SURFACE

CT specimens, unaged and aged were examined in scanning electron microscope and different fracture micromorphology was found. By high CT, the fracture surface is consisted of ductile dimples of irregular size and small inserts of cleavage (Fig. 4). No difference of dimples shape and size was distinguished between austenite and ferrite areas. By low CT, the fracture surface is consisted of a mixture of areas of cleavage with straight low and short edges, uneven, also ramified and higher ductile ridges and inserts of slight wavy intercrystalline decohesion facets (Fig. 5 and 6). The higher, ductile ridges were the final fracturing event. The fracture surface indicates that by low CT, cleavage was predominant, but also intergranular decohesion occurred and that also by the lowest CT, part of fracturing process was ductile with ductile ridges of final decohesion event.

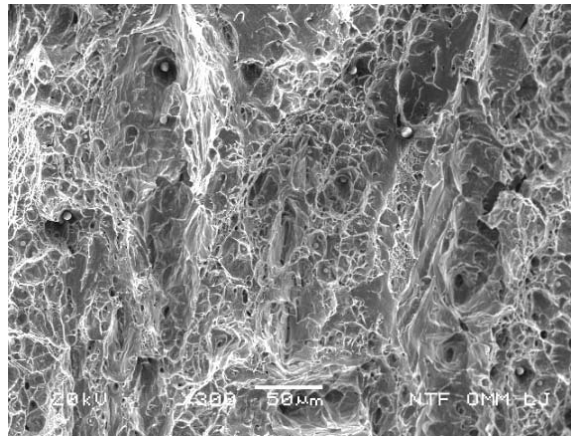


Figure 4. CT fracture surface of unaged alloy

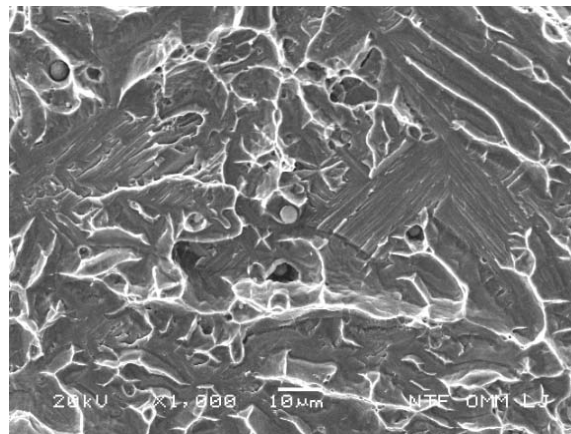


Figure 5. CT fracture surface of the alloy aged for 12 months at 350 °C

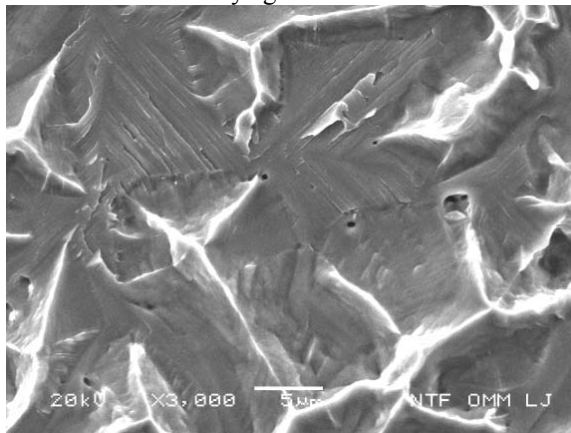


Figure 6. CT fracture surface of the alloy aged for 12 months at 350 °C

4. DISCUSSION

Experimental observations confirm that the lowering of CT is related to the increase of ferrite hardness and it is more rapid in a range of apparent low increase of hardness and that by the lowest CT, part of decohesion is ductile. Theoretically, only ferrite is propensive to ductile and cleavage decohesion, while austenite is propensive to ductile decohesion, only. The intergranular inserts on CT fracture surface show that the aging makes the alloy propensive to decohesion at the phase boundaries austenite - δ ferrite. Considering the much greater lowering of CT in the limited range of increase of hardness of ferrite and the partial intergranular fracturing, it seems logical to conclude that fast decrease of CV toughness occurs already by spinodal decomposition of a layer of ferrite at the boundary of both phases. Such decomposition generates elastic stresses sufficient for the greater and very rapid CT decrease by partial increase of ferrite hardness. The approximate thickness of the layer of spinodal decomposition was deduced with the calculation of the diffusion length of chromium, which redistribution is the essential part of the ferrite spinodal decomposition. The diffusion rate of chromium atoms from a constituent α_1 to a constituent α_2 is calculated as.

$$D_{Cr,T} = D_0 \cdot \exp\left(\frac{Q}{RT}\right) \text{ and } D_{Cr,T} = 3.7 \cdot 10^{-2} \cdot \exp\left(\frac{-257000}{RT}\right) \quad (1)$$

With $D_{Cr,T}$ chromium diffusion rate at temperature T in K and Q – activation energy for chromium diffusion in ferrite¹¹ and R – universal gas constant. The careful examination of dependences of CT versus aging time of experimental data in ^{1,2} show that the rapid CT decrease started after about 168 h at 350 °C, 720 h at 320 °C and 4320 h at 290 °C. Assuming as approximate diffusion path length $x_D \approx (D \cdot t)^{\frac{1}{2}}$ $x_{D350} = 3.1 \cdot 10^{-10}$ m, $x_{D320} = 1.7 \cdot 10^{-10}$ m and $x_{D290} = 1.0 \cdot 10^{-10}$ m are deduced from eq. (1). By aging time at end of rapid CT decrease, approximate deduced diffusion paths are $x_{D350} = 1.35 \cdot 10^{-9}$ m and $x_{D320} = 9.66 \cdot 10^{-9}$ m. The minimal width (thickness) of δ ferrite inserts is above 10^{-6} m. Disregarding the approximation of the calculation, the widths of diffusion layer are much lower than the width of ferrite inserts and support the conclusion that by aging, rapid CT decrease starts when the the spinodal decomposition are achieved in a thin surface layer of δ ferrite at the interface of austenite-ferrite.

5. CONCLUSIONS

Experimental data and their analysis support the following conclusions:

- By ageing, spinodal decomposition of ferrite in a two-phase alloy austenite - δ ferrite occurs;
- By ageing, rapid decrease of CV toughness occurs in an interval of limited increase of apparent hardness of δ ferrite. By longer ageing, the rate of decrease of CV toughness is much lower, although the apparent hardness of ferrite increases continuously;
- The fracture surfaces of unaged alloy consist of irregular ductile dimples and rarest inserts of cleavage. By aged alloy, the cleavage inserts area is greater, intergranular inserts are frequent and ductile ridges of final decohesion are observed also by the lowest CT;
- It is concluded that the initial rapid decrease of CT is due to elastic stresses generated at the phase boundary austenite δ -ferrite by the spinodal decomposition of surface layer of ferrite;
- The calculation of the diffusion path of chromium shows that by start of rapid decrease of CV toughness, the spinodal decomposition would be achieved in a layer of ferrite with much lower thickness than the width of ferrite inserts in the alloy microstructure.

The Authors are indebted to Prof. L. Kosec and Mrs N. Breskvar from MM Dpt of University of Ljubljana for SEM examinations, to Mr. M. Malešević for sample preparation and to the company Nuklearna elektrarna Krško for the support of the investigation.

REFERENCES

6. J. Vojvodič-Tuma, B. Šuštaršič, F. Vodopivec. *Nucl. Eng. Des.* 238 (2008), 1511-1517
7. J. Vojvodič-Tuma, B. Šuštaršič, R. Celin, F. Vodopivec. *Materiali in Tehnologije & Materials and Technology* 43 (2009), 179-187.
8. F. Vodopivec, B. Arzenšek, J. Vojvodič-Tuma, R. Celin. *Metalurgija* 47 (2008), 173-179.

9. G. Slama, P. Petrequin, T. Mager. Assuring structural integrity of steel reactor pressure boundary components. *SMIRT post-conference seminar*, (1983), Monterey, USA, 211.
10. A. Trautwein, W. Gysel. Influence of long term aging of CF8 and CF(M Cast steel at temperature between 300 and 500 °C on impact Toughness and Streuctural properties. *V.G. Behal A.S. melilli: Stainless Steel Castings*, ASTM STP 756 EDs. ASTM, (1982), 165-189.
11. C. Jansson. Degradation of cast stainless steel elbows after 15 years of service. *Fontenraud III-International Symposium*. Royal Abbey of Fontenraud, France, September, (1990), 1/8-8/8.
12. H.M. Chung, T.R. Leax. *Mater. Sci. Techn.* 6 (1990), 249.
13. O.K. Chopra. Estimation of mechanical properties of cast stainless steels during thermal ageing in LWR. *Trans. 13th Intern. Conf. On structural mechanics and reactor technology*, Porto Allegre, Brazil, August (1995).
14. S. Jayet-Gendrot, P. Ould, T. Meylogan. *Nucl. Eng. Des.* 184 (1998), 3-11.
15. J. Kwom, S.Woo, Y. Lee, J-C Park, Y-W Park. *Nucl. Eng. Des.* 206 (2001), 35-44.
16. H.Oikawa, Y. Iijima. Diffusion behaviour of creep resistant steels; Ed. F. Abe, T-U. Kern, R. Viswanathan. *Creep resistant steels*, Woodhead Publ. LTD, Cambridge, England, (2008), 241-266.
17. K. L. Weng et.all. The high-temperature and low-temperature aging embrittlement in A2205 duplex stainless steel. *Bulletin of the college of Engineering, N.T.U., Taiwan*, No.89. October 2003, 45-61.

Author index

- Anes V. 6
Azari Z. 117
- Badea S.G. 32
Barile C., 23
Berezin V.B. 72
Besleaga Cr. 32
Bolshakov A.M. 50
- C.Pappalettere 23
Casavola C. 23, 58
Celin R. 239
Chausov M.G. 72
- de Freitas M. 6
- Gadolina I.V. 167
Godec M. 239
Gubeljak N. 94, 130
- Kapustin V.I. 79
Kharin V. 223
Kornev V. 86
- Li B. 6
Likeb A. 94
- Makhutov N.A. 104
Maksimovskiy E.A. 79
Matvienko Y. 94, 117
Meliani M. 117
- Močilnik V. 130
Mokryakov V. 142
Moramarco V. 58
Morozov E.M. 152
- Negriu R.M. 32
Nykyforchyn H. 156
- Panasyuk V. 156
Pappalettera G. 23
Pappalettere C. 58
Petrova I.M. 167
Pluinage G. 117
Popescu I.C. 32
Predan J. 94, 130
- Reis L. 6
Reznikov D.O. 104
- Shifrin E.I. 171
Shushpannikov P.S. 171
Skvorcov O. 205
- Toribio J. 223
- Vodopivec F.239
- Zakharchenko K.V. 79
Zakharova M.I. 50
Žužek B. 239